Inkjet and screen printing
for electronic applications

Beatriz Medina Rodríguez

Inkjet and screen printing for electronic applications

A dissertation submitted in partial fulfillment of the requirements for the degree of
Doctor of Philosophy in Nanoscience
by the University of Barcelona

Author

Beatriz Medina Rodríguez

Director

Dr. Albert Cirera Hernández

Barcelona, September 2016

Nanoscience Program

Micro and Nanotechnology and Nanoscopies for Electronic Devices (MIND)

Institute of Nanoscience and Nanotechnology (IN^{2}UB)

Department of Engineering, Section of Electronics, Physics Faculty, University of Barcelona

A mi familia

Agradecimientos

Esta tesis doctoral, si bien ha requerido de esfuerzo y mucha dedicación, en ningún caso hubiese sido posible su finalización sin la cooperación desinteresada de todas y cada una de las personas que a continuación citaré y muchas de las cuales han sido un soporte muy fuerte en momentos difíciles.

En un primer lugar, quiero dar mi más sincero agradecimiento a mi director, Dr. Albert Cirera, y a mi tutor en FAE, Dr. Francisco Ramos, por haberme ofrecido la oportunidad y haberme guiado en esta etapa de maduración profesional y personal. He aprendido muchísimo de ellos y estoy segura de que seguiré haciéndolo.

También debo agradecer esta tesis al programa de becas Doctorats Industrials 2012 de l'Agència de Gestió d'Ajuts Universitaris i de Recerca (AGAUR) de la Generalitat de Catalunya que ha financiado recursos y movilidad, así como a la empresa Francisco Albero S.A.U. (FAE). Agradezco a toda la dirección de la empresa por haber contado conmigo durante estos años y seguir haciéndolo y, por supuesto, por su apuesta por la Investigación, Desarrollo e Innovación dentro del mundo industrial. Gracias también al grupo de Micro and Nanotechnologies and Nanoscopies for Electronic and Electrophotonic devices (MIND) de la Universitat de Barcelona por facilitarme sus instalaciones y equipos, así como el ofrecerme su conocimiento y ayuda a lo largo de estos casi cuatro años.

Cabe destacar también la importante colaboración de Dra. Mónica Colina, por su contribución en la puesta a punto y la caracterización de las celdas fotovoltaicas estudiadas en esta tesis, así como el apoyo de Dr. Edgardo Saucedo y Prof. Dr. Alejandro Pérez, todos ellos pertenecientes al Instituto de Investigación en Energía de Cataluña (IREC). También agradecer enormemente la colaboración de Prof. Dr. Josep María López Villegas del Grupo de Radiofrecuencia de la Universitat de Barcelona, en el diseño y caracterización de los inductores fabricados durante los últimos meses de esta tesis.

No me puedo olvidar de mis compañeros, que me han apoyado siempre y me han ayudado a progresar. Gracias a todos los trabajadores de FAE que en algún momento u otro me han ayudado, concretamente a Jose, Asun y Paula, pero sobre todo a mis compañeros del Departamento de I+D+i. Quiero agradecer a todos y cada uno de ellos; a los que aún están y a los que no, y a los que se han ido sumando recientemente. Muchas gracias a Ferran, Xavi, Carlos,

Por último, quisiera recordar a aquellas personas que he perdido durante estos años: a mis abuelos, Pedro y Lola, porque siempre que hablo de ellos me sale una sonrisa en la cara. Me pesa haberles perdido estando lejos, pero sé que me apoyaban en mis decisiones y que ahora estarían orgullosos de mí. Y también quiero mencionar a Mercé y Chente, a quienes tampoco olvido. DIP.

Content

Chapter 1

Introduction

1.1- Printed electronics technologies

Printed electronics (PE) is a set of printing methods used to create electrical devices on various substrates. Printing typically uses common printing equipment suitable for defining patterns on material, such as screen printing, flexography, gravure, offset lithography, and inkjet. Electrically functional, electronic or optical inks are deposited on the substrate, creating active or passive devices.

PE offers a great advantage when compared to traditional processes or microelectronics due to its versatility, low manufacturing cost and the possibility of generating flexible circuit components[1]. Furthermore, these techniques are suitable for roll-to-roll processes and open the possibility for printing large areas and in a large-scale production[2].

The potential of printed electronics is impossible to be fully appreciated without the knowledge on the different techniques. Screen printing, gravure and flexography are the main conventional ones. These processes operate differently in terms of pattern surfaces, relief or stencil types[3] but, each of them requires a mask or pattern to perform printing, needing a tiresome and laborious preprocessing of pattern manufacturing before they can be implemented in a fast, high-scale production. In fact, some printing processes such as flexography or gravure have a very high startup cost. They are economically only viable for very large batches.

Unlike conventional technologies, digital printing such as inkjet printing does not need a prefabricated mask and it is also a non-invasive technique being contactless with the substrate. One of the main premises of inkjet technique is its accurate positioning and precise volume drop of microliters of the functional material, providing the possibility to print very close conductive tracks (tens of microns) and extremely thin layers (< 0.3 μm) and thus minimizing device size and manufacturing costs, owing to the reduced amount of material waste[4]. Inkjet is still in development[5] and shows a great challenge in terms of performance and reproducibility and the

availability of functional materials in the market[6] compared to the conventional techniques. However, its versatility explains the high potential of the implementation in current production lines, since it gives rise to new designs, assuming more restrictive applications, and featuring the ability to print "on demand" and in a scalable way[7]. Actually, most of the cases of short run length, as rapid prototyping, make digital printing the major affordable technology[8].

There is increasing demand for high quality and low cost electronic components such as RFID tags, thin film transistor, flexible sensor and devices, super capacitor, etc., which require innovative fabrication techniques that are faster and cheaper compared to traditional production methods[9,10]. It is also expected that the market of printed electronics in automotive applications will grow to over $5.5 billion dollars in the next decade[11]. So it could be said that is one of the fastest growing technologies in the world and of vital interest to industries.

The selection of the printing technique is crucial to achieve a good result and it will largely depend on both, the material needed and dimensional and functional requirements pursued. Each technology offers different possibilities in terms of resolution, complexity, versatility, speed, layers thickness, materials, reliability and scalability. This work aims to dig deeper into two of the main techniques in the world of printed electronics: screen printing and inkjet printing for different applications and for the manufacturing of different devices. In addition, the capabilities of a technology that is currently in growing development (inkjet)[12,13] are analyzed in comparison with the mature screen printing technique to give a wider insight of the advantages and limitations that this technology offers. The totally knowledge in this technique is still in progress and it arises to be a trend in technological and scientific aspects due to the barely availability of functional materials[14] and the difficulties in achieving a precise control on the drop formation and its interaction in the final system[15,16,17]. A better understanding of these technological issues, as well as the approaching to current difficulties in electronic applications is accomplished in this thesis. Up-to-date issues as the reliability of flexible resistive gas sensors, solution-based synthesis of absorber layers in thin film solar cells and the tuning and area reducing for inductors in RF applications are tackled.

1.2- Aims and objectives

The strengths and weaknesses, as well as the strategies to overcome the limitations of two of the main printing techniques, will be discussed in detail in this thesis. A comparison between a

mature and reliable technology, screen printing (SP), that has already been well-accepted in the industry for years and a rising-up technique, inkjet printing (IP), that is pushing hard into the electronic market.

Creating a synergy between the industry and the academia, this work has been carried out in the facilities of the company Francisco Albero S.A.U. (FAE) and the University of Barcelona (UB). So that, this thesis has grown in the bosom of an established and consolidated knowledge on screen printing, whose equipment and procedures have been already studied and optimized in several PhD dissertations [18,19,20], carried out under collaboration between FAE and UB.

The main objective in this thesis arises from the need of expanding the knowledge on inkjet printing by exploring affordable new possibilities, taking as starting point the previous knowledge of screen printing. To pursue this goal, the comparison between SP and IP is presented along the thesis. The framework of this thesis is not solely an overview of the development of functional materials for both techniques, but also the investigation of its final implementation reliability in several devices for different electronic applications.

This objective devolves the achievement of several goals:

1- Generation of know-how in the formulation of different functional materials (pastes for SP and inks for IP) and the establishment of suitable criteria in the evaluation of these new solutions.

2- Fabrication of reliable and low-cost flexible resistive gas sensors platforms by means of both printed technologies, understanding the failure phenomena in the printed devices by both technologies, implementing solutions and providing reliability to them.

3- Replacement of several expensive deposition steps of absorber precursors for thin film CZTS solar cells for just one step of printing where, apart from the low-cost of the technique itself, material waste is almost nonexistent. This aims to demonstrate the possibility of including IP as a proper fabrication technique for thin film solar cells.

4- Implementation of IP for high-frequencies applications. Even if IP is quite settled for DC or low frequency applications, few results on electrical characterization at RF or microwave frequencies are present due to its low conductivity. The low thickness achievable in each IP printing makes it inappropriate and beforehand uncompetitive; however, the potential of increasing the spiral density in planar inductors becomes a good allurement for reducing the devices size. Furthermore, customization and tuning are keywords in the design of nowadays electronic circuits

and systems, providing digital printing such as IP a special interest. It is because of this, that a combination of IP, as the definer of the conductor lines, and electroless deposition, as the solution for the limited thickness is studied in here.

All of these goals are trends in current research. The development of inks is being studied for different applications such as flexible electronics[21], ceramic tiles decoration[22] or active packaging[23]. Besides, flexible sensors are important for cutting-edge applications such as wearable electronics and, nowadays, IP has become a widely used technique for flexible gas sensors applications[24,25,26]. In the case of thin film solar cells, solution-based materials are a desirable route for the synthesis of the absorber layer, and IP is moving up as an attractive technique for CZTS precursors[27], CIGS[28] or even the trendy perovskite[29]. Finally, the use of IP in RF applications is finding its way to become competitive[30] for antennas[31,32] or amplifiers[33].

1.3- Outline

The structure of this thesis dissertation can be divided in two well defined blocks. In chapter 2 and 3, both printing techniques are explained in detail, while in Chapter 4, 5 and 6, the potential of both technologies are studied for different electronic applications by means of the fabrication and characterization of different devices.

In chapter 2, the main topic is the analysis of the inkjet printing technique. This chapter follows the attainment of two different objectives: the establishment of a quality evaluation guideline for any inkjet ink and as example of it, the formulation of our own silver ink developed in our laboratory. In this sense, the most important properties for the functional materials which should be under control during its formulation are reviewed; as well as the fundamentals and main parameters during the printing process, which affect the outcome quality. Instead, in chapter 3, the fundamentals of screen printing technique are quickly overviewed due to the consolidation of the technique knowledge and the previous studies on it done in the field, and specifically at FAE Company[18, 19, 20].

In the second block of this thesis, the description of the printing techniques leads to the implementation of both, inkjet and screen printing, in different electronic fields. The chapters involving this block are focused in the printing step during its fabrication, the printing and functional material quality characterization, and the influence of this printing step in the functional performance of the devices.

Chapter 4 is a comparison between low-cost flexible resistive sensor platforms with heater fabricated by both, SP and IP techniques. The performance of these sensor platforms was checked by long-term characterization and aging tests to identify the causes of the device failure. Chemical degradation of silver is observed in SP-devices due to the flake-like morphology of the deposits but not in the smooth sintered silver tracks deposited by IP. However, the IP very thin film promotes failure by hot spot phenomena. Design improvements are, hence, implemented to overcome the drawbacks of silver corrosion and power consumption. The final devices turned to be sturdy, wearable and reliable gas sensor platforms.

In Chapter 5, IP is implemented in the step of the absorber layer synthesis for the fabrication of kesterite thin film solar cells. Copper-Zinc-Tin-Sulfur (CZTS) precursor ink is formulated and optimized for the enhancement of the solar cell performance. The influence of the formulation and the printing process is analyzed. Finally, the thickness of the deposited precursor was modified until obtained a cell with 6.55% efficiency, the higher efficiency reported with this absorber type using IP as deposition method.

In the last chapter, Chapter 6, spiral inductors are fabricating using the two printing technologies in LTCC (low-temperature-cofired-ceramics). IP, although turning out to be a suitable technology for enhancing the accuracy of narrower tracks than SP and thus, for increasing the number of turns within a concrete area, presents difficulties to achieve a certain value in electrical conductivity due to the deposition of very thin conductor layers. For this reason, in this part of the thesis, a combination of IP with electroless copper deposition is used to overcome this limitation and to develop equivalent performances using SP and IP devices.

References

[1] H.-Y. Tseng, (2011). Scaling of Inkjet-Printed Transistors using Novel Printing Techniques. University of California at Berkeley

[2] K. Suganuma (2014), Introduction to Printed Electronics, Springer, Brief of Electrical and Computer Engineering, 74

[3] M. Nandakumar and A. Paramasivam (2006), *Gravure, flexography and screen printing*, 'L' Scheme Syllabus. Sivakasi: Department of Printing Technology, Arasan Ganesan Polytechnic College

[4] T. H. J. van Osch, J. P. (2008). *Inkjet Printing of Narrow Conductive Tracks on Untreated Polymeric Substrates*. Advanced Materials 20, 343-345

[5] J. Doggart (2011). *Inkjet Printed Conductive Inks for the Fabrication of Organic Thin Film Transistors*. Hamilton, Ontario (Canadá)

[6] S. Magdassi (2010). *The Chemistry of Inkjet Inks*. Hebrew University of Jerusalem

[7] D. Baron, F. Bruening, R. Taylor (2010), *Organic and Printed Electronics-A View from the Traditional Market Place*, SMTA International Conference

[8] Y. Kawahara (2013*), Instant inkjet circuits: lab-based inkjet printing to support rapid prototyping of UbiComp devices*, Proceedings of the 2013 ACM international joint conference on Pervasive and ubiquitous computing, 363.

[9] J. Perelaer, P. J. Smith, D. Mager, D. Soltman, S. K. Volkman, V. Subramanian (2010), *Printed electronics: the challenges involved in printing devices, interconnects, and contacts based on inorganic materials*, Journal of Materials Chemistry, 20, 8446.

[10] X. Wang, T. Li, J. Adams, and J. Yang (2013), *Transparent, stretchable, carbon nanotube-inlaid conductors enabled by standard replication technology for capacitive pressure, strain and touch sensors*, Journal of Materials Chemistry A 1, 3580.

[11] Read more at: http://www.idtechex.com/research/reports/printed-and-flexible-electronics-in-automotive-applications-2016-2026-000460.asp

[12] S. Yoon, S. Sohn, J. Kwon, J. A. Park, S. Jung (2016), *Double-shot inkjet printing for high-conductivity polymer electrode*, Thin Solid Films 607, 55.

[13] T. Tanaka, K. Kadota, Y. Tozuka, A. Shimosaka, Y. Shirakawa (2016), *Improvement in photocatalytic activity of morphologically controlled Pd-supporting TiO2 particles via sol–gel process using inkjet nozzle*, Ceramics International 42 (8), 9963.

[14] H.W. Choi, T. Zhou, M. Singh, G. E. Jabbour (2015), *Recent developments and directions in printed nanomaterials,* Nanoscale, 7 (8), 3338.

[15] F. Vila Garcia (2015), *From characterization strategies to PDK & EDA Tools for Printed Electronics,* PhD. Dissertation, Barcelona, Spain

[16] J. Sun, B. Bao, M. He, H. Zhou, Y. Song (2015), *Recent Advances in Controlling the Depositing Morphologies of Inkjet Droplets,* ACS Applied Materials and Interfaces, 7 (51), 28086.

[17] J. Sun, M. Kuang, Y. Song (2015), *Control and application of "coffee ring" effect in inkjet Printing,* Progress in Chemistry, 27 (8), 979.

[18] C. López-Gándara (2012), *Comprehensive study of YSZ-based electrochemical gas sensors for automotive applications,* PhD. Dissertation, Barcelona, Spain.

[19] J. M. Fernández (2013), *Noves estructures LTCC i HTCC per a sensors de pressió capacitius i per a sensors lambda de tipus resistiu,* PhD. Dissertation, Barcelona, Spain.

[20] F. Ramos (2014), *Integración de la tecnología cerámica multicapa*, PhD. Dissertation, Barcelona, Spain.

[21] W. Zhang, E. Bi, M. Li, L. Gao (2016), *Synthesis of Ag/RGO composite as effective conductive ink filler for flexible inkjet printing electronics*, Colloids and Surfaces A: Physicochemical and Engineering Aspects 490, 232.

[22] Z. Pan, Y. Wang, H. Huang, Z. Ling, Y. Dai, S. Ke (2015), *Recent development on preparation of ceramic inks in ink-jet Printing*, Ceramics International 41 (10), Part A 12515.

[23] N. Caro, E. Medina, M. Díaz-Dosque, L. López, L. Abugoch, C. Tapia (2016), *Novel active packaging based on films of chitosan and chitosan/quinoa protein printed with chitosan-tripolyphosphate-thymol nanoparticles via thermal ink-jet Printing,* Food Hydrocolloids 52, 520.

[24] B. Andò, S. Baglio, G. Di Pasquale, A. Pollicino, S. D'Agata, C. Gugliuzzo, C. Lombardo, G. Re (2015), *An Inkjet Printed CO2 Gas Sensor*, Procedia Engineering 120, 628.

[25] M. Rieu, M. Camara, G. Tournier, J.P. Viricelle, C. Pijolat, N.F. de Rooij, D. Briand (2015), *Inkjet Printed SnO2 Gas Sensor on Plastic Substrate*, Procedia Engineering 120, 75.

[26] L. Huang, P. Jiang, D. Wang, Y. Luo, M. Li, H. Lee, R. A. Gerhardt (2014), *A novel paper-based flexible ammonia gas sensor via silver and SWNT-PABS inkjet printing,* Sensors and Actuators B: Chemical 197, 308.

[27] T. Martini, C. Chubilleau, O. Poncelet, A. Ricaud, A. Blayo, C. Martin, K. Tarasov (2016), *Spray and inkjet fabrication of Cu2ZnSnS4 thin films using nanoparticles derived from a continuous-flow microwave-assisted synthesis,* Solar Energy Materials and Solar Cells 144, 657.

[28] W. Wang, Y.-W. Su, C.-H. Chang (2011), *Inkjet printed chalcopyrite CuInxGa1−xSe2 thin film solar cells*, Solar Energy Materials and Solar Cells 95 (9), 2616.

[29] M. Bag, Z. Jiang, L. A. Renna, S. P. Jeong, V. M. Rotello, D. Venkataraman (2016), *Rapid combinatorial screening of inkjet-printed alkyl-ammonium cations in perovskite solar cells,* Materials Letters 164, 472.

[30] A. Chiolerio, V. Camarchia, R. Quaglia, M. Pirola, P. Pandolfi, C. F. Pirri (2014), *Hybrid Ag-based inks for nanocomposite inkjet printed lines: RF properties,* Journal of Alloys and Compounds 615 (1), S501.

[31] E. Sowade, F. Göthel, R. Zichner, R. R. Baumann (2015), *Inkjet printing of UHF antennas on corrugated cardboards for packaging applications,* Applied Surface Science 332, 500.

[32] T.-M. Wang, N.-W. Pu, Y.-M. Liu, W.-D. Chen, M.-D. Ger, W.-C. Lee, K.-S. Sun (2014), *Fabrication of RFID antennas on non-woven slag fiber paper,* Journal of the Taiwan Institute of Chemical Engineers 45 (1), 242.

[33] V. Camarchiaa, A. Chioleriob, M. Cottoc, J. Fanga, G. Ghionea, P. Pandolfic, M. Pirolaa, R. Quagliaa, C. Ramellaa (2014), *Demonstration of inkjet-printed silver nanoparticle microstrip lines on alumina for RF power modules*, Organic Electronics 15, 91.

Chapter 2

Functional formulations for inkjet printing

2.1- Introduction

Inkjet printing allows using a wide range of substrates (rigid or flexible, rough or smooth) with no need of any mask unlike the conventional printing techniques. Both features enhance the versatility and open the door to new possibilities. The control of every single drop makes inkjet printing accurate being able to achieve a high resolution with low material consumption. However, the long-term durability of inks depends on its stability and the physical properties (such as viscosity or surface tension) need to be absolutely controlled. Furthermore, the ink should be suitable for the substrate in terms of wettability or adhesion, among others. Also, the quality of the deposited functional material by inkjet printing depends highly, but not only, on the post-deposition treatment.

The inkjet ink formulation in the electronic field is under development, being hard to find a good option that fits the requirements in the market and being necessary to order a customized solution usually with a questionable reliability. That point gives a special interest to achieve a good knowledge of the ink formulation being able to fulfill the specific expectations and expanding the potential applications. The aim of this chapter is to dig deeply into the understanding design and evaluation of the quality of an ink for the inkjet printing technology, from its chemical and physical properties to the final electronic performance. It is a collection of experiences and a look at the real problems in inkjet printing. As example, a silver ink is formulated, because being the most developed functional ink, it allows performances comparison.

This part of the thesis has been carried out in the facilities of the University of Barcelona, in the research group Micro and Nanotechnology and Nanoscopies for Electronic Devices (MIND), Department of Engineering: Electronics.

2.2- Objectives

The structure of this chapter is strongly based in two different but parallel objectives. One of them is the establishment of a quality evaluation guideline for any inkjet ink while this route is illustrated by a silver ink developed in our laboratory as second objective.

2.2.1- Quality evaluation route

The performance of an ink can be evaluated in three levels, going from the general definition of an ink to the specific requirements expected for its final application.

Taking into account just the ink as the system under evaluation, an inkjet ink is a suitable fluid to be jetted through a nozzle. This suitability is evaluated by the accomplishment of several physical properties such as viscosity, surface tension or density within a recommended values range, to achieve the drop formation and jetting. Hence, printability in inkjet points out the control and the quality of the drop jetting.

Going deeper into the printing definition, printing is the process to obtain a printed material; hence, a printed ink should be a jettable fluid with a proper deposition onto a particular substrate. According to this, the proper droplets generation does not mean a fluid is suitable to be printable in determinate substrates. The interaction ink-substrate deals with the final printing quality. In the second level of definition, the evaluation will include the ink and the substrate as the control system. Both materials should be chemically compatible and the energy exchanged between the jetted drop and the substrate should be equitable to control the expansion of the drop among the surface and to achieve an optimal wettability. Furthermore, the substrate should withstand the post-treatment needed to obtain the functional material (thermal treatment, plasma or chemical reduction for example).

The third level of evaluation includes the final quality of the post-treated deposition in terms of homogeneity, porosity and adhesion; in a nutshell, the final functional performance of the printed material. The application and the design of the device establish others parameters that will indicate the suitability and the quality of the ink.

2.2.2- Silver ink composition used as the illustrated example

As an experimental case a silver ink has been developed in our laboratory. The silver ink formulation, the same as most metallic inks, can be carried out by two strategies: bottom-up

via organometallic route (Metal-Organic Decomposition, MOD)[1,2] or reducing agent, or top-down by metal nano-powders dispersed by some surfactant.

MOD inks, typically based on a complex of silver ion, are decomposed into its metallic form during sintering. These inks require low curing temperatures and do not need any surfactant due to the absence of solid particles, what can increase the sintering effectiveness. The main problem is that silver MOD ink usually requires of non-polar organic solvents such as xilene[2] or toluene[3], whose high volatility followed by its hazardousness and its bad printing resolution makes the nanoparticulated silver ink a good option. The nanoparticulated inks are very common because of its printability and its larger content of silver. Furthermore, the surface modification of the nanoparticles can be customized according to different solvent medium. The sintering is usually at relatively high temperatures (greater than 200 ⁰C) to achieve proper conductivity[4].

In our case, the silver ink is formulated starting from already-functionalized silver nanoparticles for polar media (Ag-V03) from Metalor[5]. The formulate optimization led to the composition showed in Table 1. Along this chapter the combination and concentration of these solvents will be explained.

	Composition (% wt.)
Ag-V03 (Ag)	18.5
Ethylene Glycol (EG)	52.5
Isopropyl Alcohol (IPA)	8
Glycerol	11
Ethylene Glycol Monopropyl Ether (EGME)	10

Table 1: Composition of the silver ink formulated

The most critical properties of each solvent used to conclude in the composition above, independently, are tabulated in Table 2.

Solvent	Viscosity (cp@25°C)[6]	Surface tension (dynes/cm@25°C)[7]	Density (g/ml@25°C)[7]	Evaporation rate (n-BuAc = 1)
EG	16.1	48.4	1.111	0.35
IPA	2.04	23,3	0.783	1.11
Glycerol	934	76.2	1.257	N/A
EGME[8]	2.7	26.3	0.913	0.22
Ethanol (EtOH)	1.07	22	0.787	3.4

Table 2: Physical properties of mainly used solvents in polar medium.

2.3- Stability as the first quality indicator

The ink stability indicates the time the chemical and physical properties remain unaltered. Therefore, the stability indicates the possibility of using the ink with certain reliability and reproducibility throughout time. The properties can change owe to the volatility of some compounds, the separation in different phases, the formation of agglomerations or some chemical reactions. The stability should be evaluated before the printability in order to do not cause a clogging or damage in the printhead. The instability of a functional ink can be a problem in productions where the average storage time is considerable.

Visual observation is usually used to control the stability of inkjet inks. However, depending on the color of the ink, it can be quite difficult to assess sedimentation phenomenon or changes in the composition. The presence of decantation usually indicates incompatibility between solvent and particles. One of the best way to obtain a stable dispersion is using nanoparticles whose stabilization is done in the early stages of the synthesis, using a reducing agent and a protective or capping agent to form a monolayer on the surface of the NP, as the polyol method[9,10]. The concentration of the capping agent (or surfactant if the stabilization is done after the synthesis) has an optimal value in which the stabilization is maximum (Fig. 1). After that, the adequate disaggregation method, such as ultrasound at the right intensity or ball milling, is useful to achieve a higher amount of dispersed particles[11].
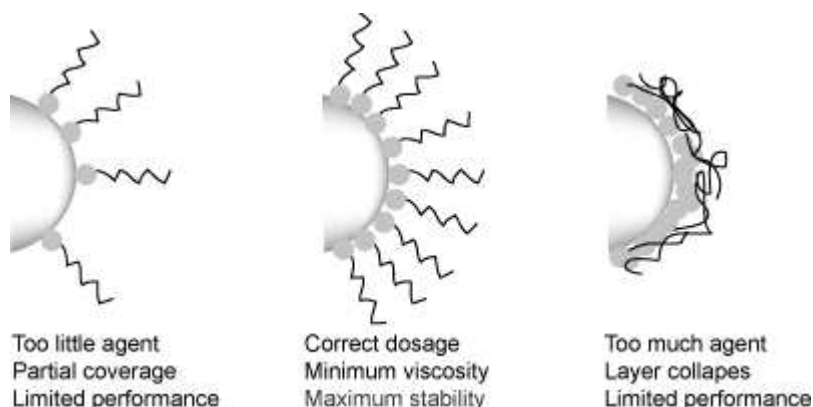
Fig. 1: Illustration of the three possible cases in terms of capping or surfactant agent concentration

Whether the NPs stabilization is carried out while synthesizing or later on the powders, aggregate formation can be prevented by two mechanisms: electrostatic and/or steric stabilization, using ionic or non-ionic surfactants respectively (see Fig. 2). When polar solvents are used, the ionic dispersants adsorb to particles, repelling one to another by electrostatic forces and maintain a stable colloidal suspension. However, the non-aqueous medium with low dielectric such as an alcoholic medium, electric barriers that prevent agglomerations are quite ineffective because the medium has a very low ionic strength and steric stabilization prevails. The non-ionic dispersants are usually polymeric containing a functional group acting as an anchor to the particle surface and a polymeric chain which acts as a barrier that prevents the strong interactions between particles. The most common non-ionic stabilizer is poly (N-vinyl-2-pyrrolidone), PVP, of different molecular weights[12,13,14].
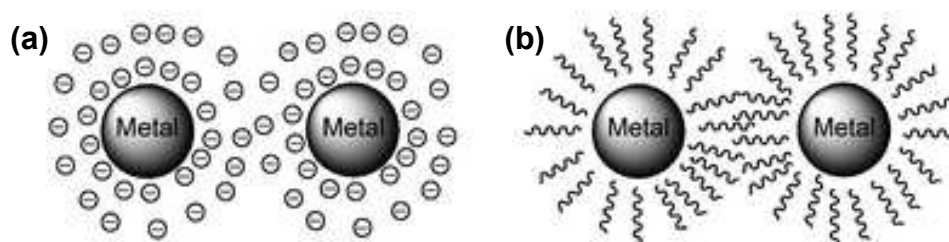
Fig. 2: Metallic particle stabilized by (a) electrostatic forces or (b) steric effect.

Although a proper dispersion can be achieved and no decantation is observed, aging due to decomposition and degradation can occur. These processes are exothermic so it can be detectable by differential scanning calorimetry (DSC). Using an isothermal at 40°C during few hours can give an idea of changes in the ink as TA Instruments proposes at their thermal solutions brochure[15].

2.4- Prediction of the printability: fluid properties requirements

The printability in inkjet is the capability of the drop formation and the jetting through the nozzles of a printhead. The ink has to be chemically and physically compatible with the cartridge and the nozzles. Usually the chemical compatibility comes with the supplier specifications where forbid some chemical species or show the pH values recommended. The nozzle diameters restrict the particles diameter to sizes smaller than 100 times the nozzle. Moreover, viscosity, surface tension, density and volatility are parameters extremely important and determine the jettability of the material[16].

2.4.1- Particle diameter

There are many different printheads in the market with a wide sort of nozzle diameter (a). The smaller the diameter, the smaller the drop volume and the smaller the possible minimum dimension printed (resolution). Even if nozzle diameters of few microns can lead to the best resolutions, for particular inks could mean a problem of clogging. To prevent the ejection standstill while printing due to the nozzle collapse, particles of 100 times smaller than the nozzle diameter should be used in the ink[17]. In practice, particles of the double size of the recommended can be jetted easily after treating them with a disaggregation method and filtering before printing.

In our particular case, a 10 pl cartridge for Dimatix DMP-2831 is used. The effective diameter of a 10 pl nozzle is 21 μm, so any particle, polymer, or aggregate should be less than 0.2 μm being conservative.

The diameter of the silver nanoparticles of our ink was checked by TEM (Fig. 3) and compared with the diameter of two commercial inks. Clearly the particles have the correct diameter to be printed. The three images show particles with d<0.1 μm.
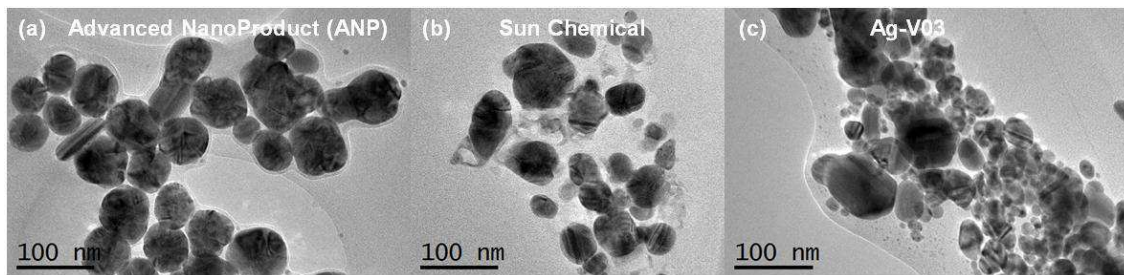
Fig. 3: TEM images of three silver inks. The commercial ones belong to (a) Advanced NanoProduct (ANP) and (b) Sun Chemical. The (c) image corresponds to the silver nanoparticles from Metalor, used in our silver ink.

2.4.2- Viscosity

In the case of Newtonian fluids like most solutions, the recommended viscosity (η) should be around 10-12 cp at the operating temperature[17] although fluid of until 30 cp can be printed in not so ideal conditions. This range can be modified depending on the printhead. For high viscosities, the filling rate of the nozzle decreases and consequently the jetting frequency. Low viscosities lead to high filling rate and jetting frequency and for that, it may cause unstable drops due to the interaction nozzles-transient pressure waves[18]. The drop can be formed as long as the viscosity is low enough to allow the nozzle refilling in approx. 100 ms.

The most common action to adjust the viscosity is the addition of different co-solvents. In our case (Table 2), the addition of glycerol (934 cp) is clearly done to increase the viscosity to good values. EG (16.1) has nearly the desirable viscosity but to adjust the rest of the properties, IPA and EGME, with 2.04 and 2.7 cp respectively, have been put in the dispersion, decreasing highly the ink viscosity.

Solid content influence

At a particular concentration of particles, the dispersion is no longer Newtonian fluid anymore. Once this limit is overpassed, there are two opposite cases (Fig. 4): a fluid which presents a shear thinning behavior, lowering its viscosity when high shear rates are applied (just like in the nozzle firing); and when the particle fraction in the fluid is too high, then the opposite behavior (thickening) happens[19].
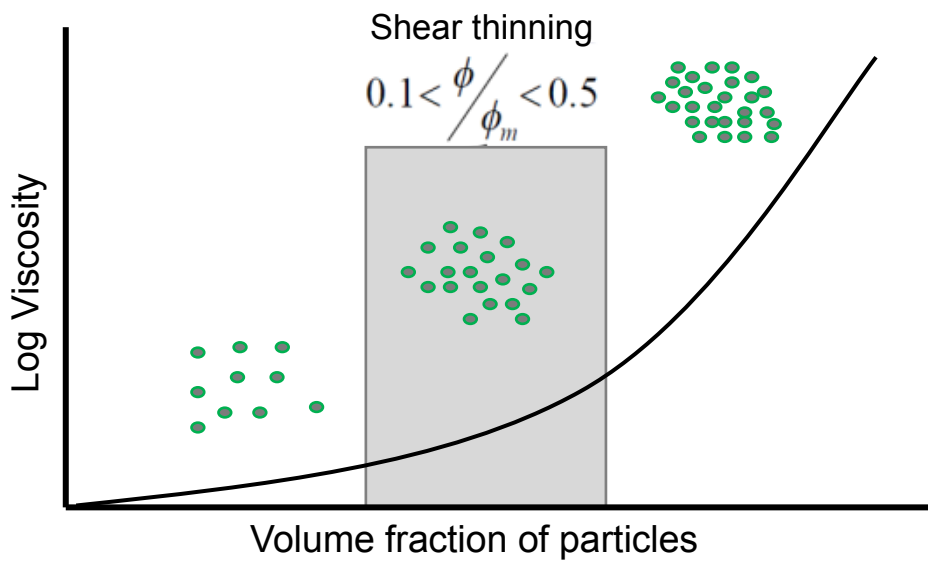
Fig. 4: Solid content influence on the rheological behavior of an ink. If the volume fraction of particle is $\phi/\phi_m <$ 0.1, the dispersion has a Newtonian fluid behavior. When $\phi/\phi_m > 0.5$, the shear thickening behavior occurs. The target behavior is in between, called "shear thinning".

Just in the first case, this fluid can be ejected and printed at higher viscosities than the recommended ones, enlarging the viscosity range up to 20-22 cp at normal shear rates. When shear thickening is presented, the ink clogs the nozzles being impossible to continue the printing.

The reason why fluids with a shear thinning behavior are printable with higher viscosities can be explained. Each printing step can be simulated with different shear rates[20]: storage ($\sim$0.001s^{-1}), nozzle filling ($\sim$10s^{-1}), waiting in print-head ($\sim$1s^{-1}), and ejection ($\sim$10^{4}s^{-1}). Thus, the evolution of the ink viscosity along the printing process can be reproduced by means of a rheometer (Fig. 5). In the case of our optimized silver ink, the viscosity has been measured at different shear rates (Fig. 6). In storage regime the viscosity is quite high, more than 100cp at $\sim$0.001s^{-1}, and slows down quickly reaching 15 cp at the rates of standby. At the highest rate about 6000s^{-1} (jetting process), the final viscosity falls to 12 cp.
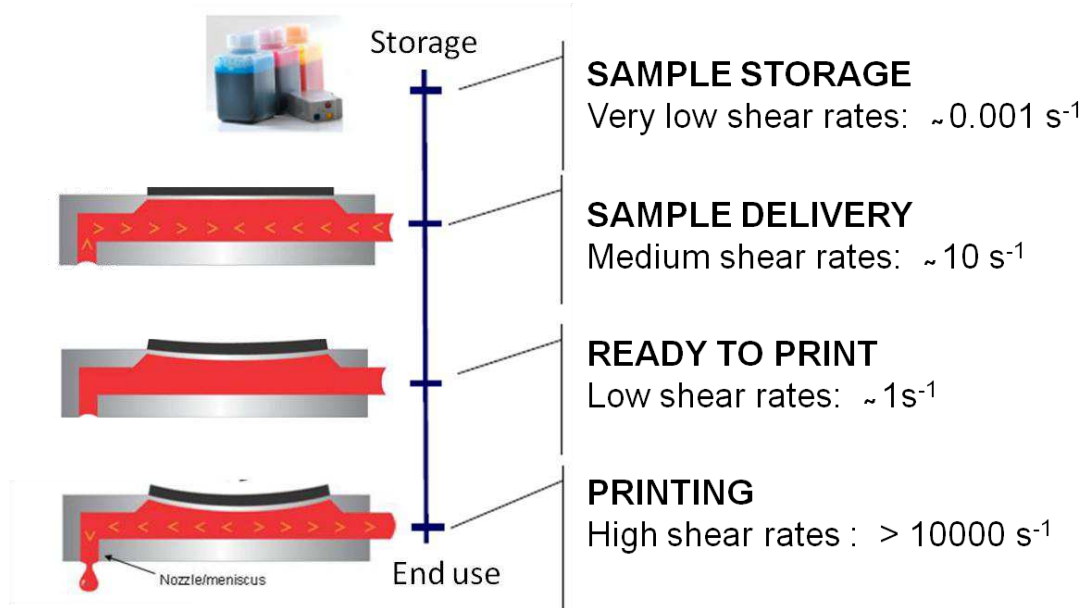
Fig. 5: Approximated shear rates corresponded to different steps on the printing process[20].

So, although the viscosity is higher than 20 cp in slow shear rates, the non-Newtonian behavior provides a suitable viscosity at the printing step (shear rate of ~10s^{-1}) even within the recommended range.
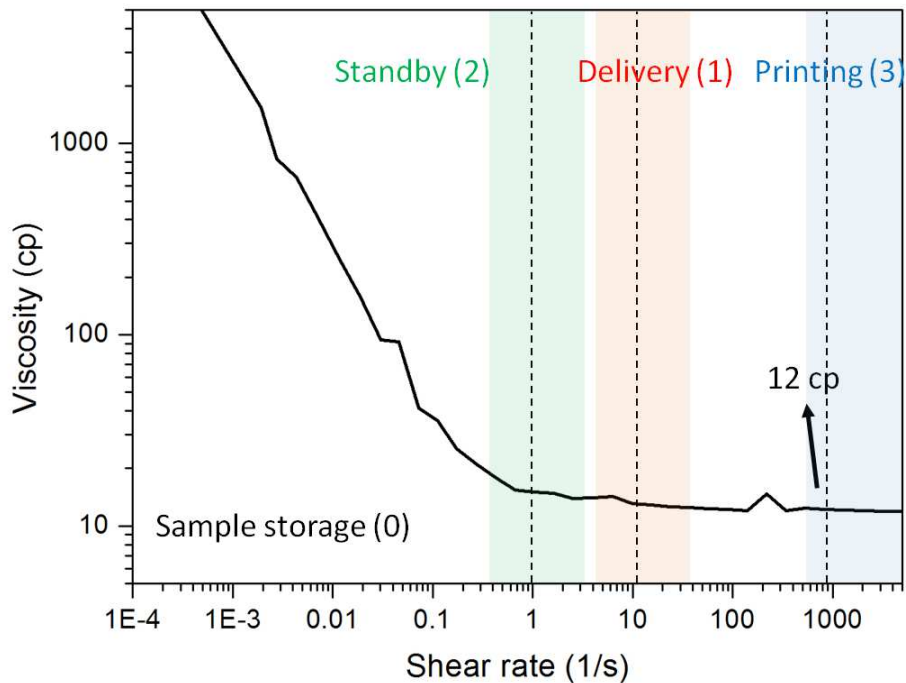
Fig. 6: Viscosity exhibited by our silver ink *from a shear rate inclining to zero to high stress shear rate. At approximately shear rates of zero, the viscosity is high what helps maintaining stability at storage. When the pumping to the inkjet nozzles occurs (delivery), the ink is within the viscosity range acceptable, becoming printable.*

It is interesting to notice that for dispersions, higher viscosities at storage usually lead to a better stability. At rest, the particles are just exposed to the gravitational force, what means that the viscosity force is the one which compensate and prevent the particles from settling, becoming a required condition for stability[21].
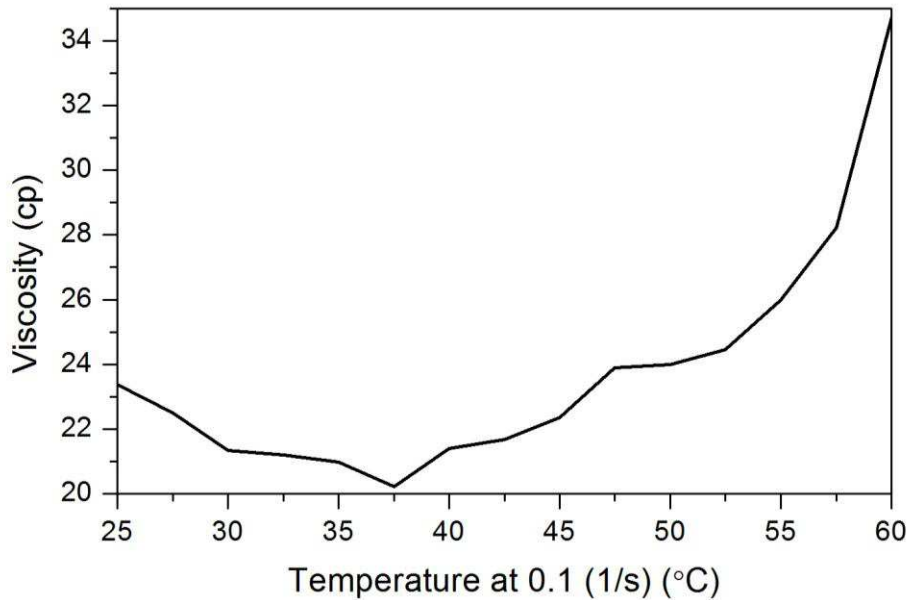
Fig. 7: Viscosity trend for our silver ink at 0,1 s^{-1} shear rate when temperature changes. Increasing slightly the temperature by 40°C the ink becomes less viscous what helps the formation drop. Higher temperatures than that can collapse the nozzle by drying and thickening the ink inside it.

2.4.3- Surface tension

The surface tension (γ) is a primary factor not just in the drop formation, but in the interaction and the wettability of the substrate. It is not a property of the liquid alone, but a property of the liquid's interface with another medium. In the case of the drop formation this interface corresponds to the ink-air interface and it is used to be higher than with the interaction with another solid medium. Thus the surface tension has to be high enough to avoid dripping of the nozzle but low enough to allow the jetting. This surface tension can be measured by a stalagmometer by the Tate's law[22] where it is said that the falling drop mass is proportional to the aperture ratio and the fluid surface tension.

This determination method consists in weighting a number n of drops of a falling liquid from a specific tip, where the capillary radius is maintained constant, using first a liquid with a known surface tension, such as water, to fix the radius variable and then calculating the unknown surface tension of the second fluid. The expression is the following:

$$m = \pi \cdot r \cdot \gamma \qquad [1]$$

Where m is the drop mass, r is the capillary radius, and γ is the surface tension of the liquid.

Assuming that the radius of the stalagmometer is the same, the ink surface tension can be determined making equal the relation between the mass and the surface tension of each liquid,

$$\pi \cdot r = \frac{m}{\gamma_{water}} = \frac{m}{\gamma_{ink}} \qquad [2]$$

$$\gamma_{ink} = \frac{m_{ink}}{m_{water}} \cdot \gamma_{water} \qquad [3]$$

Where γ_{water} is 72 dynes/cm at 25 °C.

The recommended values of an inkjet ink should be hold in the range 28-33 dynes/cm for the cartridge we use[17], to ensure a drop formation and it can be adjusted by means of solvent control, as well as the viscosity.

	Nº drops (n)	Mass (g)	Mass per drop (g)	Surface tension at 25 °C (dynes/cm)
Water	18	0.3836	0.0213	72
Ag-V03	12	0.117	0.0097	32.9
ANP	17	0.1479	0.0087	29.4

Table 3: information data from the stalagmometric method used for the surface tension determination

Our silver ink obtained a surface tension of 32.9 dynes/cm (Table 3) within the recommended range due to the addition of low surface tension solvents as IPA and EGME (Table 2), with 23.3 and 26.3 dynes/cm respectively, to the main solvent, EG, which surface tension is 48.4 dynes/cm and glycerol (76.2 dynes/cm). It is important to highlight that the surface tension, as well as the viscosity, is not an additive property what means that it is needed the experimental measurement when different solvents are involved.

Even if the value is at the top limit recommended, the printing of this ink is done at 40 °C what helps to decrease a little the room temperature surface tension.

2.4.4- Z dimensionless number

The printability can be theoretically evaluated taking into consideration inertial, viscous and surface tension forces which determine the drop formation. The quality of the drop can be predicted by the Z number, equivalent to the inverse of the Ohnesorge (Oh) parameter[16]. It can be defined as the ratio between the Reynolds number (Re) and a square root of the Weber number (We), and it is independent of fluid velocity. Therefore, when Z>10 [23], satellite drops arise instead of a single droplet, whereas if Z<2, the fluid cannot come out the nozzle. Thus, the formation of a stable drop meets the following expression:

$$Z = \frac{1}{Oh} = \frac{Re}{\sqrt{We}} = \frac{\sqrt{a \cdot \rho \cdot \gamma}}{\eta} = \frac{\sqrt{Inertia \cdot Surface\ tension}}{Viscous\ forces}\ ; 2 < Z < 10 \qquad [\,4\,]$$

Where a is the characteristic length (nozzle diameter); γ is the surface tension; η the viscosity and ρ the density of the fluid.

Another study redefines the recommended values[24] to 4<Z<14 by considering characteristics of printing such as single droplet formability, the minimum nozzle-substrate separation distance, positional accuracy, and maximum allowable jetting frequency. Printing using a fluid with Z value less than 4 resulted in droplet formation with a long-lived tail and a long time to single droplet generation degrading the positional accuracy and printing resolution. Even the accomplishing of the suitable Z number value, viscosity and surface tension has to be evaluated independently and lying within the limiting values explained before.

In the case of the Ag-V03 formulated in our laboratory, the physical properties are included in Table 4.

Ink	Viscosity (cp)	Surface Tension (dynes/cm)	Density (g/cm^3)	Nozzle diameter, a (μm)	Z Number $\frac{\sqrt{a \cdot \rho \cdot \gamma}}{\eta}$
Ag-V03	11.5	33	2.1	21	3.32

Table 4: Z number and the values of the different properties or parameters included in it.

The Weber (We = ρ·v^2·a/Υ) and the Reynolds (Re = ρ·v·a/η) numbers are represented separately in Fig. 8 so the effect of the velocity, v, can be plotted. The blue line corresponds to our ink Ag-V03 in which the velocity of the drop in flight can be modified by increasing the applied voltage during the printing, increasing the kinetic energy. Red lines indicate those velocities where the system turns to be unacceptable for a good quality printing.
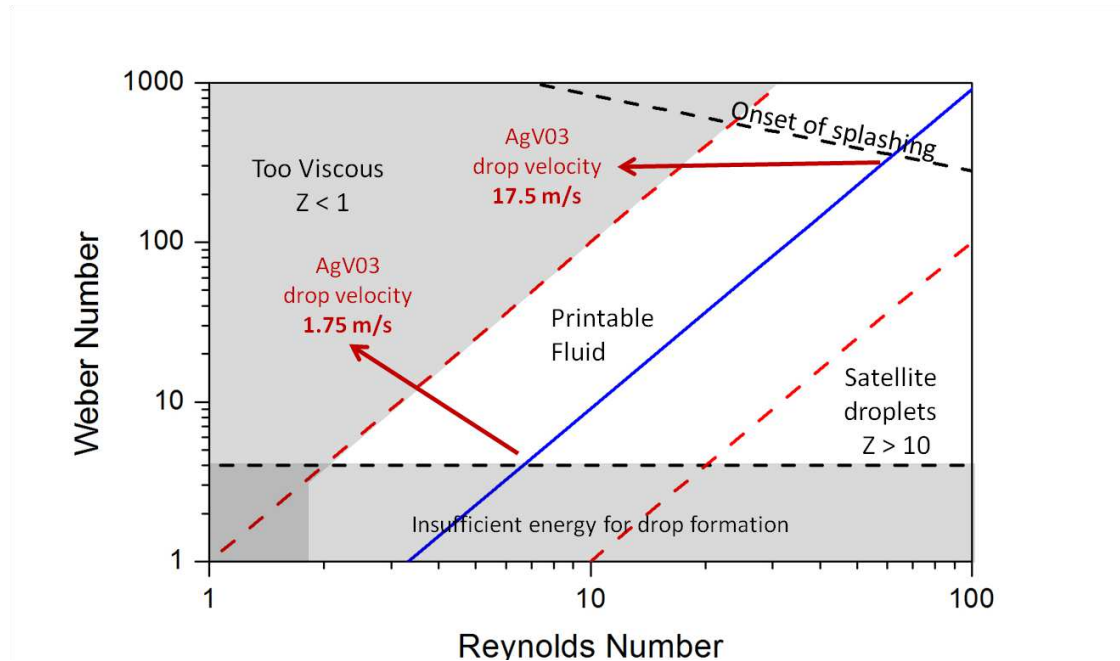
Fig. 8: Regime of fluid properties where the ejection of droplets by inkjet printing is possible. Illustration adapted from ref [25]

The Z number, which is independent of the velocity, lies on 3.32, taking into account that the nozzle diameter selected is 21 μm. This number is within the standard recommended values and near the limit of ref 24. Nevertheless, this is in totally agreement of the assumption of droplets with possible long-lived tail. As it is seen in Fig. 9 (a), the tail is formed during the printing process but the droplets are stable, without digression of their trajectory. In the case of a different formulation with Z number higher than 10, the tail is totally removed, but satellite drops appear, out of the straight trajectory (Fig. 9 (b)).
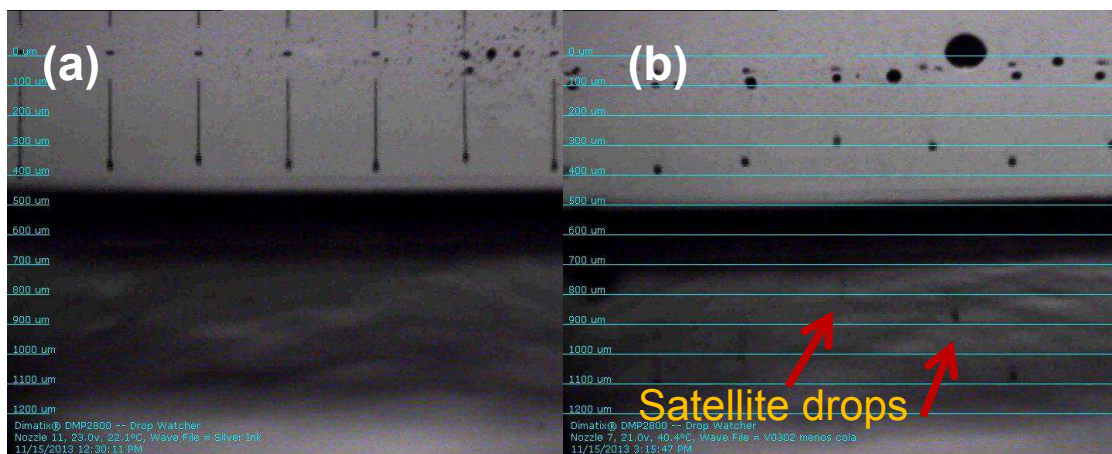
Fig. 9: Screenshots of droplets being ejected for an ink with (a) Z~4 and (b) Z>10. In the image (a) a long but stable tail can be observed whereas in (b) low, unstable and inaccurate spherical drops can be seen with satellite drops in the bottom of the picture

2.4.5- Volatility

Another critical parameter not included in the Z dimensionless number is the volatility. The importance of this property falls on how quick the ink can be dried. May be the most important effect is drying in the nozzles, causing the clogging and the printing failure. It can be studied by means of a thermogravimetric analysis (measuring the amount of ink evaporating over time) as well as by differential scanning calorimetry analysis for the printhead temperature during printing. Commonly the easy way to perform it is studying how solvent volatilizes at room temperature with a simple camera. A non-exhaustive but useful criterion is to check whether the printed material remains wet at room temperature a time reasonable higher than deposition time.

Since any ink finally has to be dried on the substrate, it should have some volatile components. For this reason inks may produce nozzle clogging eventually after some time remaining inside the cartridge. Consequently the viscosity near the nozzles may be increased in a major way. This problem is known as "the first-drop problem"[26,27]. To solve that, one could clean regularly or keep the nozzles wet.

2.5- Printing Quality: printing parameters and drop-substrate interaction

2.5.1- Variable factors for the quality adjustment

Multiple parameters and properties can modify the different requirements for a printed design. The main target features of a printing are resolution, homogeneity and adhesion to the substrate material. Some of these characteristics can be fitted mostly by the ink or substrate modification, or just by tuning parameters; usually, these features are achieved by a combination of both.

2.5.1.1- Printing parameters

The inkjet printer must be configured adapting its parameters to the ink and the substrate selected for the printing. Its quality will depend crucially on the identification of suitable values for each parameter. The adjustable parameters of the inkjet printer are voltage amplitude, waveform, frequency of injection and nozzle temperature to enhance the drop formation and

drop spacing, separation distance between the printhead and the substrate, printhead speed, substrate temperature and number of layers for the deposition quality control. In the following table (Table 5) there is a resume of the main selected parameters for a good quality printing with the Ag-V03 ink, formulated during this chapter:

Parameter	Units		Value for Ag-V03
Voltage Amplitude	V		23
Waveform	Percentage of peak voltage (%)	Slew Rate	Duration (μs)
Standby	0	0.65	3.584
Phase 1	100	0.93	3.712
Phase 2	73	0.60	2.368
Phase 3	27	0.80	1.856
Drop Speed	m/s		5
Nozzle Temperature	ºC		40
Drop Spacing	µm		25
Separation between printhead-substrate	µm		250
Substrate Temperature	ºC		60

Table 5: Printing parameters selected for the Ag-V03 ink.

Voltage amplitude and waveform

The waveform is generated and tuned by the configuration of different trapezoidal actuator pulses of voltage. It helps to control the relaxation and contraction of the piezoelectric nozzles that allows to the filling and pumping of the ink through the cavity. It tunes the drop shape with the aim of forming a spherical drop or a continuous tail that does not break into satellite droplets.

The most reliable configuration consists usually in the standby phase and three printing phases (Fig. 10). At the standby phase the piezoelectric material is slighted deflected prior initialization. Then decreasing the voltage, the piezoelectric moves upwards, turning back to the flat position and letting the fluid going into the pumping chamber, starting the printing process. At phase two or the firing pulse, the voltage increases to the maximum voltage amplitude, defecting the piezoelectric and forming the drop outside the nozzle. The final dampening step induces the drop breakout, controlling the voltage decrease until the standby position again.
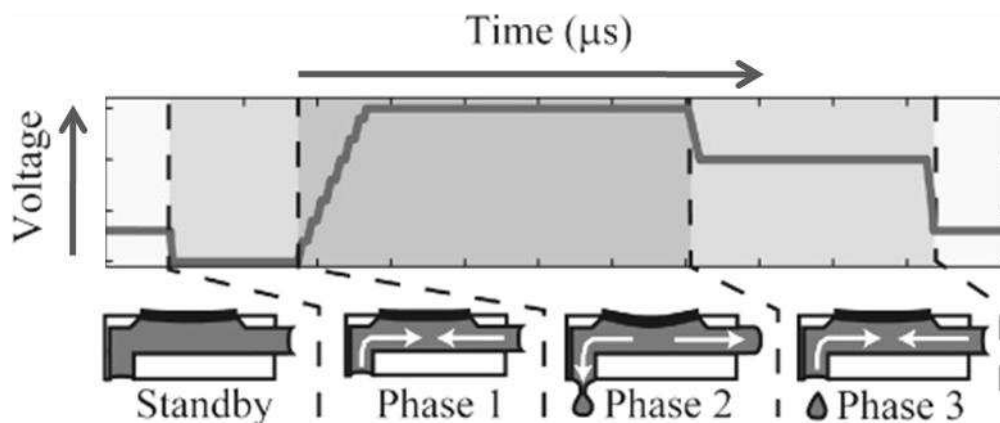
Fig. 10: Illustration of the waveform configuration by phases

Every step can be modified by the voltage, the slew rate and the duration. The different phases affect the shape and the velocity of the ejected drop differently. The steepness of the slope in the firing pulse provides the energy for initial ejection. Reducing the slew rate, the drop becomes faster. The phases 2 and 3 have the opposite effect; it slows down the drop velocity when the slew rate is increased. The dampening phase is designed to prevent the printed head from sucking air back in and control the tail-shaped drop. Increasing the drop velocity by reducing the slew rate and the duration of the first steps can lead to tails. It is not necessarily a problem but it has to be controlled that the head and the tail does not separate before arriving to the substrate.
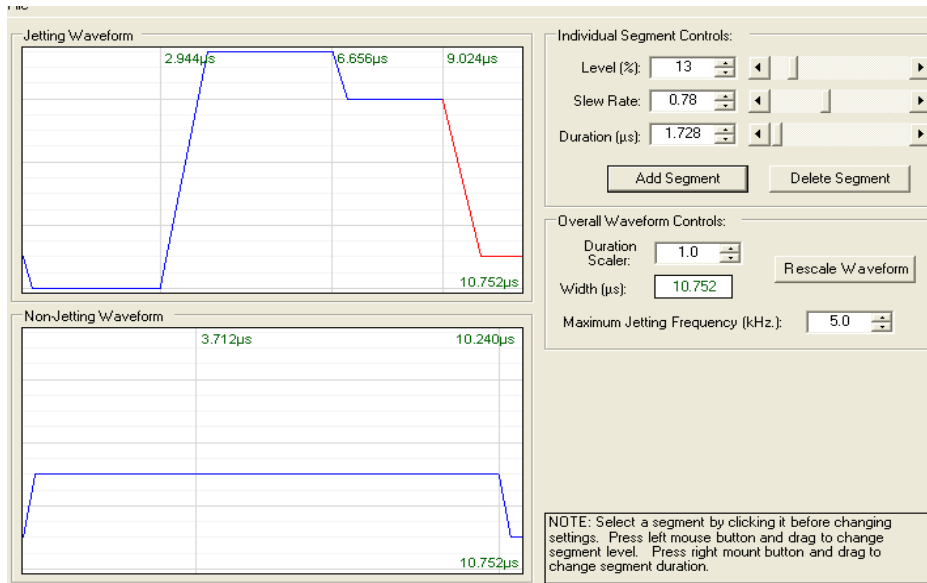
Fig. 11: Waveform configuration for the Ag-V03 ink. The values of each segment are showed in Table 5.

An example of the effect of the configuration of the waveform is illustrated in Fig. 12. In (a), the drops are stable with a controlled tail, while linking the phase 3 and the standby by leveling off the voltage to a 20 % in both steps, the drops turned to be spherical and the jetting turned to be uncontrolled and unstable. Probably, this change is caused by the low volume that fills the nozzle cavity.
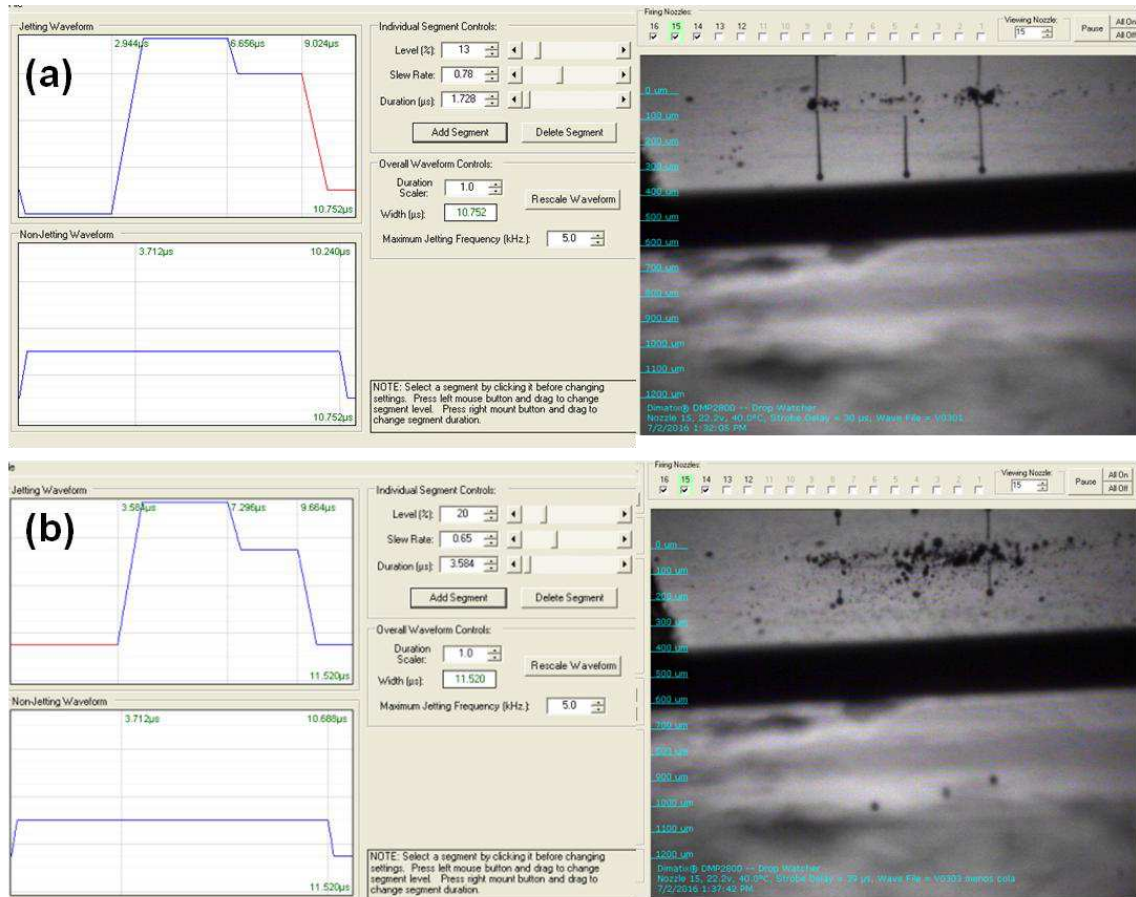
Fig. 12: Waveform and drops being ejected for Ag-V03 in two different configurations were (a) forms a tailed and stable drops while in (b) spherical drops are ejected but in a uncontrolled way. Parameters of percentage of voltage (%), slew rate and duration (µs) are (a) standby: 0, 0.65, 3.584; phase 1: 100, 0.93, 3.712; phase 2: 73, 0.6, 2.368 and phase 3: 27, 0.8, 1.856 and (b) standby: 20, 0.65, 3.584; phase 1: 100, 0.93, 3.712; phase 2: 73, 0.6, 2.368 and phase 3: 20, 0.8, 1.856.

Jetting frequency and drop speed

As it was mentioned before, the jetting frequency has to be modified depends on the ink viscosity. Viscous ink fills slowly the pumping chamber and consequently needs of lower jetting frequencies. Low viscosities lead to high filling rate and jetting frequency[18]. Furthermore the higher the frequency, the higher the positioning error[24].

The speed of the ejected drops is also important[28]. It ranges 1 to 30 m/s depending on the ink properties, recommended 1 to 6 m/s [17]. For faster drops it could produce splash after impact. For slower drops the air in between the nozzle and the substrate could whether slow it down even more or change its path and consequently the distance nozzle-substrate have to be defined again.

Nozzle temperature

The temperature of the printhead corresponds to the operating temperature of the ink what allows to print more viscous inks due to the loss of viscosity at higher temperatures than the ambient.

As it was shown before, our ink is printed at 40°C what decrease slightly the viscosity and the surface tension of it and helps printing.

Drop spacing and dot per inch (DPI)

There are two equivalent parameters to define the number of dots that can be printed in an area: drop spacing (ds), talking about the minimum distance between two consecutive drops, and dot per inch (DPI), what refers to the maximum number of drops printed in a line of an inch long. Noticing that the DPI and drop spacing is just different units to refers the same idea and the conversion between them is possible, along this thesis drop spacing will be the reference to explain its influence on the quality indicators.

In the printer used in this thesis, a Dimatix Materials Printer DMP-2831, the nozzle to nozzle spacing is 254 µm (native printhead resolution) in a single row and the smallest drop spacing is 5 µm which is equivalent to 5080 dpi[17].
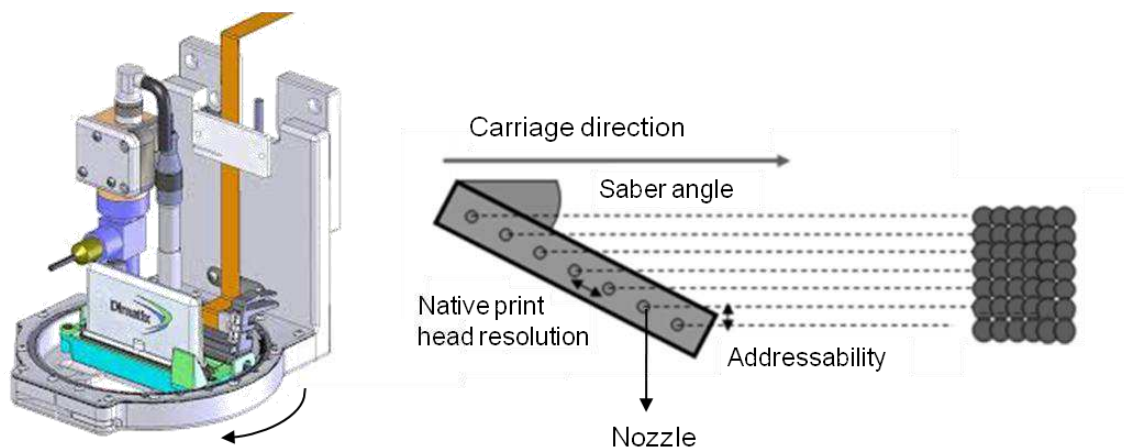
Fig. 13: Illustration of the drop spacing (addressability) and the adjustment in the Dimatix printer in terms of saber angle. As the saber angle decease, the drop spacing does too.

The drop spacing can be consider as the inherent resolution of the print system, but to distinguish from the real resolution which take into account the ink volume and the drop-

substrate interaction. The drop spacing is adjusted by placing in angle the nozzle row (Fig. 13). This angle allows the vertical separation between the lines, what is called addressability. Fig. 14 shows the deposited drops when the angle is changed.
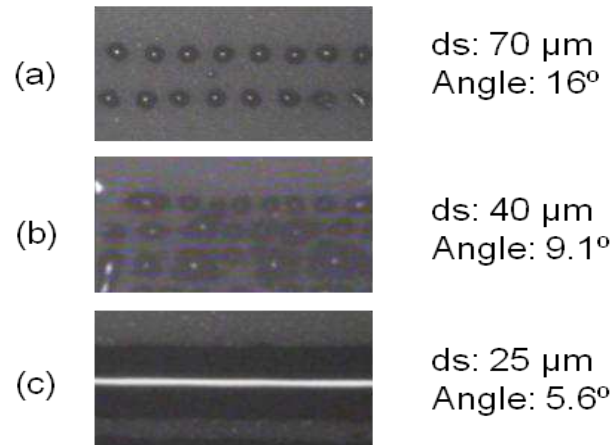
Fig. 14: Dimatix Images of the printing of Ag-V03 ink on a sintered ceramic substrate when the cartridge is placed with different angles to achieve (a) 70, (b) 40 and (c) 25 µm of drop spacing.

Separation between printhead and substrate

The distance between the nozzle and the substrate, that is, the stand-off distance, significantly influences the printing accuracy. If the separation distance between the nozzles and the substrate is very large, the air slows the drop down and changes it trajectory, losing the accurate drop placement. Furthermore, it gives time to separate the head and the tail of the drop ejected. If the separation distance is shorter than the flying distance, where the fluid ejected from the nozzle transforms into a single droplet, results in the deposition of droplets having tails and satellites, degrading the printing resolution[24]. If the patterns need to have consecutive printings in still wet depositions, the drop splashes around the printing tracks as satellite drops (Fig. 15).
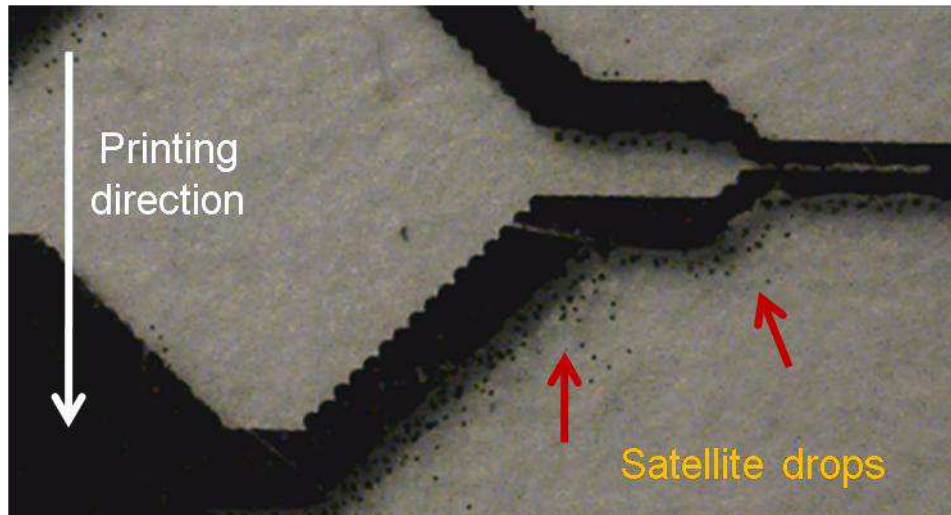
Fig. 15: Splashes forming satellite drops in the printing surroundings.

Printing or carriage speed

By increasing the carriage speed, lines are more continuous and it is quite difficult to distinguish drops individually in the substrate, they are more uniform and fine.

Usually the track resistance is higher when printed at higher speed, because it reduces the thickness and the track section.

Substrate temperature

The platen of the printer can be heated up. The maximum temperature depends on the printer and it is typically around 70 ⁰C. By increasing the platen temperature, and consequently the substrate temperature while printing prevents satellite drops and allows better quality patterns and greater distance between the tracks[29,30].

Two mechanisms affect conversely the drop: the increase of the drop temperature when gets in contact with the heated substrate decreases the viscosity[31], enhancing the wettability; and at the same time, the evaporation of the volatile components starts, causing a higher concentration of solid and thus a rapid increase in viscosity what decrease the mobility and prevents the drop mechanisms that induce a bad quality printing such bleeding, feathering and others represented in Fig. 16; and this fact decreases the droplet size and therefore the minimum print width, improving the resolution. Moderate temperatures, such 30 ⁰C, make the

first option the dominant mechanism while higher temperatures the volatile solvents evaporate earlier than the possible spreading.
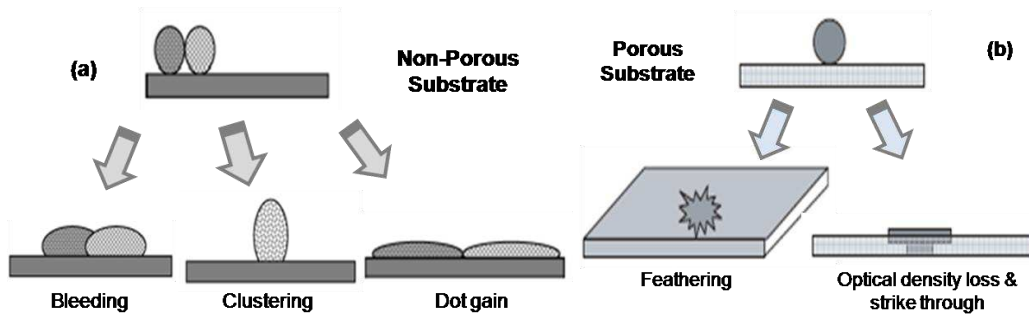
Fig. 16: Drop mechanism that leads to a bad quality printing on (a) non-porous substrates and (b) porous substrates. Illustration adapted from ref. 29.

Number of printed layers

The successive layers on the same pattern increase the line thickness, but it can also increase the width. Thus it decreases the electrical resistance, because of the larger track section. Some studies[32] have succeeded in lowering the resistance two orders of magnitude varying from three to seven layers.

2.5.1.2- Drop-substrate interaction

The quality and resolution of a printing depend not only on the physical properties of the functional ink and the proper drop formation when ejected from the nozzle, but also on the substrate it has to be printed on. The surface energy, the smoothness and the porosity of the picked substrate can change the ink performance. Fig. 17 shows the effect of the substrate replacement on the ink performance. While on PET (a) and PI (b) substrate, the resolution obtained by Ag-V03 is adequate, on PowerCoat Paper or green low-temperature-cofired-ceramic (LTCC), the definition and the homogeneity are lost. On coated-paper (c), the Ag-V03 drops tend to coalescence together leading to a bad wetting due to the differences in surface tension. In addition, the same ink onto the green LTCC (d) presents a homogenous printing due to the porosity of the substrate.
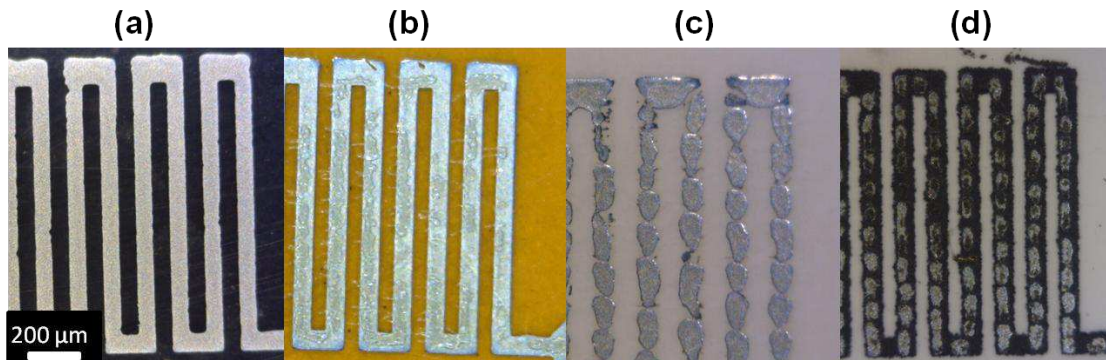
Fig. 17: Ag-V03 printed with the same printing parameters and sintered on (a) polyethylene terephthalate, PET, (b) polyimide, PI, (c) PowerCoat© Paper[33] and (d) green LTCC (no sintered).

A practical parameter to predict the ink wettability with the substrate is the contact angle, Ө, which is the angle that the tangent to the surface makes with the solid surface. Tension forces between liquid-air interface (γ_L), the liquid-solid interface (γ_{SL}), and the solid-air interface (γ_S), plays an important role:

$$\gamma_S = \gamma_L \cdot cos\theta + \gamma_{SL} \qquad [5]$$
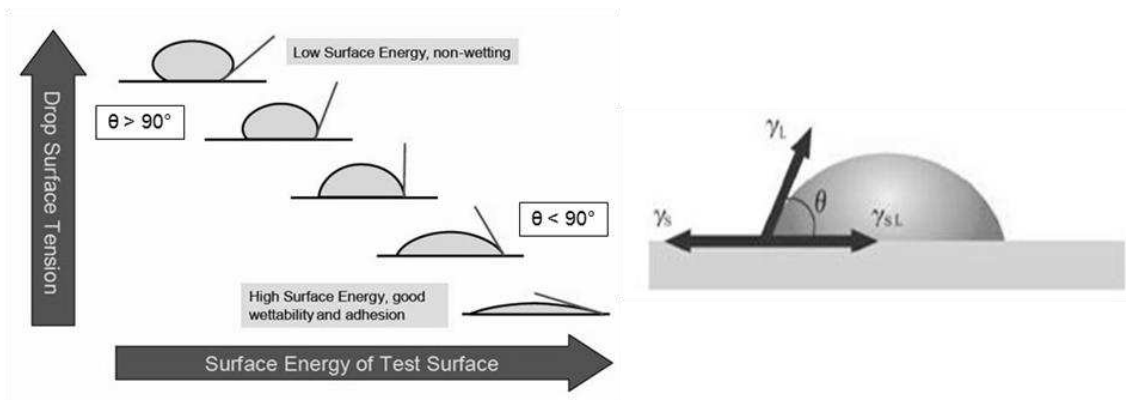
Fig. 18: Schematic diagram of the influence of the ink surface tension and the surface energy of the substrate into the contact angle and, hence, into the wettability and adhesion.

Assuming the drop shape as a sphere, the spread drop diameter can be expressed as:

$$d_{con} = d_o \cdot \sqrt[3]{\frac{8}{\tan\frac{\theta_{eq}}{2} \cdot (3 + tan^2 \frac{\theta_{eq}}{2})}}$$

Where d_{con} is the contact diameter between the drop and the substrate, d_o is the diameter of the drop in flight and θ_{eq} is the contact angle in equilibrium. The initial contact angle is

reduced when it reaches the equilibrium (Fig. 19) and it strongly depends on the ink-substrate system. On a smooth homogeneous surface, the resolution attainable from an inkjet printer is controlled by the diameter of the spread droplet, which is a function of initial drop size and contact angle. Given drops of a volume of ~1 picoliter, or $d_0 > 10$ µm, the smallest feature size with a fluid of contact angle <10° will be 30 µm.
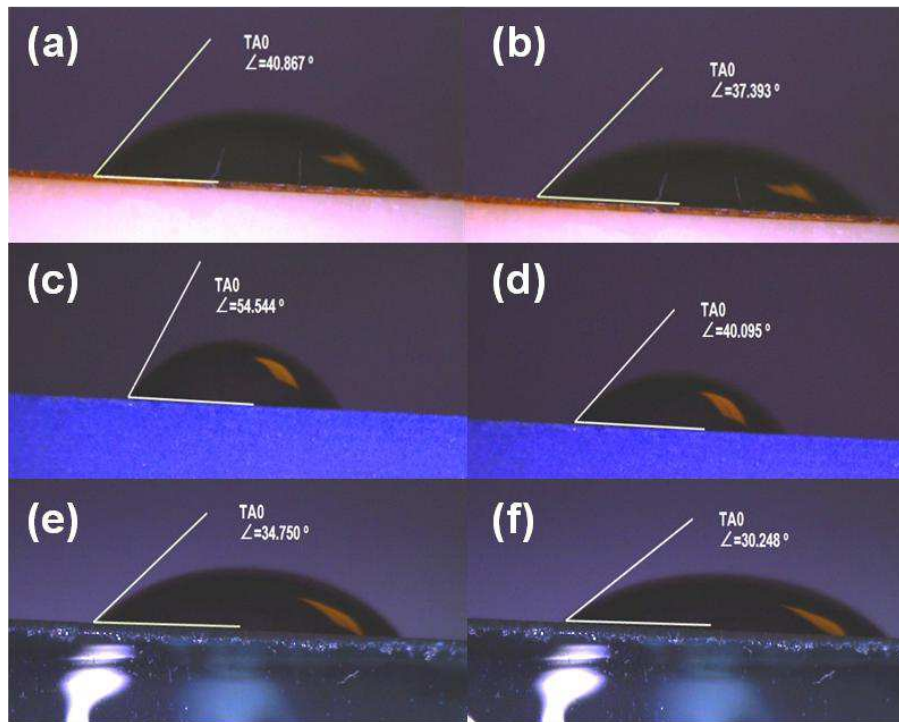
Fig. 19: Contact angle of the Ag-V03 ink on (a) polyimide substrate at t∼0 *s* and (b) t=5 s, (c) sintered LTCC at t∼0 *s* and (d) t=5 s, (e) glass at t∼0 *s* and (f) t=5 s.

The contact angle between an ink and a defined substrate can be modified by two main strategies: modifying the surface tension of the ink or the free energy of the substrate surface. The first strategy covers the co-solvent control with the addition of a low- or high- surface tension solvents such an alcohol or water respectively, or the addition of additives such as surfactants. The second strategy is modifying the free energy of the substrate and then, increasing the wettability. Increasing the substrate temperature during the printing can slightly help to this purpose, but when a stronger modification of the contact angle is needed, plasma surface treatments or chemical etching should be applied to the substrate. These treatments are in relation with the ink adhesion to the substrate and it will be introduced later.

On porous substrates there is a competition between spreading and infiltration processes as the drop impacts on the surface. These processes has been studied using a simple model for

the infiltration of fluid droplets[34,35]. This model showed that infiltration times are in the range of 100–500 ms for droplets of the size ejected by inkjet printing, which is significantly greater than the timescales for impact-driven and capillary spreading. Then, when the penetration rate is significantly slower than the spreading, the ink stays too long on the surface, resulting in undesirable mixing trans-surface wicking (feathering)[36] illustrated in Fig. 16 and Fig. 20.
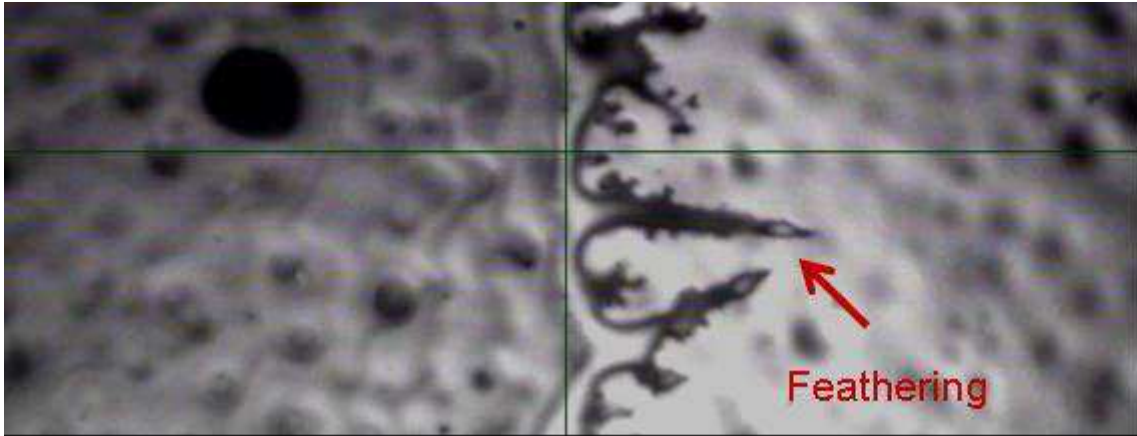
Fig. 20: Feathering caused by printing a kesterite ink (Chapter 5) onto a Molibdenum-coated ceramic, where the porosity is covered by the Mo layer but there is roughness on the surface, behaving as a porous substrate with low infiltration rate.

The main problem when printing on porous substrate consists in the considerable decrease on the effective thickness layer, as it was shown in Fig. 19 (d), and not in resolution. To overcome such drawback it is required to print multiple layers to maintain the continuity in the printing tracks or in the functional properties like in conductive tracks.

2.5.2- Printing quality indicators

2.5.2.1- Resolution

Printing resolution is defined as the capability of a printing system to reproduce image details. Printing patterns usually needs to have a good control of the resolution, what means a control on the minimum size feature. Issues concerning the wettability (contact angle/spread drop diameter) and physical properties of the ink and substrate (surface tension and velocity, porosity and temperature) will determine the horizontal and vertical diffusion.

As a resume of what was mentioned before there are many parameters that can affect to the final resolution. Z number, for example, whose high values can be printed but it results in satellite droplet formation, degrades the positional accuracy, and lowers the printing

resolution. Substrate temperature helps to fix the ink onto the substrate, avoiding the spreading and other quality defects that are detrimental for the resolution, and so on. But even if these parameters deteriorate the resolution when they are bad selected, there are two other variables that affect directly to it: the drop spacing and the wettability.

Drop spacing

Defining print resolution as the reproducibility of image pattern, it is obvious that reducing the distance between drops, finer details can be replicated. An increase in the drop spacing leads to a decrease in the volume deposited per unit length. This decrease in volume causes finer line width, increasing the resolution[37,38]. Nevertheless, the drop spacing should be selected in such a way that the drops come together in a uniform pattern, without distinction of the individual drops. In the other hand, an increase in the number of drops per unit distance (decrease in drop spacing) means a higher ink volume per printed area and this fact leads to an increase in the thickness of the printed tracks[39], but it can reduce the resolution (Fig. 21). Printings with very low drop spacing lines are too wide for practical use, which leads to poor uniformity and low roughness peaks[40].
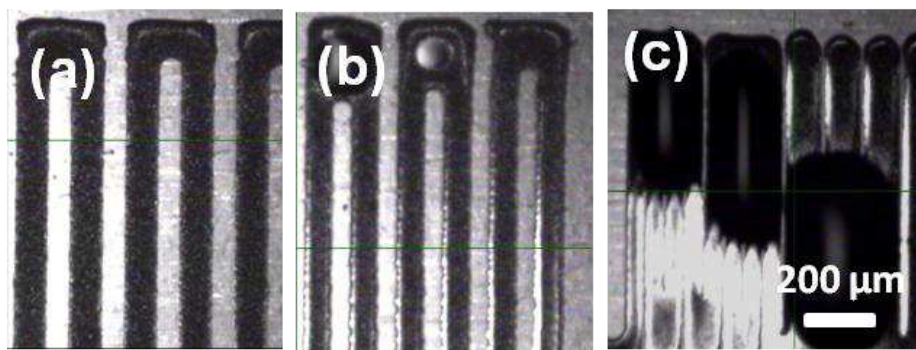
Fig. 21: Drop spacing significantly smaller than drop diameter, too much ink volume is deposited onto the substrates, accumulating and losing resolution and definition. In (a) ds = 25 μm, (b) ds = 20 μm and (c) ds = 15 μm

Wettability

The wettability is the preference of a fluid to maximize the surface contact with the substrate and spread itself over it. It describes the balance of surface and interfacial forces. When the drop impacts with the substrate, the kinetic energy is dissipated due to the viscosity and the surface energy. The drop expansion depends on this surface energy exchange[41] between ink and substrate. For dry surfaces some models can be performed[42,43,44].

The drop behavior when it impacts a solid surface is controlled by inertial forces, capillary forces, and gravitational forces. In the case of inkjet printing, where the typical density (~1

g/cm^3) and drop diameter (<100 μm), the gravitational forces (Bond number, Bo = ρ·g·a^2/γ) can be neglected. Thus, the dominant forces will be inertial and capillary. Schiaffino & Sonin[45] proposed two regimes in the drop impact: impact driven, in which the inertial forces dominate, and capillarity driven, in which the drop velocity is insignificant. These authors characterized this behavior in terms of Weber number (We=ρ·v^2·a / γ), mentioned before, which indicates the dominant force at the spreading process (Fig. 22). Low values of We number indicates the capillarity driven regime and high values concerns the impact driven one, where the drop jetting in inkjet technique works. Once the drop reaches the substrates, it is pushed radially outward by the pressure gradients caused by the impact and the inertia forces with high We, while the surface tension holds back the drop in a low We regime. The spreading of the drop in the substrate is highly dependent on its ability to flow over it. In addition, the resistance to the spreading can be foreseen as well by the Z number. Low value indicates that the drag force is due to the viscosity; while for high values, the inertial forces are dominant.
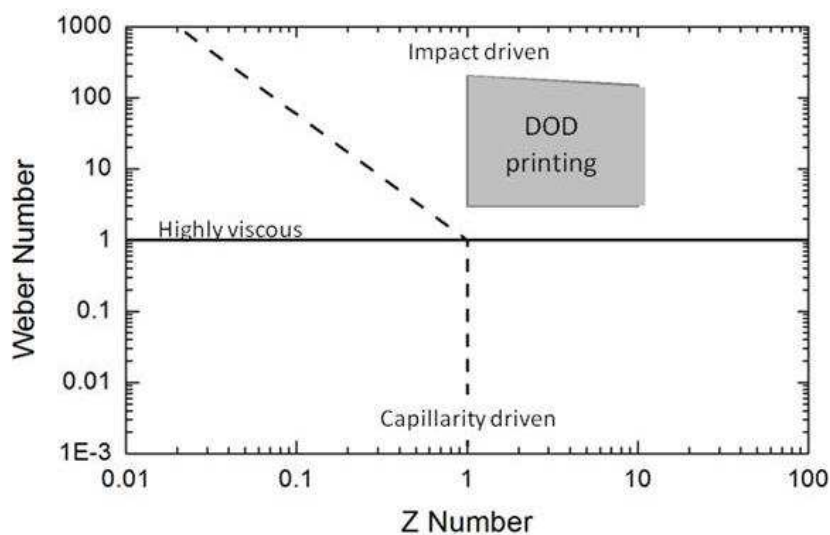
Fig. 22: The conditions for inkjet printing included in schematic diagram divided into the region where impact or capillarity are the driven force for the initial drop spreading after impact[45].

The initial impact stage is governed by kinematic behavior (inertial forces) and the sequence of the processes that happen after the impact is explained in other studies[46,28]. Establishing an dimensionless time after impact, independent of drop velocity (v) and drop diameter (d$_o$) as t*=t·(v/d$_o$), the duration of the initial stage is t* < 0.1 for inkjet printing[46] and corresponds to the impact-driven spreading. After that, viscous forces damp the spreading and surface tension forces become more important in controlling the behavior. At stages of t*=100-1000 spreading is fully controlled by capillarity. The true equilibrium is approached at t*>1000. These stages are represented in Fig. 23.
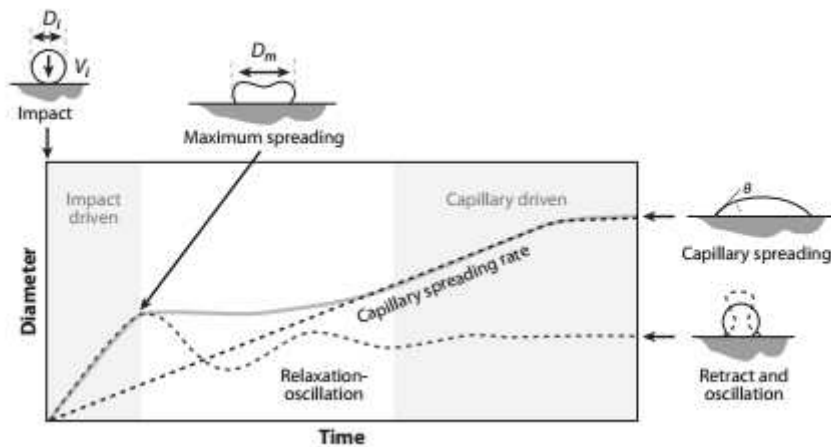
Fig. 23: Schematic illustration of the sequence of events that occurs after droplet impact on a substrate. Initial impact is followed by a series of damped oscillations before capillarity-driven flow occurs[45]

As it was explained before, the contact angle can be a good indicator of the wettability of the ink onto the substrates. When the contact angle is higher than 90° there is not wetting and the ink concentrates itself in small islands to reduce the surface in contact with the substrate. In this case it is impossible to print homogeneously and cover homogeneously the substrate to reproduce the pattern image (Fig. 24 (a)). If the contact angle is lower, the surface covering can be achieved adjusting the drop spacing (Fig. 24 (b)). The lower the contact angle, the higher the drop diameter and the easier the substrate covering and wetting.
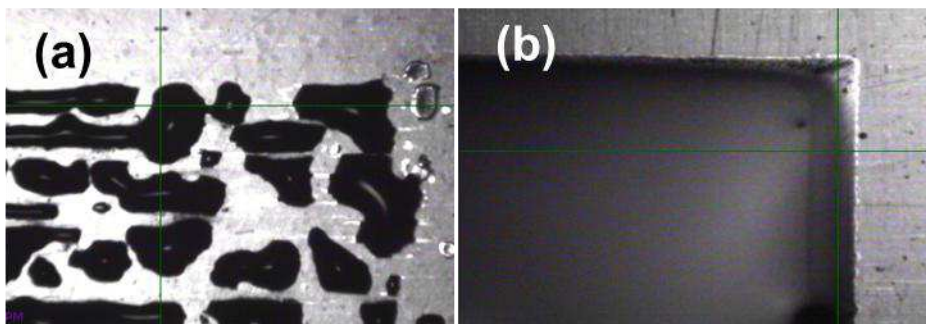
Fig. 24: (a) printing with extremely bad wetting and (b) good wetting

2.5.2.2- Uniformity and Homogeneity

Both, a good resolution and a good homogeneity in printing do not depend only on the ink and substrate properties, but also in the printing parameters. A bad selection of the drop spacing can lead to bad resolutions and decrease printing performances as it is shown in Fig. 25.
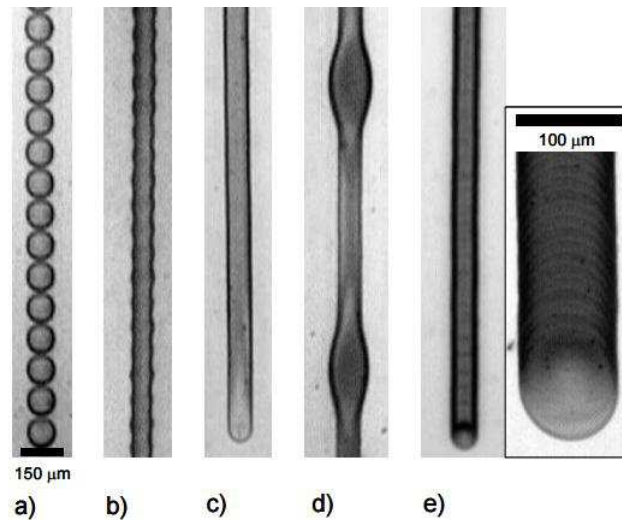
Fig. 25: (a) Drop spacing is too large for drop coalescence (individual drops). (b) Initial coalescence with a periodic irregularity (scallop). (c) After sufficient overlap a parallel-sided track occurs (uniform). (d) If the drop spacing is too small and the printing is faster than the evaporation rate, an instable form appears (bulging). (e) If the drop spacing is too small and the evaporation from single drops is faster than drop jetting, overlap drops dry individually (stacked coins)[47].

Some designs with intersections can leads to irregularities in thickness owe to the convective flows, known as Marangoni flows that produce the well known coffee ring effect after the curing process and/or coalescence forces between printed droplets before the curing process. Irregularities are found and the intersections present high volumes of material. An empirical study[48] has demonstrated that by applying several layers with different compensation patterns to intersections (angles, T shapes or crosses) can balance these irregularities presented in the morphology of printed films, improving the film homogeneity. In other words, multilevel matrix deposition reduces the coalescence effect over thickness regularity.

Not just designs with intersections lead to coalescence forces between drops. Spiral designs show ink accumulations on top of every spiral, but not at the bottom (Fig. 26).
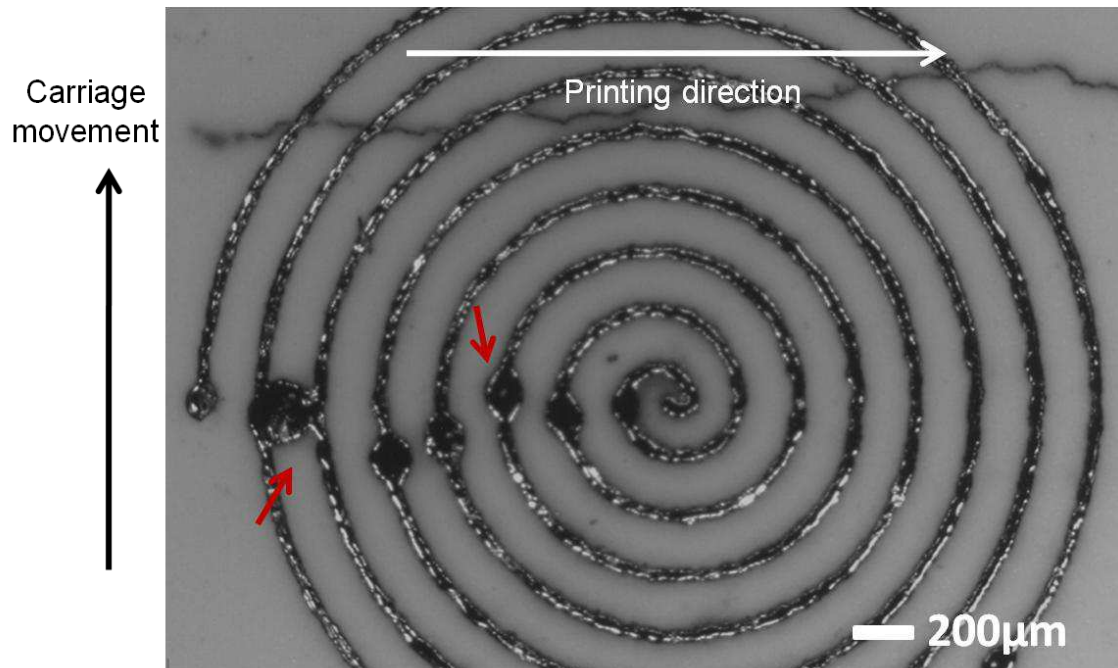
Fig. 26: Spiral design printed with our silver ink slightly modified for HF applications (Chapter 6).

In this case, the starting printing side is critical, and spherical semi-circumferences lead to coalescent drops when it starts being printed at the convex side, but not in the opposite direction. This is because flows appear when a drop gets in contact with another one, getting closer and starting the coalescence with the drop previously printed (Fig. 27).
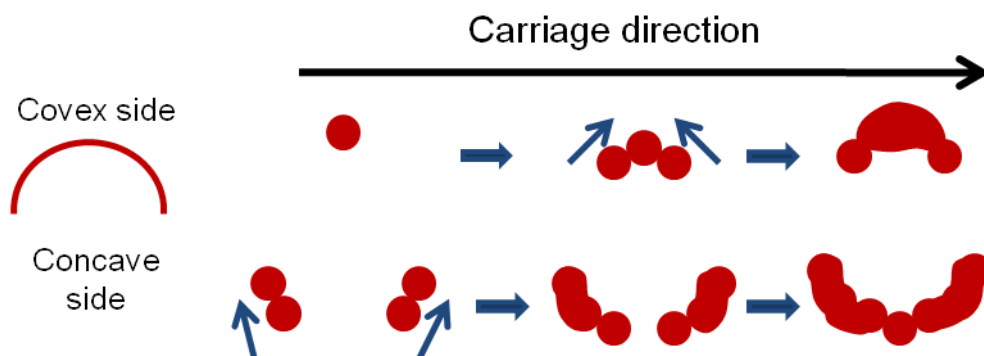
Fig. 27: Scheme of coalescence drops depending on the starting side of the printing in spirals or semi-circumferences.

Furthermore, Dan Soltman et al.[47] have demonstrated that even different substrate temperature can leads to uniforms printings, this affects to the cross section of these printed

lines. Whereas the profile is smooth and convex at low temperature, it becomes increasingly concave at higher temperature.
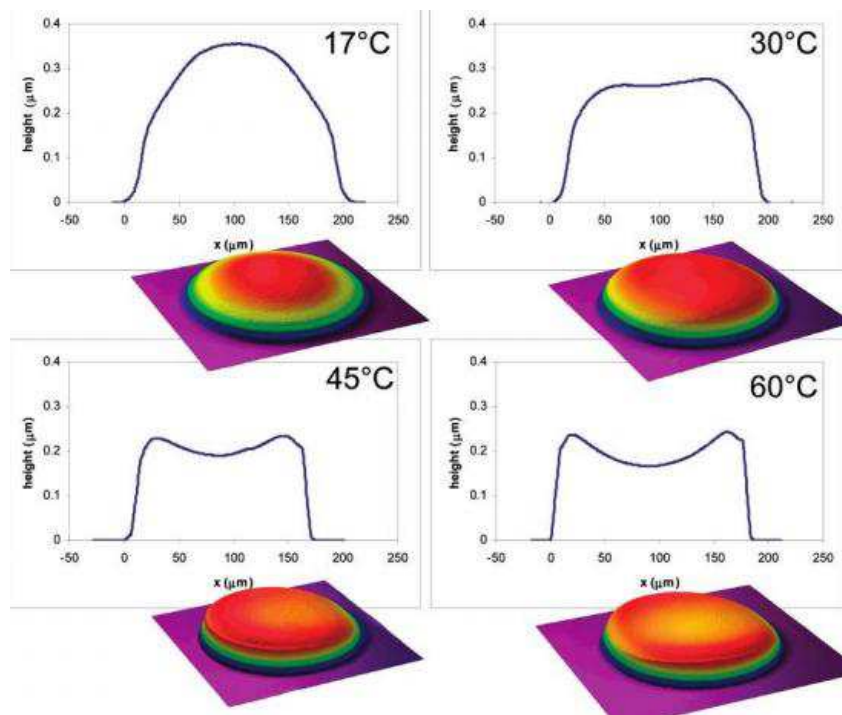
Fig. 28: Influence of the substrate temperature while printing in the cross section of the printed line.

In addition, solute distribution during drying can strongly influence the shape of a printed drop through the coffee ring effect, when solute strongly segregates to the initial contact line[49]. It depends highly on the evaporation rate and the particle concentrations. This coffee ring effect is due to the fixing nip of the drop (interface of surface-air and liquid), drying and hence increasing the evaporation rate of liquid at the interfaces, consequently establishing an internal solute flux deposited on edges to replace the evaporating fluid[50,51]. This peripheral flow continuously feeds the solidification at the contact line, and the final deposit will show a characteristic ring where the solute has segregated during the drying process.

In a medium of just one solvent, the evaporation rate will determine strongly the homogeneity of the deposition. The lower the evaporation rate, the better homogeneity and the less probability to find the coffee ring effect. In co-solvents medium, the concentration of solvents with higher boiling point should be higher to fill the peripheral areas where evaporation of the other solvents is most immediate.

By lowering the substrate temperature to reduce evaporation at the interface as it can be seen at Fig. 28; by using a solvent with a high boiling point[52] (using the Marangoni effect) or by adding some kind of additive such as laponite[53] can help to minimize this effect. Others studies remark that higher drop volumes and smaller particles diameter affect directly to the effect of the coffee ring, being more highlighted in these cases[54], but independent to the solute concentration[55].

The opposite tendency of particle transport has been noticed and studied too[56]. Particles of higher diameters segregate at the center of drying droplets. The phenomenon is primarily driven by geometric constraints and the capillary force near the contact line. The reverse motion by the capillary force in combination with the normal coffee ring effect can be really interesting besides the separation of particles with different sizes.

In the case of our ink Ag-V03, inward fluid flow can be observed (Fig. 29) due to a quick change in surface tension of the printed fluid. The most volatile solvents usually are used for the decrease in the ink viscosity, but also as a surface tension reducer. When it evaporates quickly, the rest of the co-solvents whose surface tensions are much higher, the contact area between the fluid and the substrate is strongly reduced and the fluid motion is directed toward the printing center.
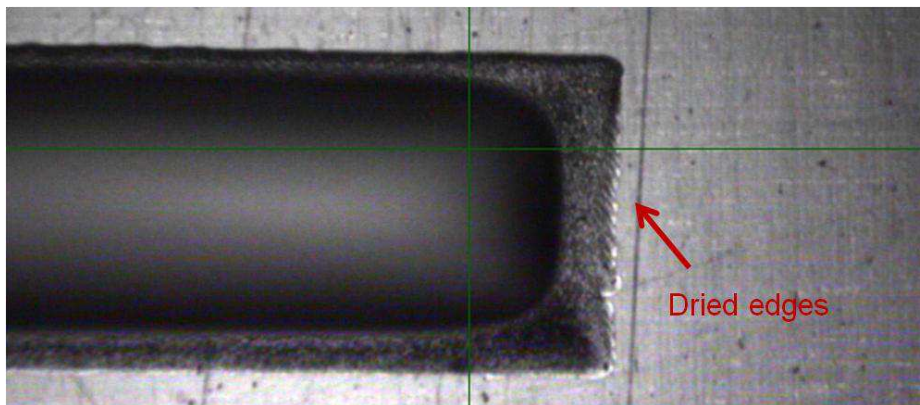
Fig. 29: Dried edges due to the evaporation of the most volatile solvent at room temperature.

This effect is strongly influenced by the evaporation rate; the quicker the evaporation, the faster the inward movement of the fluid. Hence, it depends of the volatility of the different solvents and the drying temperature (Fig. 30). To prevent this effect, the printing should be done in a substrate at temperature, where the most volatile solvent can be evaporated as it is being deposited, avoiding the movement to the interior of the pattern.
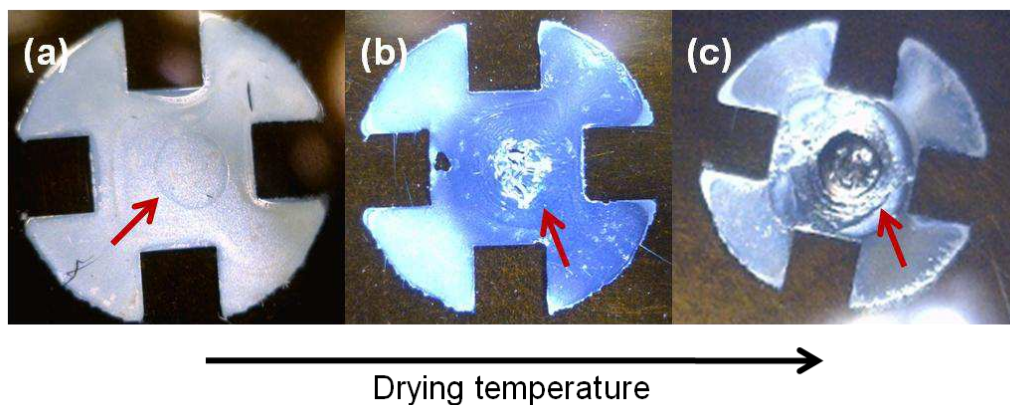
Fig. 30: Effect of the drying temperature in the inward fluid motion and particle concentration, from (a) 100 °C, (b) 175 °C and (c) 225 °C.

2.5.2.3- Adhesion

The mechanical properties of the inkjet deposition are an issue for taking into account. This includes the adhesion of the printed layer to the substrate and the cohesion between layers. The morphological and chemical properties of the interface are the most important factors to achieve a reliable adhesion. When the printing process is done onto a porous substrate is easier to control the adhesion promotion, due to the infiltration and the mechanical interlocking and fasten, but on non-porous surfaces the improvement of the adhesion is a key issue and a challenge and it can be improved by different strategies: a) modifying substrate surface properties by physical or chemical treatments[57], b) introducing an adhesion promoter layer between the substrate and the ink called a primer[58] or c) adding an adhesion promoter in the ink formulation[59].
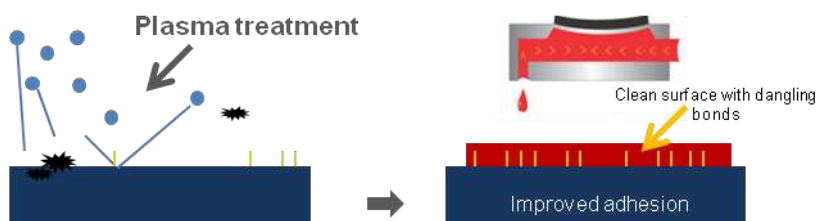
Fig. 31: Plasma treatment as a cleaner and surface modifier to enhance adhesion

As it was mentioned before, the similarities between the ink surface tension and the free surface energy lead to better adhesion between both materials. Plasma technology or acid etching can increase the surface energy of the substrate and use it as a printing variable to improve the wetting and the adhesion (Fig. 31). Furthermore, flame treatment and be used to functionalize the surface to increase bonding between ink and substrate. Hence, altering the chemical nature of the substrate has demonstrated to be a good procedure to enhance the bonding between the ink molecules and the substrate by physic- or chemisorptions. Some pretreatments of the substrate have been reported for this reason, for example, to sputter a nickel or titanium layer and oxygen ion beam irradiation, plasma treatments and chemical modification by silane.

Coating the substrate with a different material which can provide the surface of smoothness or adhesion is another solution (Fig. 32), unfortunately, coating the whole surface with a promoter layer needs to be etched later and the properties of the substrate can lead to the alteration of the resolution owe to the changing in the free energy and the uncontrolled increase in wetting.
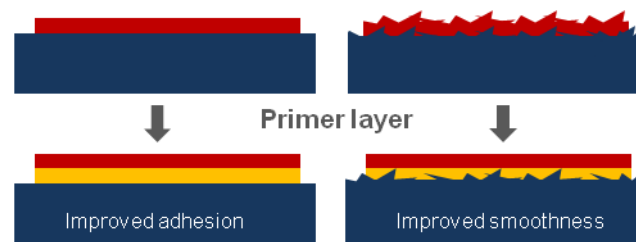
Fig. 32: Primer adhesion as adhesion and smoothness promoter layer

Modifying the formulation adding an adhesion promoter inside the ink can lead to excellent results (Fig. 33). In cofired ceramics or glass structures, the addition of glass frits to enhance the adhesion of the printing material is very usual. In the case of inkjet printing, there is already few studies using nanosized glass frit[59], but this method limits the post-treatment options to higher temperature than the glass transition treatments, to melt the glass frit while sintering. Therefore, this solution reduces the suitable substrates options and that restriction makes it impossible to use it in flexible electronics. Other interesting options have been studied, such as the use of silicone coupling agents in organometallic inks, providing in this way an hybrid link between organic material (such as polymeric substrates) and inorganic ones (metal ions) with good adhesive strength and at low temperature[57].

Fig. 33: The addition of some adhesion promoters such as glass frit inside the ink can strengthen the interaction between the ink and the substrate

To evaluate the adhesion, there is a cross cut test which consists in cutting a grid on the printed deposit with a special blade of parallel cuts, then, crossing new cuttings at 90⁰ (as the indicated in ASTM D 3359). After that, a tape is placed and adhered over the grid and later removed by seizing the free end and rapidly back upon itself at as close to an angle of 180° as possible. The grid area is inspected for the removal of coating from the substrate. The adhesion is rated in accordance with the scale illustrated in Fig. 34.

Fig. 34: Classification of the adhesion strength according to the removal coating area after the cross-cut test

2.6- Functionality

Inkjet printing is a highly attractive technology with capabilities that, in addition to color printing, are being used increasingly for printing diverse functional structures. Nowadays, for example, printed electronic circuit can be made completely by this technique. In view of various new application fields, and as conductive lines become reliable, further electronic properties are needed for the processing of different components and to cooperate or compete with thick-film screen printing. In printed circuits and components, the electrical behavior is achieved by the different compositions of the ink, such as metal, metal oxides or glass, and by its sintering or curing after printing.

Generally the functional elements necessary toward printed electronics are (1) semiconductors, (2) conductors and (3) dielectrics. Semiconducting inks are composed of semiconducting organic polymers in solvents or inorganic nanoparticles (Group III-V, II-VI and IV semiconductors and carbon species) suspended in carrier fluids. Conductive inks are composed of conductive organic polymers in solvents, metallic particles suspended in binders or organic-metallic blends. Dielectric inks are composed of organic polymers in solvents, organic polymer thermosets or ceramic-filled organic polymers.

Besides many other functionalities beyond the scope of this thesis have been recently introduced such as piezoelectric, magnetic, optic or thermoelectric.

As example of functionality, this section will deal on conductivity. In the following chapters additional functionalities are being considered.

2.6.1- Post-treatments

The selection of the ink or the substrate has to be done concurrently. The phase change from liquid to solid typically generates the functional material from the ink. For most applications this phase change usually comes after a post-treatment. Usually the aim of the secondary process is to evaporate the solvents, to sinter the functional material or to reduce the precursor by means of thermal treatment, plasma[60,61] , laser sintering[62], electrical sintering[63,64] intensed pulse light (IPL)[65], photonic and microwave exposure[66,67] by chemical reaction or even self-sintering while solvent evaporation[68]. In all these cases, solidification occurs post-deposition, and the printed pattern must retain some stability in the liquid state prior to solidification and the post-treatment conditions have to be hold by the substrate without losing its properties and change detrimentally the device performance.

Metallic sintering

The sintering is the process of compacting particles or powders to form a solid mass of material by heat or pressure without melting it to the point of liquefaction. The particles begin to flow together by diffusion and coalescence since one large particle with less surface area than two smaller ones with equal total volume is energetically favorable. Thus, a sintered part will be more completely fused and stronger when initial particles have finer size.

The sintering temperature depends on the size of the nanoparticles[69]. In the case of silver nanoparticles can achieve thermal sintered at compatible temperatures with flexible substrates such as polyimide or even PET. Common sintering temperatures for silver inks are around 200-300 °C, but they can be sintered at lower temperatures either. In the case of our silver ink, Ag-V03, the nanoparticles start to be sintered at temperature over 200 °C and the coalescence of the particles can be observed in the SEM images in Fig. 35.
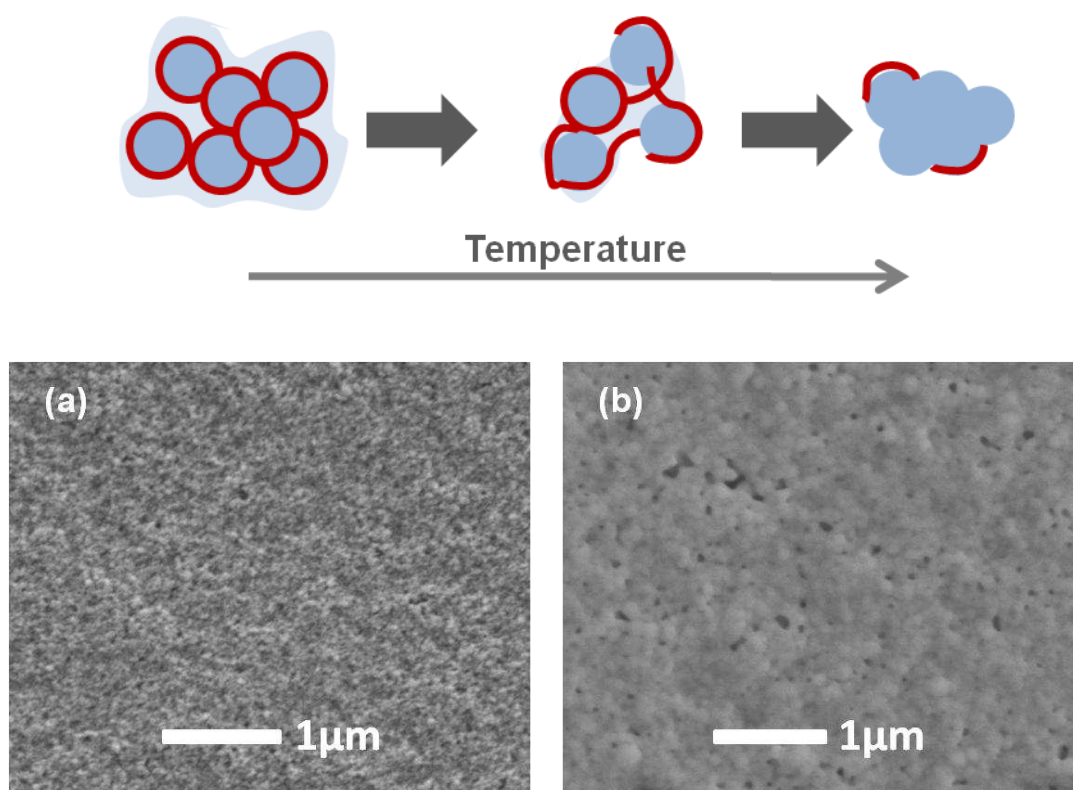
Fig. 35: Sintering process. After a thermal treatment, the nanoparticles fuse together forming a solid layer. Part of the stabilizer polymer (red-colored line) can still remain in the sintered material. The Ag-V03 was (a) dried at 185°C and (b) sintered at 250°C

To avoid possible incompatibilities with polymeric substrates that may be affected by high temperature, it have been developed different ways of sintering, such as UV are microwave and laser radiation; or other inks that allows sintering at lower temperatures as in the case of organometallic[70,71].

Leaving behind the idea of reducing the sintering temperature, in our case have been much more important the fact of preventing cracks on the metallic surface during the sintering process and avoiding the liquid flows in- and outwards. Cracks on silver tracks carry out rapid

degradation as it will be explained in Chapter 4 so it is crucial to prevent them by changing in formulation and drying process.

The first formulation consisted in a solvent medium of EG, glycerol and ethanol. Adjusting physical parameters of the ink, the printing quality was perfectly acceptable but at sintering a matte aspect was observed in every deposit after drying it (Fig. 36).
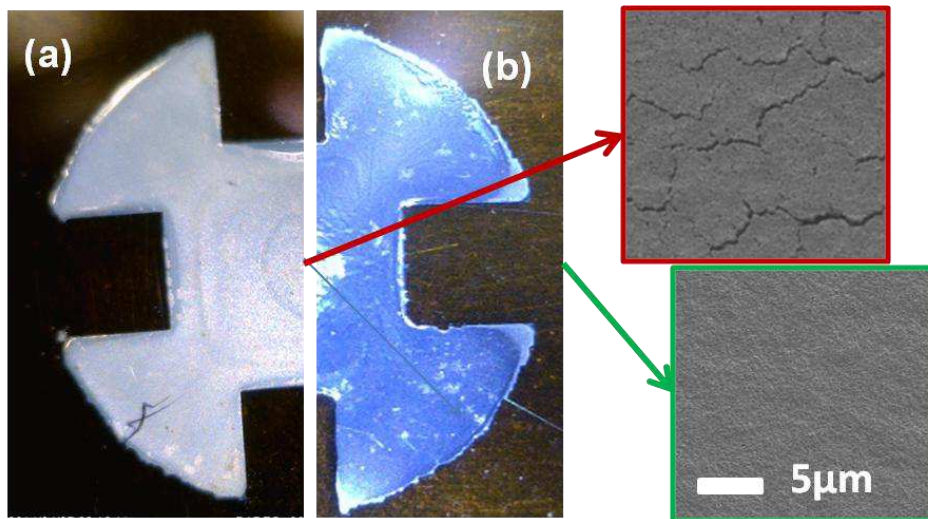
Fig. 36: Images of a silver printing after drying (a) with matte aspect and (b) with metallic bright. At the right side SEM images of the surface are shown. The (a) composition corresponds to EG, ethanol and glycerol as the solvent medium while (b) is composed by EG, glycerol and EGME.

The matte aspect of the cured deposit gets more evident with higher temperature of sintering. The ethanol, as the most volatile component in the ink composition, evaporates quickly, creating tensions in the deposit. The matte color is caused by the micro-cracks that can be observed by the SEM images (Fig. 36). These cracks can lead to earlier degradation of the silver deposit due to the higher effective surface available for the corrosive elements to reacts what is not a desired effect. The fact that the ethanol is the responsible for these micro-cracks was proved by different compositions where the ethanol was added in lower concentrations and even suppressed.

The most obvious solution to obtain a metallic aspect sintering is the replacement of ethanol for another solvent whose volatility is lower. Different composition suppressing the ethanol and changing the concentration of EGME, EG and glycerol were checked. The aim of the addition of the EGME is its low viscosity and surface tension in comparison of the more viscous solvents such the EG and glycerol besides the boiling temperature is up to 150 °C.

Nevertheless, this solvent mixture does not have proper surface tension for the polyimide substrate and when the temperature is applied for the sintering process, a movement toward the center of the deposit occurs due to the surface tension gradient what decrease the contact area of the wet drops. During a low thermal process, EGME is the first in evaporating. When the temperature ramp is low, the evaporation process occurs more gently, and the movement observed is subtler. However, the gradient in surface tension cannot be completely avoided. Higher contents of glycerol, which is the last solvent in evaporating, might maintain stable the surface tension, but the viscosity would be shot up out of tolerances to be ejectable.
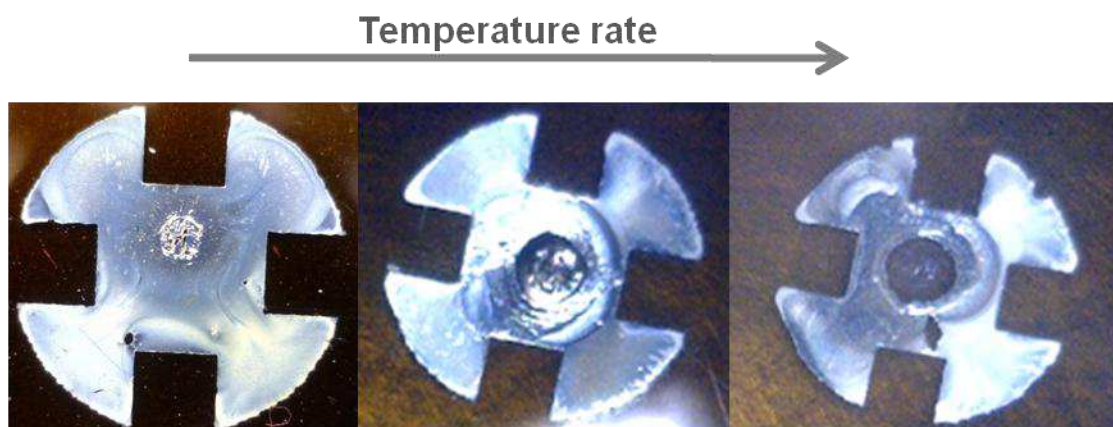
Fig. 37: Formulation where the gradient of surface tension is high between the components can leads to inward movement of the fluid when drying, being extremely important at high temperature rates.

The addition of an additive to control the surface tension gradient and to level the wet deposition could be a solution but, taking into account the functionality of the ink, the addition of an organic material that can remain after the sintering affects detrimentally to the conductivity. The supply of isopropyl alcohol (IPA) instead of the ethanol gave place to a good result, being able to curing without forming cracks. This fact might be caused because of the two –OH groups that interact better with the substrate and the silver nanoparticles.

The isopropyl alcohol evaporates immediately, causing an extremely change in the surface tension of the wet deposit, increasing it and lowering the interface area. That leads again to a dramatically movement inward, leaving even blank areas at the edges and a massive concentration in the center which cracks. Nevertheless, using a sintering of two steps, these issues can be solved. About 10 min at 150 ⁰C and 20 min at 250 ⁰C leads to a smooth surface without cracks.

The thermogravimetric analysis (TGA) and differential scanning calorimetry (DSC) analysis of the final composition indicated in Table 1 is shown in Fig. 38. The analysis was made at two temperature rates, 10 $^{\circ}$C/min and 30 $^{\circ}$C/min to be able to identify the kinetic and thermodynamic processes. As it can be seen, all solvents are volatilized at 200 and 250 $^{\circ}$C respectively, but sintering does not occur until 280 or 300 $^{\circ}$C, where an exothermic peak is observed. The sintering process is a kinetic process, so the peak is moved depending on the heating rate. At 10 $^{\circ}$C/min, the peak appears at lower temperature but being less noticeable. In the case of 30 $^{\circ}$C/min, the peak is much more significant but at higher temperatures.
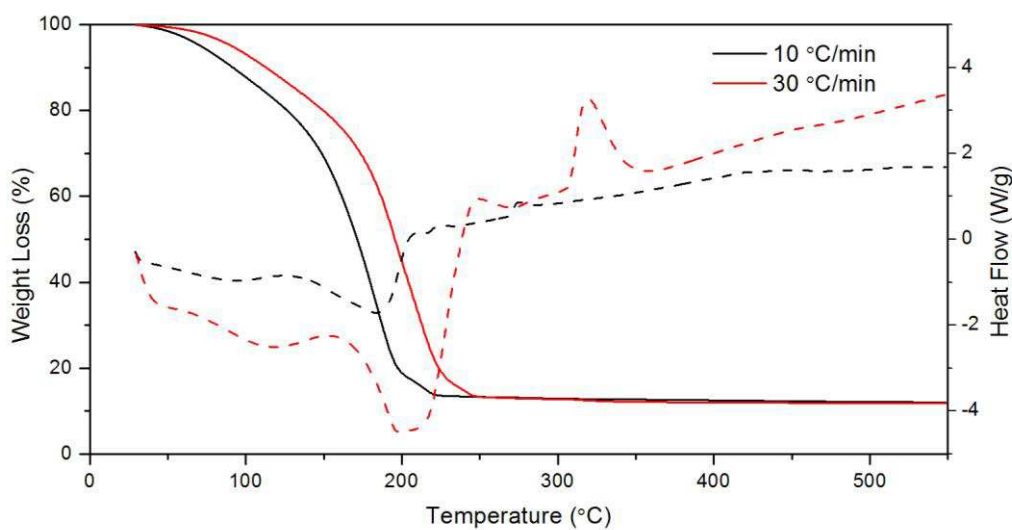
Fig. 38: TGA/DSC analysis of the silver ink with a ramp of 10°C/min and 30°C/min.

2.6.2- Conductivity

In the case of functional conducting inks, the electrical resistivity is the key parameter and it depends on the metallic element used as the functional material, the sintering grade and the organic remaining. Since particles do not melt during sintering, some voids persist what makes the sintered solid less dens than the bulk material and, usually, to have a resistivity by 10 times higher than the bulk resistivity. It is evident that when the better the sintering is, the lower the resistivity, owe to the lower contact resistance between particles which are already coalescent.
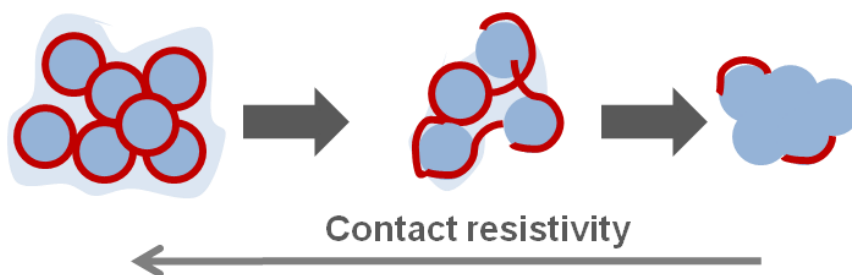
Fig. 39: Sintering process increases conductivity (decrease resistivity) since it reduces the surface per volume and enhances the contact between the particles.

Conductivity can be improved as the particle size distribution increase since it allows greater packing fraction. The smaller particle can behave as lubricant and allows higher maximum particle volume fraction too[72].
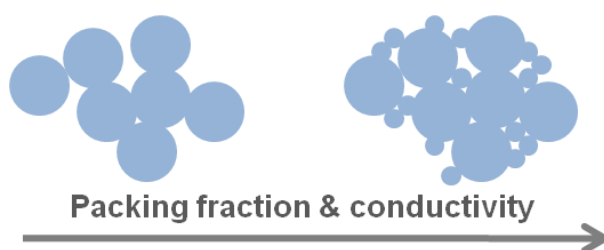
Fig. 40: Particle distribution size allows greater compacting grade and reduces the voids and the contact resistivity between particles.

As the sintering temperature of nanoparticles, overall silver nanoparticles, is low compared with the degradation of organic additives, there is always some organic residue after the sintering, avoiding a perfect contact between metallic particles and increasing the resistivity (Fig. 35). An elegant solution to this problem is the use of the correspondent metallic salt as the surfactant of the metallic nanoparticles, which must turn into a metallic state at the lowest curing temperature,. The metallic clusters, coming from the curing of the salt, will behave as a seed and the metallic grains will grow around them[73].
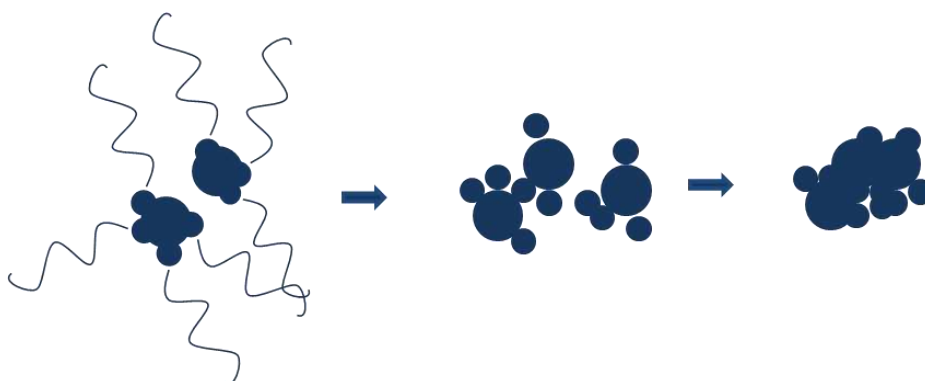
Fig. 41: The metallic nanoparticles are stabilized by an organometallic or a salt of the same metallic element. At T<Ts the organometallic is reduced to be cured and sintered later at Ts.

Nevertheless, our formulation gives place to a good conductivity as it can be shown in Fig. 42. Since the bulk resistivity of silver bulk is $1.59 \cdot 10^{-8}$ Ω, our ink is just one order of magnitude higher, as expected. Even if the DSC shows that sintering process occurs around 280 ^{o}C when temperature rate is 10 ^{o}C/min, it is not necessary to reach that temperature if the printing is maintained longer at lower temperature. Fig. 42 shows how when the sample is cured at 225 or 250 ^{o}C for a time such as 50 min, the resistivity gets lower until the same value obtained at 280 ^{o}C for a shorter period of time, around 20 min.
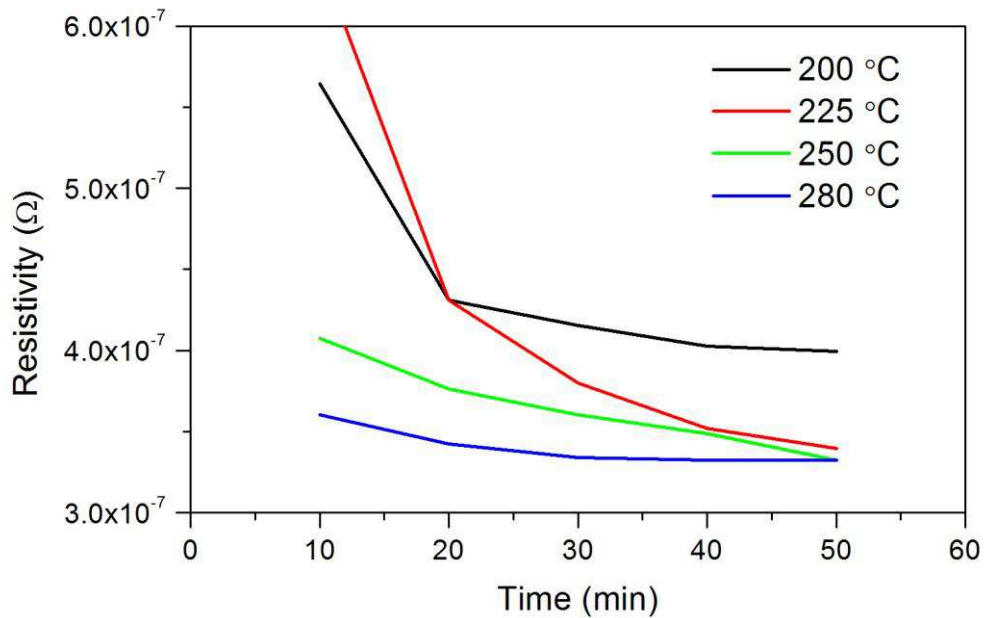
Fig. 42: Resistivity of our silver ink, Ag-V03, when cured at different temperatures in time.

References

[1] J. Perelaer, C. E. Hendriks, A. W. M. de Laat, U. S. Schubert (2009), *One-step inkjet printing of conductive silver tracks on polymer substrates*, Nanotechnology 20, 165303.

[2] K. F. Teng, R. Vest (1987), *Liquid ink jet printing with MOD inks for hybrid microcircuit,* IEEE Transactions on components, hybrids, and manufacturing technology 12, 545.

[3] J. J. Lee, J. C. Parka, M. H. Kim (2007), *Silver complex inks for ink-jet printing: the synthesis and conversion to a metallic particulate ink*, Journal of Ceramic Processing Research 8 (3), 219.

[4] J. Perelaer, A. W. M. de Laat, C. E. Hendriks, U. S. Schubert (2008), *Inkjet-printed silver tracks: low temperature curing and thermal stability investigation*, Journal of Materials Chemistry 18, 3209.

[5] Metalor available at http://www.metalor.com (consulted on November 2015).

[6] D. R. Lide ed., *CRC Handbook of chemistry and physics, Internet version 2005*. CRC Press, Boca Raton, FL.

[7] C. L. Yaw, W. Andrew, *Thermophysical properties of chemicals and hydrocarbons, 2008,* Norwich, NY.

[8] Dow Product information Brochure (E-series) available at http://www.dow.com (consulted on November 2015).

[9] K. L. Lee, B. H. Jun, T. H. Kim, J. Joung (2006), *Direct synthesis and inkjetting of silver nanocrystals toward printed electronics*, Nanotechnology 17, 2424.

[10] J. Jung, Y. H. Jo, J. Kim, H. M. Lee (2011), *A simple process for synthesis of Ag nanoparticles and sintering of conductive ink for use in printed electronics*, Journal of Electronic Materials 41 (1), 115.

[11] A. Kosmala, R. Wright, Q. Zhang, P. Kirby (2011), Synthesis of silver nano particles and fabrication of aqueous Ag inks for inkjet printing, Materials Chemistry and Physics 129 (3), 1075.

[12] P. Y. Silvert, R. Herrera-Urbina, N. Duvauchelle, V. Vijayakrishnan, K. T. Elhsissen (1996), *Preparation of colloidal silver dispersions by the polyol process. Part 1 – synthesis and characterization*. Journal of Materials Chemistry 6, 573.

[13] A. Sarkar, S. Kapoor, T. Mukherjee (2005), *Preparation, characterization, and surface modification of silver nanoparticles in formamide*, Journal of Physical Chemistry B. 109, 7698.

[14] X. Yang, W. He, S. Wang (2012), *Effect of the different shapes of silver particles in conductive ink on electrical performance and microstructure of the conductive tracks*, Journal of Materials Science: Materials in Electronics 23 (11), 1980.

[15] TA Instruments brochure *Long term stability testing of printing inks by differential scanning calorimetry* available at http://www.tainstruments.com (Consulted on November 2015).

[16] J. E. Fromm (1984), *Numerical calculation of the fluid dynamics of drop-on-demand jets*, IBM Journal of Research and Development 28 (3), 322.

[17] Dimatix guideline available at https://www.fujifilmusa.com (Consulted on November 2015).

[18] B. V. Antohe, D. B. Wallace (2002), *Acoustic phenomena in a demand mode piezoelectric inkjet printer*, Journal of Imaging Science and Technology 46 (5), 409.

[19] N. J. Wagner, J.F. Brady (2009), *Shear thickening in colloidal dispersions*, Physics Today 62 (10), 27.

[20] Malvern Instruments, *Caracterización reologica de procesos a alta velocidad de deformación* organized by IESMAT and Instituto de Tecnología Cerámica-UJI in Castellón, Spain. July 2014.

[21] *Multiple ways to optimize rheology for increased dispersion, colloidal and emulsion stability* Sponsored by Malvern Instruments Ltd. available at http://www.azom.com/article.aspx?ArticleID=11442 (Consulted on November 2015).

[22] *Methods of surface tension measurements* available at http://zzm.umcs.lublin.pl/Wyklad/FGF-Ang/2A.F.G.F.%20Surface%20tension.pdf (Consulted on November 2015).

[23] N. Reis, B. Derby (2000), *Ink jet deposition of ceramic suspensions: modeling and experiments of droplet formation*, MRS Proceedings 625.

[24] D. Jang, D. Kim, J. Moon (2009), *Influence of fluid physical properties on ink-jet printability*, Langmuir 25 (5), 2629.

[25] B. Derby (2010), *Inkjet printing of functional and structural materials- Fluid property requirement, feature Stability, and resolution*, Annual Review of Materials Research 40 (1), 395.

[26] A. Famili, S. A. Palkar, J. W. J. Baldy (2011), *First drop dissimilarity in drop-on-demand inkjet devices*, Physics of Fluids 23 (1), 012109.

[27] P. Calvert (2001), *Inkjet printing for materials and devices*, Chemistry of Materials 13 (10), 3299.

[28] A. L. Yarin (2006), *Drop impact dynamics: splashing, receding, bouncing*, Annual Review of Fluid Mechanics 38 (1), 159.

[29] S. Magdassi (2010), *The chemistry of inkjet inks*, New Jersey: World Scientific.

[30] J. Mei (2004), *Formulation and processing of conductive inks for inkjet printing of electrical components*, PhD Dissertation, University of Pittsburgh, Pennsylvania, PA (USA).

[31] Y. S. Noguchi (2006), *Organic-transistor-based flexible pressure sensors using ink-jet-printed electrodes and gate dielectric layers*, Applied Physics Letters 89, 253507.

[32] N. D. Sankır (2005), *Flexible electronics: materials and device fabrication,* PhD Dissertation, Virginia Polytechnic Institute and State University at Blacksburg, Virginia, VA (USA).

[33] PowerCoat Paper available at http://powercoatpaper.com/ (Consulted on November 2015).

[34] R. K. Holman, M. J. Cima, S. A. Uhland, E. Sachs (2002), *Spreading and infiltration of inkjet-printed polymer solution droplets on a porous substrate,* Journal of Colloid and Interface Science 249 (2), 432.

[35] M. Denesuk, G. L. Smith, B. J. J. Zelinski, N. J. Kreidl, D.R. Uhlmann (1993), *Capillary penetration of liquid droplets into porous materials*, Journal of Colloid and Interface Science 158 (1), 114.

[36] T. Lamminmäki, J. Kettle, H. Rautkoski, A. Kokko, P. Gane (2011), *Limitations of current formulations when decreasing the coating layer thickness of papers for inkjet printing,* Industrial & Engineering Chemistry Research 50 (12), 7251.

[37] T. H. J. van Osch, J. Perelaer, A. W. M. de Laat, U. S. Schubert (2008), *Inkjet printing of narrow conductive tracks on untreated polymeric substrates,* Advanced Materials 20, 343.

[38] A. Kosmala, Q. Zhang, R. Wright, P. Kirby (2012), *Development of high concentrated aqueous silver nanofluids*, Materials Chemistry and Physics 132 (2), 3.

[39] H. Y. Tseng (2011), *Scaling of inkjet-printed transistors using novel printing techniques*, PhD Dissertation, University of California at Berkeley, CA (USA).

[40] J. Doggart (2011), *Inkjet printed conductive inks for the fabrication of organic thin film transistors*, PhD Dissertation, Mc Master University at Hamilton, Ontario (Canada).

[41] J. Stringer, B. Derby (2009), *Limits to feature size and resolution in ink jet printing*, Journal of the European Ceramic Society 29 (5), 913.

[42] S. Chandra, C. T. Avedisian (1991), *On the collision of a droplet with a solid surface*, Proceedings *A* 432 (1884), 13.

[43] T. Mao, D. C. S. Kuhn, H. Tran (1997), *Spread and rebound of liquid droplets upon impact on flat surfaces,* AIChE Journal 43 (9), 2169.

[44] M. Pasandideh-Fard, Y. M. Qiao, S. Chandra, J. Mostaghimi (1996), *Capillary effects during droplet impact on a solid surface,* Physics of Fluids 8, 650.

[45] S. Schiaffino, A. A. Sonin (1997) *Formation and stability of liquid and molten beads on a solid surface,* Journal of Fluid Mechanics 343, 95.

[46] R. Rioboo, M. Marengo, C. Tropea (2002), *Time evolution of liquid drop impact onto solid, dry surfaces,* Experiments in Fluids 33 (1), 112.

[47] D. Soltman, V. Subramanian (2008), *Inkjet-printed line morphologies and temperature control of the coffee ring effect*, Langmuir 24 (5), 2224.

[48] E. Diaz, E. Ramon, J. Carrabina (2013), *Inkjet patterning of multiline intersections for wirings in printed electronics*, Langmuir 29 (40), 12608.

[49] R. D. Deegan (2000), *Pattern formation in drying drops*, Physical Review E. 61 (1), 475.

[50] E. Adachi, A. S. Dimitrov, K. Nagayama (1995), *Stripe patterns formed on a glass surface during droplet evaporation*, Langmuir 11 (4), 1057.

[51] R. D. Deegan, O. Bakajin, T. F. Dupont, G. Huber, S. R. Nagel, T. A. Witten (1997), *Capillary flow as the cause of ring stains from dried liquid drops*, Nature 389 (6653), 827.

[52] B. J. De Gans, U. S. Schubert (2004), *Inkjet printing of well-defined polymer dots and arrays*, Langmuir 20 (18), 7789.

[53] E. L. Talbot, L. Yang, A. Berson, C. D. Bain (2014), *Control of the particle distribution in inkjet printing through an evaporation-driven sol-gel transition,* ACS Applied Materials & Interfaces 6 (12), 9572.

[54] L. Shmuylovich, A. Q. Shen, H. A. Stone (2002), *Surface morphology of drying latex films: multiple ring formation*, Langmuir 18 (9), 3441.

[55] J. Fukai, H. Ishizuka, Y. Sakai, M. Kaneda, M. Morita, A. Takahara (2006), *Effects of droplet size and solute concentration on drying process of polymer solution droplets deposited on homogeneous surfaces*, International Journal of Heat and Mass Transfer 49 (19), 3561.

[56] B. M. Weon, J. H. Je (2010), *Capillary force repels coffee-ring effect*, Physical Review E. 82 (1), 015305.

[57] Y-I. Lee, Y-H. Choa (2012), *Adhesion enhancement of ink-jet printed conductive copper patterns on a flexible substrate*, Journal of Materials Chemistry 22 (25), 12517.

[58] A. Sridhar, D. J. van Dijk, R. Akkerman (2009), *Inkjet printing and adhesion characterisation of conductive tracks on a commercial printed circuit board material*, Thin Solid Films 517 (16), 4633.

[59] D. Jang, D. Kim, B. Lee, S. Kim, M. Ka (2008), *Nanosized Glass Frit as an Adhesion Promoter for Ink-Jet printed conductive patterns on glass substrates annealed at high temperature*, Advanced Functional Materials 18 (19), 2862.

[60] F. M. Wolf, J. Perelaer, S. Stumpf, D. Bollen, F. Kriebel, U. S. Schubert (2013), *Rapid low-pressure plasma sintering of inkjet-printed silver nanoparticles for RFID antennas*, Journal of Materials Research 28 (9), 1254.

[61] S. Wunscher, S. Stumpf, A. Teichler, O. Pabst, J. Perelaer, E. Beckertd U. S. Schubert (2012*), Localized atmospheric plasma sintering of inkjet printed silver nanoparticles*, Journal of Materials Chemistry 22, 24569.

[62] S. H. Ko, H. Pan, C. P. Grigoropoulos, C. K. Luscombe, J. M. J. Fréchet (2007), *All-inkjet-printed flexible electronics fabrication on a polymer substrate by low-temperature high-resolution selective laser sintering of metal nanoparticles,* Nanotechnology 18 (34), 345202.

[63] Y. J. Moon , S. H. Lee, H. Kang, K. Kang , K. Y. Kim, J. Y. Hwang, Y. J. Cho (2011), *Electrical sintering of inkjet-printed silver electrode for c-Si solar cells,* Conference Record of the IEEE Photovoltaic Specialists Conference, 37th, 001061.

[64] M. Hummelgard, R. Zhang, H-E. Nilsson, H. Olin (2011), *Electrical sintering of silver nanoparticle ink studied by In-Situ TEM Probing* PLoS ONE 6 (2), 17209.

[65] J. S. Kang, J. Ryu, H. S. Kim , H. T. Hahn (2011), *Sintering of inkjet-printed silver nanoparticles at room temperature using intense pulsed light,* Journal of Electronic Materials 40 (11), 2268.

[66] J. Perelaer, R. Abbel, S. Wünscher, R. Jani, T. van Lammeren, U. S. Schubert (2012), *Roll-to-roll compatible sintering of inkjet printed features by photonic and microwave exposure: from non-conductive ink to 40% bulk silver conductivity in less than 15 seconds***,** Advanced Materials 24 (19), 2620.

[67] C. Gaspar, S. Passoia, J. Olkkonen, M. Smolande (2016), *IR-sintering efficiency on inkjet-printed conductive structures on paper substrates,* Microelectronic Engineering 149, 135.

[68] M. Grouchko**,** A. Kamyshny, C. F. Mihailescu, D. F. Anghel, S. Magdassi (2011), *Conductive inks with a "Built-In" mechanism that enables sintering at room temperature*, ACS Nano 5 (4), 3354.

[69] P. Buffat, J. P. Borel, *Size effect on the melting temperature of gold particles*, Physical Reviews A. 13 (6), 2287.

[70] A. L. Dearden, P. J. Smith, D-Y. Shin, N. Reis (2005), *A low curing temperature silver ink for use in ink-jet printing and subsequent production of conductive tracks*, Macromolecular Rapid Communications 26 (4), 315.

[71] J. J. P. Valeton, K. Hermans, C. W. M. Bastiaansen, D. J. Broer, J. Perelaer, U. S. Schubert, G. P. Crawford, P. J. Smith (2010), *Room temperature preparation of conductive silver features using spin-coating and inkjet printing*, Journal of Materials Chemistry 20 (3), 543.

[72] G. Chabanis, *Rheological measurements on inks and suspensions*, 1st of July 2014, Castelló de la Plana. Malvern Intruments.

[73] D-Y. Shin, M. Jung, S. Chun (2012), *Resistivity transition mechanism of silver salts in the next generation conductive ink for a roll-to-roll printed film with a silver network*, Journal of Materials Chemistry 22, 11755.

Chapter 3

Functional formulations for screen printing

3.1- Introduction

Screen printing is a conventional and really mature printing technique and it was probably the first and therefore the oldest method for the fabrication of printed electronics. It was already used during the 1940s for the mass production of electronic circuits[1]. Nowadays it is common in the graphics art industry, manufacturing of printed circuit boards, and metallization of silicon solar cells.

Furthermore, screen printing has been the most prevailing deposition method in the thick film technology because of its low cost. All the metallization and dielectric components are usually deposited by this technique. It also commonly prints solder paste in the manufacturing of SMD (Surface mountain devices) on PCBs (printed circuit board**)**. The main differences in the electronics applications lies in the equipment sophistication and the mesh materials what allow a stringently control on the parameters and hence, on the resolution, thickness and outcome quality of the printing[1].

As it was mentioned in the Introduction of this thesis, the development of this part has been carried out in the facilities of the company Francisco Albero S.A.U. (FAE) where it has been previously developed a consolidated knowledge on screen printing and already presented in several PhD dissertations[2,3,4], also under the collaboration between FAE and UB. For this reason, the fundamentals and parameters of the screen printing are overviewed quicker than for inkjet printing, focusing more in example of new paste formulations developed during the completion of this thesis.

3.2- Fundamentals and main parameters in the screen printing process

3.2.1- Screen printing process

The main principle for every printing technique is the same; the deposit of a quantity of ink or paste onto a substrate where it settles on with a controlled pattern and thickness. In the case of screen printing this entails squeezing the paste through a mesh onto a surface beneath (Fig. 1).
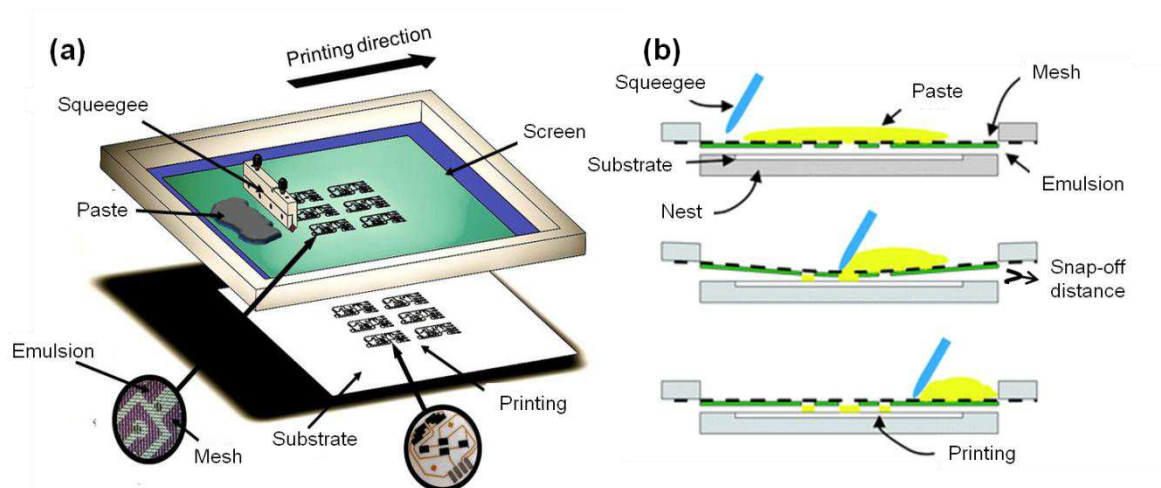
Fig. 1: (a) Different components of the screen printing and (b) screen printing process.

The essential items in screen printing consist of the material to be printed (the paste), the surface where it is being printed (substrate), the screen that defines the required pattern and the squeegee that forces the paste through the screen. The screen is composed by a frame upon which is stretched a mesh (or eventually a stencil). Attached to the mesh is found the emulsion with the negative of the required design. The squeegee comprises a holder into which is fitted a flexible, resilient rubber blade. Another squeegee with the same characteristic, or a metallic one, is used before the printing as a floodbar to spread the paste all over the mesh.

The mesh is placed in a certain snap-off distance on top of the substrate and the floodbar distributes the paste and fills the mesh (Fig. 1(b)). The printing process is initiated by the squeegee that presses against the screen mesh onto the substrate. The moving squeegee forces the paste through the open areas.

3.2.2- Specifications and features of the essential constituents of screen printing process

3.2.2.1- Screen

The screen in this technology is composed by two main parts. The screen frame that maintains the structure of the screen and the mesh that serves as the functional part. For electronics applications screen frames are nearly always made of metal and usually of aluminum alloy due to the need of hold the mesh tension without deforming itself and leading to a loose of tension in the mesh[5]. The mesh has the function of a net to hold the emulsion and to control the amount of deposited paste. It should be flexible and resilient so that it can conform to surface variations when the squeegee is pressing it and then return to its original shape. This fact allows the complete removal of the paste from the open mesh and the minimum distortion of the printed area.

There are several specifications to take into account when a mesh is selected. The conventional mesh materials are stainless steel, polyester or nylon. The selection of the material depends on the accuracy and the thickness deposition required for the printing[4]. It is known that steel mesh better maintain the proportions as they are less elastic but are much more fragile. Meanwhile polymeric ones are cheaper and more resistant to manipulation. Nylon meshes are strong and resilient but not stable; it absorbs water from the atmosphere humidity, changing its performance[5]. For all these reasons, it is stainless steel the commonly used for electronics applications.

Regardless of the mesh material, the number of threads per cm, thread diameter or open area are quite important and crucial to yield the expected result (Fig. 2).
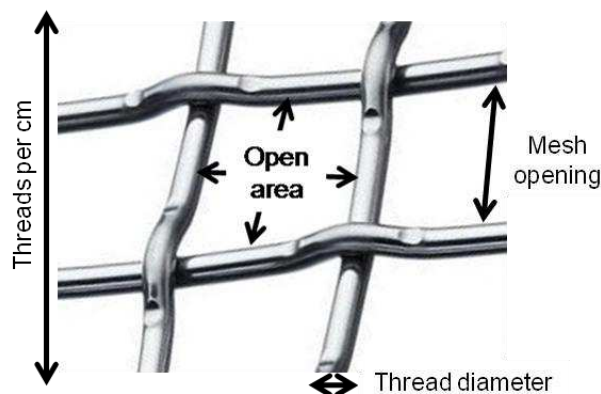
Fig. 2: Screen mesh and its parameters

These parameters affect the definition of the printing and the amount of paste deposited. It is important to highlight that the mesh opening should be at least three times the particle size of the paste and the minimum line width that can be printed is three times the mesh thread diameter[5]. Narrow lines cannot be printed with large thread diameter mesh. From a purely practical point of view, it is unwise to use mesh with wire diameters less than 24 microns; the mesh becomes both very fragile and very expensive. The open area of the mesh has a great effect on the paste passage through the screen and it depends on the parameters mentioned above.

$$Open\ area = \frac{(mesh\ opening\ )^2}{(thread\ diameter\ +mesh\ opening\ )^2}x100\%$$ [1]

The mesh thickness in the case of stainless steel is always between one and three times the thread diameter, depending on variation in hardness or stiffness encountered in stainless steel wires (Fig. 3).
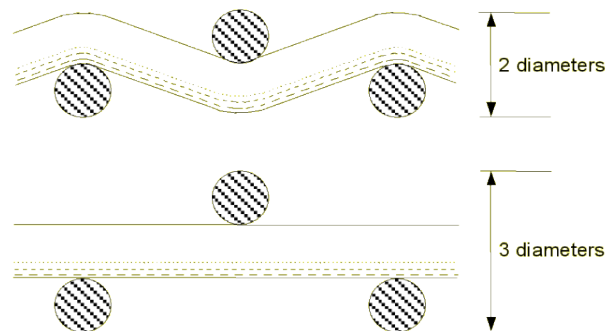
Fig. 3: Cross section of a screen mesh.

According to these definitions, the thread diameters could be compared with the nozzle diameter in inkjet printing. This is because it delimits the open area and then, the maximum particle size composing the paste. Furthermore, the open area becomes the main feature that affects the quantity of deposited material and resolution. Thinner lines can be printed with smaller thread diameters (and then reduced open areas) as well as it happens with smaller nozzle diameter in inkjet which leads to smaller drops and thus, the drop spacing for continuous lines can be reduced, giving place to better resolutions.

The mesh can be mounted under different angles. For electronic circuit it is normal practice for the mesh to be applied at 45 degrees to the frame areas for three main reason[6] explained in Fig. 4: (a) the frame deformation caused by the tense mesh is minimized when the force is

applied to the corners, preventing the tension loosen in the mesh; (b) a mesh at 45° shares the load over more filaments and (c) it is better that fine lines in screen patterns do not run parallel to the filaments because a slight misalignment between the two of them can cause "stair stepping" of the image.
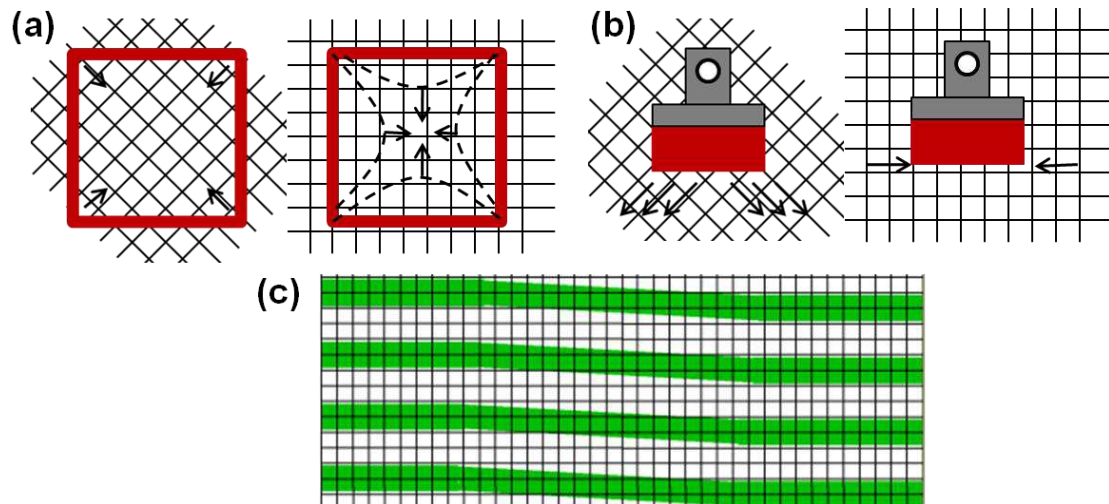
Fig. 4: (a) frame deformation due to the force of the tense mesh for 90 and 45 degrees, (b) paste load distribution when the squeegee is pressing the mesh and (c) "Stair stepping" defect caused by pattern lines crossing screen mesh at a low angle[5]

The screen tension is recommended by the manufacturer and it depends of the kind of material and parameters of each mesh. It is necessary to stretch the mesh applying high enough tension to become detached from the substrate after printing and also maintain the proper dimension of the pattern. It is also crucial to have a good distribution of the tension being homogeneous all over the screen.

The recommended value of the screen tension is always within the elastic elongation of the mesh, where the deformation caused by the printing is reversible (Fig. 5).

The advantage of using the highest of the recommended tensions is that a smaller gap can be used between the screen and the substrate, thus the smaller deflection of the screen touching the substrate usually causes no significant change in screen image size. The disadvantage is that it can be overstretched and damaged easily.
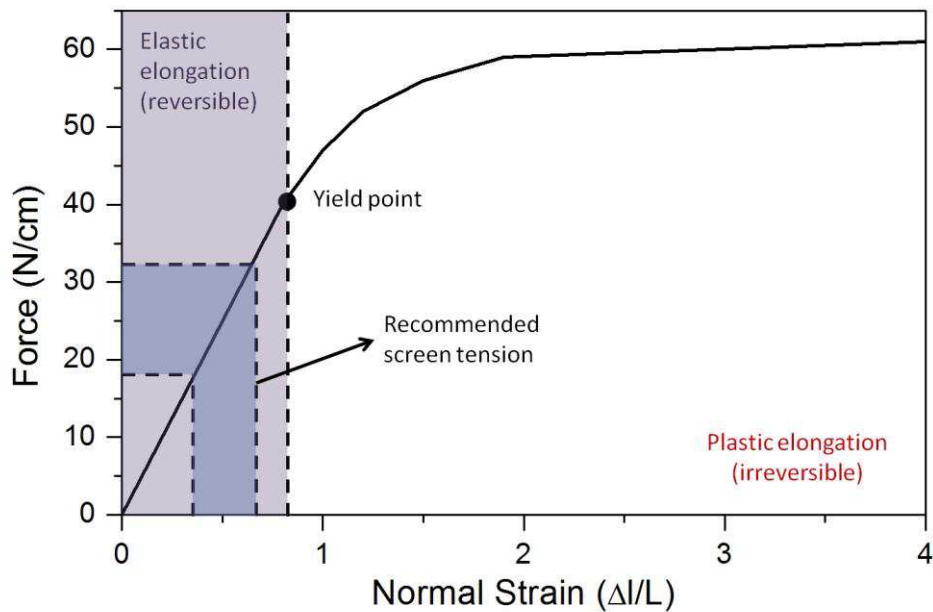
Fig. 5: Mesh elongation vs tension[7].

Emulsion thickness

The printing pattern is developed by covering the mesh with a resin or photosensitive layer on which the pattern on negative is exposed to UV and on positive is covered by an opaque pattern printed on transparent plastic. The exposed emulsion is polymerized and hardened, while those areas protected from the UV remain soft and soluble in water. After exposure, the screen is washed in warm water, which dissolves the unexposed portions, thus leaving defined open areas for the paste to pass through.

The thickness of the emulsion can be controlled. If the emulsion is too thin it will be relatively weak and it will pull back to its nearest supporting thread. The mesh will then define the boundary of the image with serrated edges (Fig. 6). When it is too thick, part of the paste remains on the mesh and it is not released[5].
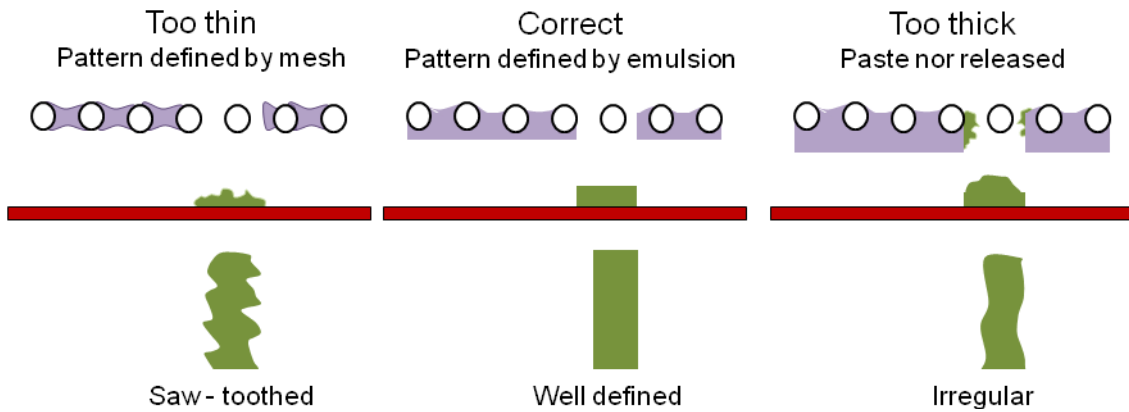
Fig. 6: Effect of the emulsion thickness on the quality of the printing.

Furthermore, the edges of the emulsion will reflect the irregularities of the mesh itself. Small cavities allow low viscosity paste to flow under the emulsion, spreading out of the define pattern. Conversely, high viscosity paste will not flow under the small cavities of the mesh to a more noticeable serration. Fig. 7 shows the two cases.
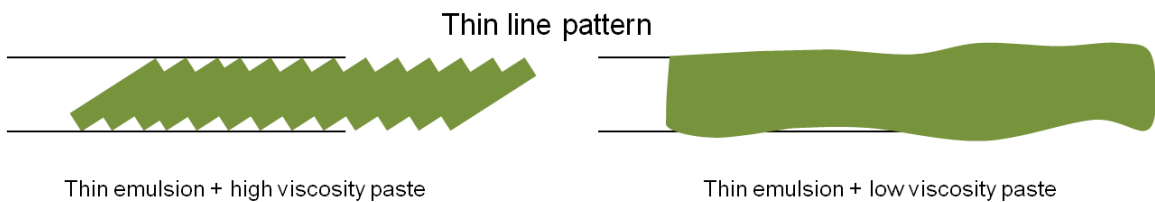
Fig. 7: Effect of a very thin emulsion on the printing when the paste is too high or too low viscosity.

In general, an emulsion thickness of at least 10 µm is necessary to overcome these problems, but for thickness over 30 µm, the paste will tend to stick in the screen rather than transfer onto the substrate. Increasing the emulsion thickness in between can help to adjust the printing thickness, especially for small and thin features, but in areas of more than 10 mm the increase in thickness is not appreciable.

3.2.2.3- Squeegee

Printing quality is not only affected by screen performances but also from squeegee features. The squeegee brings the screen into contact with the substrate and force the paste into the open areas of the screen. The edge may be deformed and penetrates cavities printing as well as conforms to the surface undulations. Blade hardness and shape are the most crucial features affecting the printing and because of that, the blade material should be flexible and resilient. The rate of wear that suffer the blade edge depends on the squeegee pressure, the paste abrasion and the type of mesh being used on the screen -greatest wear for stainless steel. Wear leads to rounded edges what leave paste on the surface instead of removing the excess. That causes bad homogeneity and uncontrolled printing quality.

The material used for the squeegee should be resistant to the paste solvents and screen cleaners. Polyurethane is currently the most widespread material for squeegees. It can be selected from different harnesses from 60 shores to 90 shores. There are squeegees in the market that combine multilayer materials with different hardness to improve the performance[4].

Selecting the proper degree requires reference to the four functions to be performed by the squeegee. In general, the softest possible grade, the greatest tolerance to meet unforeseen variations.

Blade edge profiles

The most common edges of blades are diamond and trailing (Fig. 8).
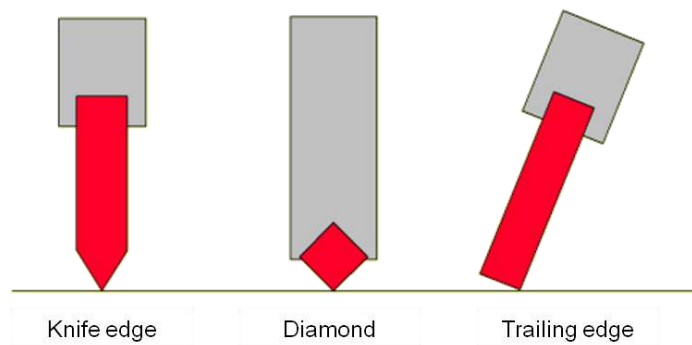
Fig. 8: Edge shapes of the squeegee blade.

The mounting system design is more controllable in diamond profiles than in trailing one in which the effective angle when printing is highly changeable depending on the pressure applied (Fig. 9). Diamond edge is commonly sharper promoting better penetration in the open areas and better removal of paste excess. Diamond squeegees are useful when thinner deposits are wanted due to the fact that the squeegee scoops paste out from the open areas when its edge is depressed into the mask cavities.
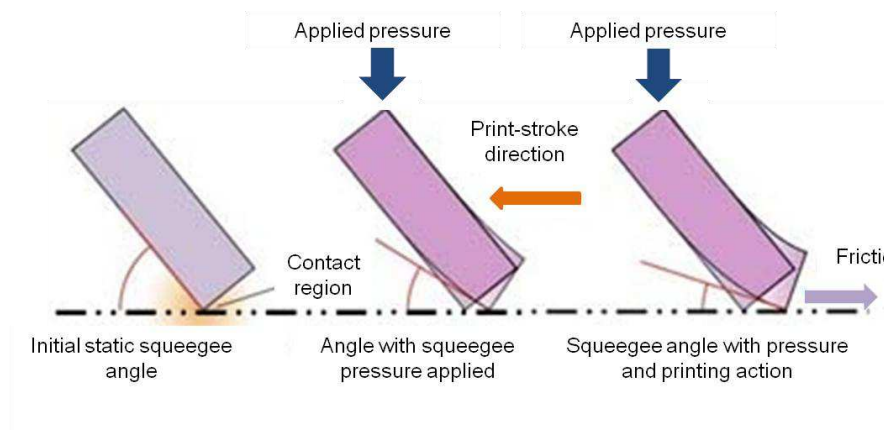
Fig. 9: Effective angle between the blade and the screen.

The effective angle affects noticeable the cavities filling and the paste removal. The lower the angle, the less effective is the pressure applied and the worse the paste removal. The paste escapes under the edge as the scraping action is reduced. On the contrary, the wider the angle, the lower the flexibility and the lower the filling time, what leads to a compromise.

It has been found by experience that a blade with 45 degrees of effective angle gives satisfactory results for the great majority of applications.

3.2.3- Process parameters

The machine parameters such as the squeegee pressure on the screen, the squeegee velocity or the separation between the screen and the substrate (Gap or snap off) also play a crucial role in the final outcome of the process. While the mesh and the emulsion thickness provide the main control of the printing thickness, the machine parameters affects mainly to the definition and the thickness uniformity. The adjustment of these parameters is defined by the

physical properties of the paste, as well as the screen and the pattern to print, being the paste the predominant item to have in consideration.

As it was mentioned, the pressure applied over the screen affects the print thickness as well; in fact, an increased pressure gives a decrease in print thickness. This happens because the squeegee presses down into the mesh and deflects into the open areas of the pattern and hence, reduces the print thickness.

The gap or snap off is the separation between the screen and the substrate (Fig. 10) and this separation must be short enough to hold the mesh deflection until its contact with the substrate. This is needed to allow the screen detaches itself immediately behind the squeegee passage. If the screen remains stuck, the quality of the printed pattern can be variable.
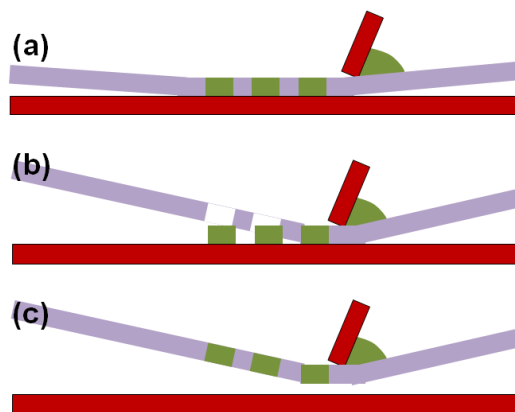
Fig. 10: Gap or distance between the screen and the substrate. (a) too low gap, (b) correct gap and (c) too high gap.

The print gap required varies with screen tension, pattern area, paste viscosity, squeegee speed, etc., but a good starting figure can be obtained by multiplying the width of the screen times 0.004 for stainless steel[6] (Fig. 11).

In addition, increased speed gives an increased print thickness. As the speed is increased so there is less time for the squeegee to enter the apertures and so the thickness will increase.

	Stainless steel	Polyester	Nylon
G	W x .004	W x .006	W x .010
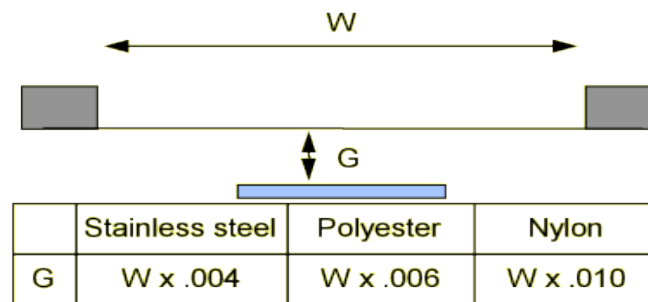
Fig. 11: How define a starting value for the gap.

3.3- About the properties and fabrication of screen printing pastes

As it was said, the essential items in screen printing is composed by the printing equipment (screen and squeegee) explained above and then the printed system correspond to the paste and substrate. The substrate, although essential, does not influence on the quality of the printing as much as the rest of the elements. This part of the chapter will go deeper into the knowledge of the influence of the physical parameters and the components of the paste in the final outcome of the printing.

As explained before the paste is displaced and forced through the open cavities of the screen. The paste flow, as the squeegee moves to print, goes forward from the initial part in touch with the blade and then goes into the cavities and the initial part, in a loop. This flow is crucial for a high quality printing and depends on two main things: the amount of paste on the screen and, especially the proper rheological behavior[1].

3.3.1- Rheology

The rheological behavior of the screen printing paste is shear thinning, what is a non-Newtonian behavior in which the viscosity decreases when the shear rate increases. This is achieved by the formulation, and the pressure and velocity during the printing.

In the case of Newtonian fluids, the viscosity (η) is constant and does not depend on the velocity gradient or on the time of effort application but it can depend on the temperature and

pressure at which it is subjected. In the non-Newtonian fluids, the relation between the strain rate and the shear rate is not linear what means that the viscosity depend on the effort applied on it. A pseudoplastic fluid loses viscosity in mixing and other shear forces is applied what is known as shear thinning performance.

It could happen that the paste shows thixotropy what means that the viscosity depends also on time of shear application. This form of pseudoplasticity describes the behavior of most screen printing pastes. Thixotropic fluids continue thinning during shearing (Fig. 12), even if the shear stress is constant. When the paste is motionless, viscosity recovers the initial value[8]. The viscosity-shear rate curve will always show a loop. This behavior is very important since the changing-viscosity attribute makes screen printing possible.
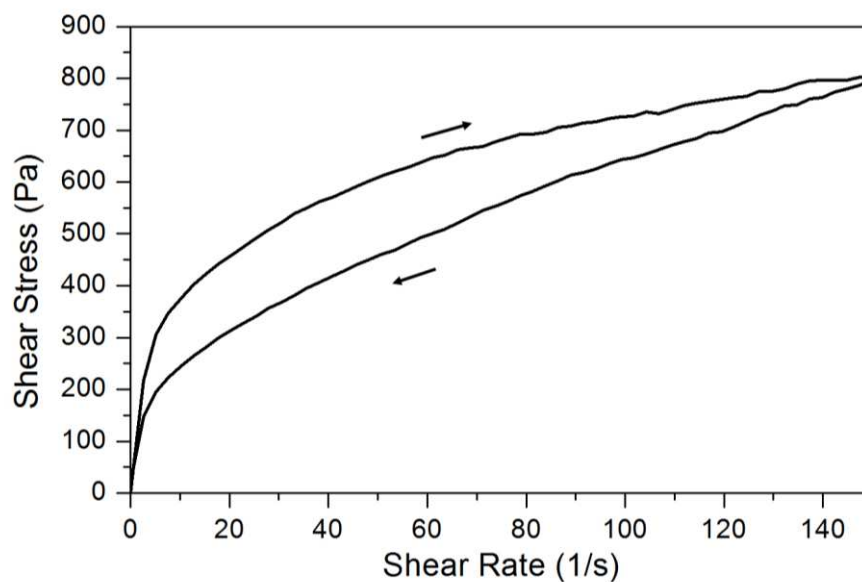
Fig. 12: Illustration of a paste with thixotropic behavior

So, a paste for screen printing commonly presents a thixotropic behavior to promote a good open mesh filling owing to the thinning and then a recovery of its viscosity when it is already on the substrate maintaining the pattern size. The paste should have a border value of shear when the paste starts to flow, as it can remain in rest when the paste is put on the screen waiting to the printing start[3].

Rheological variations of the paste during the printing process are then function of both, shear rate and time. Fig. 13 shows a representation of the paste behavior before, during and after the printing. The maximum shear rate value is found around 1000 s^{-1} when the paste is forced

to pass through the screen. This value can reach up to 6000 s^{-1} depending on process parameters and screen mesh[9].
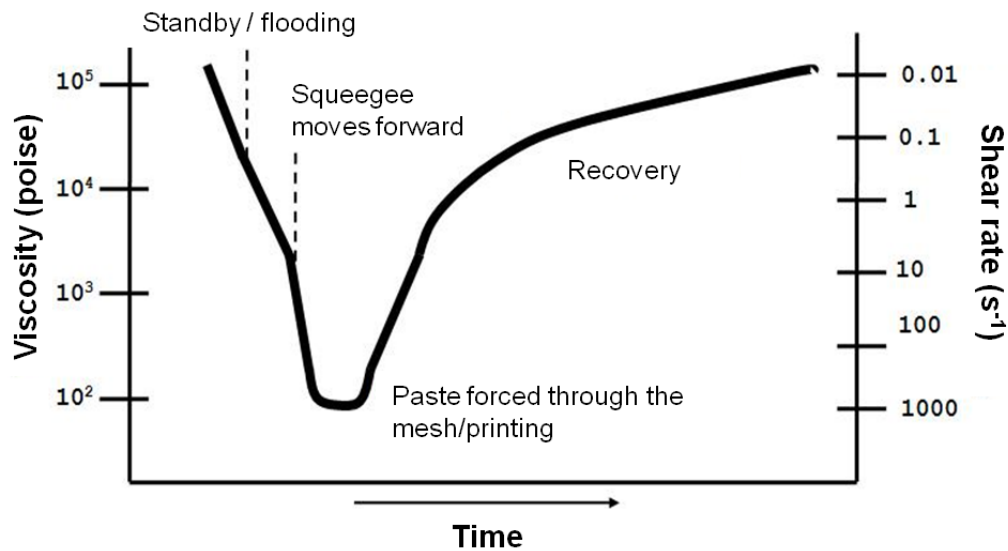
Fig. 13: Representation of the rheological performance of a paste during the screen printing process[9].

3.3.2- Components

All pastes for screen printing consist of two main components: the functional material that gives the electronic and mechanical properties of the deposit and a vehicle to adjust the proper rheology to the process. This vehicle is at least formed by the solvent and the binder. In addition, some pastes may contain different additives to improve a concrete physical property or rheological behavior.

The functional element is the active element conferring the electronic, magnetic, mechanical, piezoelectric, piezoresistive, or other property expected to the deposit. A metal will provide conductivity; a metal oxide will provide deposits of resistive or isolating type, etc. These components are usually added into the paste formulation in powders of few microns of diameter. Depending on the application it is important to choose a starting material with proper morphology and size so that the resulting deposit meets the requirements.

Instead, the binder aims to keep suspended the functional element and provide appropriate rheological characteristics to apply the paste by screen printing. The binder cannot evaporate during the drying to maintain the structure and plasticity of the deposit before the curing or

firing process. Binder burn out usually occurs at temperatures between 300 and 450 ^{o}C. A common example of binder is the ethyl cellulose. The solvent is just used to dissolve the binder providing fluidity and adjusting the final viscosity of a screen printing paste. The solvent evaporates quickly at temperatures around 100 ^{o}C. Some solvents that are used for these applications are terpineol or butyl Carbitol (monobutyl diethyl ether glycol).

Additionally, a paste formulation can include few additives with different functions such as thixotropy modifiers, plasticizers and dispersants. Furthermore, adhesion promoters can be used to improve the mechanical characteristic of the deposit and the interaction with the substrate. For the thick film technology is commonly used glass frits[10] due to their relative low melting temperature of about 500-600 ^{o}C. All these elements have to be soluble in the solvent chosen to formulate the pasta.

3.3.3- Paste fabrication

The paste fabrication aims to achieve homogeneity in the component mixture and reproducibility. Generally the process can be divided in two phases: dispersion and homogenization.

In the dispersion step, the functional powder, dispersant and solvent are mixed and occasionally, also the binder. The process must provide sufficient energy to break agglomerates and help the dispersant to wet the powder particles separating it from each other. This step is done, for instance, by a planetary ball mill (Fig. 14) where the powders are grinded and size reduced by means of impact and attrition with the balls.
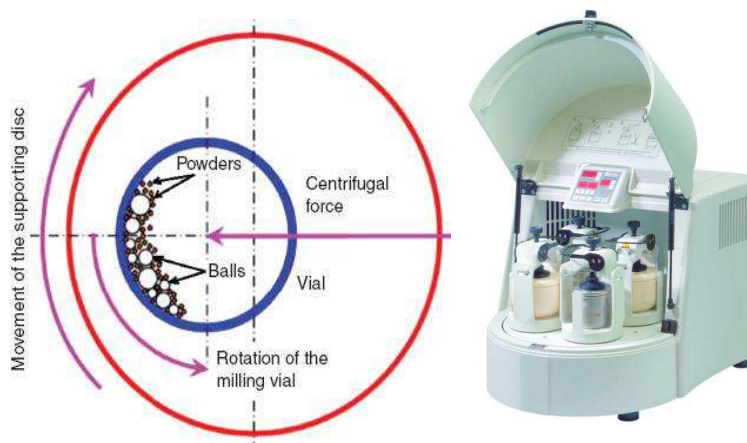
Fig. 14: Schematic diagram of a planetary ball mill

Then, the final homogeneity and refining of the paste is achieved by a three roll mill (Fig. 15) that uses shear force created by three horizontally positioned rolls rotating in opposite directions and different speeds relative to each other, in order to mix, refine, disperse, or homogenize viscous materials fed into it.
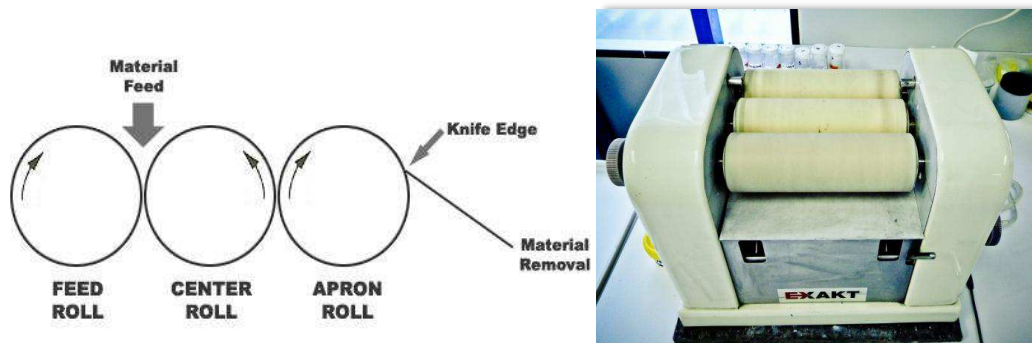
Fig. 15: Schematic diagram of a three roll miller.

3.4- Examples of formulation of functional materials

3.4.1- Formulation of an elastic silver paste

3.4.1.1- Motivation

Nowadays, due to the advance in technology and in electronic field where flexible, wearable and even skin-like patchable circuitries or sensors are needed, it is required certain characteristics such as stretchability or elasticity for the new conductor materials[11,12]. In particular and within the framework of the DINNAMIC project, circuitry onto flexible substrate must be printed. First prototypes using commercial silver paste were not functional at all since their conductive tracks on silver cracked, appearing discontinuities when the substrate suffered from stretching.

The aim of the formulation of an elastic silver paste is to overcome this drawback, giving to the silver conductive tracks elasticity to conserve its conductivity holding as much elongation as the substrate when it is deformed and stretched.

3.4.1.2- Formulation

The stretchability as the desired mechanical property can be accomplished by the use of an elastic matrix where silver can be added as conductor doping. Stretchable conductor has the current attention of flexible electronics and currently considerable effort is being made in the developing of new materials. Even if elastomeric matrix doped by carbon black is well-known, a very high resistance is achieved. Nowadays some of the most promising materials are single-wall carbon nanotubes (SWCNT)[13] or silver nanowires (AgNW)[14] in a PDMS matrix or hybrids using plasmonic welding[15].

Since just the binder and the solid remain in the printing when it dries, the mechanical properties will be giving by those two components. In this case, where the substrate is a flexible film of carbon nanofibers (CNF), the maximum temperature acceptable is around 120 °C since the matrix of its composition should not burn off to maintain the film mechanical properties. In the formulated paste, the matrix must be the polymeric matrix, which will promote the flexibility and stretchability. The vinyl acetate/ethylene copolymer (VAE) forms an elastic structure since they are internally flexibilized due to the comonomer ethylene[16] and the comonomer vinyl acetate is a rather stiff material due to its relatively high glass transition temperature (Tg), hence the resulting vinyl acetate-ethylene copolymer emulsions feature all the benefits of the homopolymer in strength and heat resistance and in addition it also offers better adhesion and coalescence properties[17]. Because of that, a commercial aqueous dispersion of VAE at 45 wt% called Mowilith® 1081 was used for this study.

The silver flake diameter is selected of few microns to increase compacting and leave less porosity. Small diameters will provide a better and easier passage through the mesh also, being possible to select a small thread diameter mesh. In this case, the flake powders were AC-6294 from Metalor® with a particle diameter smaller than 4 µm.

Being coherent with the chosen binder dispersion, the first solvent selected was water but after drying problems at early stage, the propylene glycol was fixed as the main solvent in the formulation due to the low vapor pressure (0.08 mmHg at 20 °C) that prevents the drying on the screen and during the storage.

Furthermore, a dispersing additive is necessary to produce stable formulations and ensure storage stability. These powders are completely insoluble in the solvent medium selected, so a proper dispersant additive must be found (Fig. 16 (a)). Different tests were done with Pluronic F127, Triton X100 and Multitrope 1214.

Zeta potential was the technique used to decide the proper dispersant for the system. The magnitude of the zeta potential gives an indication of the potential stability[4]; if all particles in suspension have a large negative or positive zeta potential, then they tend to repel each other and they will not tend to gather in aggregates. However, if the particles have low zeta potential values, there is no force to prevent the particles from coming together and flocculate. The dividing line between stable and unstable suspensions is considered to be in +30 mV or -30 mV. The higher the Z potential magnitude, the higher the repulsive potential between the particles and the higher the electrostatic stability.
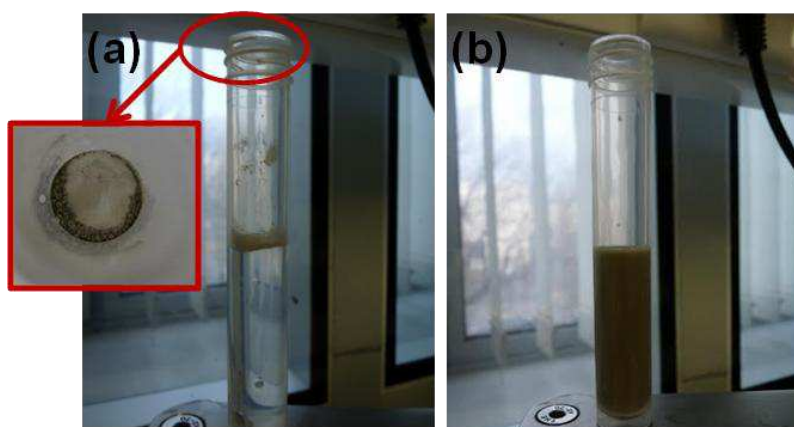
Fig. 16: (a) Silver flakes completely insoluble in water and (b) silver flakes soluble in water after the addition of a drop of multitrope 1214.

As it can be seen in Fig. 17, the silver particles show the highest absolute values of Z potential in water when Multitrope 1214 is added, higher than 50 mV whereas the pH is; what means that the particles become very stable.

Multitrope 1214 is a phosphate ether based anionic surfactant. This kind of surfactant, compared to other anionic surfactants, offer specific advantages including stability over a broad pH range and good solubility as it was experimentally proved (Fig. 17).
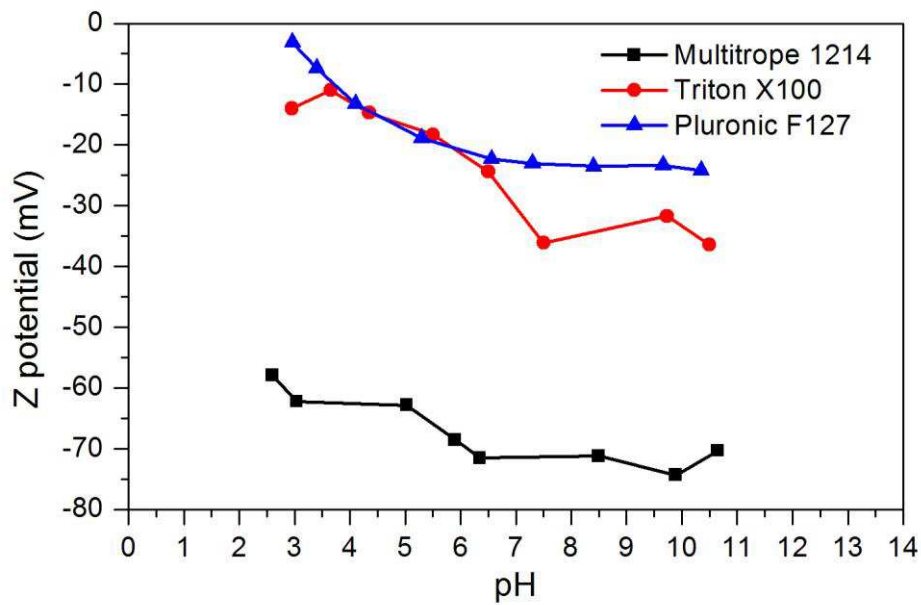
Fig. 17: Z potential vs. pH for AC-6294 silver powder with different dispersants.

As explained before, dispersants deflocculate powders and significantly reduce the viscosity of a dispersion or paste. Thus, to optimize the formula a dispersion curve can be plotted by simply measuring the viscosity as the dispersing agent is being added to the powders dispersion. Then, the minimum viscosity indicates the optimum dosage level (Fig. 18).
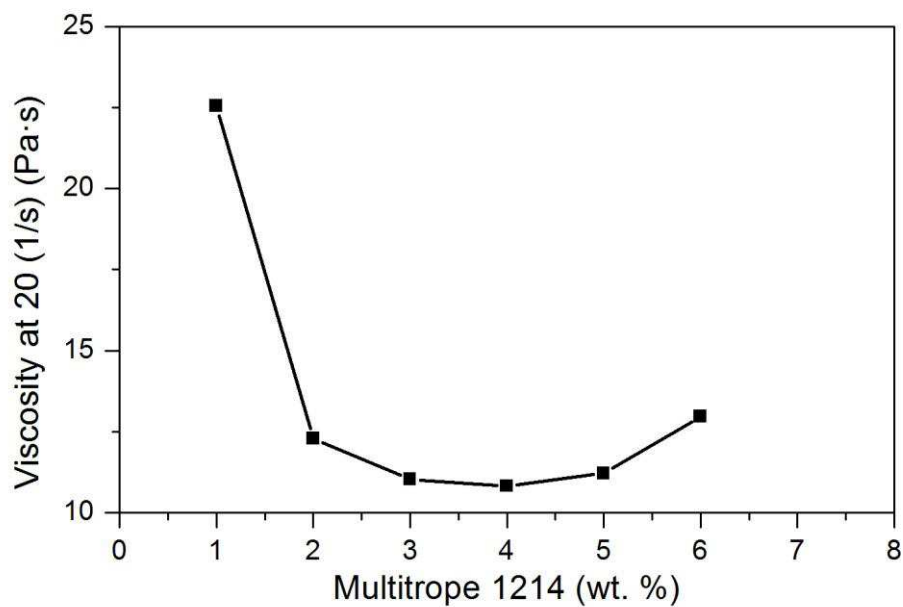
Fig. 18: Curve of the effect of the dispersant dosage into the viscosity of the dispersion at $20s^{-1}$ of shear rate.

The amount of dispersing agent required depends on the actual surface area of the powders to be dispersed. The smaller the particle size, the higher the actual surface area, hence the larger the area the dispersant has to cover. A small excess of dispersant is necessary in practice due to the new surface area creating by the mill in the dispersion step of the paste fabrication. In this case, even if the minimum viscosity is around 3.5 and 4% of dispersant, a 5% is selected for the final formula. This weight percentage is related to the solid content (the powder) and not related to the final weight of the paste.
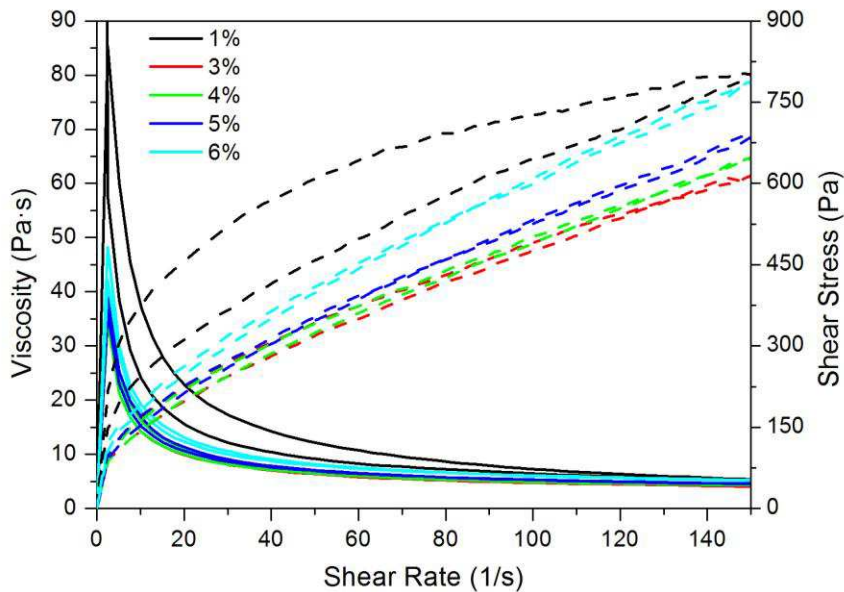
Fig. 19 proves how the performance disparities between pastes of 3-5% of dispersant do not make a different, however the lack of dispersant does.
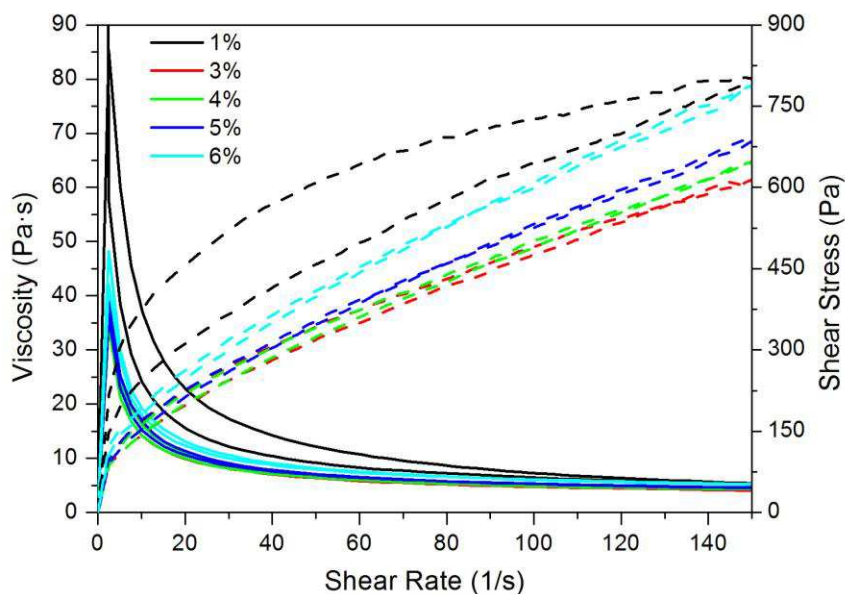
Fig. 19: (a) viscosity and (b) strain vs. the shear rate applied to the set of pastes with different dispersant dosage.

Once the optimum dispersant dosage is identified, the rest of the formulation has to be fixed. Three formulas were tested with different percentage of binder: 7, 10 and 13wt% of polymer related to the silver content. Remembering that the Mowilith dispersion has a 45% of polymer, the binder percentage is referred to the amount of just polymer added to the paste. The quantity of solvent was added until obtaining a proper aspect and good handling. Finally the amount of silver powder was fixed at [77.5-78] wt% taking into account just the solvent (propylene glycol plus water coming from the binder dispersion and the powder). The compositions of the three formulations are the ones specified in Table 1.

	wt % related to the powders and solvent			wt % related to the whole formulation		
Silver powders	**77.660**	**77.933**	**77.609**	**71.285**	**70.254**	**68.630**
Propylene Glycol (PG)	*16.279*	*13.483*	*11.162*	*14.943*	*12.154*	*9.871*
Water	*6.061*	*8.584*	*11.228*	*5.058*	*7.035*	*9.027*
Solvent (PG+water)	**22.340**	**22.067**	**22.391**	**20.001**	**19.189**	**18.897**
Dispersant	*5**	*5**	*5**	**3.656**	**3.522**	**3.446**
Binder	*7**	*10**	*13**	**5.058**	**7.035**	**9.027**

Table 1: composition of the three formulations studied to fix the binder percentage.

As it can be seen in Fig. 20 the higher the binder percentage, the higher the viscosity and the strain, being more noticeable the thixotropic behavior as well as the hysteresis loop get evident.
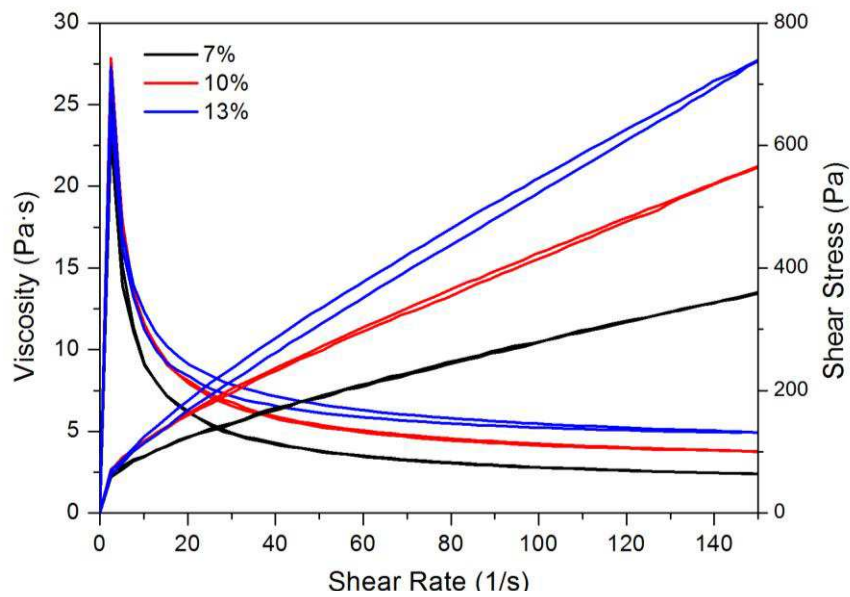
Fig. 20: Viscosity and strain vs. shear rate for pastes with 7, 10 and 13% of binder.

The binder in paste which will be dried at low temperatures, as it is the case, the binder is the responsible of the mechanical behavior of the deposit, since it is not burnt off. In the case of 7% the binder percentage is under the optimum, being clear the lack of flexibility when printed (Fig. 21).
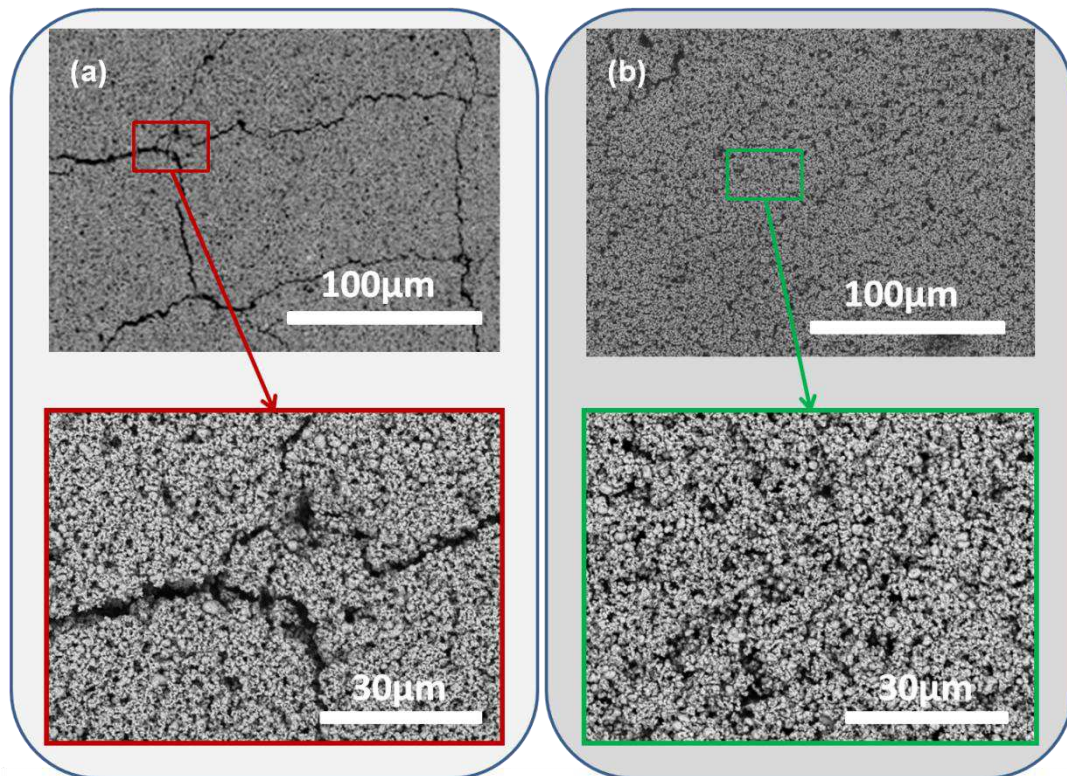
Fig. 21: SEM images after stretching (a) 7wt% and (b) 10wt% of binder.

In the case of 13% of binder, the printing process turns out properly, but it is during the screen cleaning and the storage where the problems appear. The binder polymerizes and sticks to the mesh being really hard to clean it properly as well as the higher amount of water in the solvent leads to a quicker drying. Furthermore, the paste plasticizes being not a paste anymore. So, the final formulation is fixed on the second one of the Table 1, where the binder content is intermediate.

3.4.1.3- Electrical and mechanical characterization

The elastic silver paste formulated in this chapter has been characterized and compared with three more commercial screen pastes for flexible substrates. These commercial ones are Electra ED3000, Gwent Group C2080415D2 Ag Counter Electrode and DuPont 5064 Silver Conductor.

According to the objective of this formulation, the four silver pastes were printed on flexible substrate, which cannot be dried at higher temperature than 120°C. For this reason the electrical characterization was made in samples dried 15 min at this temperature. The conductivity was measured by Van der Pauw method[18] with a four-point probe. Table 2 shows the results.

	$\rho(m\Omega\cdot cm)$
Elastic silver paste (E-Ag)	0.080195
Gwent	0.051749
Electra	0.086560
DuPont	0.041230
Ag bulk	0.001590

Table 2: Resistivity of the different silver pastes dried during 15 min at 120°C. Elastic silver paste (E-Ag) was de paste developed in this thesis. Gwent, Electra and Du Pont are commercially available flexible inks. For comparison Ag bulk data is given.

The conductivity of the silver paste formulated here is of the same order of magnitude than the commercial ones, being an order of magnitude higher than the silver bulk.

In Fig. 23 the difficulties found during the project is demonstrated. In (a) where the silver paste printed corresponds to Electra; with a slight and insignificant stretch, cracks appear in the surface creating discontinuities on the electrical conductivity. In (b) a printing with the silver paste formulated here, a significant stretch is applied to it and the silver track conforms the flexible and elastic substrate without breaking.

After the resolute problem qualitatively, a quantitative study is necessary to identify the achieved improvement in terms of elasticity. For that, a mechanical test system from Zwick Roell Z005 is used to carry out a tensile test where a strain force is applied to the printing while the electrical resistance is measured in-situ (Fig. 22).
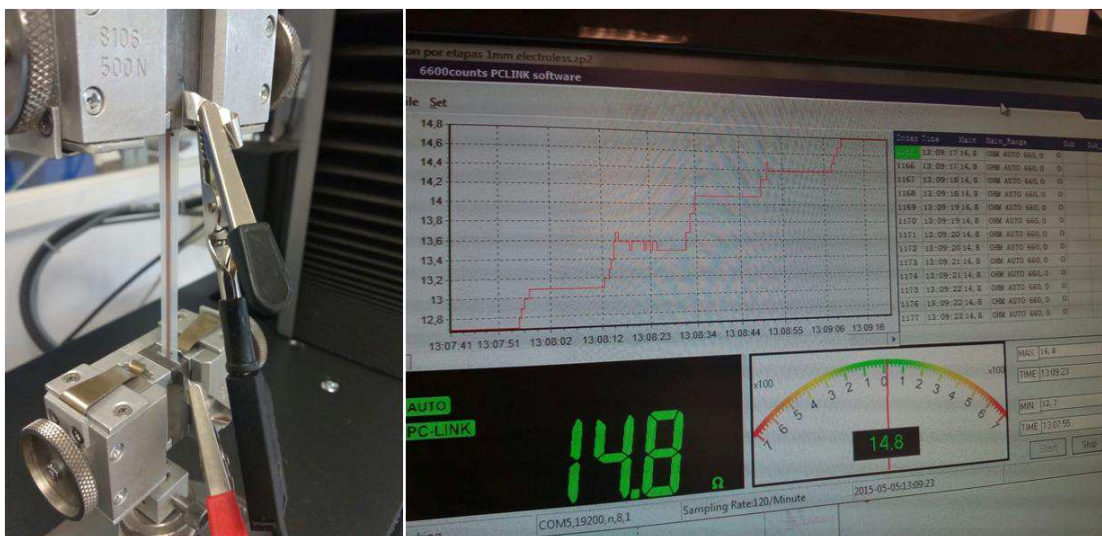
Fig. 22: The printed samples are stretched in steps of 0.5 mm using a mechanical test system while the electrical resistance is monitored during the whole test.

Lines of 30 mm long and 2 mm width are printed onto polyurethane substrate to be able to stretch the paste without the substrate breaking. The stretching is accomplished by steps of 0.5mm and then, the force is maintained during 20 s to give time for stabilizing and writing down the electrical resistance.
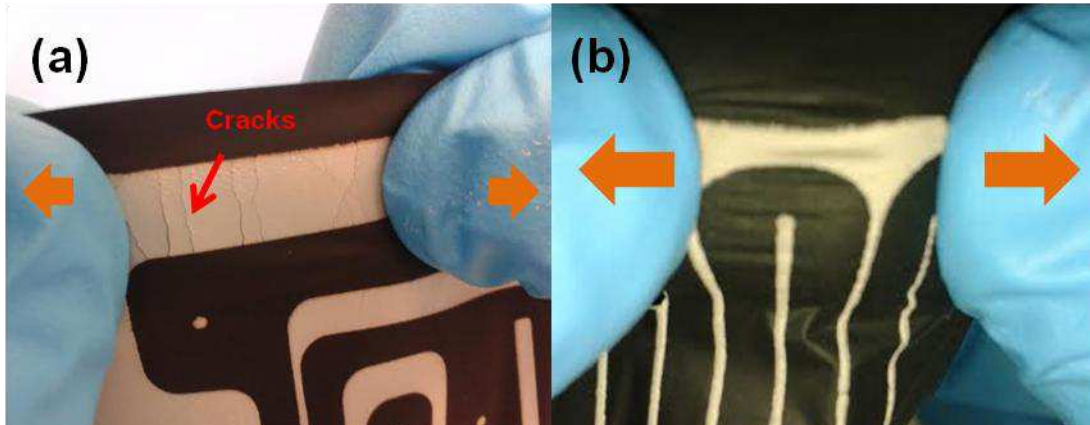
Fig. 23: Illustration of the cracks appearance when stretching the printing of (a) Electra Silver Paste and (b) the elastic silver paste formulated here.

A curve of the deformation or elongation is plotted versus the change in the resistance caused by the stretching (Fig. 24). The elongation is represented by ε and calculated as it follows:

$$\varepsilon = \frac{\Delta L}{L_0} = \frac{L-L_0}{L_0}$$

[2]

As it was shown in Fig. 23, Electra paste cracks and lose conductivity in a tiny stretch less than $\varepsilon = 0.04$ (Fig. 24). DuPont and Gwent pastes hold an elongation of 0.8 and 0.57 respectively, but increasing strongly the electrical resistance. Unlike the value of the elongation where the complete discontinuity appeared, Gwent shows a better behavior than Dupont in terms of conductivity loose while the stretching. In the case of the formulation detailed here, the elastic silver paste exhibits a much better performance. The maximum stretch that is able to hold is just the same as DuPont paste ($\varepsilon = 0.8$) while the loose of conductivity is extremely enhanced. While Dupont increases its electrical resistance more than 40 times in an elongation of 0.4, the elastic silver formulated increases less than 5 times. A stretching of 0.7 makes DuPont's jump to 80 times higher; the elastic one's still increases less than 15 times.
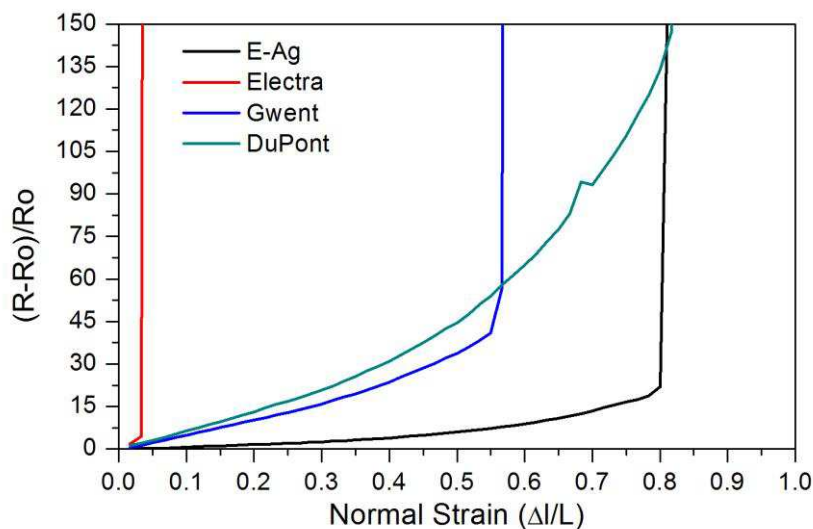
Fig. 24: Increase in electrical resistance during the stretching caused by the tensile test.

3.4.1.4- Doping with silver nanowires (AgNW)

As mentioned before, the AgNW are attracting a lot of attention due to the NW network help maintaining contact while stretching[14,15] due to its geometry and then, promote the enhancement of conductivity.

A dispersion of silver nanowires in ethanol from Grupo Antolin was used to dope the paste. The concentration is 15 mg/ml. In this case, the fact of having them in dispersion modifies the steps of the formulation process. The particles and the nanowires must be mixed and dispersed one in another. The silver powder is added in less than 4% referred to the Ag powders into a volume of 25 ml. For that, a first step where the silver powder is poured into the silver nanowires dispersion with the help of the Multitrope 1214 dispersant must be done. Then, the mixture is introduced in a pearl mill for an hour. The slurry is dried in an oven to evaporate the ethanol and later on, the temperature is increased until 350 °C to burn the dispersant.

After that, the process follows the steps explained in 3.3.3; the solid obtained in the pre-step, and the rest of the paste components are dispersed in a planetary mill and then, the paste is refined by a three roll miller.

SEM shows the nanowire-doping in Fig. 25.
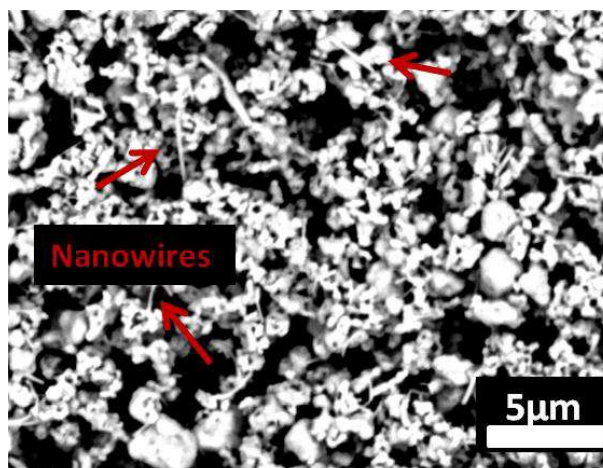
Fig. 25: SEM image of the Silver Nanowires-doped elastic paste.

The electrical characterization was carried out in the same way as the rest of the pastes, being dried at 120 °C and measuring the resistivity by the four-point probe. The results, summarized in Table 3, show a slightly reduction in electrical resistivity. Nevertheless, the main improvement is not found in the electrical resistance but in the reduction of the conductivity loss while the stretching.

	$\rho(m\Omega\cdot cm)$
Elastic silver paste	0.080195
Silver NW-doped paste	0.064807

Table 3: Comparison of the resistivity of the non-doped and the silver nanowires-dope paste dried during 15 min at 120°C.

Fig. 26 proves how the nanowires doping enhances the performance even more. The conductivity loss is practically the same as the non-doped elastic silver until an elongation of 0.4. After this, the performance is improved by maintaining the same loss rate as in the first part of the curve. The conductivity is hardly reduced and even the polyurethane substrate is broken before the electrical discontinuity.
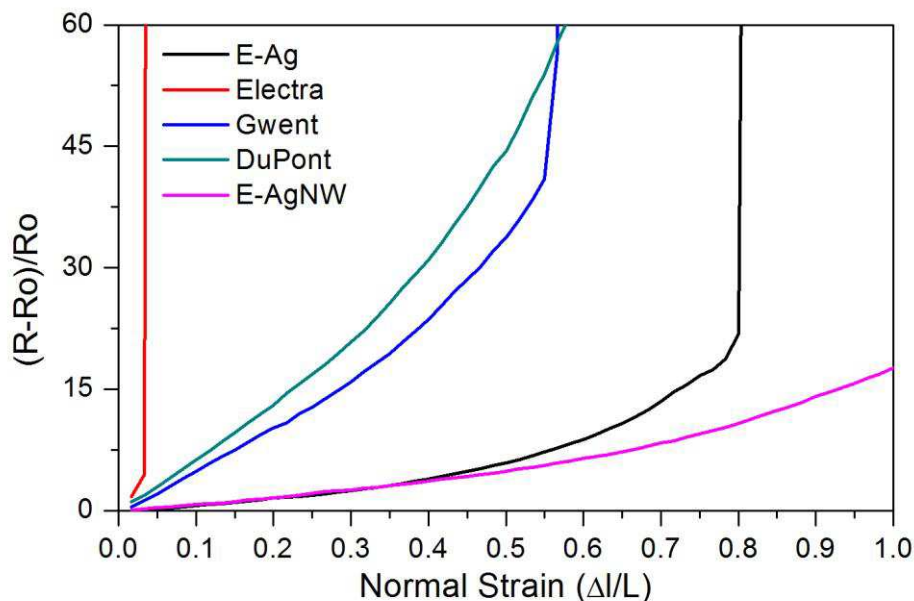
Fig. 26: Increase in electrical resistance during the stretching caused by the tensile test. The green line corresponds to the silver nanowires-doped paste where the loose of conductivity is reduced thanks to the increase in physical contact promoted by the nanowires geometry.

If an elongation of 0.7 for the silver elastic paste promotes an increase in resistivity of about 14 times, for the nanowires-doped one the increase is less than 10 times; and less than 20 times for an elongation of 1, what means when the substrate is stretched until double its size.

3.4.2- Formulation of carbon nanofibers paste

3.4.2.1- Motivation

Within the framework of the DINNAMIC project also, different devices for the automotive industry has to be designed and fabricated. Some of the designs proposed during the project do not required of large areas of carbon nanofibers –the flexible substrate for 3.4.1. For this reason, a screen paste of this material could be a good solution to save material, time and money due to the possibility of printing just those areas needed. Hence, the aim of this formulation is the substitution of that substrate.

3.4.2.2- Formulation

Due to the need of replacing a substrate which its main feature is the flexibility, and since the elastic composition selected in 3.4.1 was successful in these terms, the component selection for this paste happens to be just the same as before; the vinyl acetate/ethylene copolymer (VAE) as the elasticity promoter and the water and propylene glycol as the co-solvent system.

The proper dispersant could be changed so, a study of the Z potential of the powders dispersion with different dispersant additives are done. Multitrope 1214 and PC75 were checked firstly. The anionic dispersant Multitrope shows stable values all along the pH range for particles, both the carbon nanofiber and the silver nanowires that will be used later to improve the conductivity.

As the multitrope came out to be an appropriate one, as the Fig. 27 shows, it is the selected dispersant.
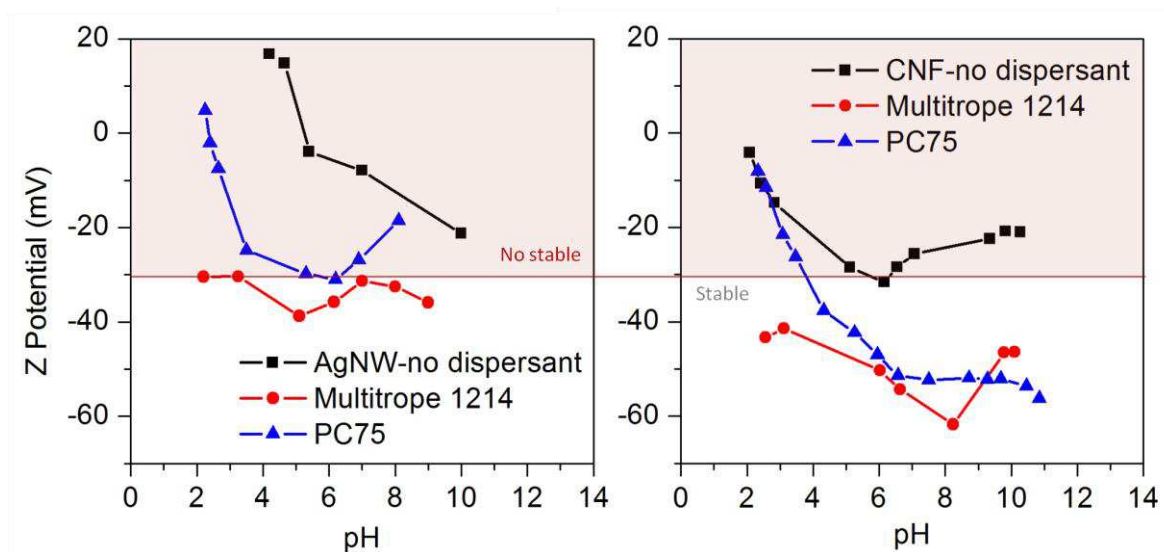
Fig. 27: Z potential of the carbon nanofibers (CNF) and silver nanowires (AgNW).

The reduction in viscosity is plotted as the dispersing agent is added to the CNF slurry. The minimum viscosity indicates the optimum dosage level, in this case, around 9% by weight of CNF (Fig. 28). The required amount of dispersant depends on the effective surface area of the solid, and since CNF has a high effective area of 150-200 m^2/g, it is expected to require that huge amount of dispersant.
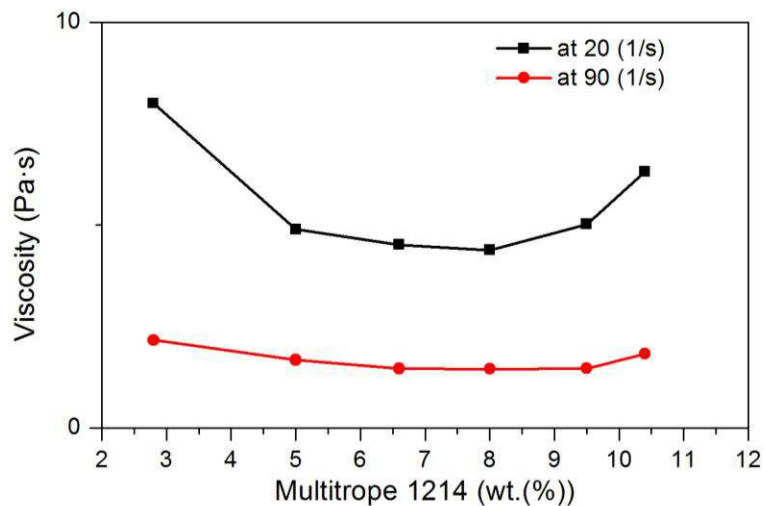
Fig. 28: Curve of the dispersant dosage effect into the viscosity at 20 s^{-1} and at 90 s^{-1} of shear rate.

Due to the high effective surface area of the CNF, the maximum solid content possible it is around the 25% in weight to obtain proper viscosity for printing. For higher amount of CNF the solvent (and the vehicle) is not able to wet properly the powder.

The binder percentage has to be selected depending on the mechanical and electrical properties. The four studied formulas are the ones specified in Table 4. As there is not commercial paste of CNF to compared and evaluate the stretching, the comparison has been done between different percentages of binder for the equivalent composition.

	wt % related to the powders and solvent			
CNF	25	25	25	25
Propylene Glycol (PG)	73	70	67	45
Water	2	5	8	30
Solvent (PG+water)	75	75	75	75
Dispersant	9.5*	9.5*	9.5*	9.5*
Binder	7*	15*	22*	100*
Binder:CNF	0.05:1	0.15:1	0.22:1	1:1

Table 4: Composition of the four studied formulations.

3.4.2.3- Electrical and mechanical characterization

A tensile test has been used to measure the increase in electrical resistance when the screen-printed paste is stretched. The increase in binder concentration reduces the loss in electrical conductivity when the paste is subjected to the test. In case of 22% w/w binder/CNF the conductivity decreases 10 times when it is stretched around 10% (Fig. 29 (a)).
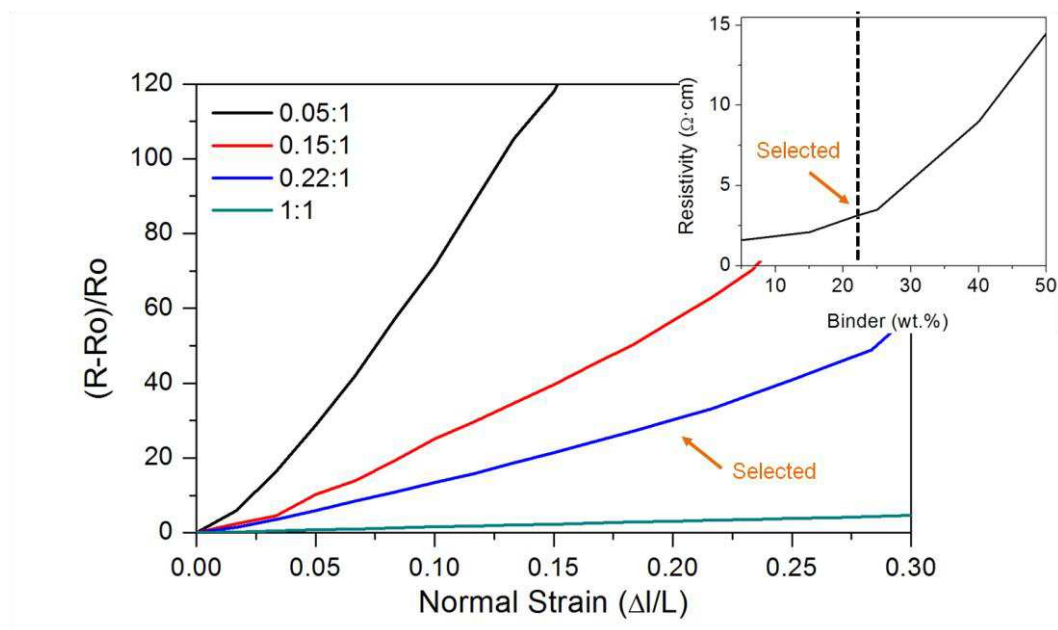
Fig. 29: (a) Increase in electrical resistance (loss of conductivity) during stretching caused by the tensile test. (b) Printing resistivity of the different formulation plotted vs. the binder percentage.

A high binder concentration improves the elastic behavior but it increases the paste electrical resistivity (Fig. 29 (b)).

3.4.2.4- Doping with silver nanowires (AgNW)

In this work we overcame the increase of resistivity related with high binder concentration by the addition of silver nanowires (Fig. 30).
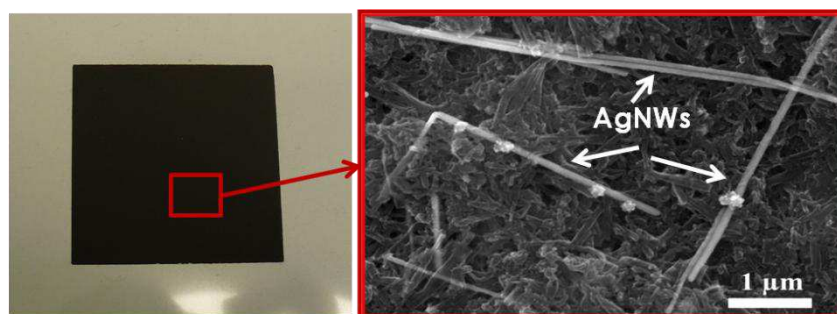
Fig. 30: SEM images of the CNF printing doped with AgNW

The addition of low amounts of AgNWs to the CNF paste reduces the electrical resistivity up to 50%, being not so noticeable this reduction in higher AgNW concentrations (Fig. 31). The resistivity saturated as the contact between the different AgNW is compromised as well with the binder concentration and it cannot be increased to a higher value.
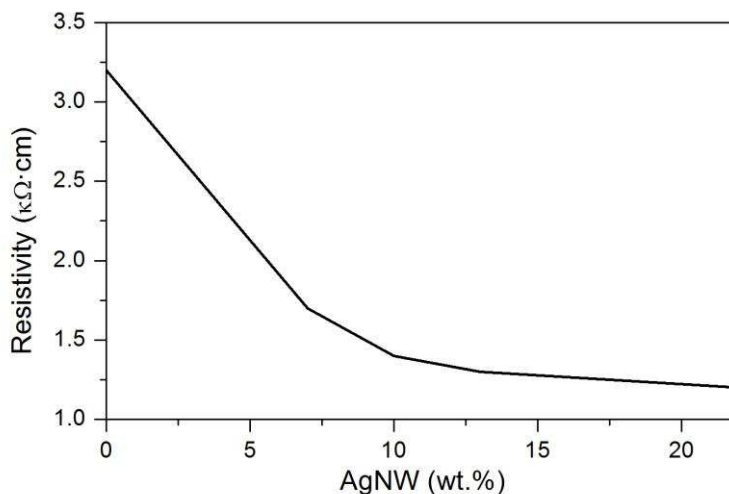
Fig. 31: Effect of the AgNW doping in the electrical resistivity of the different formulations printing.

The final conductivity obtained after the silver doping is equivalent to the CNF slurry dried without binder (and without doping) as it can be observed in Fig. 29 (b). Thus, the compromise established between the elasticity and the electrical conductivity can be solved.

References

[1] D. E. Riemer (1989), *The theoretical fundamentals of the screen printing process*, Microelectronics International 6 (1), 8.

[2] C. López-Gándara (2012), *Comprehensive study of YSZ-based electrochemical gas sensors for automotive applications,* PhD. Dissertation, Barcelona, Spain.

[3] J. M. Fernández (2013), *Noves estructures LTCC i HTCC per a sensors de pressió capacitius i per a sensors lambda de tipus resistiu,* PhD. Dissertation, Barcelona, Spain.

[4] F. Ramos (2014), *Integración de la tecnología cerámica multicapa*, PhD. Dissertation, Barcelona, Spain.

[5] A. Hobby (1990), *Fundamentals of screens for electronics screen printing*, Circuit World 16 (4), 16.

[6] A. Hobby (1997), *Screen printing for the industrial user,* DEK Printing Machines Ltd.

[7] Bopp and Co, http://www.boppmesh.co.uk/ (consulted on December 2015)

[8] K. Gilleo (1989), *Rheology and Surface Chemistry for Screen Printing*, Screen Printing 128.

[9] M. Neidert, W. Zhang, D. Zhang, A. Kipka (2008), *Screen-printing simulation study on solar cell front side Ag paste*, Photovoltaic Specialist Conference, PVSC'08 33rd IEEE.

[10] M. Carano, J. Fjelstad (2004), *Electronic materials and processes handbook*, *McGraw-Hill HANDBOOKS*

[11] C. Yu, C. Masarapu, J. Rong, B. Wei, H. Jiang (2009) *Stretchable supercapacitors based on buckled single-walled carbon-nanotube macrofilms,* Advanced Materials 21, 47, 4793.

[12] J. A. Rogers, T. Someya, Y. Huang (2010), *Materials and mechanics for stretchable electronics*, Science 327, 5973, 1603.

[13] T. Sekitaki, Y. Noguchi, K. Hata, T. Fukushima, T. Aida, T. Someya (2008), *A Rubberlike Stretchable Active Matrix Using Elastic Conductors*, Science 321, 5895, 1468.

[14] F. Xu, Y. Zhu (2012), *Highly conductive an stretchable silver nanowire conductors,* Advanced Materials 24 (37), 5117.

[15] J. Y. Woo, K. K. Kim, J. Lee, J. T. Kim, C.-S. Han (2014), *Highly conductive and stretchable Ag nanowire/carbon nanotube hybrid conductors,* Nanotechnology 25, 285203.

[16] R. Farwaha, C. Lazaroft (2012), *Recent advancements in vinyl acetate ethylene copolymers (VAE) for use in paperboard and paper coating,* PaperCon Conference, 197.

[17] L. Bittle, S. K. Singh (2012), *Meeting tomorrow's demands today: VAE-based Emulsions for the Indian paints and Coatings Market*, Wacker Chemie AG brouchure. Paintindia 63.

[18] L. J. Van der Pauw (1958), *A Method of Measuring Specific Resistivity and Hall Effect of Discs of Arbitrary Shape*. Philips Research Reports 12 (1), 1.

Chapter 4

Development of flexible printed platforms for sensor applications

4.1 Introduction

Global market demands for high quality and low-cost electronic devices. Printing techniques onto flexible polymeric substrates not only can lower the production costs but also offer the possibility to fabricate lightweight and wearable devices, unlike traditional electronic fabrication techniques such as monolithic silicon electronics[1,2,3,4].

Printed techniques have a high potential due to the possibility to work under room temperature and atmosphere pressure allowing a low-cost production[5]. Screen-printing (SP) is one of the main conventional and mature printing techniques that has demonstrated to be a useful technique in high-volume devices production; the case of inkjet-printing (IP) opens the possibility of printing very thin conductive paths, minimizing both, device size and material expenses[6], as well as the time and cost saving due to the ease in accomplishing design modifications where the mask is not needed. As it was said previously in this thesis, IP is still under development and shows a huge challenge in terms of performance and reproducibility compared to matured techniques such as SP, and also in the current assortment of functional materials available on the market[7].

Polyethylene terephthalate (PET) and polyethylene naphthalene (PEN) are both highly widespread as substrates in the current flexible electronic industry[8,9,10,11,12] Nevertheless PET and PEN have low thermal resistance and become unstable at temperature beyond 80°C and 130 °C respectively[13,14], losing their mechanical properties. Above these temperatures some others polymers, such as polyimide (PI), are required for the post-treatment of the functional material[11,15]. PI can endure a widest temperature range. Its glass transition temperature is 360°C [16] what enhances its potential application in different technological fields.

Regarding printed materials; silver is the most widely used conductive material in flexible electronics. Its excellent electrical conductivity and the possibility to be sintered at low temperatures (lower than 300 °C) make it a good prospect for flexible devices[6]. Even so, silver corrodes easily in industrial environments containing sulfide[17] or in outdoor applications due to the humidity[18] and chloride[19] even far from saltwater sources where there are inland chloride species, such as $ClNO_2$[20]. Therefore the reliability of the devices is highly compromised.

In this chapter, a comparison between silver-based on polyimide low-cost flexible sensor platforms fabricated by means of SP and IP techniques has been developed. The performance of the sensor platforms was checked by long-term characterization and aging tests to identify the causes of the device failure. Design improvements to overcome the drawbacks of silver corrosion and power consumption have been achieved, obtaining sturdy, wearable and reliable gas sensor platforms.

Inkjet platforms have been fabricated in the University of Barcelona, while screen-printed ones has been developed in the facilities of Francisco Albero S.A.U. (FAE), as well as the later characterization of all the devices.

4.2- Design and fabrication of the silver-based flexible gas sensor platforms

4.2.1- Design of the flexible platforms

There are different sensing strategies. From a point of view of accuracy, spectrographic systems coupled with some separation method like chromatography are reliable, however they lack of portability. Some optical systems, also accurate, are portable but power consumption and complexity becomes a great challenge. In the counterpart, solid-state sensors (electrochemical, resistive…) are based on reaction on sensing material. These are usually less accurate and therefore reliable, but are transportable, integrable and, in some cases, can be developed with printing techniques in a flexible approach. A comparison of these features is shown in Table 1.

The aim of this chapter is the fabrication of versatile, low-cost, flexible and reliable sensor platforms; because of that, the resistive sensors are good candidates. These sensors are simple and reliable but they lack of selectivity. Currently this technology has the attention due to few advantages over the rest of sensing methods, and the current improvements of the selectivity[21].

Characteristic	Electrochemical	Optical	Resistive
Cost	Low	High	Low
Lifetime	Short	Long	Medium
Sensitivity	Medium	Medium	High
Selectivity	Good	Excellent	Poor
Response time	Medium	Fast	Fast
Size	Medium	Large	Small

Table 1: Comparison of three gas-sensing technologies. This table has been adapted from ref. 21.

It is usual to improve gas detection using temperature modulation of the gas-sensing layer. Gas adsorption and desorption depend on temperature and the competition between the two processes defines the temperature of the maximum sensitivity[22]. When the operating temperature is moved away from this maximum, the selectivity drops. This dependence on the temperature is different for different gases, so changes in this selectivity when cooling or heating the sensing layer gives concrete profile information what allows the recognition of the gas, and hence, the selectivity[23,24]. Moreover, the adsorption and desorption processes are accelerated when the gas sensing layer operates at temperature, typically about 150 $^\circ$C for carbon allotropes as sensing material. This is the main reason to include a heater into the gas sensor platform. Such conditions of temperature limit the substrate material and furthermore increase energy consumption.

The use of multiple sensors in an array is widespread. The reason is that the combination of different signals coming from different sensors allows the discrimination and the selection of a

concrete gas and also the obtaining of redundancy information that gives more reliability to the signal in case some damage occurs in one individual sensor. In fact the extension of this idea to multiple sensor approaches to the concept of the electronic nose. In case of MOx sensors, a four-sensors array is highly widespread[25,26].

The sensor platform designed here consists thereby of a sensing part and a heater. The sensing part is composed by a four-interdigitated array of sensor electrodes and eight connection pads (Fig. 1). The connection pads were designed in such a way that fit in a clamp-like connector, as it can be seen in Fig. 2 (a). While sensing part was printed in the topside of the PI film, the heater was printed on the bottom side, being located just in the area where the printed electrodes are, allowing heating up the sensing part.

This design (Fig. 1) has been already proved to be suitable for gas sensors[25]. The line width of the interdigitated electrodes and the line strip of the heater were 150 μm and 200 μm respectively.
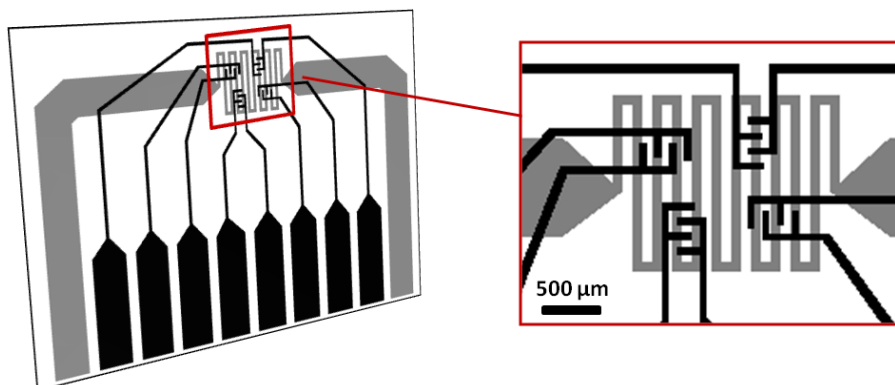
Fig. 1: Scheme of the sensing and heating parts of the printed platforms.

4.2.2- Materials and fabrication of the flexible platforms

For the SP-devices a paste based on silver flakes (C2080415D2 from Gwent Group) was used as the conductive material to print the sensing and the heating parts of the gas sensor platform (Fig. 2.a). Apical® PI from Kanegafuchi (distributed by Sertek) was used as the substrate and the SP process has carried out with a DEK Horizon 03i. After printing, the silver paste was cured at 170°C during 15 min in a muffle furnace. A 325 mesh with capillary film of 18 μm screen was selected for the printing.
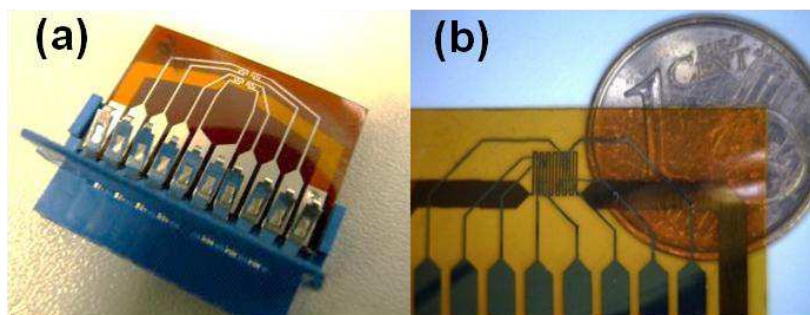
Fig. 2: (a) SP-printed and (b) IP-printed devices.

The IP-devices were printed with a Xenjet 4000 from Xennia Technology Ltd. The cartridge was a Xaar 126/50, based on piezoresistive technology to eject the ink. U5603 silver ink with 20 wt% of silver nanoparticles was provided by Sun Chemical. In this case, Kapton® PI from DuPont was used as the substrate. The IP-patterns were sintered at 225 °C for 20 min on a box oven.

In lately design improvements of the device explained in section 4.4, ISOAD 7104, an adhesive polyimide film provided by Isovolta, and PPI-SP-793-6, a thermoactivable adhesive PI from Sertek, were used as a heater protection (4.4.2) and a chemical bath of ammonium chloride solution (Planar Ultra Gold from MacDermid) and gold cyanide (AuCN) provided by Metalor as a chemical passivator of the conductive parts of the platform (4.4.3).

4.3- Characterization of the sensor platforms

The devices were calibrated and tested applying voltage pulses and monitoring their temperature. Life tests in continuous operation were carried out by applying a constant voltage to achieve an initial sensor temperature value of 120 °C. The selection of this temperature is owing to previous works done in our group that showed these platforms, implemented with carbon nanofibers as sensing material, better respond at 120 °C for NH_3 and NO_2 gas sensing[25]. Also, aging tests were done to measure their resistance at adverse atmosphere conditions.

The chemical composition of the printed silver-based paste or ink was determined by energy dispersive X-ray spectroscopy (EDXS). The surface morphology of the deposited silver was checked by field emission scanning electron microscopy (FE-SEM). Both, EDXS and FE-SEM analysis were carried out on a FE-SEM JEDL J-7100 microscope.

4.3.1- Calibration and power consumption

Once the devices were fabricated by means of SP and IP, heaters were calibrated. Pulses of voltage were applied to the heater and the temperature was monitored by a thermographic camera (NEC Thermoshot F30), as it is seen in Fig. 3. The voltage was increased until the electrodes area reached >150 ^{o}C.
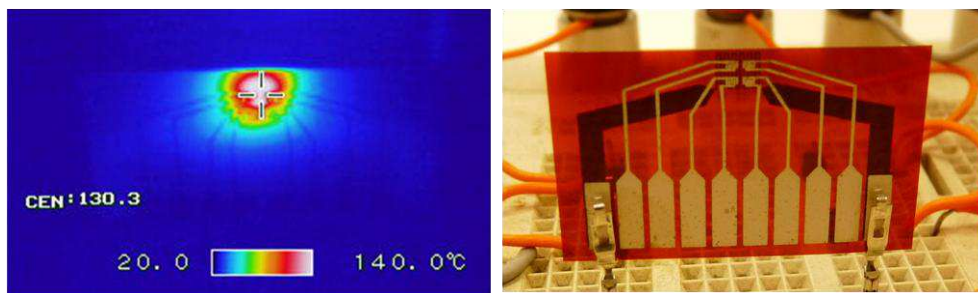
Fig. 3: Picture obtained by the thermographic camera used for the power calibration of the sensor platforms.

The measured temperature is plotted as a function of heater power consumption (Fig. 4). The sensor temperature linearly increases with power consumption of the heater, reaching around 120 ^{o}C for 200 mW. This consumption depends on the heated area and materials what are quite similar in both designs. Thus, both platforms showed similar performances as it is seen in Fig. 4.
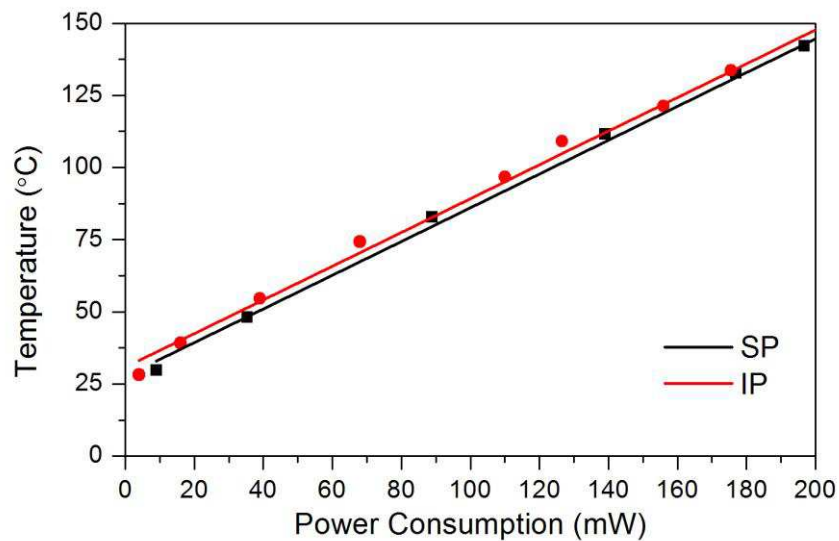
Fig. 4: Calibration plot of SP- and IP-devices. A linear dependence of the temperature of the sensing part is evidenced as a function of heater power consumption.

4.3.2- Life test and aging test

To check the endurance of the heaters, a long-term test at continuous operation was done. It is known that silver oxidizes quicker as the temperature increases[27], so the heaters were connected to a voltage source to increase the sensor part temperature up to 120 °C. Furthermore, corrosion resistance of the deposits was analyzed by salt-spray chamber and by a climate chamber.

Meanwhile the voltage was kept constant; the printed devices were maintained in continuous operation until their failure for the first long-term test. The heater electrical resistance was measured along time (Fig. 5, left). After just few hours of operation SP-heaters evidenced a change on the surface color, from silvery to brown (Fig. 5 (c)); this fact clearly indicates the presence of surface corrosion. A total device failure occurred after 300 h where the electrical resistance of the heater increases excessively. Even at earlier stages of the test, the electrical resistance increases quite significantly, so higher power consumption is needed for the same temperature, being detrimental for the heater performance and leading to a malfunction of the devices before the totally failure.
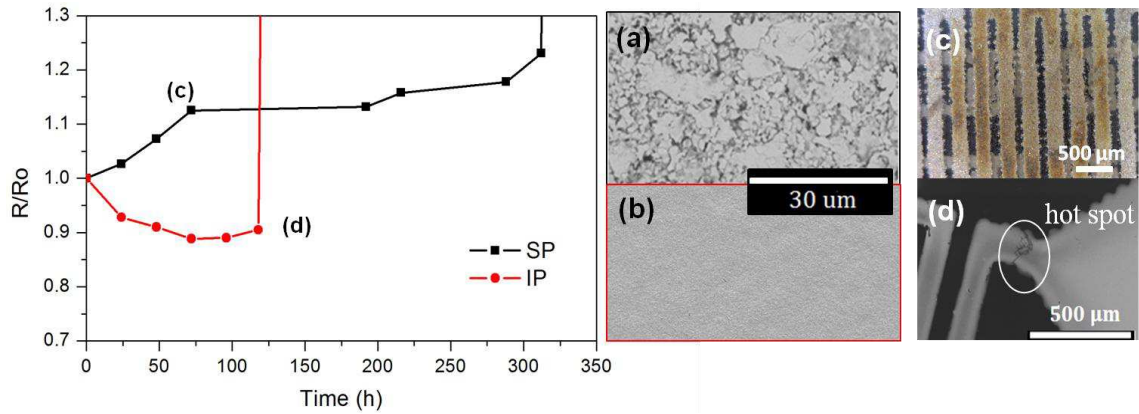
Fig. 5: On the left, electrical resistance variation at room temperature during the continuous operation for SP and IP devices. On the right, images of morphological structure of the Ag-SP (a) and Ag-IP (b) after curing taken by FE-SEM and (c) color change due to the degradation of Ag-SP after some hours of continuous operation and (d) discontinuity in the Ag-IP heater meander due to hot spot, causing the device failure after 125 h of continuous operation.

It is important to underline the fact that all the area that is heated up is degraded quickly; not only the heaters, but the sensing electrodes too. The EDXS analysis showed that only Ag and C elements were present in the as-deposited tracks (Table 2). After the SP-device failure, new elements as S, Cl and O were found, what indicates a change of the track composition due to a surface corrosion. Furthermore, different studies[28,29,30] show that the porosity and roughness of metal coating surfaces accelerates the corrosion process. The FE-SEM images of SP-printings showed a non-homogenous, porous and full of porous surface, induced by the flake-like structure (Fig. 5 (a)), which makes easier the penetration of the reactive species, like S, Cl and O, into the deposit structure, causing then the premature failure.

Element	SP devices (wt. %)		IP devices (wt. %)	
	Before test	After test	Before test	After test
Ag	92	79	98	95
C	8	8	2	3
S	0	6	0	0
Cl	0	3	0	0
O	0	4	0	2

Table 2: EDX results for the composition of the printed deposits before and after the long-term test at continuous operation after t>100 h, point in which the IP platforms failure.

Regarding IP-devices, the total failure occurred in 140 h (Fig. 5, left) earlier than SP-devices, but no surface corrosion evidences were found. EDXS analysis showed no significant variation on the deposit composition of IP-devices after the failure (Table 2). FE-SEM images (Fig. 5 (b)) showed a homogeneous surface without the presence of holes or defects. A completely smooth surface is reached by means of the sintering process of the silver nanoparticles. IP-devices showed then an almost inexistent porosity that minimizes the silver exposed to the atmosphere, slowing down the penetration of reactive elements and so the corrosion. Thereby, corrosion seems not to be the cause of these IP-devices failure.

A detailed examination revealed the presence of some discontinuities on the silver tracks after the life tests. These discontinuities appeared at vulnerable and weak parts of the design (see Fig. 5 (d) and Fig. 6) or at printing defects (bubbles, impurities...). Unlike the SP-devices, where the single layer track thickness was around 20 μm, the single printed layer of the IP-tracks was 300 nm thick, what might promote the formation and the fast evolution of cracks and hot spots in a short period of time.
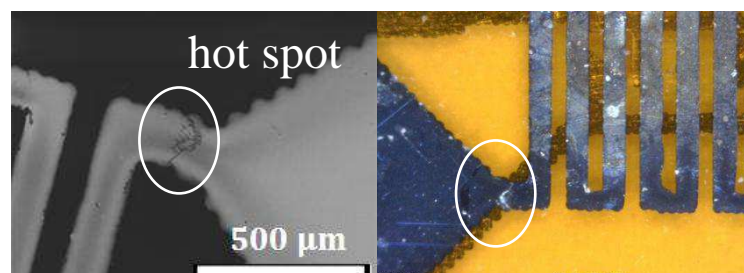
Fig. 6: Hot spot occurred in Inkjet printed-heater during the continuous life-time operation.

In the case of the aging tests, the adverse atmosphere conditions were simulated in a salt-spray chamber and in a climate chamber. The salt-spray test was performed with a 50 g/L of NaCl concentration during 72 h while climate chamber tests were performed with 95% humidity using two-hours on/off cycles keeping a temperature constant at 100 °C during 72 h.

The aging tests showed more obvious the penetration of the reactive species into the silver deposit structure. The SP-heater resistance was increased around 7.6% and 10% after the climate and the salt-spray chambers exposure respectively. However for IP-devices the increase of the resistance was quite low; 1.3% and 2.7% for climate and spay-salt chambers respectively lower than SP-devices.

These results will be compared in the next sections with the improvements of the corrosion protections carried out during the thesis.

4.4- Design improvements

4.4.1- Reduction of power consumption

At this point it seems that IP-technique can be pointed as the best route to fabricate such flexible sensing platforms. For this reason, IP heater design was optimized to achieve lower power consumption. As said previously, the very first devices showed a power consumption of almost 200 mW at a temperature of 120 ^{o}C (Fig. 4). For new design, the heated area was reduced by narrowing the strips as it is shown in Fig. 4.a. Before the selection of this design, the reduction of the heated area and the narrowing of the strips were studied separately. It is known that the dissipated energy that has to be generated by the heater to warm up the zone to a concrete temperature is a function of the amount of material that is heated, what means, a function of the heated area; the larger the area, the higher the consumption. This fact is in completely agreement with the result in our case: the power consumption was reduced to 110 mW at 120 ^{o}C for inkjet-printed heaters (Fig. 7) which implies a reduction of a 25% on power consumption which value corresponds also, to the heating area reduction (26%). The narrowing of the strips gives place to a larger length for the heater meander and that is positive to obtain a better reproducibility in the performance of the heater. Slight changes in thickness (small changes in drop volume due to variation in the jetting voltage, for example) or defects are softened due to a better distribution of the heat dissipation.
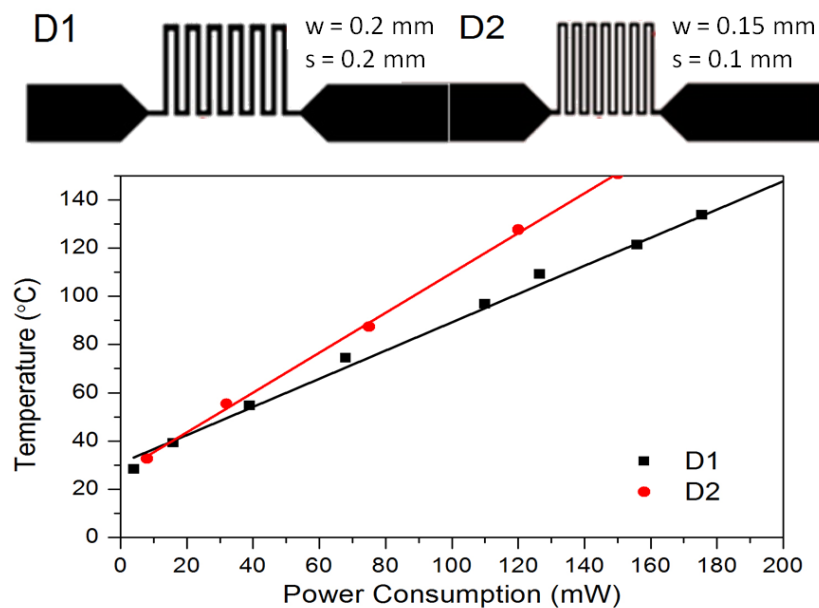
Fig. 7: Sensor temperature as a function of the heater power consumption of the previous design (D1) and the new one (D2).

Silicon technology can be energetically a little more efficient using advanced micromechanization, around few tens of mW for 200 ℃[31,32], but the fabrication process is extremely expensive and time consuming. An alternative can be the ceramic technology because it is cheaper, but in this case the power consumption increases excessively on the order of hundred times more[33,34], as well than on glass-based devices[35]. Therefore, the methodology here proposed can be considered like a good alternative to both technologies, reaching a low-consumption and low-cost sensor platform.

4.4.2- Heater protection by atmosphere isolation

With the aim to improve the life-time of the designed platforms and to prevent the premature failure of both, SP- and IP-devices, an atmospheric isolation of the silver heaters by a suitable adhesive PI tape was carried out. A first adhesive PI layer (PPI-SP-793-6) was tested but the result was the opposite of the expected. These adhesive flew significantly into the porosity when high temperature is applied, hindering the conductivity and increasing even quicker the electrical resistance during the continuous life test (Fig. 8).
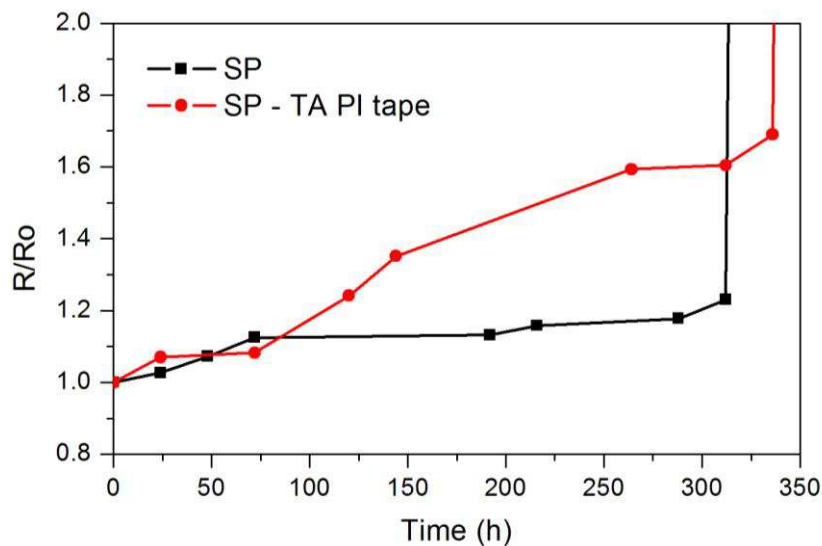
Fig. 8: Performances of SP heaters during the continuous life test when (a) no protection is applied and (b) the TA PI buried it for protection.

An adhesive with higher TAK strength and better resistance to higher temperature were checked. In this case, an ISOAD 7104 PI layer provided by Isovolta was selected. It has to be noticed that after the device protection, devices were laminated to remove all the air that could be trapped between the two layers. By means of the proper selection of the adhesive PI

layer, the heater protection was achieved. Continuous life test showed an increase of the lifetime of protected SP- and IP-devices more than ten times compared with the un-protected ones (green dotted line in Fig. 9 (a) and blue dotted line in Fig. 9 (b) respectively).
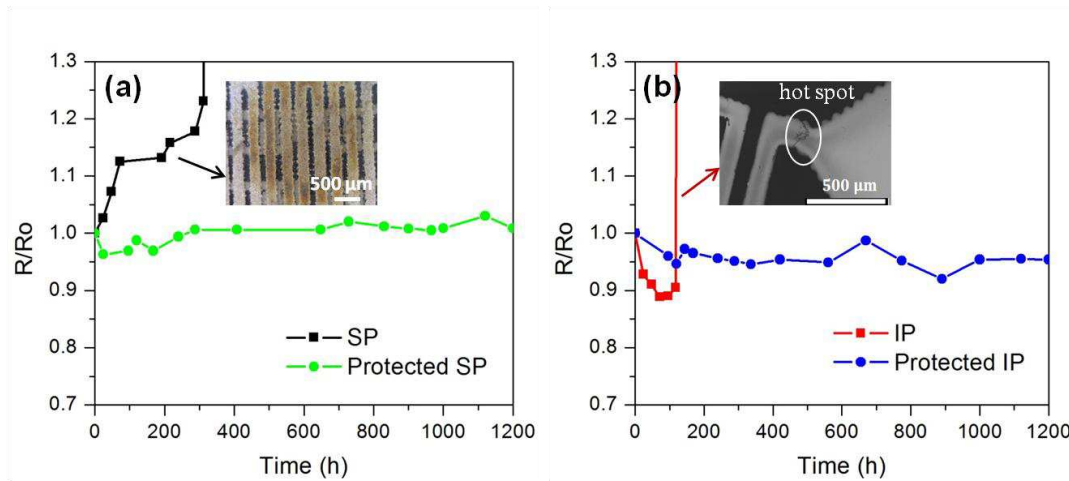
Fig. 9: Heater performances of (a) SP and (b) IP devices at continuous operation. Unprotected devices and ISOAD PI layer protected ones are compared.

No degradation after 1000 h of continuous operation at 120 $^{\circ}$C and no consequential deterioration on the device performance were observed. However, the SP-electrodes of the sensing part, which could not be protected from the atmosphere, corroded in few hours due to the porous presence, as it was previously mentioned. Instead, the IP-devices showed no corrosion on the electrodes after 1000 h of continuous operation. Furthermore, it has been demonstrated that heater protection not only improves SP- but also the IP-devices.

Aging tests on the protected devices revealed smaller increase of electrical resistance than on unprotected-devices. An increase around 0.6% and 2% was observed in the case of SP-devices for climatic and salt-spray chambers respectively. No significant variation in electrical resistance of IP-devices was measured. Then, long-term reliability was achieved by means of the heater protection for both SP- and IP-devices, just the unprotected electrodes made the difference.

	Salt-spray chamber test ΔR/Ro (%)	Climate chamber test ΔR/Ro (%)
SP	10.0	7.6
Protected SP	2.0	0.6
IP	2.7	1.3
Protected IP	0.1	0.1

Table 3: Variation of the electrical resistance for the different devices after the aging test

In addition, the on/off test was adjusted taking into account that the expected working mode of the heater of these sensors will be intermittent. Heaters were subjected to 40000 on/off cycles. The cycle duration is 120 s where during 40 s the heater is on at operating temperature and 80 s off. The starting temperature was 120 °C, and later on, the temperature was increased every 10000 cycles until 175 °C where the test was finished with 40000 on/off cycles with the highest variation in the electrical resistance of 1.5% for SP and just 1% for IP-devices (Fig. 10). This result proves the reliability of the protected heaters in intermittent operation mode fabricated by both techniques.
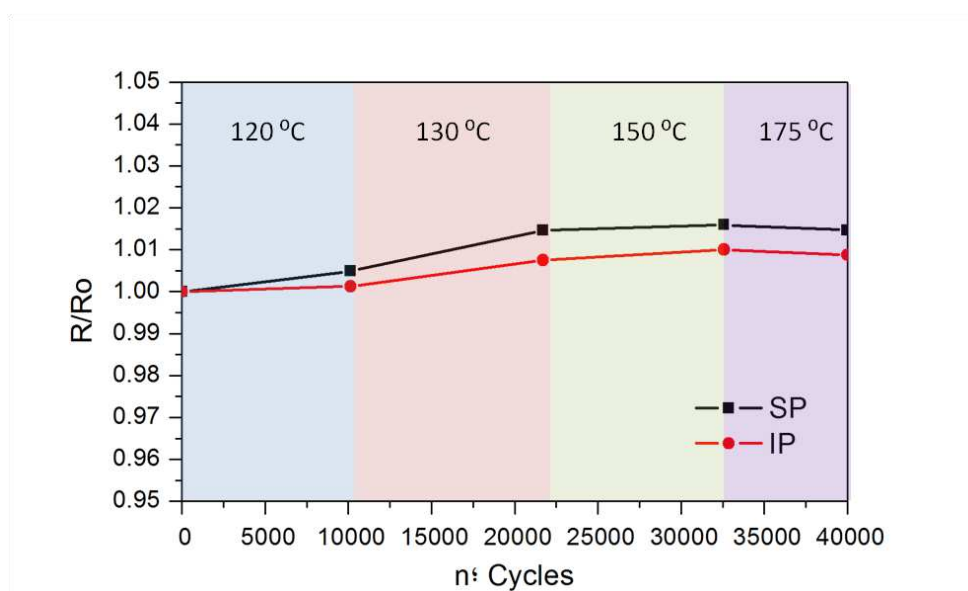
Fig. 10: Variation in the electrical resistance of the heater for SP and IP devices during an on/off cycles test. The temperature was increased every 10000 cycles.

It is worth to mention that this novel flexible-platform was implemented with deposited carbon-based materials as the gas sensing material, by means of electrospray technique. The success of this system has been proved in Ref. 21 by measuring different gases such as NH_3 or NO_2.

4.4.3- Electrodes protection for SP devices

As it was introduced above, the protection with an adhesive layer only prevents the degradation of the silver buried, what means that the interdigitated electrodes remains unprotected. Since the electrodes remain exposed to the atmosphere and to the corrosive species, a different solution has to be set out, and especially in the case of SP, where the degradation is quite evident and really quick (Fig. 11),
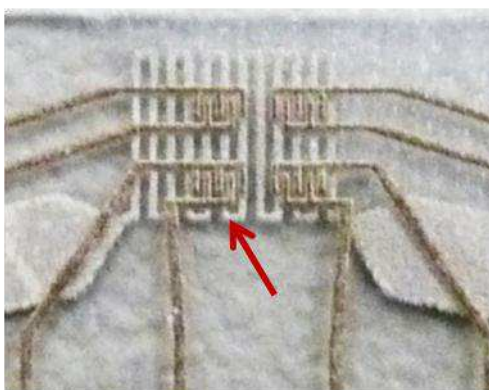
Fig. 11: Silver electrodes degraded after operation. In this case, the image is taken on a PET substrate due to its transparency that allows to see the starting color of the silver tracks in the bottom side of the PET. It can be clearly seen the effect of the degradation in the color change of the interdigitated which turned to be brown, in contrast to the silvery or white that can be observed in the heater (which is printed in the other side of the PET).

The replacement of silver by a more noble metal seems to be a necessary modification. Gold is the most noble of metals; it is the only metal that does not react with oxygen or sulfur at any temperature[36].

4.4.3.1- Silver paste substitution by a gold paste

The replacement of the screen printing paste by BQ331, a gold paste from DuPont, for the electrodes was carried out. Both aging test were done to prove the no degradation of the interdigitated electrodes and there were no difference at all. EDX shows the same composition before and after the gold printing was subjected to the climatic and salty spray chambers.
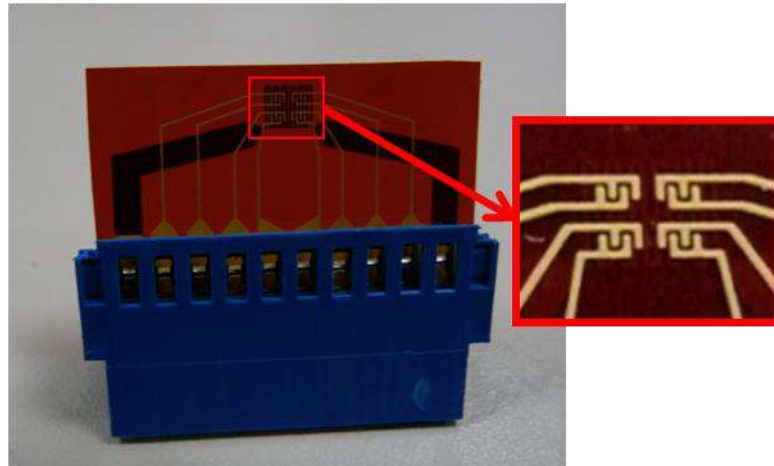
Fig. 12: SP devices with gold electrodes

The drawback of gold paste as the solution falls in the final cost of the device; since while the silver paste has a cost of 0.90 €/g, the price of the gold paste shoots up 70.65 €/g. Hence, the objective of fabricating a low-cost device starts to totter. Furthermore, the gold paste dries really quickly in the screen, being impossible to print few tapes consecutively and increasing the material waste.

A design change was considered, trying to reduce the amount of gold necessary for the circuitry in contact with the atmosphere. This new design concept is represented at Fig. 13.
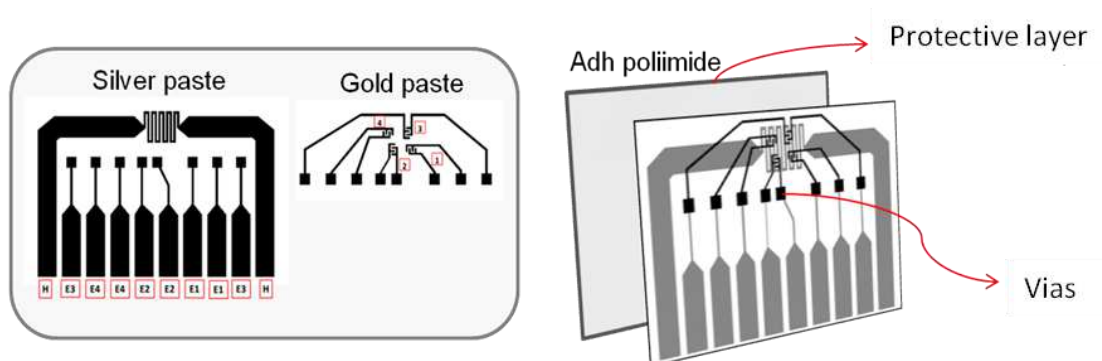
Fig. 13: Design of the gold surface reduction. In this design the heater and the pads connection (of heater and electrodes) are printed in silver and buried and protected with the polyimide layer selected in 4.4.2. Interdigitated electrodes are printed in gold and they are connected with their pads by silvery vias.

The electrodes connection pads are buried with the heater and connected with the superficial gold electrodes by vias. This design allows printing all the pads in silver and reducing costs.

4.4.3.2- Heater and electrodes protection by gold plating

Gold plating is a method of depositing a thin layer of gold onto the surface of another metal, most often copper or silver, by chemical or electrochemical plating. It is usually used in electronic industry to prevent corrosion or to offer weldable solutions.

There are different types of gold plating[37] and because of gold price, it has always been important to deposit it only in those areas and at such thickness as the application actually required. In this case, just few microns are needed for the silver protection, so a flash bath is enough.

The gold plating will be carried out by galvanic replacement. A galvanic replacement reaction is a type of oxidation-reduction (redox) chemical reaction when an element or ion moves out another element taking its place - that is, one element is replaced by another. In a redox reaction, the electrochemical potential differences between two species in the system promote spontaneity conditions, thus the species with higher electrochemical potential can be reduced by promoting oxidation of the element with more negative potential.

Gold has a high reduction potential and therefore, when the gold is properly complexed in a solution, it has a marked tendency to reduce itself in the presence of another metal of lower reduction potential. Fig. 14 shows the substitution of the very superficial layer of silver atoms by gold.
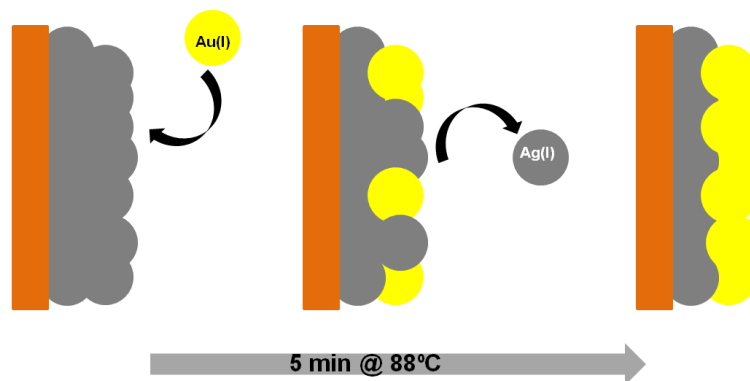
Fig. 14: Illustration of the silver galvanic replacement by gold.

The electrochemical reaction between silver and gold is the following:

$$Au(I) + Ag \rightarrow Au + Ag(I) \qquad [1]$$
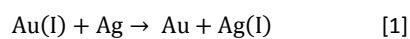
Since galvanic replacement into the chemical bath is a purely surface process, as there is no longer Ag in contact with the Au dissolution bath the process stops. The layer does not grow

over time at all what means a material save control. Nevertheless this very thin gold layer is enough to protect the silver from the atmosphere.

The surface protection by means of gold plating would show important advantages regarding the screen paste substitution. The more important one would be the possibility of removing the adhesive PI layer what brings to material saving and ridding process of few steps such as stacking and laminating and decreasing the technological risk in the case of the vias-design proposed for the gold area reduction in 4.4.3.1.

The process designed for a correct deposition of gold needs of an acidic cleaning of the silver surface. This cleaning treatment consists in dipping the sample into an acidic solution at 5% of HNO_3 during 5 min at room temperature. This treatment prevents the surface from oxides and sulfides, leading the metallic silver exposed to the atmosphere again.

After the cleaning, the samples are immersed in a solution containing Au(I). Traditionally, gold has been plated from cyanide complex solutions, $[Au(CN)_2]^-$, because of the exceptionally stability[38].

In this case the bath is formulated with a commercial ammonium chloride solution (Planar Ultra Gold from MacDermid) and AuCN as gold salt at 1 g/l of Au(I)% provided by Metalor. The conditions of the chemical bath are 88 ^{o}C and a pH (25 ^{o}C) of 4.7. After few minutes (t<5 min) a light yellow hue is observed on the silver surface. Even if it is hard to notice the color change by naked eyes, silver replacement by gold was checked by SEM (Fig. 15) and EDS (Fig. 16) images and EDX spectra (Fig. 17).

SEM images show the change in the morphology after the gold replacement (Fig. 15).
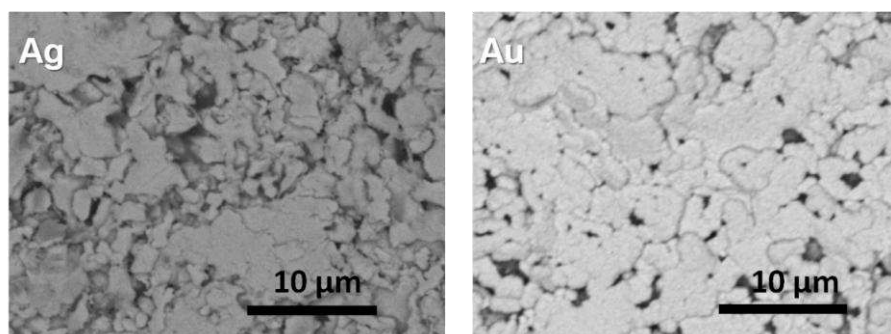
Fig. 15: SEM images of the silver paste and the silver protected by a gold layer after the galvanic replacement on the gold bath plating.
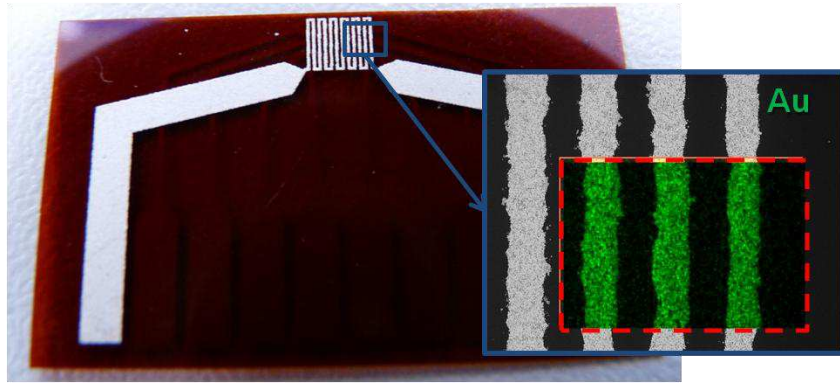
Fig. 16: EDS scanning of gold-protected silver.
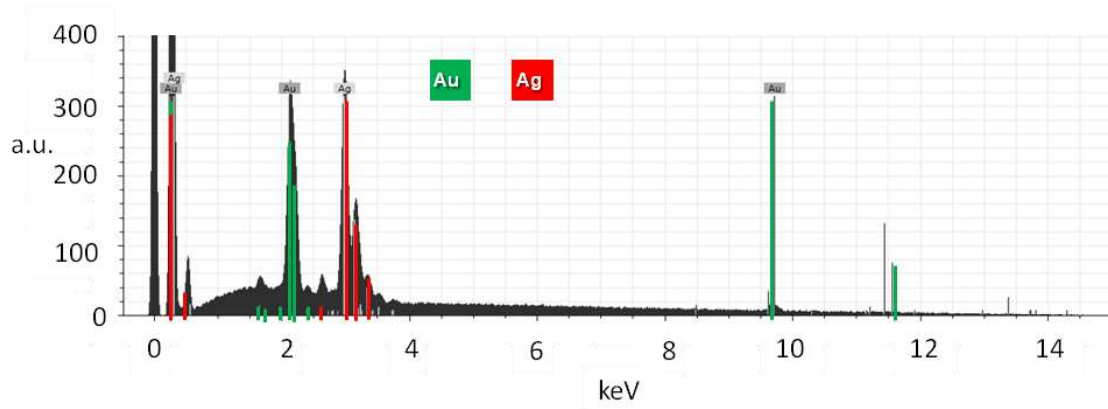
Fig. 17: EDX spectra where the presence of gold is corroborated at a 50%

Silver sensor platforms were fabricated following the starting design. The gold protection was carried out with the chemical bath explained above and then, the platforms were exposed to the same test validation than the previous devices.

The life tests were passed as it is shown at Fig. 18 where it can be observed that the electrical resistance does not vary more than a 5% after 1000 h of continuous operation.
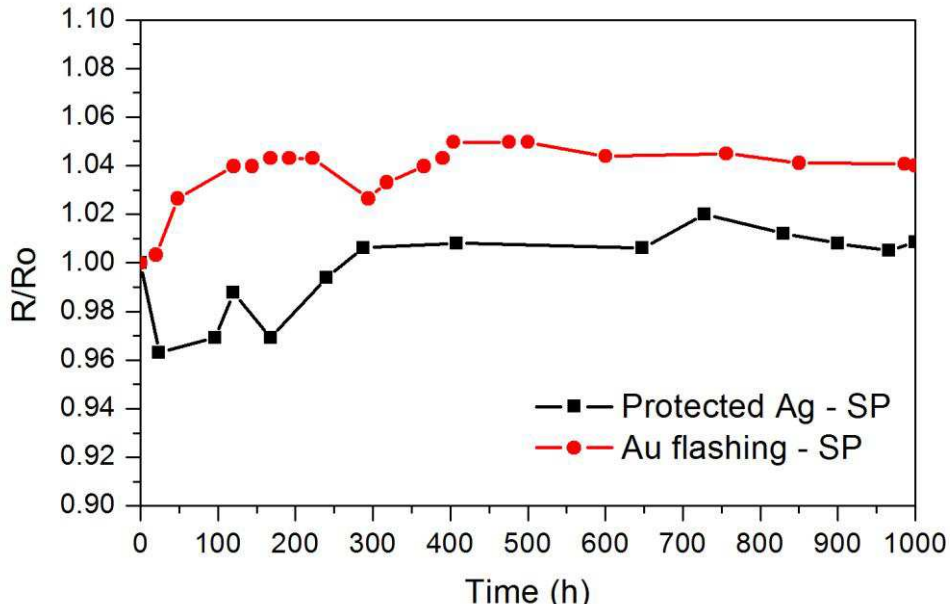
Fig. 18: Heater performance of (a) adhesive PI layer protection and (b) gold plating protection.

The same situation is found for the aging tests of salty and climatic chamber (Table 4).

	Salt-spray chamber test $\Delta R/Ro$ (%)	Climate chamber test $\Delta R/Ro$ (%)
SP	10.0	7.6
PI protected SP	2.0	0.6
Au plating protection	0.6	0.6

Table 4: Electrical resistance variation after (a) salt-spray and (b) climatic chamber of unprotected SP-heaters, adhesive PI layer protection and gold plating protection.

These results ratify the protection expected by the gold layer without the need of an adhesive polyimide film to bury the silvery heater.

Cost breakdown

Using a gold protected layer for both, heater and electrodes, can look like an expensive solution. Because of that, an estimation of the material and manufacturing costs has been done for the different devices.

For this comparison, four different reliable designs have been taken into account. These four structures are represented in Fig. 19.
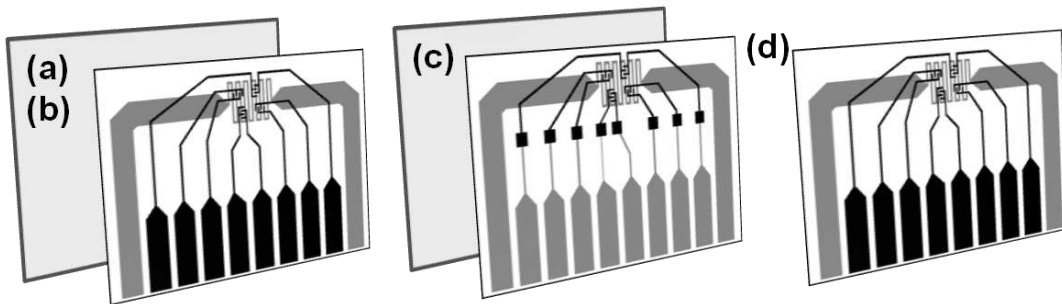
Fig. 19: Different structures used for the sensor platforms fabrication. (a) silver inkjet ink for the whole conductive circuitry of the sensor plus the protected polyimide layer for the heater, (b) silver screen-printed heater plus the protected polyimide layer and gold printed electrodes with the same design of (a), (c) silver heater and pads buried by the protective PI layer and interdigitated in gold and (d) whole structure of silver screen-printed and protected by gold plating.

For the structure breakdown a batch of 35 substrates of 60 sensors each has been estimated (Table 5).

PARAMETERS RELATED TO THE LOT SIZE		
Substrate size	60	sensors/substrate
Substrate per lot	35	Substrate/lot
Lot size	2100	Sensors/lot
COMMON COST FOR ALL THE PROCESSES		
Energy consumption	0.1517	€/kWh
Operator cost	20.00	€/h

Table 5: Parameters related to the lot size and common cost used for all the process steps.

The steps sequence of the process is the following one: blanking, punching, via filling, (inkjet- or screen-) printing, stacking, lamination and gold plating. Some of these steps are not needed depending on the structure (Table 6).

The cost of the manufacturing has been divided in fungibles (cleaning needs), tools (cutting blades or vacuum bags), worker (€/h) and equipment (€/h). Costs by steps and structure are summarized in Table 6.

PROCESS STEP	€/sensor			
	(a)	(b)	(c)	(d)
Blanking	0.0002	0.0002	0.0002	0.0002
Punching	-	-	0.0131	-
Via filling	-	-	0.0109	-
Printing	0.0165	0.0168	0.0168	0.0168
Stacking	0.0141	0.0141	0.0141	-
Lamination	0.0355	0.0355	0.0355	-
Gold Plating	-	-	-	0.0023
Total	**0.07**	**0.07**	**0.09**	**0.02**

Table 6: Manufacturing costs by structure and process steps. (a) Design of Ag-IP and protective PI layer (b) Ag-SP heater plus the protective PI layer and Au-SP electrodes, (c) Ag-SP heater and pads buried by the protective PI layer and interdigitated in Au-SP and (d) whole structure of Ag-SP and protected by gold plating.

As materials, are considered the inks or pastes, the substrate and the protection (adhesive PI layer or gold plating bath). The costs related to the materials are summarized in Table 7. Screen pastes and inkjet ink cost are calculated taking into account the estimated printed material (g) needed to cover the device area and the material waste (on the screen or inside the inkjet circuitry) for a batch described in Table 5 and divided by the number of total sensors. For the substrate and the adhesive layer protection is the cost for the substrate area divided by number of sensors in it (it also considers the trimmings waste); and in the case of gold plating bath, a maximum of 7 substrates is fixed for 600 ml of gold bath.

Material	€/sensor			
	(a)	(b)	(c)	(d)
Ag	0.0246	0.0152	0.0377	0.0411
Au paste	-	2.0346	0.2692	-
PI	0.0095	0.0095	0.0095	0.0095
Adhesive PI	0.0242	0.0242	0.0242	-
Gold solvent	-	-	-	0.0121
Gold Cyanide	-	-	-	0.1394
Total	**0.06**	**2.08**	**0.34**	**0.20**

Table 7: Material costs by structure. (a) Design of Ag-IP and protective PI layer (b) Ag-SP heater plus the protective PI layer and Au-SP electrodes, (c) Ag-SP heater and pads buried by the protective PI layer and interdigitated in Au-SP and (d) whole structure of Ag-SP and protected by gold plating.

Then, the summary of the final cost of the platform depending on the materials and the procedure steps has been calculated and it is shown in Table 8.

SUMMARY	(a) Silver ink	(b) Silver & Gold printing	(c) Silver & Gold printing Gold area reduced	(d) Silver priting & gold plating
Manufactoring	0.07 €/sensor	0.07 €/sensor	0.09 €/sensor	0.02 €/sensor
Material	0.06 €/sensor	2.08 €/sensor	0.34 €/sensor	0.20 €/sensor
TOTAL	**0.12 €/sensor**	**2.15 €/sensor**	**0.43 €/sensor**	**0.22 €/sensor**

Table 8: Cost summary for the four different structures of the sensor platforms. (a) Design of Ag-IP and protective PI layer (b) Ag-SP heater plus the protective PI layer and Au-SP electrodes, (c) Ag-SP heater and pads buried by the protective PI layer and interdigitated in Au-SP and (d) whole structure of Ag-SP and protected by gold plating.

It seems clearly that the fabrication of a low-cost and reliable flexible sensor platforms needs of silver protection. In the case of inkjet printing, where the amount of ink is higher controlled and shows a smooth surface after sintering, the adhesive PI layer for the heater is enough. In the case of screen printing, the flake-like morphology brings also the need of the electrodes protection; to solve this fact, the gold plating of all the silver circuitry for the corrosion protection is the proper one.

4.5- Examples of device performances

The functionality of these platforms has been tested by the company SENSOTRAN S.L.[39] under the framework of the Trilobits project (identification and detection of toxic gases) for benzene sensing. Carbon nanotubes (CNT) decorated by some metals were deposited by electrospray on the interdigitated electrodes as the sensing material. These CNTs were synthesized by the Rovira I Virgili University. Some examples of these measurements are summarized below:
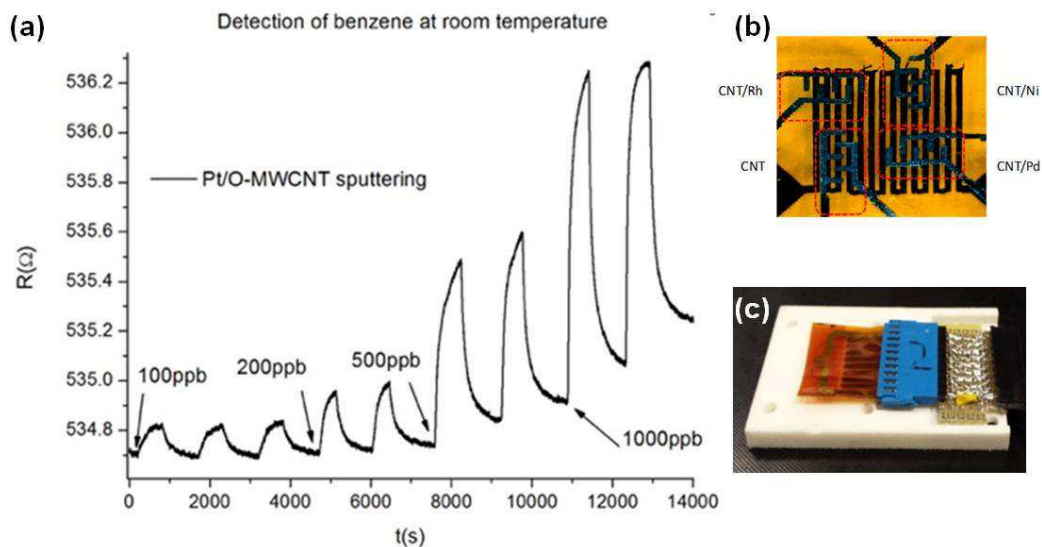
Fig. 20: (a) Detection of benzene at room temperature due to the variation in the resistance of the sensing material deposited on the interdigitated electrodes when benzene molecules are adsorbed in it, (b) image of the four electrodes in a IP-device and the corresponding sensing material on each of them and (c) IP-device located on the measurement chamber before close it.
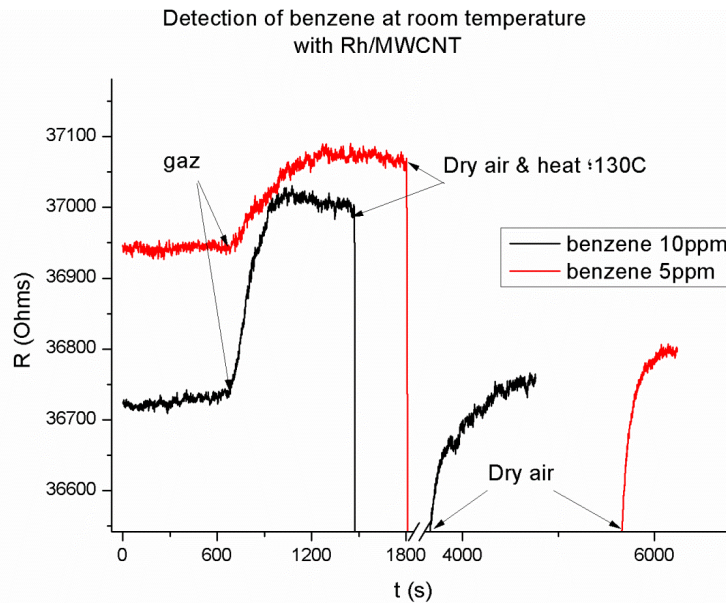
Fig. 21: Sensing response of Rh/MWCNT deposited in one of our printed platforms at room temperature and drying and heating cycle for the deadsorption of the benzene molecules and the sensing material cleaning.

4.6- Conclusions

Flexible gas sensor platforms fabricated by means of screen- and inkjet-printing were tested by continuous life tests maintaining 120 ^{o}C during heater operation. Early device failure, caused by chemical degradation, is observed in SP-devices due to the flake-like morphology of the deposits. No noticeable deterioration occurs in IP-conductive tracks of silver nanoparticles. However, the very thin film obtained by inkjet printing promotes a failure by hot spot phenomena. Both kind of failure are prevented by the heaters isolation from the atmosphere by an adhesive PI tape. The SP- and IP-heater lengthen their life time more than 10 times the unprotected ones. The homogeneity and the smooth surface of IP-devices make them more reliable in those areas which cannot be isolated by the PI layer, such as the electrodes. In the SP-devices, a gold protection by means of galvanic replacement using a chemical plating bath is used achieving reliable sensor platforms based in both technologies.

An estimated pricing of the few designs implemented here has been done, corroborating the low-cost of these structures.

Furthermore, for IP-devices an improvement of the heater design by reducing the exposed area has shown a decrease of power consumption of 25%, what position the sensor platform

as a low-cost and low-powered consumer device. It also demonstrates that the synergetic combination of polymeric substrates with printed electronics is a good alternative to substitute the monolithic silicon and the ceramic technologies.

References

[1] W. A. MacDonald, M. K. Looney, D. MacKerron, R. Evesn, R. Adam, K. Hashimoto, K. Rakos (2007), *Latest advances in substrates for flexible electronics*, Journal of the Society for Information Display 15 (12), 1075.

[2] Z. Bao (2000), *Materials and fabrication needs for low-cost organic transistor circuits*, Advanced Materials 12 (3), 227.

[3] N. D. Sankır (2005), Flexible electronics: materials and device fabrication, Ph.D. Dissertation, Virginia Polytechnic Institute and State University in Blacksburg.

[4] E. Menard, M. A. Meitl, Y. Sun, J. U. Park, D. J. L. Shir, Y. S. Nam, S. Jeon, J. A. Rogers (2007), *Micro-and nanopatterning techniques for organic electronic and optoelectronic systems*, Chemical Reviews, 107 (4), 1117.

[5] F. C. Kebs (2009), *Fabrication and processing of polymer solar cells: A review of printing and coating techniques*, Solar Energy Materials & Solar Cells 93 (4), 394.

[6] V. Zardetto, T. M. Brown, A. Reale, A. Di Carlo (2011), *Substrates for Flexible Electronics: A Practical Investigation on the Electrical, Film Flexibility, Optical, Temperature, and Solvent Resistance Properties*, Journal of Polymer Science Part B: Polymer Physics, 49, 638.

[7] A. Hudd, (2010), *The Chemistry of Inkjet Inks* S. Magdassi (Ed.), WorldScientific, New Jersey-London-Singapore, 3–18.

[8] Y. Sun, J. A. Rogers (2007), *Inorganic semiconductors for flexible electronics*, Advanced Materials 19 (15), 1987.

[9] A. Sazonov, D. Striankhilev, C.-H. Lee, A. Nathan (2005), *Low-temperature materials and thin film transistors for flexible electronics*, Proceedings of the IEEE 93 (8), 1420.

[10] S. F. Jahn, T. Blaudeck, R. R. Baumann, A. Jakob, P. Ecorchard, T. Rüffer, H. Lang, P. Schmidt (2010), *Inkjet printing of conductive silver patterns by using the first aqueous particle-free MOD ink without additional stabilizing ligands*, Chemistry of Materials, 22 (10), 3067.

[11] D. Kim, J. Moon (2005), *Highly conductive ink jet printed films of nanosilver particles for printable electronics*, Electrochemical and Solid-State Letters 8 (11), 30.

[12] S. Magdassi, M. Grouchko, O. Berezin, A. Kamyshny (2010), *Triggering the sintering of silver nanoparticles at room temperature*, ACS Nano 4 (4), 1943.

[13] Y. Zhang, J. Zhang, Y. Lu, Y. Duan, S. Yan (2004), *Glass Transition Temperature Determination of Poly(ethylene terephthalate) Thin Films Using Reflection–Absorption FTIR,* Macromolecules 37 (7), 2532.

[14] P. J. Cygan, J. P. Zheng, S.-P. S. Yen, T. R. Jow (1993), *Thermal treatment of polyethylene-2,6-naphthalate (PEN) film and its influence on the morphology and dielectric strength*, Conference on Electrical Insulation and Dielectric Phenomena, Annual Report, 630.

[15] Y. I. Lee, Y. H. Choa (2012), *Adhesion enhancement of ink-jet printed conductive copper patterns on a flexible substrate*, Journal of Materials Chemistry 22 (25), 12517.

[16] Available in DuPont datasheets http://www.dupont.com/content/dam/dupont/products-and-services/membranes-and-films/polyimde-films/documents/DEC-Kapton-summary-of-properties.pdf (Consulted on December 2015).

[17] D. Minzari, M.S. Jellesen, P. Moller, R. Ambat (2011), *Morphological study of silver corrosion in highly aggressive sulfur environment*, Engineering Failure Analysis 18 (8), 2126.

[18] H. Lin, G. S. Frankel (2013), *Accelerated atmospheric corrosion testing of Ag*, Corrosion 69 (11), 1060.

[19] D. Liang, H. C. Allen, G. S. Frankel, Z. Y. Chen, R. G. Kelly, Y. Wu, B. E. Wyslouzil (2010), *Effects of Sodium Chloride Particles, Ozone, UV, and Relative Humidity on Atmospheric Corrosion of Silver*, Journal of Electrochemical Society 157 (4), 146.

[20] C. E. Lemon (2012), *Atmospheric Corrosion of Silver Investigated by X-ray Photoelectron Spectroscopy*, Ph.D. Thesis, The Ohio State University.

[21] G. Neri (2015), *First Fifty Years of Chemoresistive Gas Sensors*, Chemosensors 3, 1.

[22] S. R. Morrison (1987), *Selectivity in semiconductor gas sensors*, Sensors and Actuators 12 (4), 425.

[23] N. P. Zaretskiy, L. I. Menshikov, A. A. Vasiliev (2012), *On the origin of sensing properties of the nanostructured layers of semiconducting metal oxide material,* Sensors and Actuators B: Chemical 170 148.

[24] J. Fonollosaa, L. Fernández, R. Huerta, A. Gutiérrez-Gálvez, S.Marco (2013), *Temperature optimization of metal oxide sensor arrays using Mutual Information*, Sensors and Actuators B 187, 331.

[25] S. Claramunt, O. Monereo, M. Boix, R. Leghrib, J. D. Prades, A. Cornet, P. Merino, C. Merino, A. Cirera (2013), *Flexible gas sensor array with an embedded heater based on metal decorated carbon nanofibres*, Sensors and Actuators B: Chemical 187, 401.

[26] A. Abdelhalim, M. Winkler, F. Loghin, C. Zeiser, P. Lugli, A.Abdellah (2015),*Highly sensitive and selective carbon nanotube-based gas sensor arrays functionalized with different metallic nanoparticles*, Sensors and Actuators B 220, 1288.

[27] J. Sakai, L. Aoki, K. Ohsaka, Y. Ishikawa (2005), *Sub-micrometer order corrosion of silver by sulfur vapor in air studied by means of quartz crystal microbalance*, International Corrosion Congress, 19.

[28] A. Varea, E. Pellicer, S. Pané, B. J. Nelson, S. Suriñach, M. D. Baró, J. Sort (2012), *Mechanical properties and corrosion behaviour of nanostructured Cu-rich CuNi electrosdeposited films,* International Journal of Electrochemical Science 7, 1288.

[29] O. Bersirova, V. Kublanovsky, L. Anufryiev, I. Rubtsevich (2004), *Corrosion behavior of electroplated silver coatings*, Materials Science 10 (1), 11.

[30] O. L. Bersirova, V. S. Kublanovskii (2012), *Corrosion properties of electrodeposited thin coatings of polycrystalline silver*, Materials Science 48 (2), 197.

[31] J. Cerdà, A. Cirera, A. Vilà, A. Cornet, J.R. Morante (2001), *Deposition on micromachined silicon substrates of gas sensitive layers obtained by a wet chemical route: a CO/CH_4 high performance sensor*, Thin Solid Films, 391 (2), 265.

[32] M. Vilaseca, J. Coronas, A. Cirera, A. Cornet, J.R. Morante, J. Santamaria (2008), *Development and application of micromachined Pd/SnO₂ gas sensors with zeolite coatings*, Sensors and Actuators B: Chemical 133 (2), 435.

[33] C. Moldavan, O. Nedelcu, P. Johander, I. Goenaga, D. Gomez, P. Petkov, U. Kaufmann, H.-J. Ritzhaupt-Kleissl, R. Dorey, K. Personn (2007), *Ceramic micro heater technology for gas sensors*, Romanian Journal of Information Science and Technology 10 (1), 43.

[34] B. Jiang, T. Maeder, A.J. Santis-Alvarez, D. Poulikakos, P. Muralt (2014*), A low-temperature co-fired ceramic micro-reactor system for high-efficiency on-site hydrogen production*, Journal of Power Sources, 273, 1202.

[35] A. J. Santis-Alvarez, M. Nabavi, B. Jiang, T. Maeder, P. Muralt, D. Poulikakos (2012), *A nanoparticle bed micro-reactor with high syngas yield for moderate temperature micro-scale SOFC power plants*, Chemical Engineering Science 84, 469.

[36] R. J. Puddephatt (1978), *The chemistry of gold*, Elsevier Science Ltd, US.

[37] A. M. Weisberg (1997), *Gold plating, A brief history and current explanation of the process,* Products Finishing Magazine

[38] H. Honma, K. Hagiwara (1995), *Fabrication of gold bumps using gold sulfite plating,* Journal of Electrochemical Society, 142 (1), 81.

[39] www.sensotran.com

Chapter 5

Development of an absorber precursor for photovoltaic applications

5.1- Introduction

5.1.1- State-of-the-art and motivation

The solar panel is an enduring icon of the quest for renewable energy. First generation solar cell is the conventional crystalline silicon solar cell (c-Si), whose wafer's thickness is up to 200 μm but a different type of technology came up to be an efficient, cost-effective solution and it took its place next to the traditional silicon wafer-based panels; this technology is the thin-film solar cell. A thin-film cell is a second generation solar cell that is made by depositing one or more thin layers of semiconductor materials (CdTe, CIGS, a-Si, p-Si) on a substrate, such as glass, plastic or metal. The thinness of the cell is the defining characteristic of the technology. Unlike silicon-wafer cells, which have light-absorbing layers that are traditionally 200-350 μm thick, thin-film solar cells have light-absorbing layers that are just few microns thick[1]. This allows thin film cells to be lightweight, lower cost than traditional ones and even flexible due to the wide versatility of substrates that can be used. This characteristic gives these cells a high potential for special applications such as wearable and architectural integration.

Thin-film technology, the above mentioned as second generation, has always been cheaper but less efficient than conventional c-Si technology (first generation). However, it has significantly improved over the years. The lab cell efficiency for CdTe [2] and Cu(In,Ga)Se$_2$ (CIGS) [3] is now beyond 21%, outperforming multicrystalline silicon although slightly lower than the record efficiency for mono-crystalline cells which reaches 25.6 %[4]. Among thin-film photovoltaic (PV) technologies, CdTe and CIGS are the most established ones and both technologies have already achieved a certain place in the market since reported module efficiencies are around 12-16%[5]. Unfortunately, the use of highly scarce materials such as indium[6] and potentially toxic elements, such as cadmium[7], is implicit in the fabrication of this kind of cells. Due to this fact, all the strategies

involving not only a lower environmental impact but also a lower production cost are more than attractive for all the PV market stakeholders. Thus, $Cu_2ZnSn(S,Se)_4$ (CZTSSe) solar cells have become a potential competitor to their equivalent CIGS due to their high potential efficiency, non-toxic nature, lower cost and the high abundance of their elements at the earth crust[8].

Besides, the replacement of vacuum steps by atmospheric processes, like solution-based ones, can significantly reduce the manufacturing cost of solar cells and modules. In particular, $Cu_2ZnSn(S,Se)_4$ (CZTSSe) solution-based solar cells are attracting the attention of the PV community due to the promising results already obtained. The record efficiency of a CZTSSe solar cell reported so far corresponds to 12.6% using a hydrazine pure-solution process[9]. This efficiency and its progression over the last years have stimulated research to enhance the electrical performance of CZTSSe solar cells. Although the hydrazine pure solution process has led to the best result obtained so far, less hazardous non-hydrazine solution-based routes have been also successfully explored. Thus, different solvents as hexanethiol, ethanol and dimethyl sulfoxide (DMSO) have been tested. The resulting devices have exhibited efficiencies values in the range of 8 and 8.5%[10]. Another important aspect corresponds to the synthesis of inks, which can be based on nanoparticles and/or metallic salts. Efficiency values around 8% for CZTSSe solar cells have been reported using DMSO as solvent and spin coating as deposition method[11,12]. More recently, additional improvements achieved on the buffer/absorber interface have allowed reaching an efficiency value as high as 10.5 % using DMSO and spin coating[13].

Regarding the deposition methodology, spin coating appears to be the preferred technique to demonstrate the feasibility of solution routes for solar cell lab-scale fabrication. It is a quite accepted fact that spin coating is not a suitable methodology for large-area devices and high-volume production as important solution losses do always occur after every single deposition. This limitation, among others, has led to the exploration of technologies that can be applied to large-areas, thus facilitating the industrial scaling-up. Particularly, methodologies adequate for roll-to-roll processes exhibit clear advantages when industrial prospection is considered. The doctor-blade method, which has already led to efficiencies of 7.5 and 8.4% for CZTSe[12] and CZTGeSSe[14] solar cells respectively, is the most common roll-to-roll compatible strategy. Doctor-blade allows not only large-area depositions but also a more adequate utilization of the precursor ink in comparison to spin coating. Nevertheless, additional tools for series interconnection of the cells are still necessary for the fabrication of modules. Direct write techniques can potentially offer an answer to the major problems related to the large-area deposition and the fabrication of modules. These techniques allow writing exactly the adequate patterns for the series

interconnection of cells with the additional advantage of avoiding excessive losses of material. Inkjet printing is a direct-writing technique that has been recently applied for the deposition of CZTS ink[15] with reported efficiencies of 6.4%. The excellent control of the amount of material delivered (drop by drop process) and the accuracy in every deposited drop location give inkjet printing a perfect fit for being employed as a deposition technique for solar cell precursor ink.

In this chapter, we used inkjet printing to deposit a CZTS precursor solution. The influence of the drying temperature of the precursor layer and two different reactive-annealing treatments for the CZT(S,Se) absorber synthesis were investigated and its influence on the electrical performance of the cells analyzed. Finally, the thickness of the deposited precursor was modified for the analysis of its effect on the electrical performance of the complete solar cells.

The formulation of the precursor ink for the absorber layer has been done in Francisco Albero S.A.U. (FAE) while the printing and drying study of the precursors layer has been carried out in the University of Barcelona. The selenization of the precursor layer, the fabrication and the opto-electronic characterization of the solar cells have been done by the Research Group on Solar Energy Materials and Systems of Dr. Alejandro Pérez-Rodríguez in The Catalonia Institute for Energy Research (IREC).

5.1.2- Solar cell fabrication and structure

A solar cell is an electronic device, which directly converts light into electricity. Light produces both a current and a voltage to generate electric power on the solar cell. This process requires firstly, a material in which the absorption of light raises an electron-hole pair to a higher energy state, and secondly, the movement of this pair from the solar cell into an external circuit (Fig. 1). Photovoltaic energy conversion relies on semiconductor materials in the form of a p-n junction. This p-n junction forms a diode where the current movement only occurs in reverse direction, from the n- to the p-type material. Hence, the light-absorber material received the photon, which generates a free electron-hole pair within the p-n junction and then, the electrons move across the cell towards the n-type material layer and being collected in the front contact and holes towards p-type material, being collected in the rear contact. The p-n junction is enclosed between the two electrodes. These conductive contacts are situated onto the front and the rear side of the cell to collect the electrons.
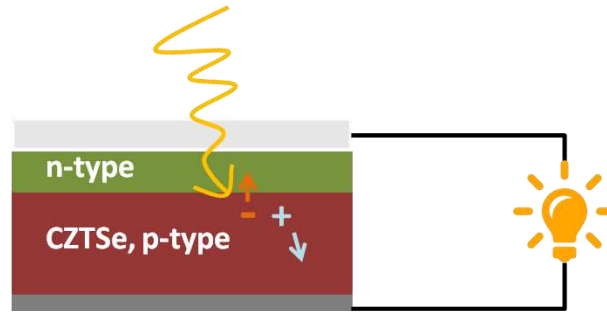
Fig. 1: Schematics of a CZTS solar cell.
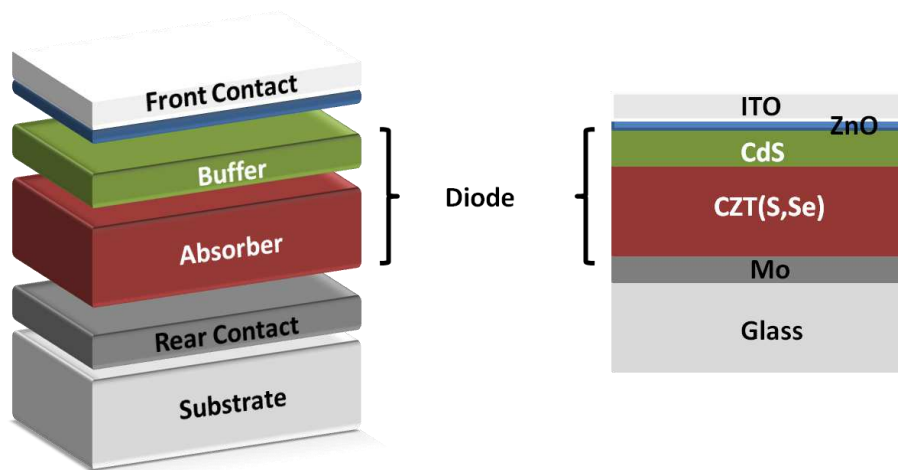
Fig. 2: Structure of the different layers forming a solar cell and the corresponding materials used in this work.

In our case, the conductive rear contact is a sputtered molybdenum layer deposited in a glass substrate. The front contact or the negative electrode is a transparent conductive oxide (TCO) whose transparency allows the light to reach the semiconductor materials and the p-n junction; in this case, the chosen TCO is the widely used indium doped tin oxide (ITO) because of its sheet resistivity. The p-n junction is built joining the absorber layer formed by CZTSe kesterite structure and the chemically deposited n-type buffer layer[16] of cadmium sulfide (CdS), as it can be seen in Fig. 2. The role of the intrinsic ZnO is to cover pinholes in the CdS layer to avoid leakage currents along the pn-junction[17].

The aim of this chapter is the formulation and evaluation of the absorber layer, which will be inkjet-printed onto the molybdenum layer using a CZTS precursor ink. After the deposition of this precursor layer and its drying process, the fabrication of the whole solar cell and the optoelectronic measurements were carried out by the Catalonia Institute for Energy Research (IREC)[18]. For the synthesis of the CZT(S,Se) absorbers, the printed precursors are submitted to a Se

reactive annealing in a conventional tubular oven with 100 mg of Se and 5 mg of Sn, using graphite boxes (23.5 cm^3 in volume). Then, different etchings removes the secondary phases of SnSe[19] and ZnSe[20] and 50 nm of the n-type material (CdS) is deposited by chemical bath deposition (CBD) to finally complete the solar cell devices by depositing the intrinsic-ZnO window and the ITO front electrode by means of reactive DC-pulsed sputtering.

Kesterite structure and properties

A semiconductor material can be considered propitious for thin film absorber as long as it has a direct band gap (E_g) between 1 - 1.5 eV and a high absorption coefficient[17] of $\alpha > 10^4$ cm^{-1}. The emerging compound kesterite - $Cu_2ZnSn(S,Se)_4$ - consisting of earth abundant, and lower priced materials than others thin film absorber as CIGS has attracted a lot of research interest in the last years. After some disagreement if the structure adopted by Cu_2ZnSnS_4 was the kesterite or stannite (Fig. 3), it became accepted that it crystallizes in the kesterite structure, which is energetically more favorable[21].
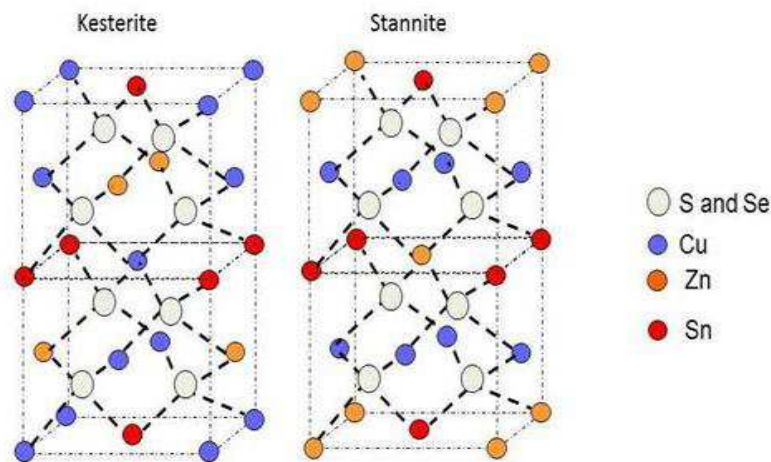
Fig. 3: Kesterite and stannite structure for Cu_2ZnSnS_4.

The band gap of CZT(S,Se) kesterite can be tuned by adjusting the S/(S+Se) ratio. A band gap of $\sim$ 1.0 eV is found for pure CZTSe [22] while $E_g \sim$ 1.5 eV is for pure CZTS[23]. The absorption coefficient of kesterite[24] is reported to be above E_g is $> 10^4$ cm^{-1}.

5.1.4- Optoelectronic parameters

As it was said before, the solar radiation generates free pair carriers, which move across the cell and are collected in the front and rear contacts. This movement generates a voltage and a current inside the cell. The maximum voltage is that one that is generated when there is no pair

movement (current is zero) and it is known as the open-circuit voltage, V_{oc}. In the same way, the maximum current possible in the cell occurs when the voltage across the cell is zero and it is called short-circuit current, I_{sc}. This current depends on the cell area, so it is common to list the short-circuit current density instead (J_{sc} in mA/cm^2), rather than the short-circuit current. The fill factor, FF, is the parameter which, in conjunction with V_{oc} and I_{sc}, determines the maximum power from a solar cell. In addition, the efficiency is the most commonly used parameter to compare the performance of one solar cell to another. Efficiency is defined as the ratio of the output energy from the solar cell to the incident radiant energy.

$$\eta = \frac{FF \cdot V_{oc} \cdot I_{sc}}{P_{in}}$$

$$FF = \frac{P_{max}}{I_{sc} \cdot V_{oc}}$$
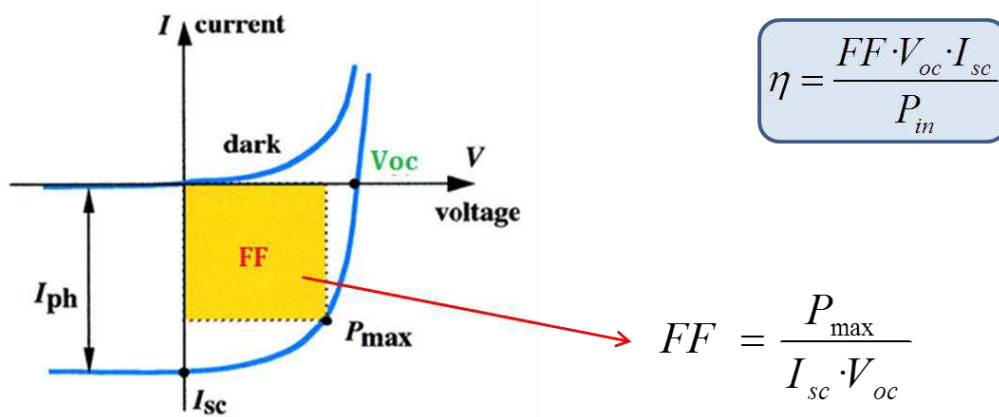
Fig. 4: IV curve and parameters of a solar cell

Usually, the solar cell performance is plotted as the IV curve with the superposition of the IV curve of the solar cell diode in the dark with the light-generated current (Fig. 4). The FF is the area of the largest rectangle which will fit in the IV curve and it gives an idea of the "squareness" of the curve. The higher the squareness, the closer to the maximum power performance. The higher voltage, the larger possible FF since the roundness of the curve takes up less area. However, large variations in open-circuit voltage within a given material system are relatively uncommon. The most significant variation in maximum FF is produced by the utilization of different materials.

A bad performance of the cell gives a low FF (far from ideal diode performance) and it depends also on the presence of parasitic resistive losses. Resistive effects in solar cells reduce the efficiency of the solar cell by dissipating power in the resistances. The most common parasitic resistances are series resistance (R_s) and shunt resistance (R_{sh}), see Fig. 5. The series resistance is the opposition to the current and it appears mostly on the interfaces between the layers. A high resistance in electrons flux means a high Joule effect and consequently, it reduce cell efficiency. Unlike the series resistance, the shunt resistance is the one that opposes the flux of electrons in an alternative current path; it avoids the escape of electrons in a wrong direction. The path

diversion reduces the amount of current flowing through the solar cell junction and reduces many opto-electronic parameter from the solar cell such as the voltage, the intensity the current density and, moreover, the efficiency.
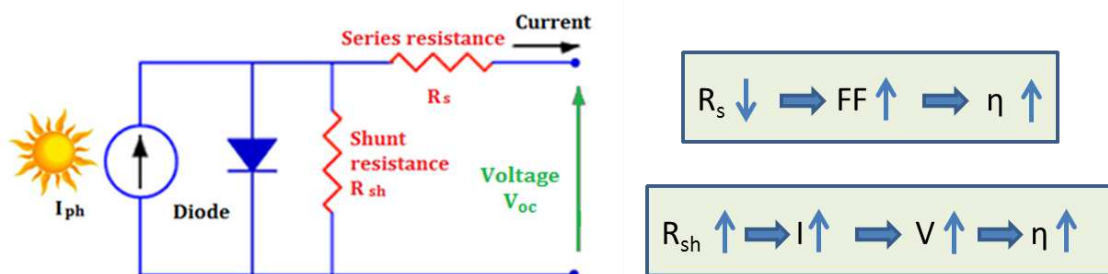
Fig. 5: Representation of the electrical circuit in a solar cell

In this work, an ABET Technologies Sun 3000 Class AAA solar simulator was used for the solar cell J-V curve measurements.

5.2- CZTS precursor study

During this study, two different formulations of CZTS inkjet ink have been compared. Following a route previously reported in the literature[11] and using the same precursor materials, the ratio between them were modified. A pre-solution A was formulated, dissolving the precursors materials into the dimethyl sulfoxide (DMSO) and, maintaining the precursors ratios, the physical properties were tuned for the proper jetting using inkjet technology; this optimized solution turned to be called Solution A.

Additionally, a second solution named as Solution B were also formulated, but with different ratios. In this case, and considering that it is already reported that higher efficiencies for CZTS solar cells are obtained with ratios around Cu/(Zn + Sn)=0.8 and Zn/Sn= 1.2 [25], the most significant modification was carried out in the variation of the ratio between the thiourea and the rest of components, (Cu+Zn+Sn)/S. This modification brought about different cell performances giving evidences of the important of the composition of the precursor ink into the opto-electrical parameters. Best results are obtained with low-sulfur content what might be detrimental for secondaries phases formation.

Furthermore, the influences of the drying process and the layer thickness of the precursor have been studied as well.

5.2.1- Formulation of a kesterite precursor inkjet ink

The different formulations are included in Table 1.

Components	Pre-Solution A	Solution A	Solution B
$Cu(CO_2CH_3)_2 \cdot H_2O$	0.92 M	0.65 M	0.46 M
$SnCl_2 \cdot 2H_2O$	0.63 M	0.45 M	0.32 M
$ZnCl_2$	0.64 M	0.457 M	0.32 M
$SC(NH_2)_2$	3.04 M	2.17 M	1.51 M
DMSO	8 ml	5 ml	5 ml
BYK380N	-	1 % wt	1 % wt
Cu/(Zn+Sn)	0.724	0.717	0.718
Zn/Sn	1.015	1.015	1.000
(Cu+Zn+Sn)/S	0.720	0.717	0.195

Table 1: Composition and precursors ratios for the different solutions.

The salts are added to the solvent in the following order: firstly, copper (II) acetate monohydrate (99.99 % from Aldrich) into the dimethyl sulfoxide (DMSO) solvent. In this initial step, the Cu salt does not completely dissolves due to its very limited solubility. Some aggregates of the Cu salt are formed into a deep blue solution containing part of dissolved Cu. Secondly, after about 20 s of stirring, the tin (II) chloride dihydrate (99.995% from Sigma-Aldrich) is added to the mixture contributing to the dissolution of some of the copper aggregates and changing the solution color to dark green. After that, the zinc (II) chloride anhydrous (99.99% Alfa-Aesar) addition, after about 20 s of stirring, reduces perceptibly the size of the remaining aggregates and the solution color changed to a lighter green. The fourth step of the solution preparation consists in the addition of the thiourea (99% from Sigma-Aldrich), which leads to a last color change of the precursor solution to light yellow. The mixture is stirred over night until all the salts are completely dissolved. Fig. 6 shows the color changes of the precursor solution.
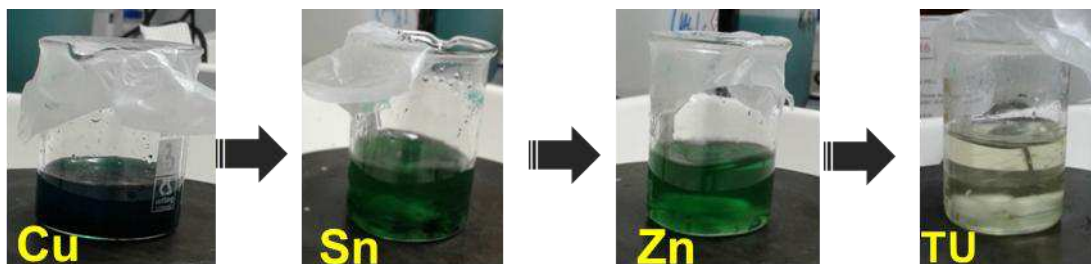
Fig. 6: Images of the precursor solution after the addition of each salt.

The color change from green to light yellow has been explained elsewhere[11,12] and it is a consequence of a Cu^{2+} reduction to Cu^+ in combination with a solvation/stabilization of metal ions by DMSO and/or chloride anions. Nevertheless, according to the route followed for this preparation, described by H. Xin et al.[11], a colorless solution is expected after all the stages. The final light yellow color obtained might be associated to non-reduced Cu^{2+} anions still remaining in the solution.

Both compositions here studied are prepared following exactly the same route and regarding the optimal precursor materials addition order reported.

Once all the components are diluted in the DMSO solvent, the rheological features and the surface tension of the solution were adapted to the requirements of the printing technique. In this sense, recommended values of viscosity for the 10 pl nozzles used in this study range from 8 to 18 cp, whereas surface tension might be between 25-35 dynes/cm to achieve an acceptable drop formation. The contact angle between the droplets and the Mo-covered substrate must be as low as possible to get a proper wettability and to control better the thickness of the layer. The thinner the layer the most homogeneous dried precursor formed. The pre-solution A was formulated according to the composition specified in Table 1. This initial solution did not fulfill the requirements since the resulting viscosity was 67 cP and the contact angle exhibited a value of 33⁰. Thus, after several ink modifications, the precursor solution was finally diluted at 25% in weight using the same solvent, DMSO. This dilution allowed the reduction of the viscosity down to 14 cP and the contact angle to 16⁰. Nevertheless, even if the surface tension was suitable for a good drop formation, the interaction with Mo-covered glass substrates was not good enough to form a continuous layer and to achieve the required stability during the drying process of the deposited solution (Fig. 7). This happens because of the differences surface tension between the Mo layer and the ink.
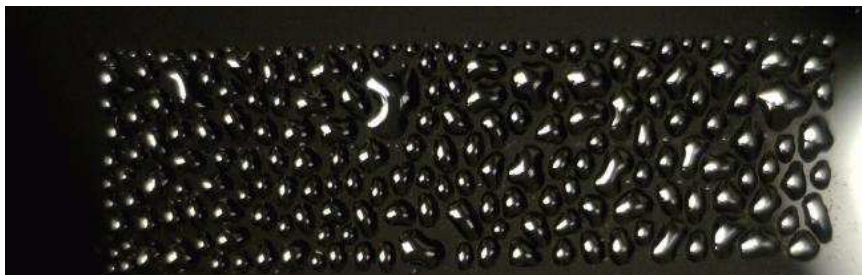
Fig. 7: Diluted and printed CZTS solution onto a Mo-covered glass substrate showing a bad interaction due to the differences in surface tension between the ink and the substrate.

High surface tension combined with low viscosity carries out an uneven surface and avoids the spreading over the substrate. In these cases, an additive with leveling properties can help to lower the surface tension of the solution and give stability on the surface. The leveling agents are additives with controlled compatibility that migrate to the surface of the fluid preventing the uneven surface and homogenizing it. Fig. 8 shows how a leveling agent works according to its compatibility with the medium.
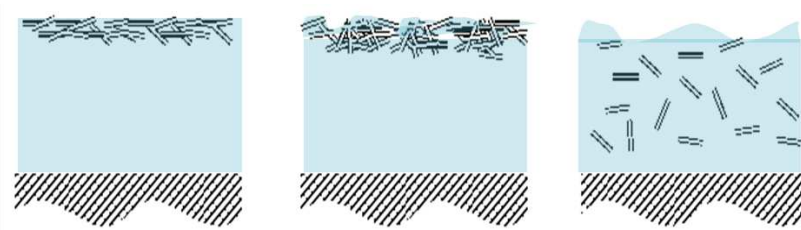
Fig. 8: Illustration of the leveling agent with the fluid when the compatibility is (a) optimum, (b) too low and (c) too high.

After the incorporation of the organic additive BYK380N at 1% by weight allowed reaching a contact angle lower than 10° (Fig. 9) while keeping the viscosity in a value of 15 cP.
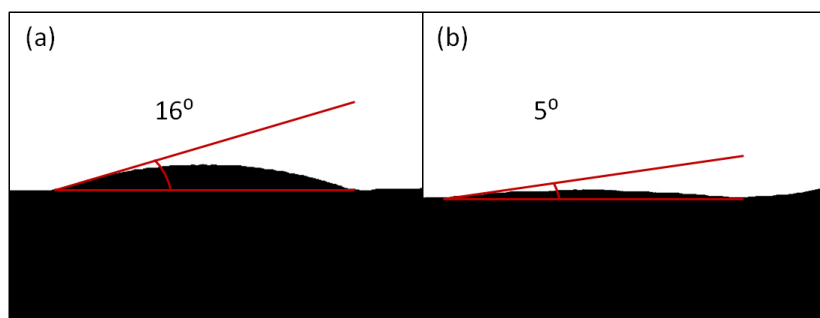
Fig. 9: Contact angle of (a) Solution A without the leveling agent (pre-solution A diluted at Solution A concentrations) and (b) Solution A. These images were taken by a Horizontal Optical Dilatometer Misura ODLT.

This additive is an acrylic leveling agent that reduces surface tension while improving deposition uniformity over the substrate and reduces cratering. After all these changes, the printed solution exhibited adequate wettability properties (Fig. 10), allowing an adequate layer formation and, finally, a very good stability of the printed layer during the drying process. This solution is the one called Solution A from now on.

Fig. 10: Printed CZTS solution with a 1% wt. of leveling additive onto a Mo-covered glass substrate showing a full wetting.

Solution B was formulated and tuned to exhibit the suitable printable properties of viscosity and surface tension. The composition is also showed in Table 1. The main difference lies on the thiourea content, where the (Cu+Zn+Sn)/S ratio falls down from 0.717 to 0.195. The leveling additive was needed again to achieve a good wettability.

5.2.2- Inkjet printing process

5.2.2.1- Printing parameters tuning

A Dimatix (model DMP-2831) ink-jet printer with cartridge of 16 nozzles of 10pl each one was used for printing the precursor layer.

The propulsion voltage was 23.0 V for the droplet jetting and the waveform applied to the piezoelectric nozzles was optimized to obtain a stable drop. The head of these drops drags a long tail what slows down the drop velocity. A homogeneous tail shape may be maintained without breaking off forming satellite drops. The printhead height was settled on 350 μm. The drying process of the printed layers was carried out in a hot plate until complete evaporation of the solvent (approximately around 2 min).

It has been necessary to optimize the printer parameters for a well-defined and continuous precursor layer. Once the proper drive voltage is controlled for the suitable drop velocity, the main parameter to be optimized is the drop spacing (ds), which is measured in microns. As Fig. 11

shows, the selected drop spacing for the CZTS printing was 30 μm to assure a complete covered-Mo

Fig. 11: Printing of the CZTS ink with 75, 50 and 30 ds (or microns).

5.2.2.1- Drying process

Different drying temperatures (180, 220 and 280 °C) were tested in this work to find the drying conditions giving place to the best photovoltaic performance. This study was carried out using Solution B-samples due to its contribution to a better cell performance (see section 5.2.3.1- Ink formulation influence on the cell performance). A X-ray florescence spectrometer (Fisherscope XVD) was used to evaluate the relative concentration of elements in the precursors and absorbers. In addition, a crystallographic analysis was carried out by means of a X-ray diffractometer (Siemens D500) in a 2θ configuration ranging from 12° to 80°. Morphological characterization of the different structures was evaluated by scanning electron microscopy (SEM) through a Zeiss series Auriga microscope using an accelerating voltage of 5 kV.

The common thickness for the CZTS absorber layer[26] is around the 2 μm, being the precursor layer of 1 μm before the selenization step. In order to obtain a precursor layer of this thickness, the sequential printing of at least three layers was required. A drying step on a hotplate was applied after the deposition of each layer. A first result to be highlighted consisted in a change of the color of the printed layers from transparent to black (Fig. 12) as the solvent evaporated during the drying process, suggesting that the precursor salts already react at these relatively low temperature forming sulfide compounds. This color change was always observed regardless of the selected drying temperature. The drying duration was 2 minutes for all the experiments presented in this work. The influence of the drying temperature on the crystallization of the absorber was evaluated. For this purpose, three different drying temperatures (180, 220 and 280 °C) were selected to perform a morphological and structural study. Fig. 13 shows top-view and cross-section SEM images of the three precursors dried at the mentioned temperatures.

Fig. 12: Dried CZTS printing of two 2.5x5 cm dried at 280⁰C. This sample was printed with solution B.
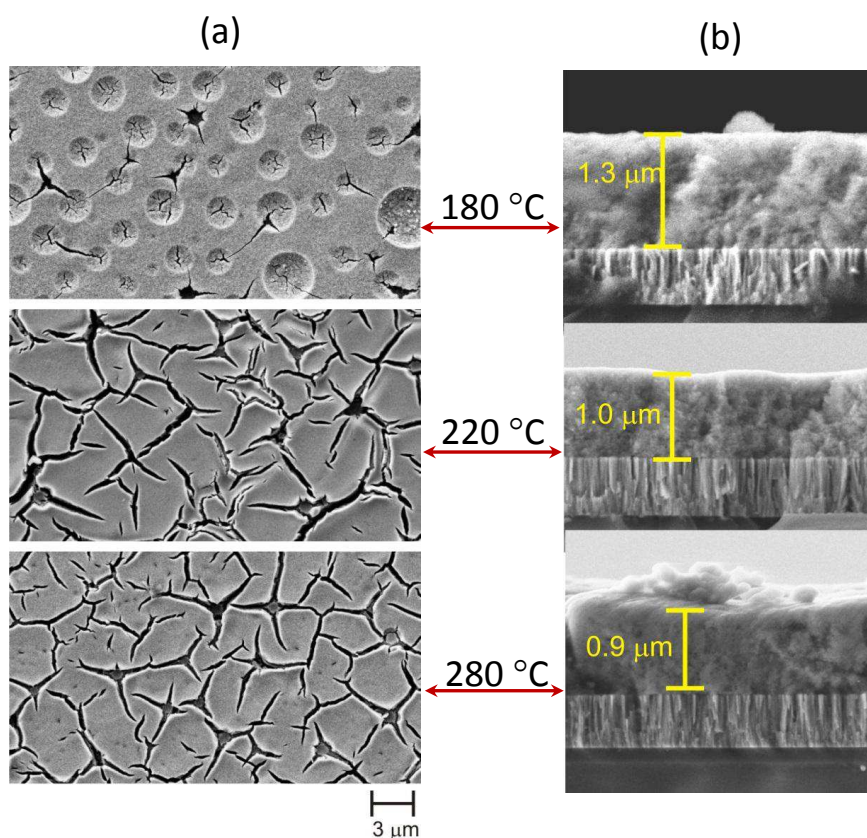
Fig. 13: SEM images of the (a) surface and (b) cross-section of the solution B-precursors dried at different temperatures.

Bubbles and cracks can be identified in the precursor that was dried at the lowest temperature. These bubbles were not observed as drying temperature increased. On the contrary, the generation of cracks is more evident as drying temperature increases since cracks are larger and wider than those observed for the lowest temperature. That seems to be owing to tensions when the layer is dried at so high temperature (thermal shock). The cross-section images give evidence of a denser structure for the precursor that was dried at 280 °C. As a consequence of this densification, a slight decrease in the thickness of the structure is expected as temperature increases.

An X-ray fluorescence analysis (XRF) of these precursors demonstrated a notable difference on the amount of sulfur in the 280 °C sample when compared with the other ones. As far as the remaining elements are concerned, no significant differences could be evidenced from the XRF results.

Fig. 14 shows the relative concentrations of Cu, Zn, Sn and S as well as the ratios between elements. Even if the kesterite structure should have a stoichiometric ratio of Cu/(Zn + Sn) = 1, Zn/Sn = 1 and (Cu + Zn + Sn)/S = 1, ratios of around Cu/(Zn + Sn)=0.8 and Zn/Sn= 1.2 gives place to cells with higher efficiencies[25]. This is mentioned frequently as an empirical rule that the Cu poor and Zn rich growth condition gives the highest solar cell efficiency[23,27,28]. According to the trend observed for the ratios, the desired Cu-poor and Zn-rich part of the phase diagram seem to be more achievable with the higher drying temperature but still the Zn content should be higher. The Zn deficit could be a problem of the hydratation of the anhydrate salt, what implies an error in the added mass of Zn.
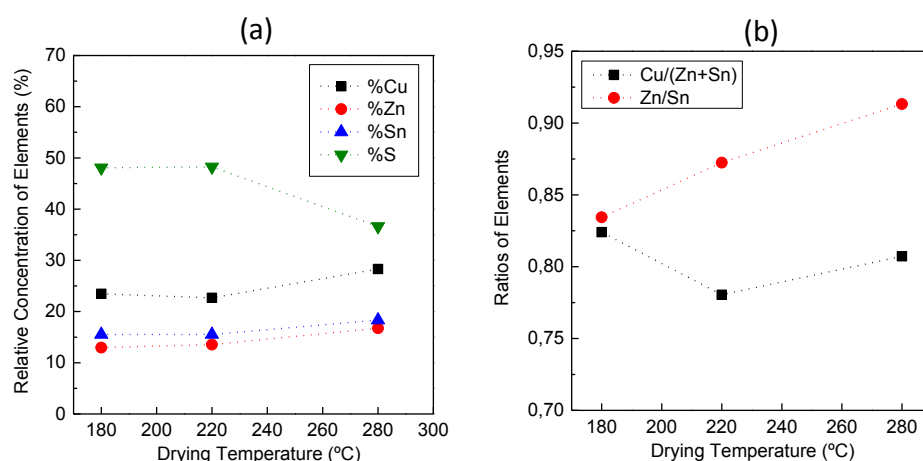
Fig. 14: XFR analysis of the solution B-CZTS precursors dried at different temperatures.

Drying temperature influence on the absorber formation

The three precursors, dried at the different temperatures under study, were simultaneously annealed under a Se reactive atmosphere to create the absorbers. A two-step annealing (400 °C less than 1 mbar Ar-Flow for 30 min and 550 °C under 1 bar for 15 min) was selected for the synthesis of these first absorbers (see section 5.2.3.2- Selenization process influence on the absorber formation). The absorber surface and cross-section images resulting from precursors dried at different temperatures are presented in Fig. 15 and Fig. 16. It can be noted that the

higher the drying temperature the larger the grain size of the absorber. In addition, the absorber produced with the lowest drying temperature precursor exhibited practically no crystallization as only very fine-grains can be distinguished.
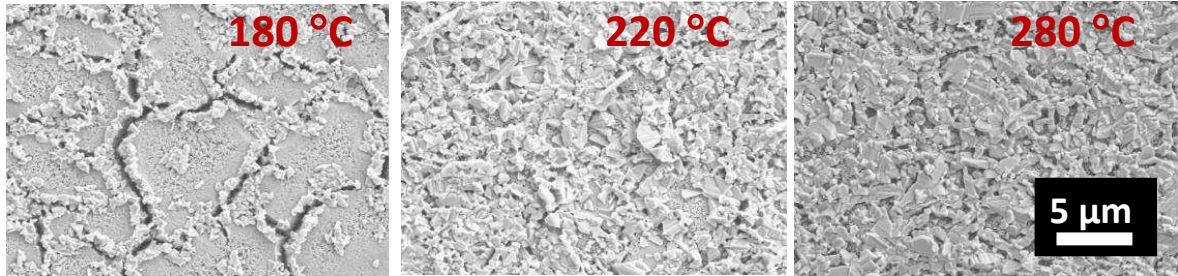
Fig. 15: SEM images of the solution B-CZT(S,Se) absorbers surface whose precursors were dried at three different temperatures and simultaneously annealed under a Se reactive atmosphere.
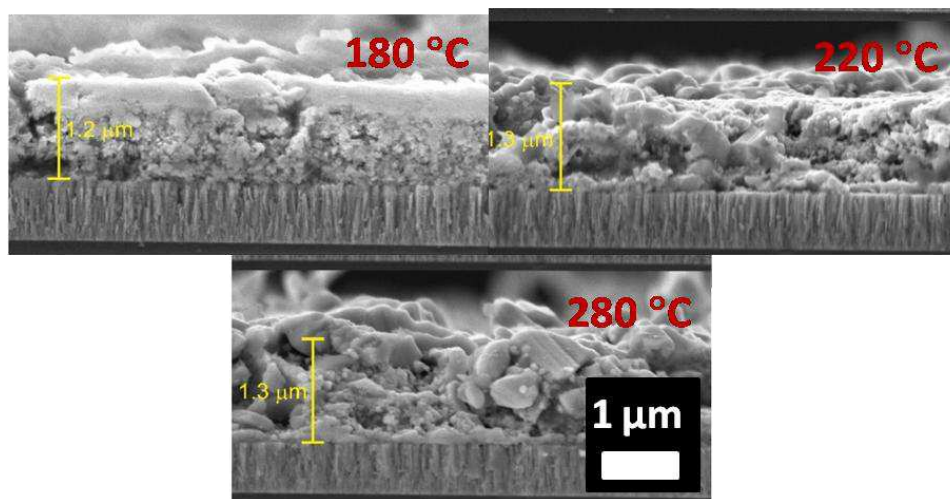
Fig. 16: Cross-section images of the solution B-CZT(S,Se) absorbers whose precursors were dried at three different temperatures and simultaneously annealed under a Se reactive atmosphere.

In order to get a deeper insight into the influence of the drying temperature on the crystallization process, XRD measurements of the absorber were carried out. Fig. 17 shows the XRD patterns obtained for the absorbers dried at the three different temperatures. The main aspects to be pointed out are: (1) Regardless of the drying temperature, a slightly lower value of the $Cu_2ZnSnSe_4$ lattice parameter (a = 5.651 Å) than the ICDD data base of card #00-052-0868 (a = 5.693 Å) was obtained, thus indicating the presence of Sulfur-Selenium mixed kesterite $Cu_2ZnSn(S_xSe_{1-x})_4$. (2) A $CuSn_{3.75}S_8$ phase with a lattice parameter of a = 10.6 Å, higher than the value of 10.393 Å from the ICDD #01-075-2266, was identified only in the 180 °C absorber. This higher value can be attributed to the presence of S atoms with higher atomic radius than Se atoms. (3) Finally, the

identified CZT(S,Se) peaks exhibited higher intensity and lower FWHM as the drying temperature increased. These results revealed that higher drying temperatures led to better structural properties of the absorbers.
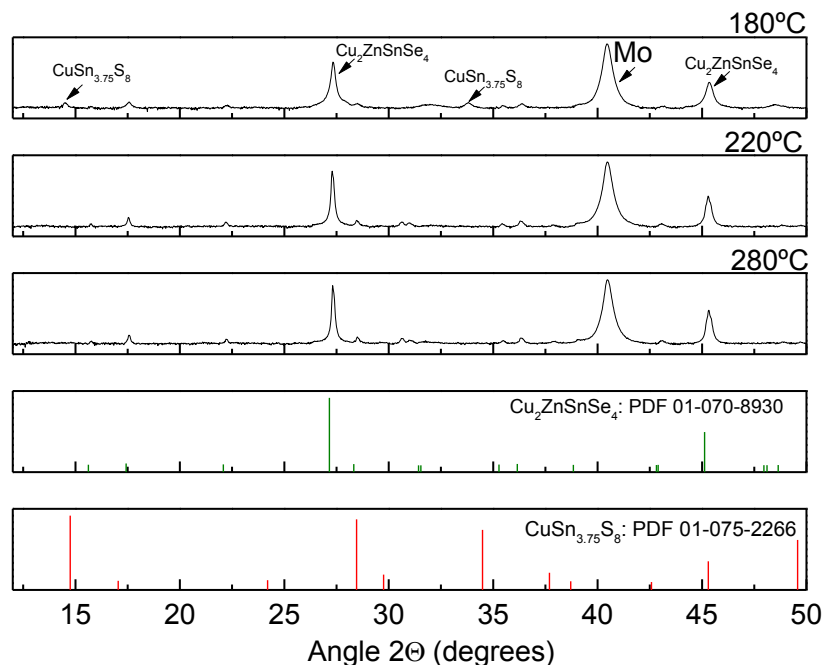
Fig. 17: XRD patterns of the solution B-absorbers obtained from precursors dried at different temperatures.

Thermal characterization of the CZTS ink and understanding of the drying process

For the understanding of what happens during the drying process, a system of Thermogravimetry (TGA) and Differential Scanning Calorimetry (DSC) from Mettler Toledo (Model 1-star) was employed to study the thermal response of the precursor solution.

The simultaneous application of thermogravimetric analyses (TGA) and differential scanning calorimetry (DSC) of the precursor solution revealed that solvent evaporation occurs from about 50 °C as can be verified in Fig. 18 (a). The loss of weight starts at 50 °C and reaches a 20% of its initial value at around 300 °C. This mass decrease is attributed, at least until the vaporization point of the DMSO at 189 °C, to the evaporation of the solvent. Higher temperatures involve the decomposition of the different compounds present in the solution. In order to get a better understanding of the different decompositions potentially involved in the drying process, the heat flow released by the precursor solution and by some individual salts diluted in DMSO was analyzed by means of DSC. Fig. 18 (b) shows the heat flow per weight as a function of

temperature for the precursor solution and some of the salts added to the DMSO (inset graph). Two zones, where highly exothermic reactions appear, can be distinguished. The first one is located in the temperature range from 125 to 300 °C, where the detected DSC bands could correspond to the decomposition of the species formed by the metal ions, the different counter ions and thiourea. The second zone, which can be found between 400 and 525 °C, may be associated to a complex decomposition of thiourea[29].
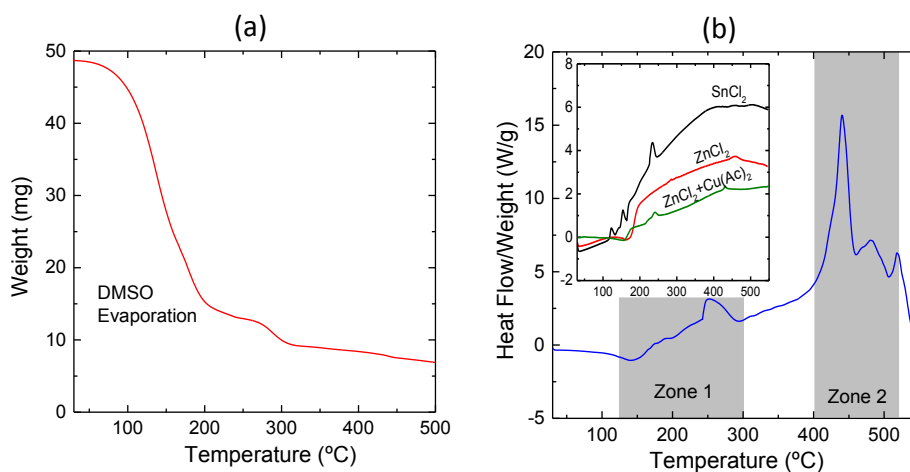
Fig. 18: (a) Thermogravimetric analysis (TGA) and (b) differential scanning calorimetry (DSC) of the precursor solution.

This analysis agrees with the experimental result of using 280$^\mathbf{o}$C as the drying temperatures to obtained better solar cell performance.

5.2.3- CZTSSe solar cell fabricated by the printed absorber

5.2.3.1- Ink formulation influence on the cell performance

The ratio of the precursor materials is an important variable in the quality absorber formation and its contribution in the solar cell performance. Both solutions were printed under the same conditions and deposited in a 1.2 µm precursor layer dried at 280$^\mathbf{o}$C during 2 min. The selenization process and the rest of the fabrication steps of the solar cell were identical.

The cross-sections were observed by SEM to identify the crystal grains formed by the selenization (Fig. 19). Larger grains are formed in the solution B-absorber what concurs with the opto-electronic characterization.
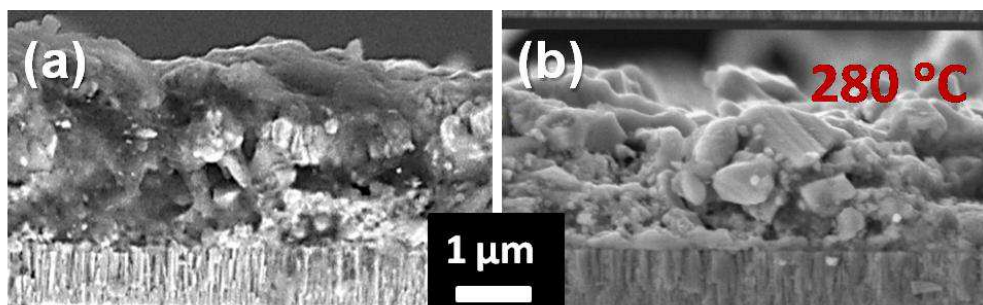
Fig. 19: Cross section of the absorber obtained by the (a) solution A-precursor and (b) solution B-precursor.

The opto-electronic parameters were measured for solar cells fabricated with both absorbers what showed the better quality absorber performance for the one obtained with the solution B-precursor. The maximum power conversion efficiency obtained by solution A-absorber was of 2.91% while for solution B-absorber was 4% (Fig. 20 on the left). This difference in efficiency was caused for an increase in the open circuit voltage (Fig. 20 on the right) what means a higher quality in the absorber layer due to a decrease in free-pair carrier recombination.
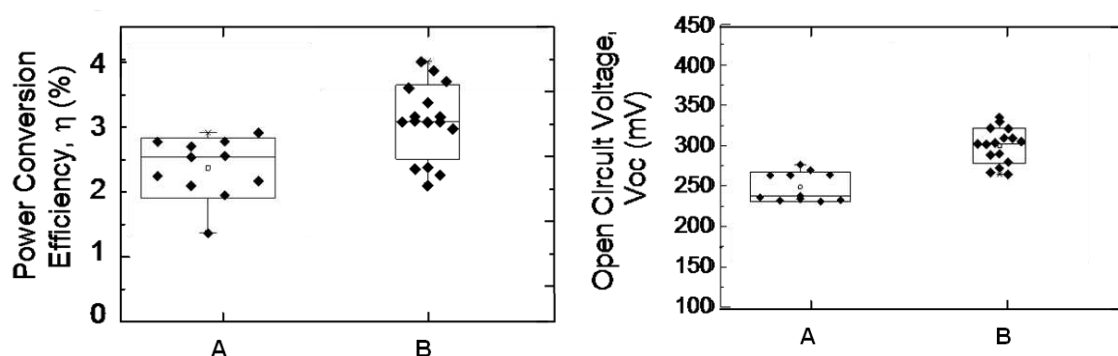
Fig. 20: Power conversion efficiency and open circuit voltage for cells fabricated with solution A- and solution B-precursors.

The variations in the rest of the opto-electronic parameter were insignificant.

Both compositions in solution A and B were repeated several times bringing about the same result what manifests the role of the thiourea (TU) in the formation and crystallization of the absorber. The reason for a better performance when the TU content is reduced in the composition of the precursor ink is still under study. One possible reason is that higher contents of TU favor the formation of secondary phases such as SnS. In Fig. 21 can be seen that the combination of TU with Sn produces an exothermic peak in the DSC near 450 °C that it is seen for solution A as well. The peak is moved at higher temperature (500 °C) in solution B what it is more in agreement with the

formation of a quaternary CZTS and it not seen in any other combination of TU with the rest of compounds individually.
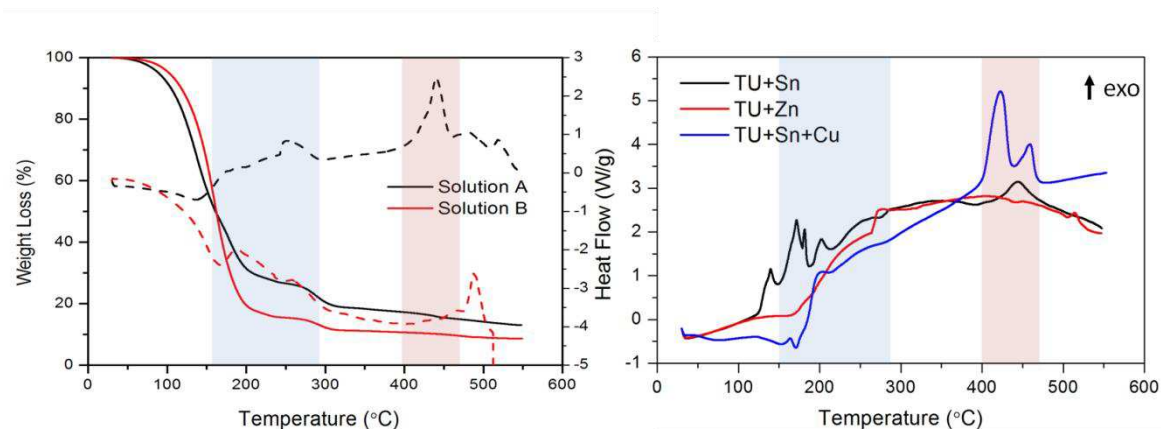
Fig. 21: On the left is showed the TGA and DSC of the two inks under study (solution A and B). On the right, the composition of the ink is divided in three DMSO solutions containing thiourea (TU) in combination of Sn, Zn or Sn and Cu, and the DSC is plotted. The blue-zone corresponds to the decomposition of the counter-ions (acetate and chloride) that happens a "low" temperatures and the red-zone represents the formation of possible secondary phases of Sn and S from the TU.

5.2.3.2- Selenization process influence on the absorber formation

For the synthesis of the CZT(S,Se) absorbers, the dried layers were submitted to a Se reactive annealing in a conventional tubular oven with 100 mg of Se and 5 mg of Sn, using graphite boxes (23.5 cm^3 in volume). Two treatments of Se reactive annealing were tested and their influence on the electrical performance of the final devices was evaluated. The alternative treatments consisted in either one or two temperature steps.

In order to find an optimal reactive annealing treatment for the inkjet precursor dried at 280 °C, two different reactive annealing processes were compared. As mentioned in the experimental section, one and two-step annealing treatments were evaluated. The first treatment comprised a single temperature step of 550 °C under 1 Bar of Ar-Se pressure for 45 min. The second treatment consisted in a two-step annealing: the first one was carried out at 400 °C for 30 min in a 1 mbar Ar-flow and the second one was performed at 550 °C for 15 min under 1 Bar of Ar-Se pressure.

SEM images of the absorber surface corresponding to the two types of annealing treatments are shown in Fig. 22. Both samples were obtained with solution B-precursors. A mix between large crystalline grains and fine grains can be clearly distinguished in the one-step absorber. Similar grain mixtures have been reported in several studies using single-step annealing treatments and

where not only conventional tubular furnaces[11] but also rapid thermal reactors are employed[12,13]. When focusing of the crystallized part, this exhibits a medium grain size that is larger than the one obtained in the two-step annealed absorber. Thus, the two-step annealing treatment gives place to smaller crystals, which are almost completely distributed over the surface. In this absorber, the non-crystallized material is not easily recognized but it is present in those zones where the crystals are not touching each other.
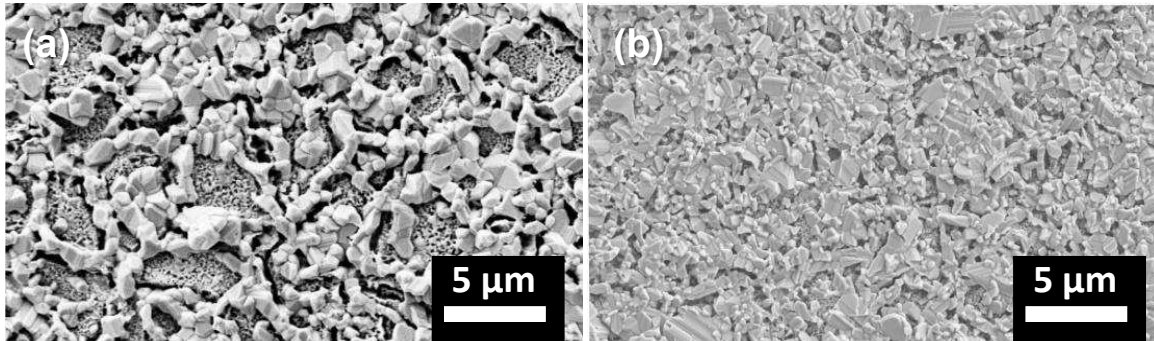
Fig. 22: Top-view images of the solution B-CZT(S,Se) absorbers dried at 280°C and annealed with either (a) 1-step or (b) 2-step selenization treatment.

Fig. 23 shows the XRD patterns of the two types of absorbers according to the applied annealing treatment. Again, as in the drying temperature comparison, a Sulfur-Selenium mixed kesterite $Cu_2ZnSn(S_xSe_{1-x})_4$ can be identified. Furthermore, secondary phases, such as SnSe(S) or CuSe(S), were identified in both types of absorbers. Nevertheless, the evaluation of the peak intensity revealed a stronger presence of these secondary phases in the absorber annealed with the 2-step treatment. In addition, the 1-step annealed absorber exhibits a higher intensity for the peaks corresponding to $Cu_2ZnSnSe_4$, which is in good agreement with SEM results, where larger crystals were observed.
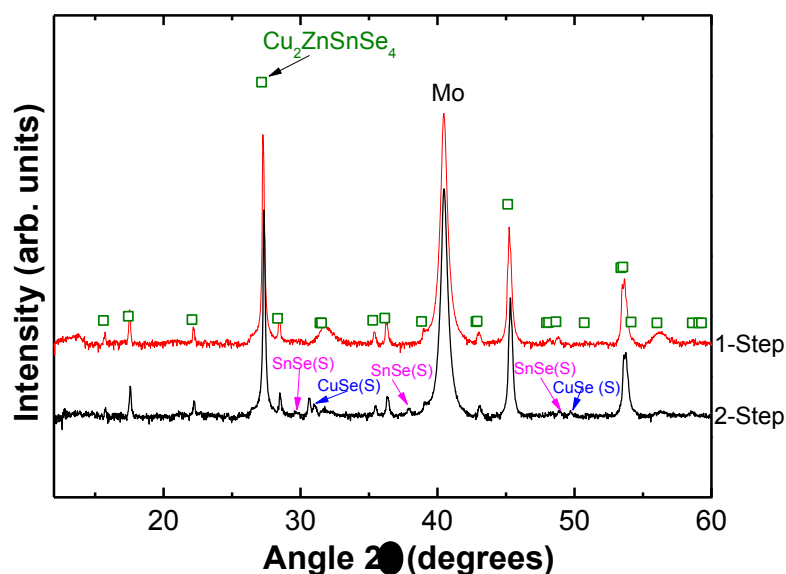
Fig. 23: XRD patterns of the solution B-absorbers carried out with the 1-step and the 2-step annealing treatment.

Despite the presence of non-crystallized areas in the one-step absorber, larger crystals, even if they are not completely distributed over the surface, could lead to better photovoltaic properties due to fewer grain boundaries. At least a part of the non-crystallized material may be organic material remaining from the solvent and the additive added to the solution to enhance its wettability. Similar organic layers, consisting basically of carbon and selenium, have been recently reported for CIGSSe absorbers synthetized from nanoparticle inks[30]. In such work, the fabricated solar cells exhibited 15% efficiency regardless of the presence of this organic fine-grain layer. However, the presence of residual carbon is always undesirable so modifications of the additive and solvent need to be explored to minimize it.

The two types of absorbers (1- and 2-step annealing) were used to finalize solar cells. Fig. 24 (a) shows the power conversion efficiency of the two types of fabricated cells. Although the efficiencies did not reach high values for any of the absorbers, it is noted that the 1-step annealing led to cells with a better electrical performance. The difference in efficiency can be probably related to the lower current resulting from the 2-step annealing treatment. Fig. 24 (b) shows that the 1-step cells exhibited an average short circuit current density of 22.5 mA/cm^2 while the 2-step treatment gives place to devices with 15 mA/cm^2. Hence, it can be deduced that the photogenerated current transport is more efficiently achieved when the absorber consists of larger crystals even if their distribution is not uniform over the complete surface.
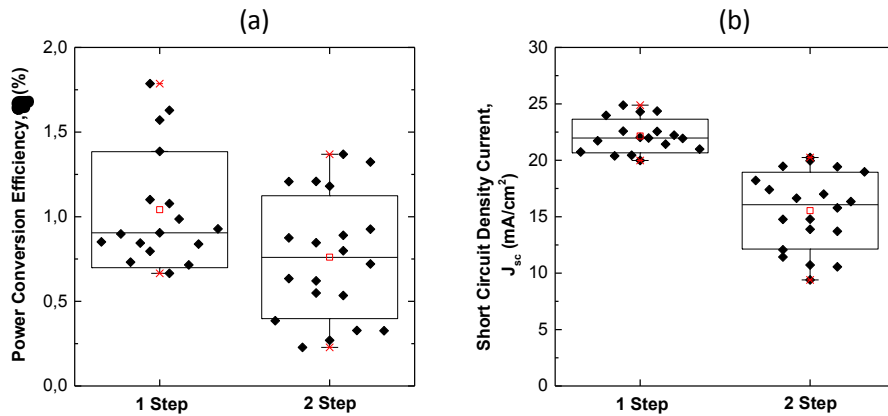
Fig. 24: (a) Power conversion efficiency and (b) Short circuit current density of devices fabricated with 1-step and 2-step annealing absorbers. Solution B-precursors of 600nm thickness.

Nevertheless, this non-uniformity might be the cause of the poor efficiency. In order to improve the electrical performance of the solar cells, the surface of the absorber should be completely crystallized. For that purpose, one strategy was explored in this investigation which consisted in the increase of the number of layers deposited by inkjet for the precursor formation. As expected, this also translates into an increase of the absorber thickness after the annealing treatment. According to previous results, a drying step at 280 °C between layers and a 1-step annealing treatment were applied to investigate the influence of the absorber thickness on the electrical response of the devices, on account of a more adequate absorber crystallization.

5.2.3.3- Precursor thickness influence on the solar cell performance.

In addition, the number of printed layers was also varied to analyze its influence on the photovoltaic response. It is known that an important issue for designing an efficient solar cell is that the electrons and holes generated in the absorber layer reach the electron collectors. This requires that the thickness of the absorber is thinner than the diffusion lengths of the charge carriers. But the absorber should be thick enough to maintain separated the carriers far from the depletion region of the p-n junction to block the electron pass in the opposite direction[31].

Fig. 25 shows the characteristic J-V curve of three solar cells whose CZTS precursor has been printed to form the absorber, using different numbers of printed layers to increase the thickness. Being more specifics, the number of layers is three, five and six layers corresponding to 600, 1150 and 1230 nm of crystallized absorber, respectively. It is clear how the first solar cell has a bad performance, very far from the ideal diode. Table 2 shows that the shunt resistance for this cell (a

measure of the difficulties found for the electrons to escape in an alternative path) is really low ($17.2 \ \Omega \cdot cm^2$) compared to the others two (74.4 and $174.4 \ \Omega \cdot cm^2$). This is the reason for the low FF and efficiency. It can be assumed that the thinness of the absorber allows some defects in which the molybdenum electrode is in contact with the n-layer directly and even that it is too thin making difficult the separation of the carrier pair generated by the photons, allowing the electron movement in both directions, recombining and avoiding the recollection in the electrode. This dreadful pair separation is evident in the low voltage in open circuit (200.5 mV compared to 360 mV for the double thickness).
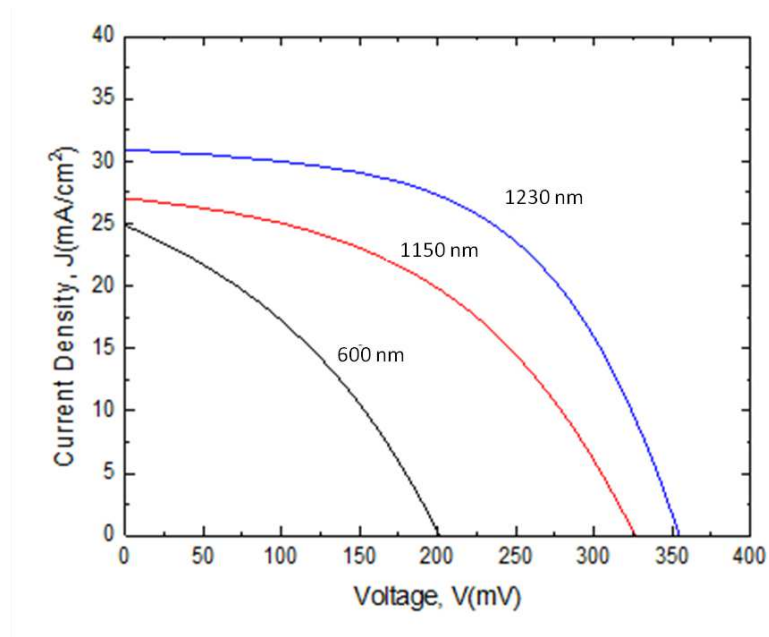
Fig. 25: J-V curve of the solar cell fabricated with the printed solution B-CZTS absorber with different thicknesses.

Precursor Thickness (nm)	J_{sc} (mA/cm^2)	V_{oc} (mV)	FF (%)	η (%)	R_{shunt} ($\Omega \cdot cm^2$)	R_{series} ($\Omega \cdot cm^2$)
600	24.4	200.5	36.6	1.8	17.2	2.1
1150	26.9	325.7	45.5	4.0	70.4	2.2
1230	29.8	362.9	54.3	5.9	174.4	1.5

Table 2: Optoelectronic parameters for the solar cell fabricated with printed solution B-absorber of different thicknesses.

In Fig. 26 the optoelectronic parameters are plotted versus the different absorber thicknesses. As it can be seen, an enhancement in the PV performance is achieved as the absorber thickness increases. Indeed, the open circuit voltage (V_{oc}) exhibited a significant improvement, which can be indicative, among others, of a better passivation of the interfaces. Cross-section images corresponding to each evaluated thickness are also included in Fig. 26. These images revealed that the increase of the thickness led to larger crystals. Nevertheless, a fine-grain structure is present even in the thickest absorber. The average conversion efficiency for the best group of cells resulted in about 5 % with 31 mA/cm^2 and 330 mV of short circuit current density and open circuit voltage respectively.
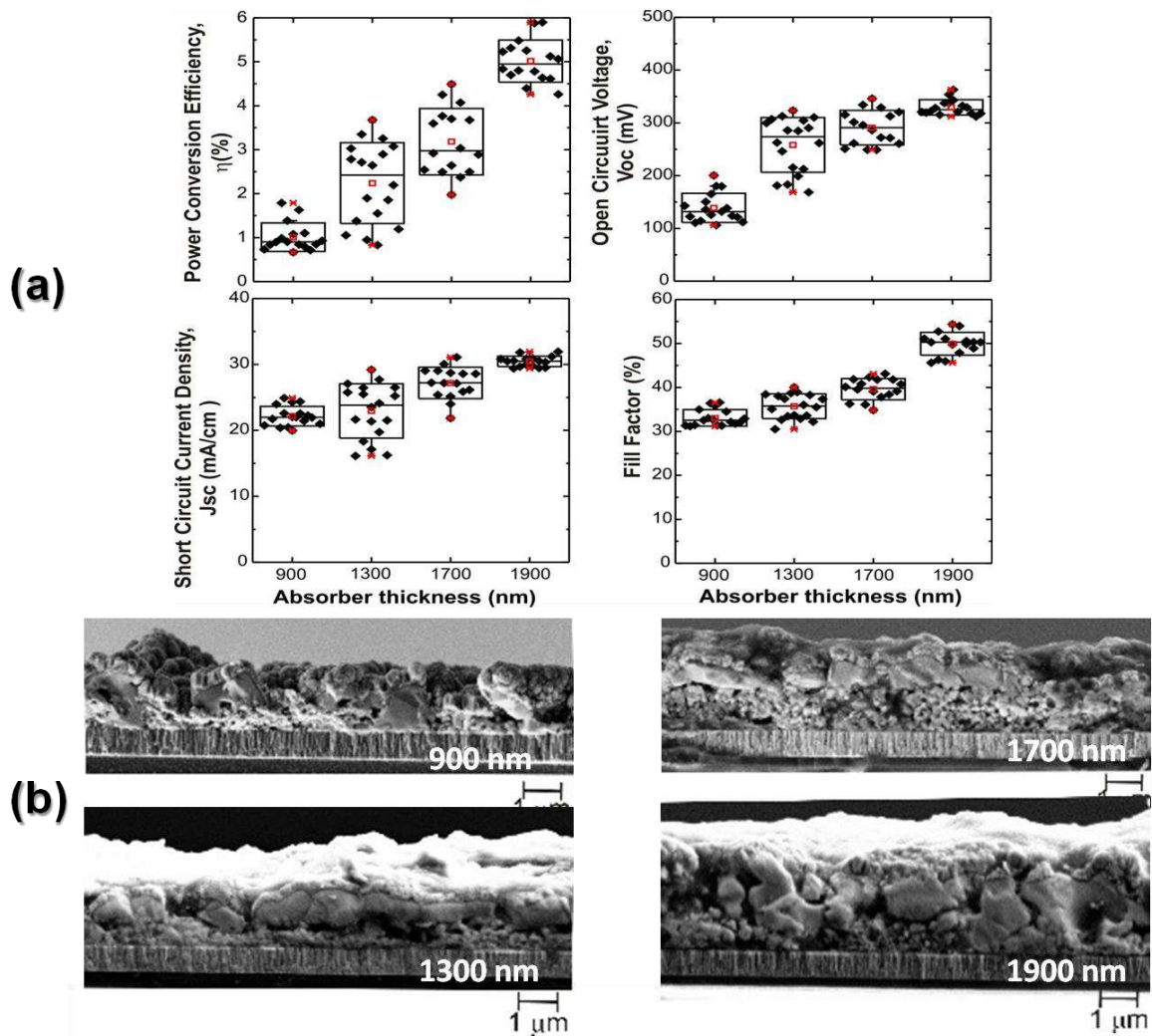
Fig. 26: (a) Optoelectronic parameters obtained from solar cell devices prepared from different absorber thicknesses and (b) cross-section images of the four absorbers.

The spectral response of the solar cell at different wavelengths allows the analysis of the photons contribution to the short-circuit current, indicating the efficiency of the charge carriers collection in the cell contacts. The quantum efficiency (QE) is defined as the ratio of electron-hole pairs generated and the incident photons; it is the device efficiency converting the incident photons into electron-hole pairs. Ideally, the QE curve has a square shape being constant over the measured solar spectrum (500 to 700 nm). However, in real solar cells, the QE is reduced for pair-carriers recombination effects.

The EQE is evaluated by regions: the first region is taken from 300 nm up to 450 nm (far ultraviolet) and corresponds to the performance of the front contact and buffer layer. The second region corresponds to the visible range of the spectrum (400 to 700 nm) and the EQE corresponds to the absorber performance. The last region of the EQE corresponds to the range from 700 to 1200 nm and it gives information about not only the absorber quality but also about the quality of the back reflector (optical properties of the rear contact) of the cell.
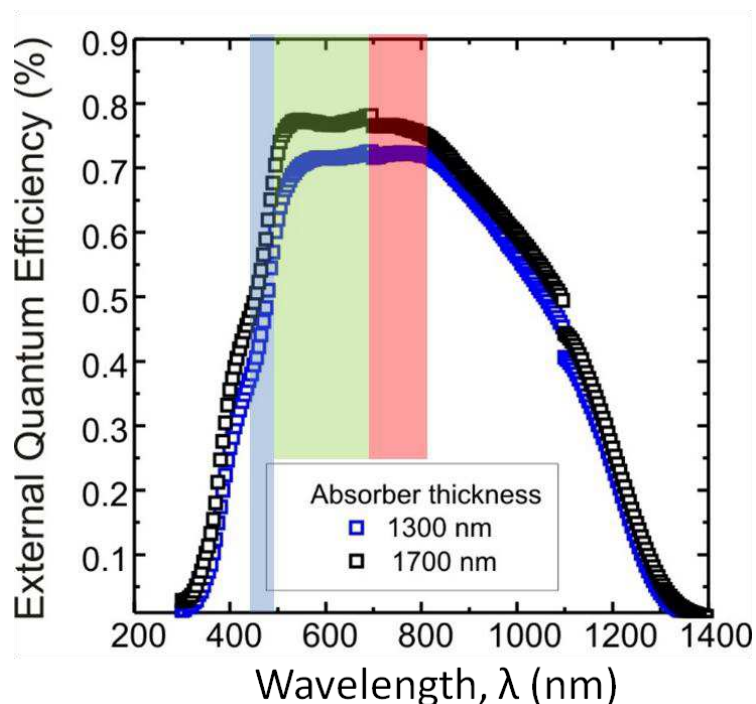
Fig. 27: External quantum efficiency vs. wavelength of two solar cells fabricated with the solution B-precursor of 1300 and 1700 nm of absorber thickness.

The reduction of the overall QE is caused by the reflection of the incident radiation and low diffusion length (Fig. 27). The blue-colored region response is reduced due to front surface recombination and buffer – absorber interface deficiencies. In the cells fabricated in this thesis, the response in these wavelengths should be the same; the slight differences are caused by experimental uncertainty. The red-colored region response is reduced due to rear surface

recombination and absorber-rear contact deficiencies. No light is absorbed bellow the band gap so the QE is zero at long wavelengths.

As expected, the quantum efficiency spectra is changed noticeably just in the efficiency of the absorber bulk. The improvement according to the thickness is quite evidence, increasing the quantum efficiency. It shows how the increase of the kesterite absorber does not lead to a higher grade of recombination, but a large zone of carrier-pairs generation.

Regarding the best individual cell result, a 0.09 cm^2 solar cell exhibiting 6.55% efficiency was achieved with the thickest absorber. Fig. 28 shows the dark and illuminated J(V) curves for this cell. Despite the clear deficit in V_{oc} (365.9mV), this device exhibits the best efficiency reported for solar cells fabricated by means of inkjet printing so far, neither even without metal grid nor antireflecting layer[15]. In addition, the absorber leading to the best cell was analyzed by X-ray fluorescence. These measurements revealed ratios of Cu/Zn+Sn and Zn/Sn of 0.85 and 1.03 respectively, which cannot be considered as completely included in the Cu-poor and Zn-rich phases. Indeed, further experiments are needed to find an optimized ink composition leading to the right phases. Furthermore, about 6 % of sulfur and 40 % of selenium were also measured by XRF. This sulfur-selenium composition resulted in a S/S+Se ratio of $x = 0.127$.
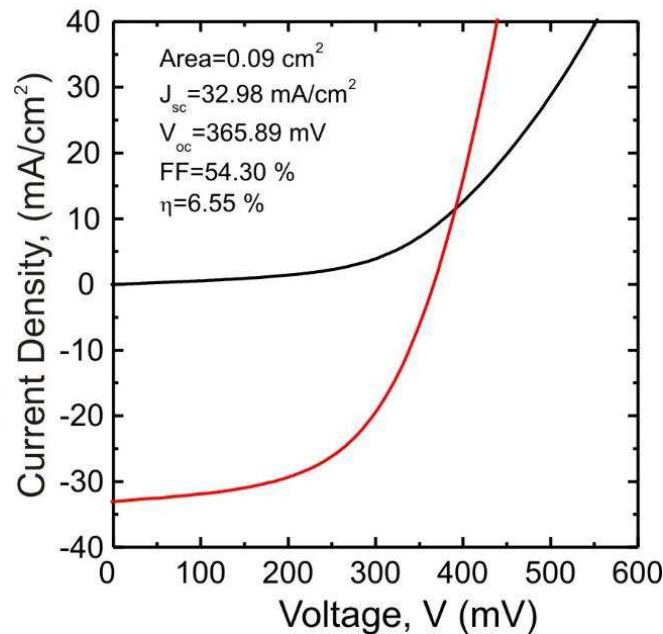
Fig. 28: J(V) curve for the best solar cell.

The energy band gap of $Cu_2ZnSn(S_xSe_{1-x})_4$ can be calculated by a Vegard's law[22]:

$$E_g(x) = x \cdot E_g(CZTS) + (1-x) \cdot E_g(CZTSe) - b \cdot x \cdot (1-x) \qquad [1]$$

where the bowing parameter b is assumed[22] as 0.1 eV. A band gap of 1.5 eV for CZTS and 0.96 eV for CZTSe can be also assumed[19,32] for the calculation of $E_g(x)$. Thus, a value of 1.02 eV for the absorber band gap was estimated from the above mentioned relationship for the best solar cell under study. Separately, a band gap value of 1.04 eV was estimated from the extrapolation of the quantum efficiency. Both values exhibit a good agreement; thus confirming the estimated percentage of sulfur obtained by XRF.

5.3- Conclusions

Inkjet printing was used to deposit the CZTS ink for the fabrication of kesterite solar cells. Two thermal processes involved in solar cell fabrication, drying in between inkjet printing layers and annealing for selenization, were studied in regards to the structural characteristics of the resulting absorbers and the electrical performance of the solar cells. In that sense, the highest drying temperature evaluated (280 °C) allowed a better crystallization of the absorber. In addition, a mixed sulfur-selenium kesterite phase was obtained regardless to the applied drying temperature. Moreover, 1- and 2-step Se reactive annealing treatments were investigated to optimize the solar cell electrical response. Larger crystals and less secondary phases were identified in the 1-step annealed absorber. After tuning the thermal processes, a variation of the number of printed layers was carried out. The thickest absorber gave place to the best inkjet CZT(S,Se) solar cell, which exhibited a 6.55% efficiency without metallic grid nor anti-reflective coating.

5.4- Future work

According to these results, next steps are quite clear. Cell performances obtained in here are quite promising, especially because there are few possible improvements that can be applied without many complications that might lead to best cell efficiencies and performances. The future steps are listed below:

(1) The absorber composition shows a deficit in Zn while best efficiencies are found in the Zn-rich zones. The ratios of Cu, Zn, Sn and S in the initial salt solution can be tuned in order to achieve the optimal structural ratios in the absorber formation and enhance the cell performance.

(2) The effect of the thiourea into the formation of secondary phases should be further studied and its content in the formulation optimized.

(3) These results have been yielded without the use of anti-reflective coating (ARC), that it is proved[33,34,35,36] to have positive effect in the cell efficiency due to the reduction in light reflection losses.

(4) Metallic grids are also helpful to improve the recollection of electrons and enhance the cell performance[37,38]. The incorporation of silver screen- or inkjet-printed grids could be an improvement in our cell.

(5) Alkaline doping is already known as a potential efficiency improvement[39,40,41]. Na or K salts can be added directly into the inkjet ink to enhance the cell performance in just one step.

(6) Search for an improvement in buffer-absorber interface.

Besides, we should consider the advantages of the direct printing of IP technology for the design of other parts of the solar cell, such as the transparent front contact or the silver metallic grid. Finally the possibility of printing individual solar cells properly arranged in serial or parallel becomes an interesting approach that should be considered.

References

[1] A. Slaoui, S. Bourdais, G.Beaucarne, J. Poortmans, S. Reber (2012), *Polycrystalline silicon solar cells on mullite substrates*, Solar Energy Materials & Solar Cells 71, 245.

[2] M. A. Green, K. Emery, Y. Hishikawa, W. Warta, E. D. Dunlop (2015), *Solar cell efficiency tables* (Version 45), Progress in Photovoltaics: Research and Applications 23, 1.

[3] P. Jackson, D. Hariskos, R. Wuerz, O. Kiowski, A. Bauer, T. M. Friedlmeier, M. Powalla (2014), *Properties of $Cu(In,Ga)Se_2$ solar cells with new record efficiencies up to 21.7%,* Physica status solidi - Rapid Research Letters 9 (1), 27.

[4] Fraunhofer Institute for Solar Energy Systems, ISE. *Photovoltaics report,* archieved on https://www.ise.fraunhofer.de/en/downloads-englisch/pdf-files-englisch/photovoltaics-report-slides.pdf (2015). Consulted on May 2016.

[5] I. Ketaro, Ed. (2015), *Copper zinc tin sulfide-based thin film solar cells*, John Wiley & Sons, Inc.

[6] I. L. Repins, M. J. Romero, J. V. Li, S.-H. Wei, D. Kuciauskas, C.-S. Jiang, C. Beall, C. DeHart, J. Mann, W.-C. Hsu, G. Teeter, A. Goodrich, R. Noufi (2013), *Kesterite successes, ongoing work, and challenges: A perspective from vacuum deposition*, IEEE Journal of Photovoltaics 3 (1), 439.

[7] D. B. Mitzi, O. Gunawan, T. K. Todorov, D. A. R. Barkhouse (2013), *Prospects and performance limitations for Cu − Zn − Sn − S − Se photovoltaic*, Philosophical Transsactions of the Royal Society A 371, 20110432.

[8] S. Siebentritt, S. Schorr (2012), *Kesterites-a challenging material for solar cells*, Progress in Photovoltaics: Research and Applications 20 (5), 512.

[9] W. Wang, M. T. Winkler, O. Gunawan, T. Gokmen, T. K. Todorov, Y. Zhu, D. B. Mitzi (2014), *Device characteristics of CZTSSe thin-film solar cells with 12.6% efficiency*, Advanced Energy Materials 4 (7).

[10] H. Azimi, Y. Hou, C. J. Brabec (2014), *Towards low-cost, environmentally friendly printed chalcopyrite and kesterite solar cells*, Energy Environmental Science 7 (6), 1829.

[11] H. Xin, J. K. Katahara, I. L. Braly, H. W. Hillhouse (2014), *8% Efficient $Cu_2ZnSn(S,Se)_4$ solar cells from redox equilibrated simple precursors in DMSO*, Advanced Energy Materials 4 (11), 1301823.

[12] T. Schnabel, M. Löw, E. Ahlswede (2013), *Vacuum-free preparation of 7.5% efficient $Cu_2ZnSn(S,Se)_4$ solar cells based on metal salt precursors*, Solar Energy Materials and Solar Cells 117, 324.

[13] M. Werner, D. Keller, S. G. Haass, C. Gretener, B. Bissig, P. Fuchs, F. La Mattina, R. Erni, Y. E. Romanyuk, A. N. Tiwari (2015), *Enhanced carrier collection from CdS passivated grains in solution-processed $Cu_2ZnSn(S,Se)_4$ solar cells*, ACS Applied Materials and Interfaces 7 (22), 12141.

[14] Q. Guo, G. M. Ford, W.-C. Yang, C. J. Hages, H. W. Hillhouse, R. Agrawal (2012), *Enhancing the performance of CZTSSe solar cells with Ge alloying*, Solar Energy Materials and Solar Cells 105, 132.

[15] X. Lin, J. Kavalakkatt, M. C. Lux-Steiner, A. Ennaoui (2015), *Inkjet-printed $Cu_2ZnSn(S,Se)_4$ solar cells*, Advanced Science 2 (6), 1500028.

[16] S.-N. Park, S.-J. Sung, J.-H. Sim, K.-J. Yang, D.-K. Hwang, J. H. Kim, G. Y. Kim, W. Jo, D.-H. Kim, J.-K. Kang (2015), *Nanostructured p-type CZTS thin films prepared by a facile solution process for 3D p–n junction solar cell,* Nanoscale 7, 11182.

[17] C. M. Sutter-Fella (2014), *Solution-processed kesterite absorbers for thin film solar cells*, PhD Dissertation, ETH-Zürich, Switzerland.

[18] Catalonia Institute for Energy Research, available on http://www.irec.cat/ consulted on May 2016.

[19] H. Xie, Y. Sanchez, S. Lopez-Marino, M. Espindola-Rodriguez, M. Neuschitzer, D. Sylla, A. Fairbrother, V. Izquierdo-Roca, A. Perez-Rodriguez, E. Saucedo (2014), *Impact of Sn (S, Se) secondary phases in $Cu_2ZnSn(S,Se)_4$ solar cells: a chemical route for their selective removal and absorber surface passivation*, ACS Applied Materials and Interfaces 4 (6), 12744.

[20] S. Lopez-Marino, Y. Sanchez, M. Placidi, A. Fairbrother, M. Espindola-Rodriguez, X. Fontane, V. Izquierdo-Roca, J. Lopez-Garcia, L. Calvo-Barrio, A. Perez-Rodriguez, E. Saucedo (2013), *ZnSe etching of Zn-rich $Cu_2ZnSnSe_4$: an oxidation route for improved solar-cell efficiency*, Chemistry-A European Journal 19 (44) 14814.

[21] S. Chen, X. G. Gong, A. Walsh and S.-H. Wei (2009), *Crystal and electronic band structure of Cu_2ZnSnX_4 (X=S and Se) photovoltaic absorbers: First-principles insights*, Applied Physics Letters, 94, 041903.

[22] S. Chen, A. Walsh, J.-H. Yang, X. G. Gong, L. Sun, P.-X. Yang, J.-H. Chu, S.-H. Wei (2011), *Compositional dependence of structural and electronic properties of $Cu_2ZnSn(S,Se)_4$ alloys for thin film solar cells*, Physical Review B 83 (12), 125201.

[23] D. B. Mitzi, O. Gunawan, T. K. Todorov, K. Wang and S. Guha (2011), *The path towards a high-performance solution-processed kesterite solar cell*, Solar Energy Materials and Solar Cells, 95, 1421.

[24] C. Persson (2010), *Electronic and optical properties of Cu_2ZnSnS_4 and $Cu_2ZnSnSe_4$*, Journal of Applied Physics, 107, 053710.

[25] S. Chen, A. Walsh, X.-G. Gong, S.-H. Wei (2013), *Classification of lattice defects in the kesterite Cu_2ZnSnS_4 and $Cu_2ZnSnSe_4$ earth-abundant solar cell absorbers,* Advanced Materials 25 (11), 1522.

[26] S. Giraldo, M. Neuschitzer, T. Thersleff, S. López-Marino, Y. Sánchez, H. Xie, M. Colina, M. Placidi, P. Pistor, V. Izquierdo-Roca, K. Leifer, A. Pérez-Rodríguez, E. Saucedo (2015), *Large efficiency improvement in $Cu_2ZnSnSe_4$ solar cells by introducing a superficial Ge nanolayer,* Advanced Energy Materials 5 (21), 1501070.

[27] H. Katagiri, K. Jimbo, W.S. Maw, K. Oishi, M. Yamazaki, H. Araki, A. Takeuchi (2009), *Development of CZTS-based thin film solar cells,* Thin Solid Films 517, 2455.

[28] H. Wang (2011), *Progress in Thin Film Solar Cells Based on Cu_2ZnSnS_4*, International Journal of Photoenergy 2011, 801292.

[29] S. Wang, Q. Gao, J. Wang (2005), *Thermodynamic analysis of decomposition of thiourea and thiourea oxides*, Journal of Physical Chemistry B 109 (36), 17281.

[30] S. M. McLeod, C. J. Hages, N. J. Carter, R. Agrawal (2015), *Synthesis and characterization of 15% efficient CIGSSe solar cells from nanoparticle inks*, Progress in Photovoltaics: Research and Applications 23 (11), 1550.

[31] Solar Cell Operational Principles from TU Delft OpenCourseWare

[32] W. Ki, H. W. Hillhouse (2011), *Earth-abundant element photovoltaics directly from soluble precursors with high yield using a non-toxic solvent*, Advanced Energy Materials 1 (5), 732.

[33] Barbara Swatowska, Tomasz Stapinski, Kazimierz Drabczyk, Piotr Panek (2011), *The role of antireflective coatings in silicon solar cells – the influence on their electrical parameters,* Optica Applicata 41 (2), 487.

[34] G. Wakefield, M. Adair, M. Gardener, D. Greiner, C. A. Kaufmann, J. Moghal (2015), *Mesoporous silica nanocomposite antireflective coating for Cu(In,Ga)Se$_2$ thin film solar cells,* Solar Energy Materials and Solar Cells 134, 359.

[35] P. M. Kaminski, F. Lisco, J. M. Walls (2014), *Multilayer broadband antireflective coatings for more efficient thin film CdTe solar cells,* IEEE Journal of Photovoltaics 4 (1), 452.

[36] S.-Y. Kuo, M.-Y. Hsieh (2014), *Efficiency enhancement in Cu$_2$ZnSnS$_4$ solar cells with subwavelength grating nanostructures,* Nanoscale 6, 7553.

[37] I. Burgues-Ceballos, N. kehagias, C. M. Sotomayor-Torres, M. Campoy-Quiles, P. D. Lacharmoise (2014), *Embedded inkjet printed silver grids for ITO-free organic solar cells with high fill factor*, Solar Energy Materials and Solar Cells 127, 50.

[38] J.-S. Yu, I. Kim, J.-S. Kim, J. Jo, T. T. Larsen-Olsen, R. R. Sondergaard, M. Hösel, D. Angmo, M. Jorgesen, F. C. Krebs (2012), *Silver front electrode grids for ITO-free all printed polymer solar cells with embedded and raised topographies, prepared by thermal imprint, flexographic and inkjet roll-to-roll processes,* Nanoscale 4, 603.

[39] S. Lopez-Marino, Y. Sanchez, M. Espindola-Rodriguez, X. Alcobe, H. Xie, M. Neuschitzer, I. Becerril, S. Giraldo, M. Dimitrievska, M. Placidi, L. Fourdrinier, V. Izquierdo-Roca, A. Perez-Rodriguez, E. Saucedo (2016), *Alkali doping strategies for flexible and light-weight Cu$_2$ZnSnSe$_4$ solar cells*, Journal of Material Chemistry A, 4, 1895.

[40] Z. Tong, C. Yan, Z. Su, F. Zeng, J. Yang, Y- Li, L. Jiang, Y. Lai, F. Liu (2014*), Effects of potassium doping on solution processed kesterite Cu2ZnSnS4 thin film solar cells,* Applied Physics Letters 105, 223903.

[41] Z.-Y. Zhao, X. Zhao (2014), *First-principles study on doping effects of sodium in kesterite Cu$_2$ZnSnS$_4$,* Inorganic Chemistry 53 (17), 9235.

Chapter 6

Development of spiral inductors for radiofrequency applications

6.1- Introduction

Customization and tuning are keywords in the design of nowadays electronic circuits and systems. Combining both features is not an easy task. On one hand, full-custom design can be accomplished using a single integration technology but at expenses of mass production and null tunable capabilities. On the other hand, almost full-tunable designs can be performed by interconnecting lumped components on a Printed Circuit Board (PCB) but at expenses of poor reliability and small series production. In between these two extremes, Low Temperature Co-fired Ceramic technology (LTCC) combines the reliability of a clean-room integration process with the versatility of a PCB implementation. Passive components can be embedded into the LTCC substrate, screen printed on it or soldered, together with active counterparts, as surface mounted devices (SMD)[1]. Roughly, the number of soldered components enhance the tuning capabilities but at the expense of the reliability. Among passive components inductors and transformers can be embedded very easily into the LTCC substrate or screen-printed on it, increasing reliability. In the RF frequency bands from tens of MHZ to few GHz, the size and performance of these magnetic components are comparable to those of their SMD counterparts. However, a set of mask is required to implement LTCC inductors and transformers leading to less tuning capabilities and unavoidable waste of printing material. In this framework, the objective of this work is to improve the tuning capabilities of LTCC technology applied to the design of RF circuits and systems without degrading its reliability. To achieve this goal, critical inductors will be implemented as a post-processing step on the LTCC substrate by using Inkjet printing and electroless growth. Inkjet printing allows tuning without degrading accuracy and reliability. Electroless growth, allows thick metal fabrication to achieve high inductor performance.

Hence, the aim of this chapter is the comparison of the screen- and inkjet- technology applied to the radio frequency field; most precisely, it aims to demonstrate the potential of Inkjet printing combined with electroless growth to implement high performance RF inductors on standard LTCC substrates. Enhanced customization and tuning are the main advantage of this technological combination in front of standard low temperature co-fired ceramic technology with screen-printing as the printing technique.

Inkjet printing for the fabrication of the inductors has been done in the University of Barcelona. LTCC substrates, screen printing and electroless deposition has been carried out in Francisco Albero S.A.U. (FAE) facilities. RF inductors were designed and measured by the Research Group of Radiofrequency of Prof. Dr. J.M. López-Villegas of the Engineering Department: Electronics of the University of Barcelona.

6.1.1- Inductance and quality factor

The inductor is a passive component that adds inductance (L) to the circuit, what means that stores energy in a magnetic field as long as an electrical current flows through it. All circuits have, in practice, some inductance, which may have beneficial or detrimental effects. For a tuned circuit, inductance is used to provide a frequency-selective circuit. Practical inductors may be used to provide filtering, or energy storage, in a given network.

Inductance is a measure of the amount of energy that can be stored in the magnetic field created by the inductor and depends on the electrical characteristics of the conductors, the area and length occupied by it.

The quality factor (Q) of an inductor is a figure of merit for the quality of the component. It is the ratio of the energy stored in electromagnetic fields and the energy dissipated during one cycle, and it is a measure of its efficiency. The higher the Q-factor of the inductor, the closer the behavior to an ideal and lossless inductor. It can be expressed as the ratio of its inductive reactance to its resistance at a given frequency

$$Q = \frac{\omega \cdot L}{R} = \frac{2 \cdot \pi \cdot f \cdot L}{R} \qquad [1]$$

where L is the inductance, R is the inductor's effective series resistance, ω is the radian operating frequency, and the product $\omega \cdot L$ is the inductive reactance. The inductor's series resistance converts electric current through the coils into heat, thus causing a loss of inductive quality.

Physical phenomena affecting the inductor performance

At high frequencies, particularly radio frequencies (RF), inductors have higher resistance and others losses in their performances. Series resistance arises from the metal resistivity in the inductor and it is closely related to the quality factor. As such, the series resistance is a key issue for inductor modeling. When the inductor operates at high frequencies, the metal line suffers from the skin and proximity effects, and series resistance becomes a function of frequency[2]. Thus, the main physical phenomena affecting the performance of inductors are both, skin[3,4] and proximity effect[5], which reduce the effective cross-sectional area of the conducting current, increasing the series resistance and reducing the current[6,7]. These effects become more serious in very thin conductor lines as those ones printed by means of inkjet and where the current is strongly hindered. Also, the dielectric losses and parasitic capacitance due to the adjacent turns, which commonly are at slightly different potential, play to the detriment of the ideal performance.

Design parameters affecting the Q-factor

An inductor is based on a conductor track rolled in a spiral on a planar substrate. The geometric parameters that define an inductor are inner diameter (d_{in}) and outer diameter (d_{out}), the track width (w), the spacing between adjacent conductor tracks (s) and the number of turns (N). Fig. 1 shows the layout of inductors of different shapes, pointing out these parameters.

(a)   (b)   (c)
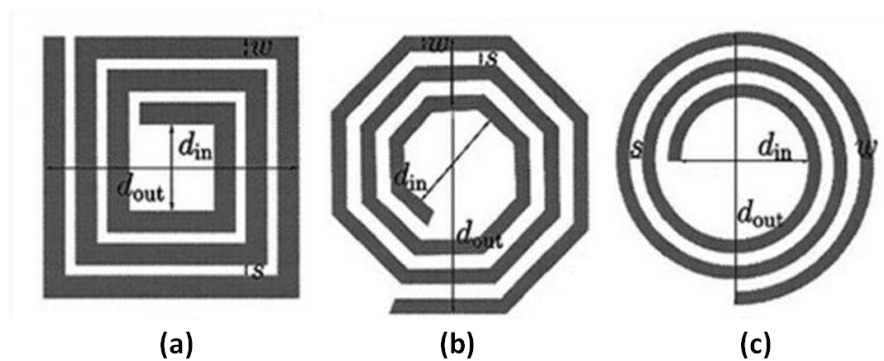
Fig. 1: Examples of layout of planar inductors where the geometric parameters are showed for different shapes, from (a) rectangular to (d) circular inductors.

Linewidth and thickness are two parameters which are closely related; both are variables really important in the inductor design and affect similarly to the Q-factor. Wider and thicker lines increase the cross-section of the inductor and hence, reduce the DC resistance and this fact goes on benefits to the Q-factor. However, wider lines also increase the parasitic capacitance due to the eddy currents and here comes the limitation in increasing the linewidth. As it can be expected, wide spacing between turns leads to smaller parasitic capacitance and hence, better Q-factor. It also gives place to larger areas and so, larger inductance. Each parameter, which has an effect increasing the inductor area, such as larger diameters, wider lines or spacing or higher number of turns, has also an effect increasing the inductance.

In the case of the number of turns, it generates higher magnetic fields for a given amount of current[8], but also higher parasitic capacitances as well. The RF resistance increases due to the Eddy current and parasitic capacitance, and hence, the maximum Q-factor point decreases with the increase of number of turns[9]. Nevertheless, increasing the number of turns improves Q-factor due to the exponentially increase of the inductance while the resistance varies linearly with the turns; and the same happens with the diameter. So, the inkjet-printing technology, which is a more precise and capable of reducing the line width, gives the possibility of enlarging the number of turns within the same area due to its higher resolution. The enhancement of small inductors performances becomes feasible, as long as the thickness lack could be solved.

6.1.2- Geometrical design and material considerations

There is an increasing demand in the area of radio frequency applications to use cost effective planar inductors and to make integrated circuits smaller. This implies reducing the size of the elements used in the design. Inductors are usually larger than any other element used in communication circuits. Spiral type planar inductors are widely used in the design of power amplifiers, oscillators, microwave switches, combiners, and splitters, etc. for ISM applications at the HF range.

Circular inductors

Traditionally, spiral inductors are made in square shape due to its ease of design and support from drawing tools[10]. However, the most optimum pattern is a circular spiral because it suffers less resistive and capacitive losses.

Both square and circular spiral inductors are being used in RF and microwave integrated circuits. It has been reported that the circular geometry exhibits better quality factors than square ones[11] at the expenses of a slight increase in the occupied area; circular configuration shows about 15% - 20% higher Q-factor and self-resonance frequency values than the square configuration[12,13].

The fact that circular inductors are not so widely used is because they consist in a more complex pattern than polygonal and only a few commercial layout tools support such a pattern. Hexagonal and octagonal structures have been used as alternatives, as they resemble closely to the circular structure. It has been reported that the series resistance of the octagonal and circular shaped inductors is 10% smaller than that of a square shaped spiral inductor with the same inductance value[14].

In this thesis, the circular shape has been chosen due to better inductor performances and considering the capabilities of both, screen- and inkjet- printing, to reproduce such as shapes (Fig. 2).
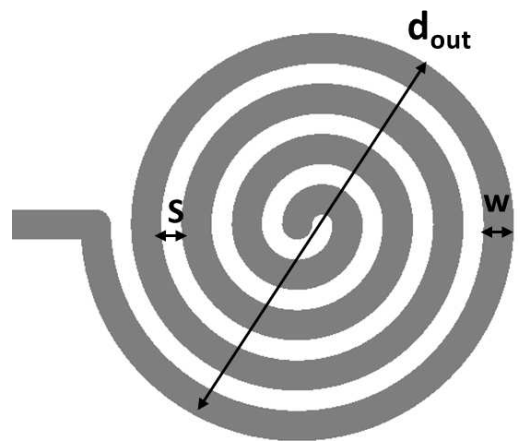
Fig. 2: The circular inductor designed for this thesis where the inner diameter is not considered.

LTCC technology in RF applications

Since the introduction of Si spiral inductors[15], many authors have reported higher performance inductors on Si substrates[16,17]. However, a major drawback of Si technology is its proneness to high RF losses in the semiconducting substrate[18,19] inducing Eddy currents. This is an important; limiting factor in the implementation of high-quality passive inductors, vital for the design of RF filters and oscillators. Also, in the world of integrated circuits (ICs), on-chip inductors are something to be avoided because integrated inductors consume valuable die area and

traditionally have very low Q-factor due to thin metal traces and substrate-induced losses[20,21]. One solution to this problem is to move the inductors off-chip, using low-temperature co-fired ceramic (LTCC). LTCC is often preferred for high performance applications, as an IC can be directly mounted on it while passive components and interconnects can be embedded on any number of layers. Traditionally, inductors in LTCC have taken the form of printed spiral traces of moderate thickness, and can, hypothetically, be of any size[22]. Hence, the Q-factor of LTCC inductors can exceed that in radio frequency ICs. More important is that LTCC components are free of the I^2R losses caused by currents in the semiconductor substrate that degrade the performance of on-chip components so strongly[23].

6.1.2- Electroless deposition as a complementary technique for inkjet printing in RF applications

Inkjet printing, although turning out to be a suitable technology to enhance the accuracy of narrow tracks and to increase the number of turns within a concrete area, presents difficulties to achieve a certain value in thickness due to the deposition of very thin conductor layers. This fact suggests the need to overcome the relatively lower electrical conductivity of the inkjet printed circuitry[24]. Very high conductivities, close to those of the bulk metals, are achieved using inkjet printing technique but the profile of printed structures, which are thinner than a micron, increases their resistance[25]. In addition, the minimization of high-frequency losses is found for a layer thickness in the order of the skin depth, what means the thickness in which the majority of the current is concentrated. The effect of conductive layer thickness has been previously studied, for example in a patch-antenna[25] where it is maintained that the thickness of metals should be around the skin depth or in a monopole[26] which indicates thickness of several skin depths. Nevertheless, the adequate DC conductivity does not necessary result in good high-frequency performance, as the printing resolution, quality and also the roughness can affect the high-frequency losses[27]. Depending on the frequency and the conductivity, several printed layers may be required for the corresponding thickness[28,29,30] but this fact brings about the need of higher sintering energy, increase in process time and dimensional inaccuracy of printing multiple stacked tracks[24]. In ref. 24 they tried to minimize this time-consuming multiple layers re-printing just in critical areas. Nevertheless, a more efficiency method to increase in thickness is the widespread electroless; a low-cost technology for the production of metal deposits that it is also easily scalable, highly selective, high purity and does not require vacuum or excessively high working temperature.

Electrochemical model

Electroless plating is an auto-catalytic chemical technique used to deposit a layer of a metal on a surface. In the electroless process, unlike the electrodeposition where the metal cation is reduced applying a current density, the metal cation reduction occurs by electrochemical reaction on the surface of an activated substrate in presence of a reducing agent. This implies that both oxidation and reduction reactions must take place in the localized solution-substrate interface. In addition, the activated substrate acts as a catalyst to initiate the deposition of the electroless metal, then the electroless metal deposit itself functions as a continuously renewed autocatalytic film and the process of electroless deposition continues until it is removed from the solution.

The electrochemical model to understand the electroless process is known as Mixed-Potential Theory (MPT) introduced by Wagner and Traud[31] and it have been verified in various corrosion processes[32,33]. The mixed potential theory consists of two simple hypotheses; (a) any electrochemical reaction can be divided into two or more partial oxidation and reduction reactions and (b) there can be no net accumulation of electric charge during an electrochemical reaction or in other word, it is a restatement of the law of conservation of charge. That is, a metal immersed in an electrolyte cannot spontaneously accumulate electric charge, what means the total rate of reduction must equal the total rate of oxidation.

Generically, the overall reaction that occurs in the electroless process can be expressed as it follows:

$$M^{z+}_{solution} + Red_{solution} \xrightarrow{catalytic\ surface} M_{Metal} + Ox_{solution}$$

[2]
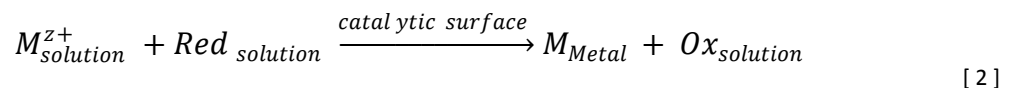
Being the reduction reaction:

$$M^{z+}_{solution} + ze \xrightarrow{catalytic\ surface} M_{metal}$$

[3]

And the oxidation one:

$$Red_{solution} \xrightarrow{catalytic\ surface} Ox_{solution} + ze$$

[4]
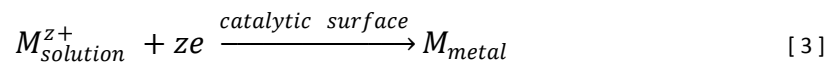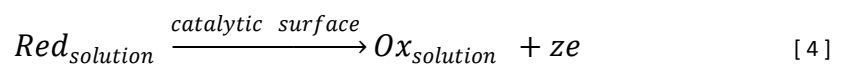
The process speed, in the simplest case, depends on the concentrations of reducing agent and metal ion, although there are cases where the limiting step of the half-reactions is the diffusion of the reagent, determining the overall speed to the speed of the half reaction.

The complexity of electroless resides primarily in the substrate activation process and the chemistry of the bath. In the solution, apart from the presence of the metal ion and the reductant, the presence of others chemical species can be necessary to carry out the deposition in a controlled and effective way. For example, complexing agents prevent hydroxides, oxides or different metal salts from precipitating, and promote the adsorption of the metal ion on the catalyst surface. Furthermore, the system should be maintained at a pH range determined in order not to modify the electrochemical equilibrium potential of the electroactive species and thus, prevent the electrochemical reaction from occurring uncontrollably within the bath.

In relation to the final properties of the deposited metal, such as morphology, electrical resistance, purity, mechanical properties, adhesion or corrosion resistance depend mostly on the intrinsic properties of the deposited material, although factors related to the deposition process and the composition of the solution, temperature, velocity, catalytic activity chosen for the activation process and hydrogen adsorption materials are also a useful tool for modulating and modifying the properties of the deposit depending on the desired application.

Substrate activation: Palladium-doped silver ink as activator seed

In any electroless process is crucial the activation step. The classic solution used for the activation of substrates is the incorporation of palladium on the surface; the more consolidated way in the industry is the combination of Pd and Sn [34]. In general, the activation step is considered the stage with the largest impact in production costs within the electroless process.

Electroless copper deposition is widely used in commercial printed circuit board industries, using palladium as activator. A palladium chloride solution has been printed by some authors as catalyst seed for copper in HF applications [28] and also nanoparticles of vinyl acetate/Pd [35]. Furthermore, silver can also serve as an activator for copper electroless plating reaction as a replacement for the conventional $SnCl_2$, $PdCl_2$, or Pd colloid activator. Silver inkjet inks have been already validated as a suitable seeds for copper electroless [36,37].

Nevertheless, copper presents high degree of corrosion and it is for this reason that a nickel electroless was also tested in this thesis to be followed by a gold deposition that is able to prevent the conductor tracks from corrosion. In addition, this finishing treatment improves connection reliability between the printed circuit boards and the electronic component [38]. The issue found was that even if nickel electroless is commonly used on copper pattern [39], it needs a strong

activation on Cu surface and it is still undergoing modification and improvement. While there has been some commercial testing of copper and nickel based catalysts, none have yet matched the versatility and cost-effectiveness of palladium catalysts[34]. Copper does not have a catalytic action for the oxidation of hypophosphite[40], the most widely used reducing agent for Ni electroless.

During this thesis, the silver ink was doped by palladium nanoparticles to be able to (a) activate the silver surface for Ni electroless (avoiding the Cu layer and removing one step) and (b) achieve the most propitious conditions for the Cu deposition, improving its deposition rate.

6.2- Design

A set of inductors has been designed to be fabricated by the two proposed technologies to compare their equivalent inductance and their quality factors as a function of frequency. RF inductors were designed by RF-group of Prof. J.M. López-Villegas of the Engineering Department: Electronics of the University of Barcelona and fabricated in this thesis at the laboratories of FAE and MIND-group also at the Engineering Department.

For the standard LTCC technology using screen printing, spirals with a linewidth of 300 μm and 200 μm of distance between turns has been designed changing the number of turns to N= 4, 6 and 8 corresponding to outer diameters of 4.40, 6.40, 8.40 mm. To approach to the resolution limit of standard screen-printing spirals of 150 μm separated by 100 μm are designed too, occupying the same area of the previous set.

In the case of screen-printing, the designs are made by draftsight (Fig. 3) and the image is exactly reproduced in the screen. In the case of inkjet printing, the circular spiral design is drawn in a pixel layout. A pixel corresponds to a drop ejected by the printer. Setting the drop spacing in a preliminary study of the ink to a 23 μm (~1118 DPI), the spirals are drawn taking into account the equivalent of 1 pixel = 23 μm.

The geometrical dimensions (i.e. turn width and turn spacing) were reproduced maintaining the number of turns and the outer diameter from screen-printing designs to inkjet printing ones. The wider spiral is drawn by 11 pixels line and separation of 6 pixels. The thinner spiral, with a line of 1 pixel leaving a space of 4 pixels in between.

Furthermore, thinner linewidth has been reproduced by inkjet to increase the number of turns within the same area. As it was shown before in chapter 2, there are zones or drawing with a certain tendency to accumulate ink and it reduces the resolution. This drawback has been

overcome by the removal of pixels in the problematic area (Fig. 4). Similar solutions in crossing designs have been implemented before[41].

The spirals drawn for inkjet will be printed directly onto the sintered substrate to achieve better resolution.
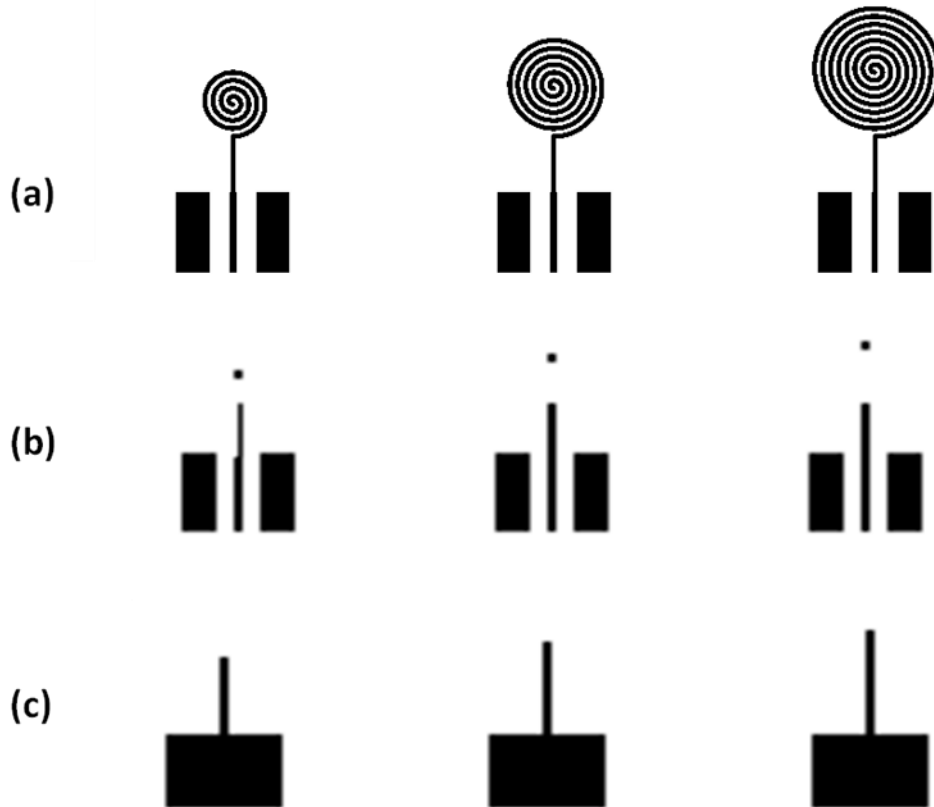
Fig. 3: Layout of the set designed by draftsight for screen printing.(a) Top side of the reference spiral inductors fabricated using standard LTCC technology plus screen-printing, (b) Base substrate: Pads, back ground and via but circular spiral omitted to be printed later by inkjet plus electroless and (c) bottom side showing ground connection.

Fig. 4: Layout of a semi-spiral drawn for the inkjet printing process. On the left, the 11-pxl spiral and, on the right, the 1-pxl spiral. The number of pixels (drops) is reduced in those zones of ink accumulation.

6.3- Spiral inductors fabrication

The whole set of samples has been prepared using LTCC as the base technology (Fig. 5). In our case eight layers of green ceramic are stacked and laminated to form a 3D structure of low temperature sintering. The substrate is made by mixing ceramic and glass powders of specific composition, and small quantities of binding agent and solvent to create homogeneous slurry. In this thesis, the LTCC powder was provided by Heraeus with reference 51528B. The slurry was formulated in FAE company and then, cast to form sheets of uniform thickness (about 200 µm in our case) of green LTCC. Once dried, these green sheets can be easily cut and processed to fabricate the sintered substrate.
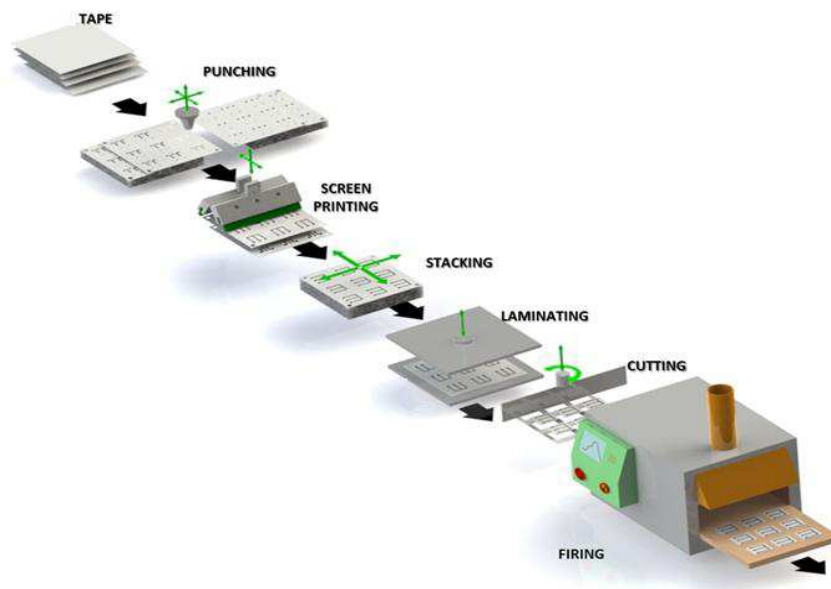
Fig. 5: LTCC multilayer technology steps[42].

Prior to the stacking, metallic parts are defined as shown in Fig. 3 using screen-printing of a silver paste specially formulated for the co-sintering with the ceramic substrate (TC7303-Ag provided by Heraeus). Back metallization is accomplished using the same procedure.

The vertical connections between metal layers for the electrical feedthroughs are brought about by 150 µm punched via, which are filled with a viscous silver paste (CN33-493 from Ferro). Furthermore and due to the selected connector, two square cavities are punched in both sides of the pads to align easily a removable connector. These cavities are made by the overlapping of punching with a 1x1 mm square puncher (Fig. 6).
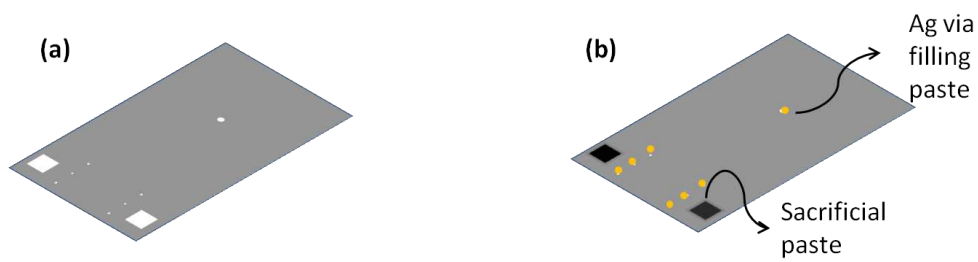
Fig. 6: Cavities and vias for (a) after punching step (b) after via filing and stacking process.

Once the top metallization is printed, eight green ceramic sheets are stacked in order. The first layer is the one with the top spiral printed on it, then the rest of punched layers with the filled vies and cavities to give the specific thickness to the sintered device (1 mm). It is during the stacking process that the cavities are filled by a sacrificial paste made by a polymeric vehicle which burns at lower temperature than that one when the LTCC sintering starts, but it prevents the cavities deformation during the manipulation and the different fabrication steps.

The stacked substrate is again printed on the bottom sheet for the ground connection. After drying the silver printing, the whole structure is laminated at 5000 psi for 30 min in an isostatic laminator. After that, the devices are split by an automatic cutter machine.
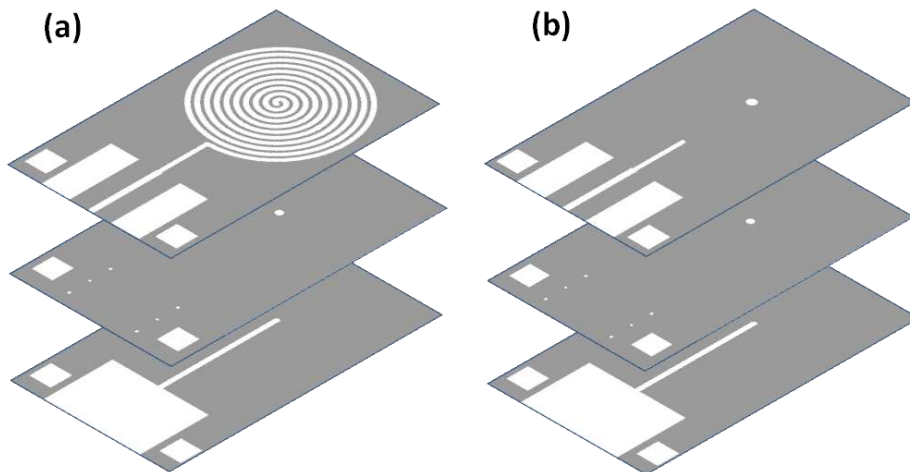
Fig. 7: Structure of the LTCC substrates where the layer in the middle is repeated as long as the desired thickness is achieved. (a) represents the planar spirals by screen printing (b) is the base substrate layer used for the inkjet printed devices.

The free sintering process of the LTCC is made in a furnace. The temperature is increasing slowly, at a rate of 2 ⁰C/min to burn the organics before the sintering and then the temperature is hold

during 2 h at 870 °C. For the free sintering process, none direction is constrained during the firing and sintering process and hence, the substrate suffers from shrinkage, than in the case of our LTCC material is 14% in both, X and Y direction.

6.3.1- Screen printed inductors

The first subset of samples (reference samples) has been fabricated using the standard LTCC process described above. Different compact spirals of circular shape have been printed on the top surface. The external termination of the spiral has been connected to the measurement pads and a central via has been used to connect the internal termination to the back ground metallization. Fig. 8 shows an example of the obtained inductors. On the left, the front view of three spiral inductors of 4, 6 and 8 turn, respectively. On the right there is a back view of the structure showing the back ground connection. In all the cases, there are the two cavities of 2x2 mm^2 to align the removable SMA connector used to the electromagnetic characterization.
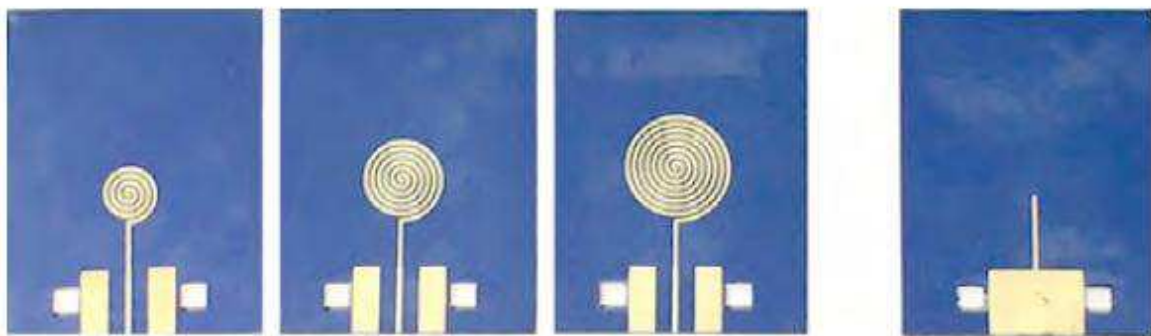
Fig. 8: Reference spiral inductors fabricated using standard LTCC technology. On the left, front view of 4, 6 and 8 turns inductors. On the right, back view showing the ground connection.

The mesh selected for the screen was 400 mesh of stainless steel to reach a good resolution for those spirals of 150 μm. The parameters used for the well-defined spiral lines were fixed in 6 Kg of pressure, a gap of 1.5 mm and a squeegee velocity of 60 mm/s to obtain a good reproducibility of the defined design (Fig. 9).
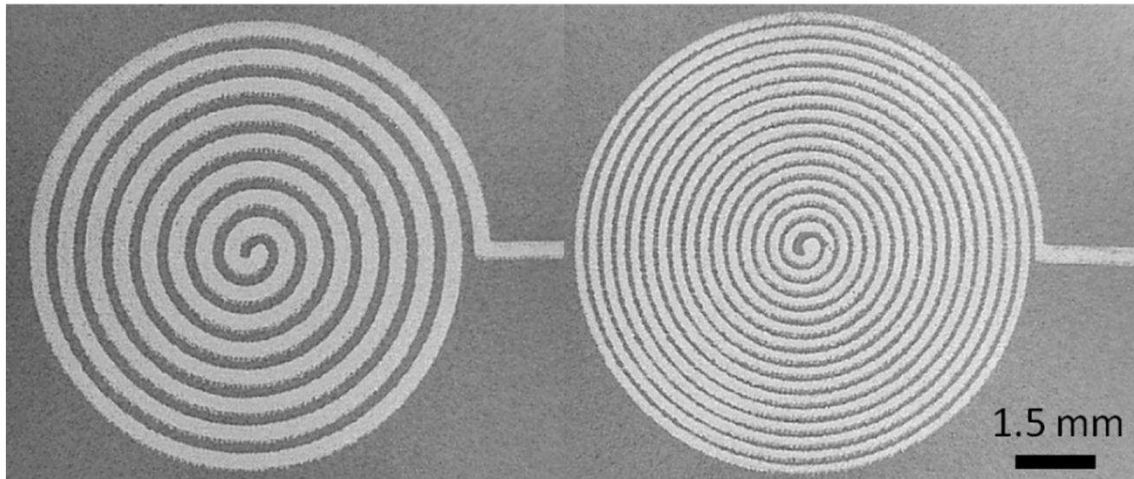
Fig. 9: Images of screen-printed inductor of 8 turns before sintering of 300 and 150 μm of linewidth respectively.

6.3.2- Inkjet-printed + electroless inductors

Inkjet printing

Aiming to compare just the spirals performance, the preconfigured LTCC substrates fabricated as explained in Fig. 3 (b) are used. Pads, back ground and via are implemented as previously but omitting the top spiral. The spirals are directly printed by inkjet on the sintered LTCC substrate (Fig. 10) and the geometrical dimensions (turn width and turn spacing) are reproduced maintaining the number of turns and the outer diameter.
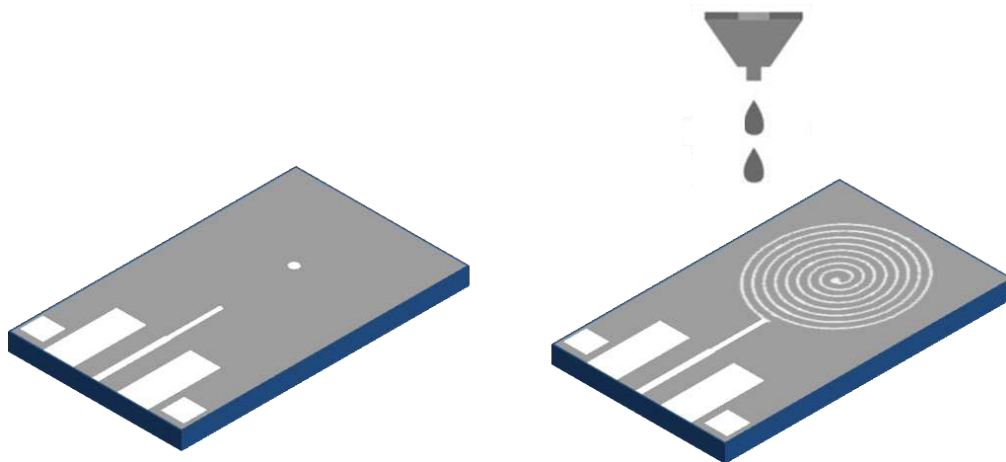
Fig. 10: Spiral printed by inkjet printing onto the sintered LTCC substrate with the screen printed pads on it.

Until this last step, the fabrication process of this second subset of samples is the same that the one of the reference ones.

The inkjet inductors are printed with the Ag-V03 ink formulated before in chapter 2. This ink was used both, doped using Pd in catalytic amount to perform the best conditions for the electroless activation and without doping.

The Ag-V03/Pd ink is introduced in a Dimatix cartridge of nozzles of 10 pl. The voltage is set to obtain drops of 700 mm/s and the firing frequency is maintained to 5 kHz. The drop spacing was fixed to 28 µm for the spiral with wider lines and 23 µm for the thinner lines to promote the coalescence between the drops to achieve continuous lines but being in a compromise with the prevention of high amounts of ink that can short-circuit the spiral. The temperature of the nozzles was set at 40 ^{o}C and the temperature of the substrate at 60 ^{o}C. The meniscus pressure was 4.5 mmH$_2$O and the printhead height 250 µm.

For those spirals reproducing wider lines, the design is totally achieved by inkjet printing (Fig. 11), but for those spirals whose linewidth is adjusted to the limit resolution of the system, ink accumulation is promoted on the top side of the substrate. That limits the resolution itself.
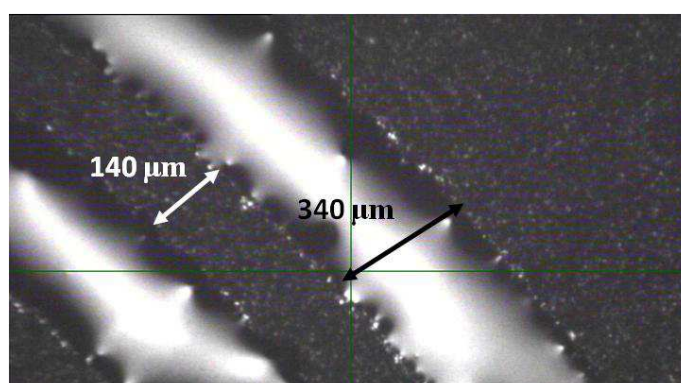
Fig. 11: Dimatix image of the lines of 11 pixels at a drop spacing of 28 µm.

Even if the substrate temperature induces the drying before the coalescence between the drops on top side, this fact is not fast enough to completely prevent it. Thus, the final solution came after removing some pixels in those zones where the ink accumulates during the printing. As it is shown in the design section, the pattern design is modified until optimized the printed spiral. Fig. 12 clarifies the influence of the selected pattern model.
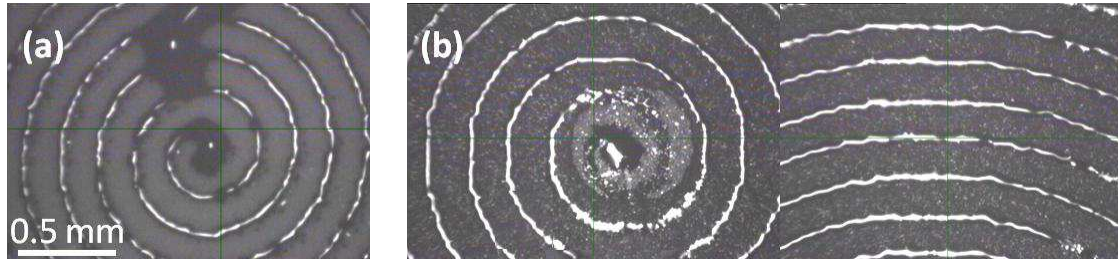
Fig. 12: Dimatix images taken of the wet printing (a) using the pattern without optimization at room temperature and (b) using the optimized pattern – removed pixels in risky zones.

So, on top of the spiral some pixels are removed to avoid the ink accumulation and the short-circuit. Once the spiral is printed, the silver tracks are sintered at 225 °C for 10 min. Fig. 13 shows a device fabricated by this procedure.
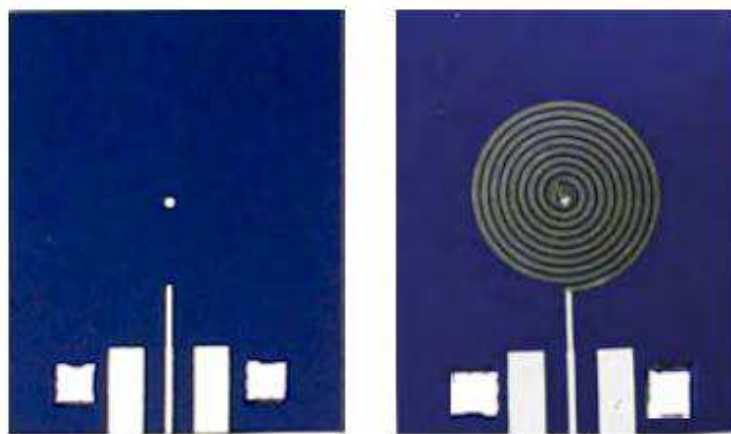
Fig. 13: Example of a substrate (a) before and (b) after the inkjet-printed spiral.

Electroless deposition

As it was said before, the thickness of the inkjet silver is well below the skin depth of common metals in the RF frequency range, becoming a current limiting factor. Electroless deposition is then a good candidate to overcome the high sheet resistance of the inkjet printed tracks. For this reason, two metall electroless deposition has been tested in this thesis.

Electroless copper deposition:

The electroless bath is formulated as follows: copper (II) sulfate pentahydrate solution (0.0315 M $CuSO_4 \cdot 5H_2O$) with formaldehyde (0.167 M CH_2O) as reducing agent[43]. EDTA is used as the complexing agent to prevent the precipitation in the solution. The pH is maintained to 12.5 by

adding sodium hydroxide (NaOH). The plating temperature was 60 °C and 2, 2'-dipyridyl was served as a brightener and surfactant, respectively, to improve the quality of the copper layer.

Every 1h a 0.25% in volume of formaldehyde is added to replace the quantity used and/or evaporated.

To prevent premature copper degradation, the inductors are immersed in a commercial antitarnish bath (METEX M667 from MacDermid) for 2 min.

Electroless nickel deposition:

The formulation of the bath used in this thesis is composed by nickel sulphate (0.1 M $NiSO_4 \cdot 6H_2O$) as nickel source in solution with sodium hypophosphite (0.35 M NaH_2PO_2) as reducing agent. The pH is adjusted to 5.5 with ammonia. The nickel solution contains a 10% of phosphor. The temperature is maintained to 95°C.

Gold flashing:

The gold flashing was previously expained in chapter 4. This chemical bath consists in a galvanic replacement of the very last layer of the metal surface by gold. The aim of this bath is the corrosion protection.

First route: Ag inkjet+ Cu+Ni+Au

In the first case, the silver ink V03 without any modification is used for defining the spiral. Then, the copper deposition is followed by a nickel electroless and finished by a gold flash alredy used in Chapter 4 (Fig. 14). Copper is the best candidate to growth for its high and similar conductivity to silver, as well as the possibility to used silver inkjet ink directly as seeds. However, this sequence aims to protect the copper surface from corrosion. In addition, nickel can contribute improving the mechanical properties and affording easier soldability; but especially, it can serve as the seed to the gold deposition. Gold flash directly on copper is possible but it has no sense due to the gold difussion into the copper, leaving the surface unprotected.
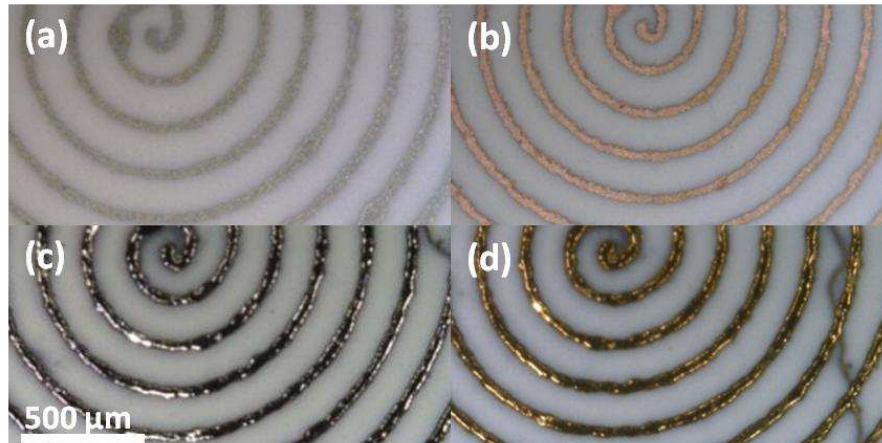
Fig. 14: Images of a spiral printed on LTCC with the silver ink Ag-V03 formulated in Chapter 2. (a) Silver ink Ag-V03, (b) Cu electroless on Ag-V03, (c) Ni electroless on Cu, (d) Au flashing on Ni.

Two issues were found in this electroless combination that makes this solution unfeasible. First, Ni reduction is not activated in a controlled way in the copper surface. This is because the hypophosphite does not oxidize in copper presence[40] and this problem is illustrated in Fig. 15 (a). Apart from the activation issue, copper electroless on smooth inkjet-printed silver surface does not reach a significant deposition rate. Fig. 15 (b) shows a growth of about 0.5 µm in 2h of immersion in Cu electroless bath whereas Ni layer grew 12 µm in just 0.5 h when the proper activation is achieved. This fact points out the possibility of using Ni deposition, not just for the advantages that provides as an intermediate layer for gold finishing, but for the significant deposition rate and increase in thickness in comparison to Cu.
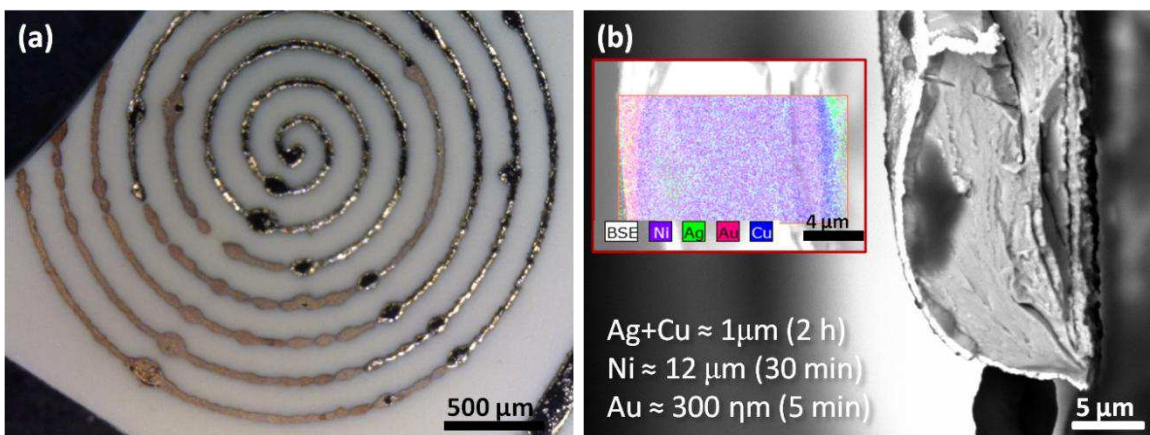
Fig. 15: (a) Ni electroless on previously deposited Cu by electroless presenting a bad activation where part of the uncovered Cu surface is left. (b) SEM image and EDS mapping of the cross-section of a spiral line after 2h immersed in Cu electroless bath, 30 min of Ni electroless and 5 min of gold flashing.

Afterwards these results, two options are considered trying to be competitive with the screen-printing option:

1. The uncontrolled activation of Ni deposition onto Cu lines makes interesting the idea of managing the growth without the Cu layer. Hence, activating the Ni reduction directly into the inkjet-printed tracks leads to the need of doping the silver ink with small quantities of palladium (second route).

2. The Pd doped silver ink is used as seed for Cu deposition too, trying to make faster the deposition rate (third route).

Second route: Ag/Pd inkjet + Ni+ Au

In the literature, a direct Ni deposition by means of electroless onto the silver tracks has been reported[44] although there is no information about the activation step, if needed. To ensure about the proper activation of the silver surface, palladium catalyst is used to initiate the Ni reduction reaction. The activation pre-treatment is skipped by adding the Pd catalyst directly into the inkjet ink. The same formulation as the silver ink called Ag-V03 in chapter 2 of this thesis is used for this purpose but being doped with less than 0.5 % in weight of palladium black from Sigma-Aldrich. Previously to the addition of Ag nanoparticles, the equivalent to 0.5% in weight of Pd black was dispersed in the vehicle of the ink. Different dispersants were tested to get a proper homogeneity. Finally, PVP of Mw=10.000 provided by Sigma Aldrich was used in a concentration of 0.25% in weight in relation to the Pd black. The solution was immersed in ultrasounds during 30 min, and then filtered by a 0.45 μm filter. Some amount of Pd is lost during the filtration step, so less than the 0.5% in weight is added in relation to Ag concentration. Once the palladium is dispersed in the solvent, silver nanoparticles are added.

In Fig. 16 shows the inkjet printed spiral made of the silver AgV03/Pd after the Ni deposition and Au finishing. As it is seen in Fig. 16 (b), the nickel layer grows significantly on the catalyzed silver lines leading to a 16 μm layer in just 30 min.
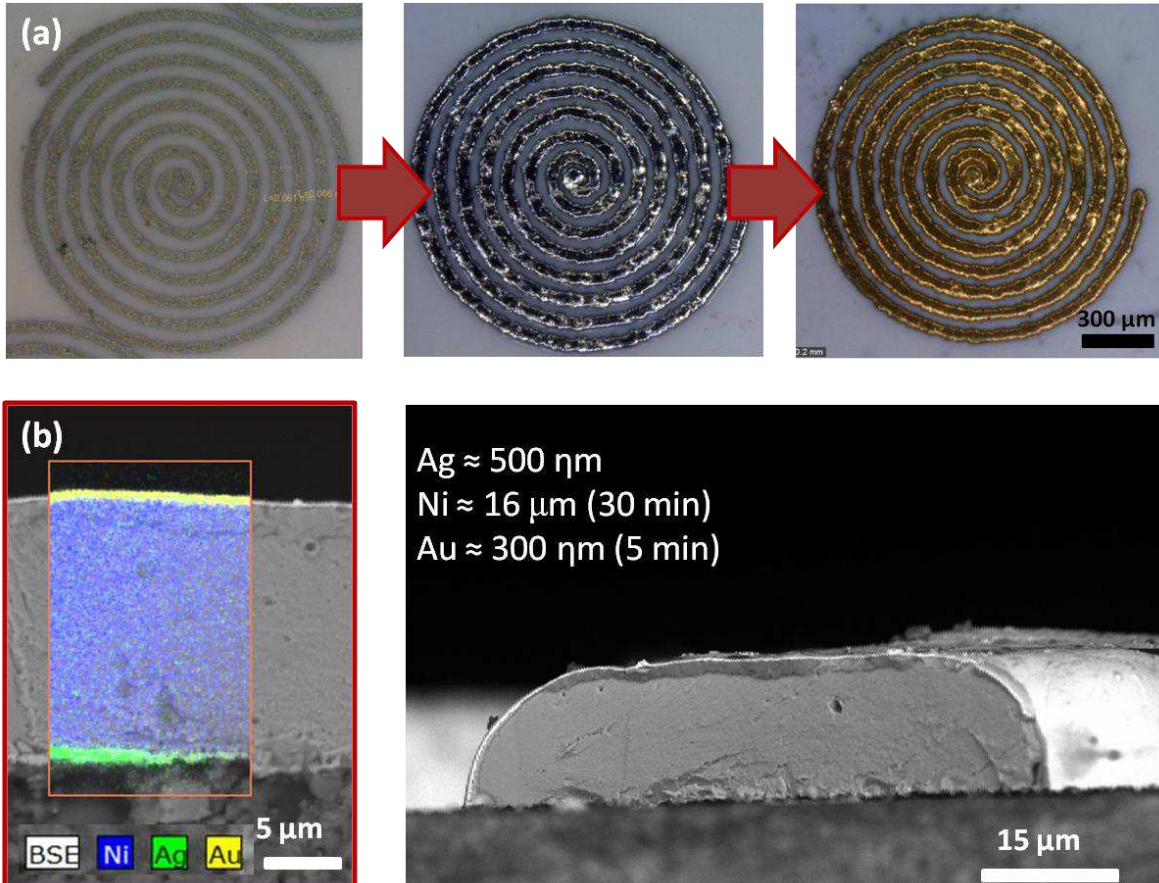
Fig. 16: Inkjet-printed spiral line after 30 min immersed in Ni electroless bath and 5 min in Au flashing bath. (a) Top view image of the spiral after the three steps, silver printed, Ni deposition by electroless and Au finishing, (b) EDS and SEM image of the cross-section of the printed spiral line.

After these results, spiral inductors were fabricated. 40 min of immersion in the Ni bath was done and just 5 min for the gold flashing.

Third route: Ag/Pd + Cu (+ antitarnish)

Low copper deposition rate showed in the first route leads to use the palladium doped silver formulated for catalyzing the nickel reduction. In this case, the deposition rate significantly increased from barely 0.01 µm/min to 0.04 µm/min as average rate in the whole process of 2.5 h. Fig. 17 shows the growth of copper layer onto the Pd/Ag inkjet lines.
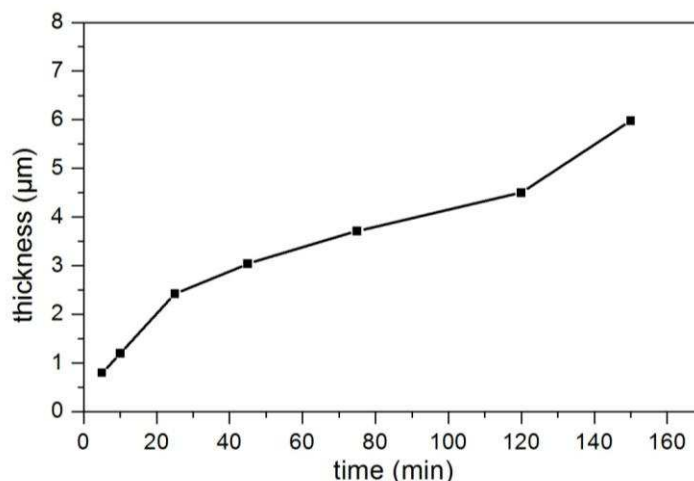
Fig. 17: Deposit thickness in function of immersion time in the electroless Cu bath.

Even if the literature proclaims silver as better reductant for formaldehyde than palladium[45], the better catalytic effect of Pd in our case can be understood as the effect of Pd nanoparticles that are not sintered as the silver and it can serve as catalytic centers where the reaction happens quicker and promotes a faster coalescence of the copper grains.

6.4- Inductors characterization

6.4.1- Material and geometrical characterization

In the case of RF devices, the material properties and the geometrical dimension become crucial.

The substrate, common in both cases, shows a relative permittivity for frequencies up to 15 GHz and equal to 7.2 ± 0.2. The loss tangent is below $5 \cdot 10^{-4}$ for the entire frequency range.

In the case of the screen-printed samples, the metal thickness is 9 µm, leading to a sheet resistance of 2 mΩ/□. The reference samples used for the comparison with Cu deposition on Ag/Pd showed 300 µm of linewidth spaced by 200 µm (Fig. 18). A set of inductors of 4, 6 and 8 turns are fabricated, obtaining outer diameters of 3.75, 5.5 and 7.30 mm, respectively. The samples approaching the resolution limit of the screen printing showed dimensions of 155 µm of linewidth and 90 µm of spacing between the turns.
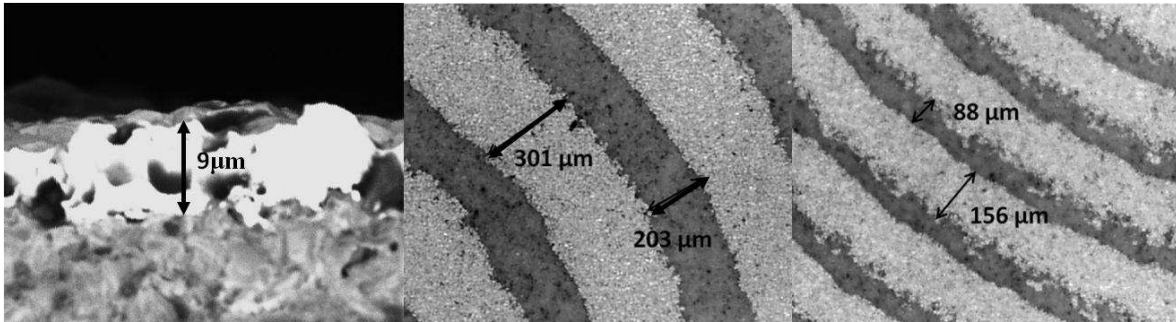
Fig. 18: SEM images and measurement for a references samples fabricated by screen-printing technique.

For inkjet printing in combination of electroless inductors, the geometrical dimensions were reproduced maintaining the number of turns and the outer diameter. Turns width was fixed to 340 µm separated by 140 µm (Fig. 11).
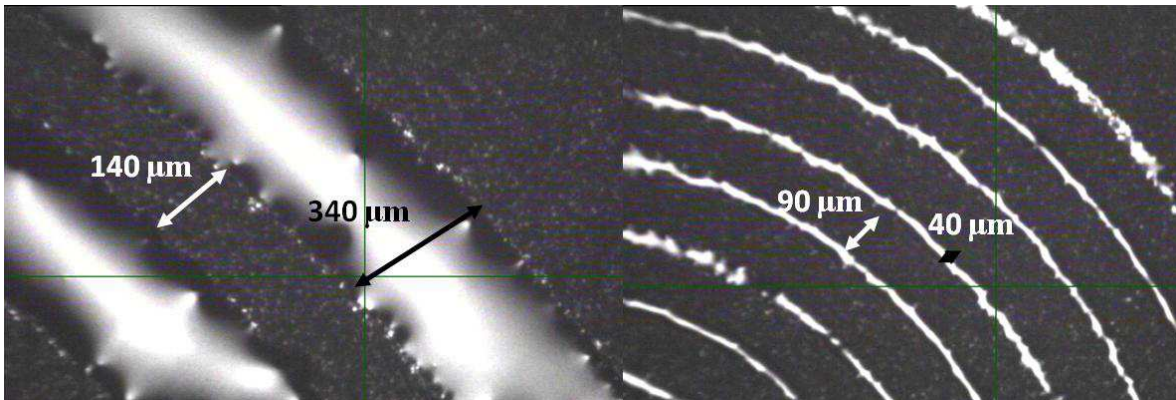
Fig. 19: Dimatix images of the inkjet printed spirals of lines reproducing reference samples dimensions and approaching resolution limit.

The spirals approaching to resolution limit of inkjet was immersed during 40 min in the Ni bath explained before, following the second route (Fig. 20). About 20 µm thick is obtained, leading to a resistance of 37 Ω, when comparing with 9 µm of screen-printed silver shows to be one order of magnitude higher. Obviously this is because of the much higher electrical resistivity of nickel.
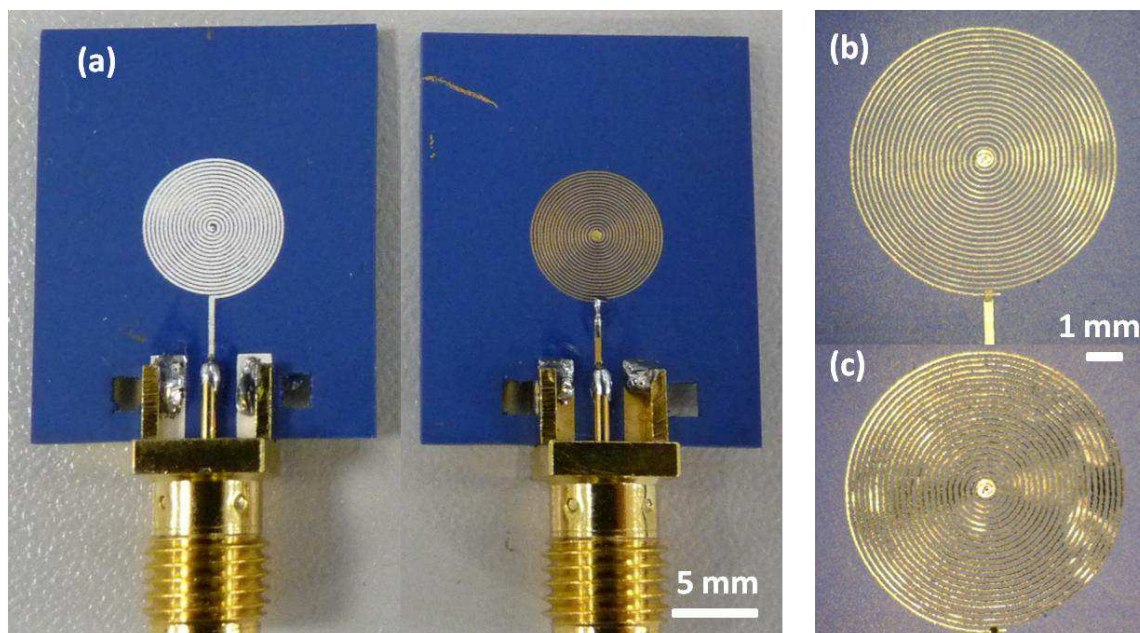
Fig. 20: (a) Screen- (left) and Inkjet- printed spiral using Ni electroless and gold finishing (right), both at the standard resolution of each technology, (b) Inkjet spiral printed with Ag-V03/Pd and (c) spiral after the Ni growth and gold protection.

Longer time was left immersed in the Ni bath but then, cracks appears in the very thick Ni, leading to electrical discontinuities (Fig. 21), rejecting this second route as a competitive solution.
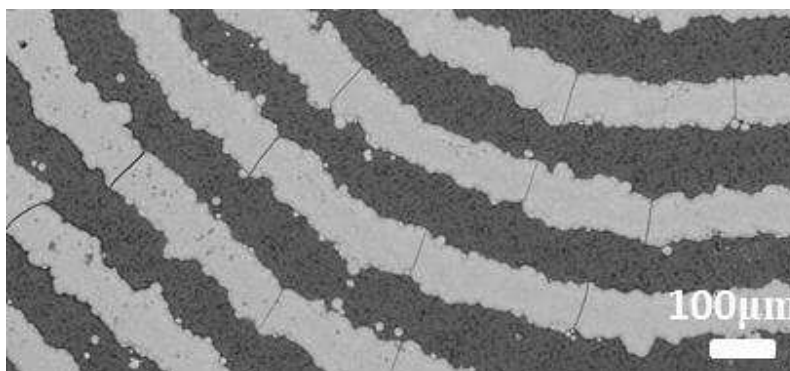
Fig. 21: Cracks appearance in the Ni lines after 1 h of Ni immersion.

Following the third route, wider inkjet spirals were immersed in the Cu bath. After 2.5 h, the Cu deposited reached 6 µm thickness deposition and a lateral overgrowth that leaded to final dimension of 350 µm separated by 130 µm (Fig. 22). The copper layer has a sheet resistance equal to 3 mΩ/□.
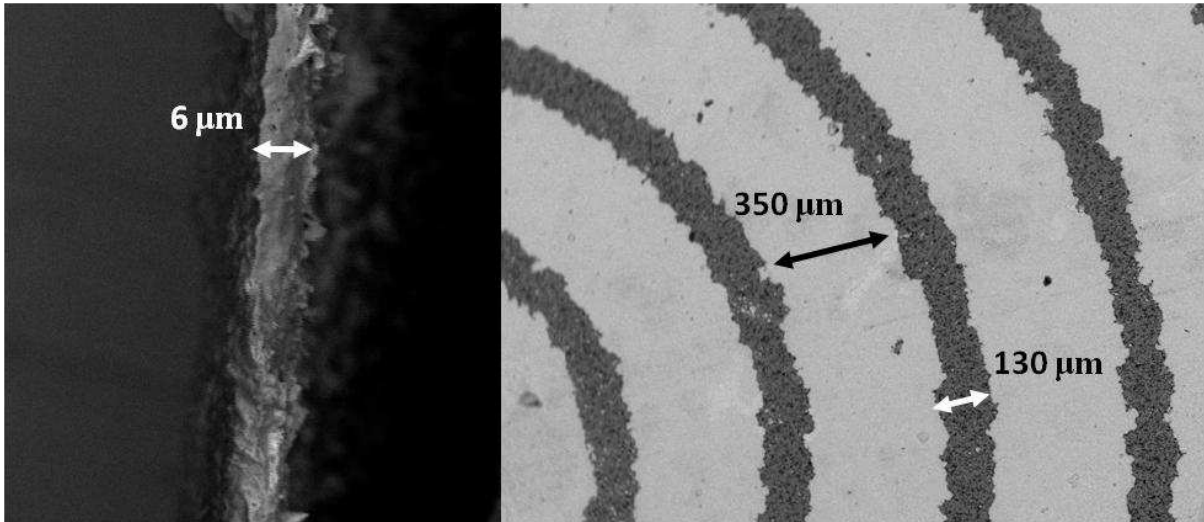
Fig. 22: SEM images and dimension measurement for the inductors fabricated by Inkjet printing in combination with 2.5 h of Cu electroless.

These final dimensions and sheet resistance made these spirals perfectly comparable to the screen-printed ones. Fig. 23 shows inductors fabricated following this third route.
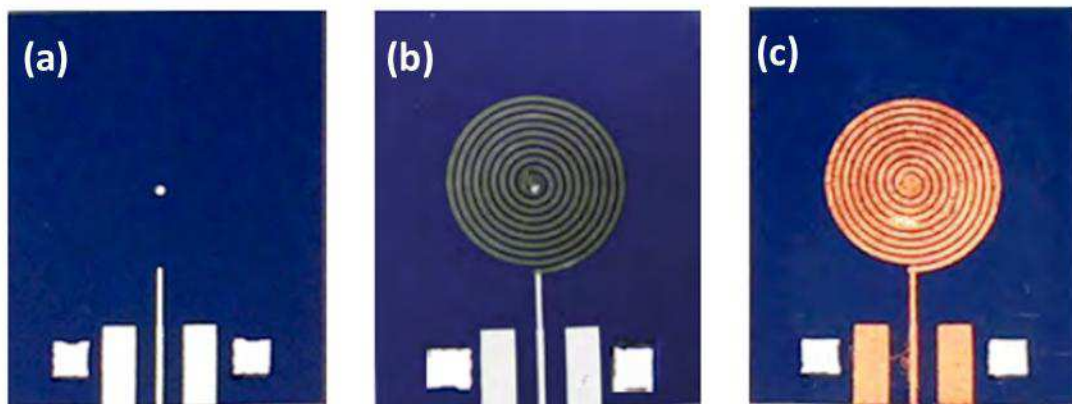
Fig. 23: Example of spiral inductor fabricated using LTCC technology combined with inkjet printing and electroless growth: (a) Base LTCC substrate, (b) Spiral obtained by inkjet printing of Silver doped with palladium and (c) final inductor structure obtained after electroless deposition of copper on the silver seed.

According to these results, it can be conclude that the second route (Ag/Pd+Ni+Au) has been implemented accomplishing the technological requirements, achieving a reproducible and fast electroless deposition but that this combination is not suitable to reach performances equivalent to the inductors fabricated by the standard LTCC technology using screen-printing as the metal-deposition technique. This route can be useful for other kind of applications where the electrical

resistance does not need to be as low as possible, but certain values, impossible to reach by just inkjet, should be obtained.

In the case of the third route, electrical sheet resistance as low as the screen-printed inductors is approached. Increasing the immersion time in the electroless bath, even lower ones could be achieved. The functional characterization of the inductors fabricated by this third route as commented in the following section.

6.4.2- Functional characterization

The electromagnetic characterization of all inductors has been carried out using an ES071C Vector Network Analyzer (VNA) from Keysight Technologies in the installation of RF group from the UB. The samples have been connectorized using a removable end launch SMA connector from Southwest Microwave Inc. Fig. 24 shows an example of the final assemblies. On the top of the figure reference and inkjet + electroless 6 turn inductors are shown. In order to characterize and model the effects of pads and the removable SMA connector test structures (i.e. open and short) have also been designed and fabricated. These test structures are shown on the bottom of Fig. 24. The scattering parameter S11 has been measured in the frequency range from 1 MHz to 2 GHz for all the samples and test structures. The pad + connector modeling as well as the de-embedding of their effects from the scattering parameter measurements of the inductors have been carried out using the processing capabilities of the Advanced Design System (ADS) from Keysight Technologies.

Fig. 24: Example of connectorized 6 turns spiral inductors fabricated using LTCC technology combined with inkjet printing and electroless growth (top left) and standard LTCC technology (top right). Connectorized open and short test structures used for de-embedding are also shown (bottom).

From the corrected data after de-embedding the Equivalent inductance and de Quality factor of the inductors have been calculated according to the following expressions:

$$L_{eq} = \frac{imag\ (Z_{ind})}{2 \cdot \pi \cdot f} \qquad [5]$$

$$Q = \frac{imag\ (Z_{ind})}{real\ (Z_{ind})} \qquad [6]$$

where, Z_{ind}, is the inductor impedance derived from the scattering parameter and, f, is the measurement frequency. Fig. 25 shows an example of the obtained results. The equivalent inductance and the quality factor of two 8 turns inductors are plotted on the figure. Continuous lines correspond to the reference inductor fabricated using the standard LTCC process. Dashed lines correspond to the inductor fabricated using LTCC combined with Inkjet printing and electroless deposition.
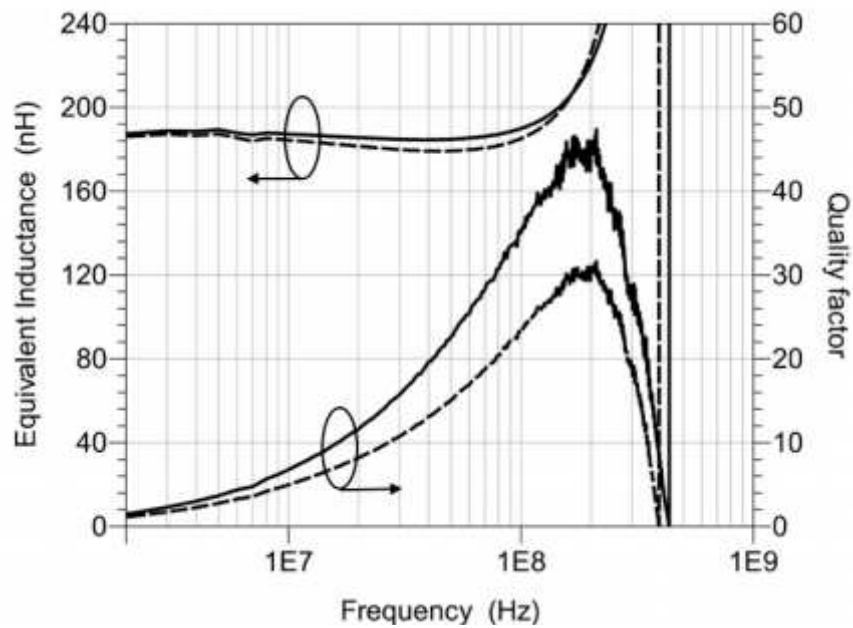
Fig. 25: Equivalent inductance and Q-factor of 8 turns inductors. Continuous lines represent screen-printed inductor performance and dashed lines the inkjet+ Cu electroless inductor performance.

6.4.3- Discussion

In Fig. 25 it can be observed that at low frequencies both inductors, SP and IP, have almost the same equivalent inductance (187 nH and 186 nH, respectively). This fact confirms that both structures have almost the same geometrical dimensions. Concerning the quality factor, the maximum appears at about 200 MHz for both inductors. However, there is a difference in the peak value. For the reference sample, $Q_{max} \approx 45$, while for the inkjet + electroless sample, $Q_{max} \approx$ 30. This result is consistent with the difference in the sheet resistance values (i.e. 2 mΩ/ and 3 mΩ/, respectively). Looking at the self-resonance frequency (SRF), at which the equivalent inductance and the quality factor go down to zero, a weak difference between both inductors structures is found. For the reference sample, SRF ≈ 435 MHz, while for the inkjet + electroless sample, SRF ≈ 393 MHz. This result is consistent with an increase in the fringing capacitance between turns in the inkjet + electroless sample due to the lateral overgrowth of copper. The same behavior is observed when 4 turns and 6 turns inductors are compared. Table 1 summarizes the obtained results for the whole set of samples under study. The first column corresponds to the sample identification. The suffix "SP" indicates that the sample is a reference inductor fabricated using the standard LTCC technology with screen printing. The suffix "IP+E" indicates that the sample is an inductor fabricated using LTCC technology in combination with Inkjet printing and electroless deposition. The second column shows the number of turns of the circular

spiral. Next column shows the values of the low frequency limit of the equivalent inductance. The peak value of the quality factor and the corresponding frequency are shown in the fourth column. Finally, the last column shows the values of the self-resonance frequency.

According to these results, the overall performance of the inductors fabricated using the LTCC in combination with inkjet printing and electroless deposition (third route) is quite similar to that of pure LTCC inductors. Moreover, taking into account that thicker copper layers can be obtained just increasing the duration of the autocatalytic process, it could be possible to obtain even better performance using the proposed process combination than using pure LTCC technology. In addition to this, the high resolution of inkjet printing will allow the fabrication of denser spirals with increased inductance density per unit area. However, attention must be paid to control printing dimensions to compensate lateral overgrowth.

Inductor figures				
Sample	# turns	L_{DC} (nH)	Q_{max}	SFR (MHz)
S4_SP	4	36	52@600 MHz	1290
S4_IP+E	4	33	45@590 MHz	1190
S6_SP	6	88	53@350 MHz	742
S6_IP+E	6	85	38@350 MHz	725
S8_SP	8	187	45@200 MHz	435
S8_IP+E	8	186	30@200 MHz	393

Table 1: Results of the performances of different inductors fabricated by screen printing (SP) and inkjet+electroless (IP+E).

6.5- Conclusions

In this work standard LTCC technology, using screen printing, is combined with inkjet printing and electroless growth to fabricate high performance RF inductors. Different routes to increase in thickness by means of different electroless chemical baths have been tested to approach thickness and sheet resistances similar to the screen printing technology. The combination of Ag-Pd catalyzed inkjet ink and the nickel electroless allows the design of thin-line spirals, due to the inkjet technology, and the achievement of very thick lines deposition in a short period of time (16 µm in 20 min), being the high resistivity of Ni (in comparison with silver or copper) the main drawback of this route. Nevertheless, a different route using also the catalyzed ink and the copper deposition, better results are obtained even if the deposition rate is much lower than for nickel route (6 µm in 2.5 h). Important to highlight is the necessity of the catalyzed ink to achieve a reasonable deposition rate (less than 1 µm in 2h is obtained without Pd catalyst).

The electromagnetic behavior of the resulting devices with copper deposition has been characterized in the frequency range from 1 MHz and 2 GHz. The obtained results in terms of Equivalent inductance and Quality factor have been compared with those corresponding to inductor devices fabricated using standard LTCC technology with screen printing. For comparison shake, the number of turns of the inductor spiral and the outer dimensions have been kept constant. The overall performance of the inductors fabricated using the LTCC in combination with Inkjet printing and Electroless deposition is quite similar to that of screen-printed inductors. Furthermore, the high printing resolution achievable with inkjet printing, together with the possibility of obtaining thick metal layer by electroless deposition, will allow the fabrication of denser spirals with increased inductance density per unit area without degradation of their quality factor, as well as, the tunability and rapid prototyping of inkjet technology can accelerate the test of design and simulations. Work is under progress to verify these potential capabilities of the proposed technological combination.

References

[1] S. Ahyoune, J. Sieiro, J.M. Lopez-Villegas, N. Vidal, T. Carrasco, F. Ramos, J.M. Fernandez-Sanjuan (2013), *Scalable LTCC library for system-in package design*, Design of Circuits and Integrated Systems DCIS. Donosti.

[2] Y. Cao, R. A. Groves, N. D. Zamdmer, J. O. Plouchart, R. A. Wachnik, X. Huang, T. J. King, C. Hu (2002), *Frequency-independent equivalent circuit model for on-chip spiral inductors*, Proceeding IEEE Custom Integrated Circuits Conference, 217.

[3] E. Pettenpaul, A. G. Siemens, H. Kapusta ; A. Weisgerber ; H. Mampe (1988), *CAD models of lumped elements on GaAs up to 18 GHz*, IEEE Transactions Microwave Theory Techniques 36 (2), 294.

[4] N. A. Talwalkar, C. P. Yue, S. S.Wong (2005), *Analysis and synthesis of on-chip spiral inductors*, IEEE Transactions Electron Devices 52 (2), 176.

[5] W. N. Kuhn, N. M. Ibrahim (2001), *Analysis of current crowding effects in multiturn spiral inductors*, IEEE Transactions Microwave Theory Techniques 49 (1), 31.

[6] A. M. Niknejad (2002), *Analysis, design and optimization of spiral inductors and transformers for Si RF ICs*, IEEE Journal of Solid-State Circuits 33 (10), 1470.

[7] H.-C. Lu , T. B. Chan , C. C.-P. Chen , C.-M. Liu , H.-J. Hsing, P.-S. Huang (2010), *LTCC spiral inductor synthesis and optimization with measurement verification*, IEEE Transactions Advanced Packaging, 33, 160.

[8] A. Eroglu (2011), *Planar inductor design for high power applications,* Progress In Electromagnetics Research B, 35, 53.

[9] I. J. Bahl (2001), *High-performance inductors*, IEEE Transactions on Microwave Theory and Techniques 4, 654.

[10] T. Chiu (2003), *Integrated on-chip inductors for radio frequency CMOS circuits*, Master Dissertation, The Hong Kong Polytechnic University.

[11] J. Aguilera (2001), *A guide for on-chip inductor design in a conventional CMOS process for RF applications*, Applied Microwaves and Wireless, 56.

[12] B. Rejaei, J. L. Tauritz, and P. Snoeij (1998), *A predictive model for si-based circular spiral inductors*, Topical Meeting on Silicon monolithic integrated circuits in RF systems, Ann Arbor, 148.

[13] J. Aguilera, J. Melendez, R. Berenguer, J. R. Sendra, A. Hernandez, J. del Pino (2002), *A novel geometry for circular series connected multilevel inductors for CMOS RF integrated circuits*," IEEE Transactions on Electron Devices 6, 1084.

[14] S. Chaki, S. Aono, N. Anodoh, Y. Sasaki, N. Tanino, O. Ishihara (1995), *Experimental study on spiral inductors*, IEEE International Microwave Theory and Techniques Symposium.

[15] N. M. Nguyen, R. G. Meyer (1990), *Si IC-compatible inductors and LC passive filters*, IEEE Journal Solid-State Circuits, 27 (10), 1028.

[16] K. B. Ashby, W. C. Finley, J. J. Bastek, S. Moinian, I. A. Koullias (1994), *High Q inductors for wireless applications in a complementary silicon bipolar process*, Proceedings Bipolar and BiCMOS Circuits and Technology Meeting, Minneapolis, 179.

[17] J. N. Burghartz, M. Soyuer, and K. Jenkins, "Microwave inductors and capacitors in standard multilevel interconnect silicon technology," IEEE Trans. Microwave Theory Tech, vol. 44, no. 1, pp. 100-103, Jan. 1996.

[18] J.N. Burghartz (1997), *Silicon RF technology - the two generic approaches*, Proceedings 27th European Solid-State Device Research Conferences.

[19]] D. Lovelace, N. Camilleri, G. Kannell (1994), *Silicon MMIC inductor modeling for high volume, low cost applications*, Microwave Journal, 60.

[20] W. B. Kuhn, X. He, and M. Mojarradi (2004), *Modeling spiral inductors in SOS processes*, IEEE Transactions Electron Devices 51 (5), 677.

[21] N. M. Nguyen, R. G. Meyer (1990), *Si IC-compatible inductors and LC passive filters*, IEEE Journal Solid-State Circuits 25 (4), 1028.

[22] K. C. Eun, Y. C. Lee, J. W. Lee, M. S. Song, C. S. Park (2004), *Fully embedded LTCC spiral inductors incorporating air cavity for high Q-factor and SRF*, Proceedings 54th Electronic Components Technology Conference 1, 1101.

[23] A. P. Boutz, W. B. Kuhn, (2011), Performance of High-Q Inductors in LTCC using FTTF Techniques, IEEE Transactions on components, packaging and manufacturing technology 1, 8, 1125.

[24] V. Pynttäri, E. Halonen, H. Sillanpää, M. Mäntysalo, R. Mäkinen (2012), *RF Design for inkjet technology: antenna geometries and layer thickness optimization,* IEEE Antennas and Wireless Propagation Letters 11, 188.

[25] M. Mäntysalo, P. Mansikkamäki (2009), *An inkjet-deposited antenna for 2.4 GHz applications*, AEU, International Journal Electronics and Communications 63 (1), 31.

[26] A. K. Sowpati, V. K. Palukuru, V. Pynttari, R. Maikinen, M. V. Kartikeyan, H. Jantunen (2010), *Performance of printable antennas with different conductor thickness*, Progress In Electromagnetics Research Letters 13, 59.

[27] V. Pynttari, R. M. Makinen, V. K. Palukuru, K. Ostman, H. P. Sillanpaa, T. Kanerva, T. Lepisto, J. Hagberg, H. Jantunen (2010), *Application of wide-band material characterization methods to printable electronics*, IEEE Transactions Electronics Packaging Manufacturing 33 (3), 221.

[28] B. S. Cook, Y. Fang, S. Kim, T.Le,W. B. Goodwin, K. H.Sandhage, M. M. Tentzeris (2013), *Inkjet catalyst printing and electroless copper deposition for low-cost patterned microwave passive devices on paper*, Electronic Materials Letters 9 (5), 669.

[29] I. Ortego, N. Sanchez, J. Garcia, F. Casado, D. Valderas, J. I. Sancho (2012), *Inkjet printed planar coil antenna analysis for NFC technology applications*, International Journal of Antennas and Propagation 2012, 1.

[30] B. Cook , C. Mariotti , J. Cooper , D. Revier , B. Tehrani , L. Aluigi , L. Roselli, M. Tentzeris (2014*), Inkjet-printed, vertically-integrated, high-performanceinductors and transformers on flexible LCP substrate*, IEEE MTT-S International Microwave Symposium, 1.

[31] Wagner, W. Traud (1938), *Z. Electrochemistry* 44, 391.

[32] E. J. O'Sullivan (2002), *Fundamental and practical aspects of the electroless deposition reaction*, Chapter 5, Advances in Electrochemical Science and Engineering, R.C. Alkire and D.M. Kolb, Wiley - VCH, 225

[33] P. Bindra, J. R. White (1990), *Fundamental Aspects of Electroless Copper Plating*, Electroless Plating - Fundamentals and Applications, G.O. Mallory and J.B. Hajdu, William Andrew Publishing/Noyes, 289.

[34] G.A. Krulik (1982), *Tin-Palladium Catalysts for Electroless Plating. Their widespread use during the coating of non-conducting substrates***,** Platinum Metals Review 26, 58.

[35] C.-C. Tseng, Y.-H. Lin, Y.-Y. Shu, C.-J. Chen, M.D. Ger (2011), *Synthesis of vinyl acetate/Pd nanocomposites as activator ink for ink-jet printing technology and electroless copper plating*, Journal of the Taiwan Institute of Chemical Engineers 42 (6), 989.

[36] A. Shridbar, D. J. van Dijk, R. Akkerman (2009), *A comparative study of two conductive inkjet inks for fabrication of RF circuit structures,* Large-area, Organic & Printed Electronics Convention, LOPE-C 2009, 23.,

[37] C.-Y. Kao, K.-S. Chou (2007), *Electroless copper plating onto printed lines of nanosized silver seeds*, Electrochemical and Solid-State Letters 10 (3), 32.

[38] M. Kato, K. Niikura, S. Hoshino, I. Ohno (1991), *Electrochemical behavior of electroless gold plating with ascorbic acid as a reducing agent*, Journal of The Surface Finishing Society of Japan 42 (7) 729.

[39] H. Watanabe, H. Honma (1998), *Direct electroless nickel plating on copper circuits using DMAB as a second reducing agent*, IEMT/IMC Symposium, 2nd 1998, 149.

[40] I. Ohno, S. Wakabayashi, S. Haruyama (1985), *Anodic oxidation of reductants in electroless plating*, Journal Electrochemical Society 132 (10), 2323.

[41] E. Diaz, E. Ramon, J. Carrabina (2013), *Inkjet patterning of multiline intersections for wirings in printed electronics*, Langmuir 29 (40), 12608.

[42] F. Ramos (2014), *Integración de la tecnología cerámica multicapa*, PhD. Dissertation, Barcelona, Spain.

[43] Y. Shacham-Diamand, V. M. Dubin (1997), *Copper electroless deposition technology for ultra-large-scale-integration (ULSI) metalization*, Microelectronics Engineering 33, 47.

[44] R. Cauchois, M. Saadaoui, J.Legeleux, T. Malia (2010), *Wire-bonding on inkjet-printed silver pads reinforced by electroless plating for chip on flexible board packages*, Proceeding 3rd Electronic Systems and Integration Technology Conference, Berlin, 1.

[45] E. Steinhäuser (2010), *Potential low-cost palladium-alternatives for activating electroless copper deposition*, Circuit World 36 (3), 4.

Conclusions and future works

The main objective was expanding the knowledge on inkjet printing (IP) by exploring affordable new possibilities, taking as starting point the previous knowledge of screen printing (SP). To pursue this goal, the comparison between a mature and reliable technology that has already been well-accepted in the industry for years, SP, and a rising-up technique that is pushing hard into the electronic market, IP, is presented during this thesis.

A quick overview of the two printing techniques is done in the following paragraph:

Screen printing is a mature and conventional technology which requires a mask or pattern to perform printing, needing a tiresome and laborious preprocessing of pattern manufacturing. SP is compatible with highly viscous materials, including conductive pastes and even dielectric adhesives. In general, SP pastes are suitable for high concentration and high temperature substrates such as ceramic technology.

Unlike conventional technologies, Inkjet does not need a prefabricated mask and it is also a non-invasive technique being contactless with the substrate. One of the main premises of IP is its accurate positioning and precise volume drop of microliters of the functional material, providing the possibility to print very close conductive tracks (tens of microns) and extremely thin layers (< 0.3 μm) and thus minimizing device size and manufacturing costs, owing to the reduced amount of material waste. IP inks must contain nano-sized particles (< 100 nm) to not clog the nozzles of the printer, and their physicochemical properties are much more restrictive than for SP (8-12 cps viscosity and surface tension 25-35 dynes/cm).

This thesis has been not solely an overview of the techniques fundamentals and the development of functional materials, but also the investigation of its final implementation reliability in several devices for different electronic applications. After the application of both technologies in several fields, the general conclusions that can be drawn are listed below:

(1) The ink formulation for IP is much more restrictive and complex than paste formulation. Because of that, a good control of the physical parameters and even the nanoparticles size becomes crucial for a good quality printing. Nevertheless, non-particulate precursor inks can be formulated much more easily than for SP pastes, due to the possibility of managing without binder and other rheology promoters.

(2) IP is a good alternative to the SP technique for some electronic devices, especially in those ones whose rapid prototyping can offer key information for the design and the corroboration of the performance simulations.

(3) Those devices which are liable to the corrosion, the smaller particle size in IP promotes particle sintering at lower temperature and because of that, it can partially prevent it. However, the smaller thickness in each printing deposition can lead to more frequent defects and in case of heaters, more frequent hot spot locations.

(4) IP is suitable for the fabrication of devices which require of very thin layers of less than few microns. SP cannot afford this kind of thickness deposition.

(5) Even being an advantage for some applications, the same very thin layers affordable for IP becomes a drawback in those electronic applications where lowering the sheet resistance is a crucial feature. The poor thickness is an issue to solve in, for example, RF devices. Printing many layers to obtained several microns cannot be competitive with SP and complementary techniques are needed to overcome this problem. In this thesis has been demonstrated that the combination of IP and electroless can be an alternative to SP for RF applications

Specific conclusions in each application field are:

(1) Regarding flexible electronics, the fabrication of reliable devices is a challenge. Common flexible substrates require low temperature post-treatment what implies silver as the most widely used material for conductive tracks. During this thesis the need of silver protection to prevent the atmosphere corrosion because of its detrimental effect on the device performances has been demonstrated. Most concretely, it has been observed that the morphology of the silver deposit strongly affects the corrosion rate. In this regard, the smoothness of the inkjet-silver deposit due to the complete nanoparticle sintering, hinders the attack of corrosion agents in comparison with the flake-like structure of the silver paste for screen printing. However, the thin film obtained by inkjet printing promotes failure by hot spot phenomena. Both kind of failure are prevented by the isolation from the atmosphere by an adhesive polyimide tape or gold protection by a chemical plating bath. It has been also demonstrated that the synergetic combination of polymeric substrates with printed electronics is a good alternative to substitute the monolithic silicon and the ceramic technologies in gas sensor platforms, because of its

low-cost, what is corroborated with the estimated pricing showed in this thesis, and its low-powered consumption heaters.

(2) Inkjet printing becomes an interesting technique for solution-based fabrication of thin film solar cells. The replacement of vacuum steps by atmospheric processes significantly reduces the manufacturing cost of solar cells and modules. Digital printing, such as inkjet, allows the possibility of module fabrication without the need of scribing. In this thesis it has been demonstrated the suitability of inkjet printing for the CZTS precursor deposition for the absorber layer and the importance of the thickness in the cell structure. Cells of 6.55 % of efficiency have been developed after the reduction of sulfur content in the ink formulation and the optimization of the layer thickness. Reducing the sulfur content seems to reduce the secondary phases formation during the kesterite crystallization and the optimized thickness rose up to 2 μm. These results were achieved without grid or anti-reflective coating, what means that the cell performance could be improved even more including these components in the final cell fabrication.

(3) In RF applications, IP introduces the handicap of the lacking thickness of every printing layer. In these cases, screen printing is the best option because of the proper deposition thickness that allows good sheet conductivities. Nevertheless, this inkjet printing drawback can be overcome by electroless deposition and furthermore, increase the potential of rapid prototyping and resolution that inkjet can offer over screen printing. This has been demonstrated in the fabrication of spiral inductors using both printing techniques and achieving similar electromagnetic performances.

In the field of thin films solar cells, work is still in progress to optimize the ink formulation in terms of zinc and sulfur content and the addition of doping agent as sodium. Besides, it should be considered the advantages of the digital printing of inkjet technology for the design of individual solar cells properly arranged in serial or parallel becomes an interesting approach that should be considered. Furthermore, other parts of the solar cell, such as the transparent front contact or the silver metallic grid, can be also printed by inkjet.

Regarding RF inductors, the fabrication of denser spirals with increased inductance density per unit area without degradation of their quality factor will be possible due to the high printing resolution achievable with inkjet printing and then, the target of sheet resistance can be met by the increase in thickness by electroless deposition. Moreover, the tunability and rapid prototyping

of inkjet technology can accelerate the test of design and simulations. Work is under progress to verify these potential capabilities of the proposed technological combination.

Resumen en lengua oficial

Introducción

La electrónica impresa permite la impresión de dispositivos electrónicos mediante técnicas propias de las artes gráficas, como son la serigrafía (*screen-printing*) y la inyección de tinta (*inkjet-printing*), con la particularidad de que utiliza tintas con propiedades eléctricas: conductoras, semiconductoras o aislantes. La electrónica impresa ofrece una gran ventaja en comparación con procesos tradicionales o la microelectrónica debido a su versatilidad, bajo coste de producción y posibilidad de generar componentes y circuitos flexibles.

La selección del método de impresión es crucial a la hora de alcanzar un buen resultado y depende en gran parte de los materiales necesarios y de los requerimientos dimensionales y funcionales que se pretendan alcanzar. La serigrafía, el huecograbado y la flexografía son las principales técnicas de impresión convencional. En general, este tipo de tecnologías requieren una máscara o patrón para poder realizar la impresión, necesitando así un preproceso de fabricación adicional. A diferencia de las tecnologías convencionales, la impresión digital como la impresión por inyección de tinta no necesita una máscara prefabricada y además no entra en contacto con el sustrato. La colocación exacta y precisa de la gota de volumen micrométrico facilita la impresión de pistas conductoras muy estrechas (unas decenas de micras) y minimiza así el tamaño del dispositivo, los costes de material y la fabricación. Pero a diferencia de la serigrafía, la inyección de tinta para electrónica aún muestra un gran desafío en cuanto a rendimiento y reproducibilidad comparada con las mejores técnicas convencionales, así como en la disponibilidad de materiales funcionales en el mercado. Aun así, cada tecnología ofrece posibilidades diferentes en cuanto a complejidad, resolución, grosor de capas y materiales.

La disponibilidad de las tintas o pastas de diferentes materiales no está compensada en ambas tecnologías: mientras que para serigrafía existe un mercado maduro, la formulación de tintas *inkjet* que se adapten a las exigencias de las diferentes aplicaciones o procesados (temperaturas de proceso/funcionamiento, adhesión, funcionalidad…) es de gran complejidad y es un tema de investigación actual. El reducido tamaño de las nanopartículas dificulta la producción de tintas con alta concentración debido a la fuerte aglomeración que presentan. Este hecho junto al grosor nanométrico de la capa de tinta depositada por *inkjet* limita la respuesta funcional de la impresión.

En esta tesis, las dos técnicas han sido empleadas ante diferentes escenarios donde los requerimientos se han definido por la funcionalidad y la aplicación del dispositivo a desarrollar.

Estructura de la tesis

En el primer capítulo se definen los objetivos de la tesis y se describe su estructura.

Los dos siguientes capítulos describen la inyección de tinta (Capítulo 2) y la serigrafía (Capitulo 3) en términos de fundamentos, parámetros y formulación de materiales funcionales adaptados a los requisitos de cada metodología.

La inyección de tinta ha ganado atención en los últimos años ya que es una técnica no invasiva, que no necesita máscara y que ofrece una alta resolución en comparación con la serigrafía, el cual consiste en el movimiento de una rasqueta (*squeegee*) que empuja la tinta (o pasta funcional) sobre la malla de una pantalla introduciéndola en las áreas abiertas y dejando así la deposición del material sobre el sustrato.

El capítulo 2 es una hoja de ruta para la formulación de tintas eyectables por *inkjet* y la optimización de parámetros de impresión para la obtención de una impresión de calidad. A su vez, dicha ruta es ilustrada mediante el seguimiento de la formulación de una tinta conductora de plata desarrollada durante esta tesis. En una primera parte se describe las propiedades críticas de un fluido para la predicción de su *printabilidad* por el método de inyección de tinta. Las tintas adecuadas para esta técnica debe contener partículas de tamaño nanométrico (< 100 nm) para no obstruir los *nozzles* de la impresora, y sus propiedades físico-químicas son mucho más restrictivas que para la serigrafía (viscosidad de entre 8-12 cps y tensión superficial de 25-35 dynes/cm). En segundo lugar, se describen los indicadores de calidad de la impresión, que son función directa de la optimización de los parámetros de impresión como de la interacción tinta-sustrato y, por último, la validación de la funcionalidad.

El capítulo 3 describe los fundamentos y los principales parámetros en el proceso de serigrafía, así como una revisión a la reología, componentes y proceso de fabricación de las pastas funcionales. Como ejemplo del proceso de formulación y fabricación de pastas se ha explicado paso por paso la selección de componentes y fabricación, así como la posterior caracterización de dos pastas conductoras elásticas basadas en plata y nanofibras de carbono. Es compatible con materiales altamente viscosos, incluyendo tintas conductoras, pastas dieléctricas e incluso adhesivos. En

general, las pastas de serigrafía son de alta concentración y adecuadas para sustratos de alta temperatura de procesado como la cerámica.

A lo largo de los capítulos 4, 5 y 6, el potencial de ambas tecnologías de impresión ha sido estudiado en diferentes escenarios mediante la implementación de la etapa de impresión en la fabricación de diferentes dispositivos electrónicos y su afección en la funcionalidad final del dispositivo.

El capítulo 4 es una comparación de la fiabilidad y robustez de plataformas sensoras flexibles de bajo coste fabricadas por inyección de tinta o serigrafía, donde se ha encontrado una relación directa entre la morfología de la plata depositada por ambas técnicas y su causa de fallo en funcionamiento prolongado. A lo largo del capítulo se han implementado mejoras en el diseño para la prevención de fallos prematuros evitando la degradación de las pistas de plata.

En el capítulo 5, la posibilidad de imprimir capas muy finas mediante inyección de tinta se ha empleado para la síntesis de precursores de la capa absorbente en una celda solar de tecnología de capa fina. La formulación y optimización de una tinta de precursores de cobre, zinc, estaño y azufre (CZTS) ha sido empleada para la formación de kesterita. La influencia de la etapa de impresión y secado en la formación de los cristales de kesterita, así como su posterior influencia en la funcionalidad de la celda ha sido estudiada. Finalmente, se han obtenido celdas de 6,55% de eficiencia, siendo la más alta reportada hasta la fecha utilizando este tipo de absorbente por *inkjet*.

En el capítulo 6, la fabricación de inductores en LTCC deja patente la desventaja de la inyección de tinta sobre la serigrafía para aplicaciones de radiofrecuencia (RF), donde su escaso grosor de capa es un claro hándicap para la obtención de conductividades elevadas. Dicho factor limitante es abordado con la combinación de la inyección de tinta con la deposición química (*electroless*) de níquel y cobre. Se han obtenido inductores con funcionalidad equivalente fabricados por serigrafía y combinación de inyección de tinta y deposición química de cobre. Al solventar la problemática del grosor como factor limitante, el potencial que la inyección de tinta presenta para la fabricación de inductores con mayor densidad de espiras y así para la reducción del área, crea gran interés y queda pendiente como trabajo futuro.

Conclusiones

Esta tesis no ha sido sólo una visión general de los fundamentos de las dos tecnologías y el desarrollo de materiales funcionales adecuados a ellas, sino también el estudio de su fiabilidad en su implementación en varios dispositivos electrónicos para diferentes aplicaciones. Después de aplicar ambas tecnologías en varios campos, las conclusiones generales que pueden extraerse son los siguientes:

(1) La formulación de tinta para inyección de tinta es mucho más restrictiva y compleja que la formulación de pasta para serigrafía. Debido a eso, un buen control de los parámetros físicos e incluso sobre el tamaño de las nanopartículas se convierte en un aspecto crucial para obtener una buena calidad de impresión. Sin embargo, las tintas no-particuladas de precursores pueden formularse mucho más fácil que para pastas de serigrafía, debido a la posibilidad de gestionar sin ligante y otros promotores de la reología.

(2) La inyección de tinta es una buena alternativa a la técnica de serigrafía para algunos dispositivos electrónicos, especialmente en aquellos cuya fabricación rápida de prototipos puede ofrecer información clave para el diseño y la corroboración de las simulaciones.

(3) En aquellos dispositivos que son susceptibles a la corrosión, el tamaño de partícula para *inkjet*, que es mucho menor que para serigrafía, promueve la sinterización a una temperatura menor y debido a eso, la corrosión se puede prevenir parcialmente. Sin embargo, las capas tan finas que son depositadas por esta técnica puede dar lugar de manera más frecuente a defectos y, en el caso de calefactores, a puntos calientes que llevan al fallo del dispositivo.

(4) La inyección de tinta es adecuada para la fabricación de dispositivos que requieren capas muy finas, de menos de unas pocas micras. La serigrafía no puede competir en estos valores de espesor.

(5) Aun siendo una ventaja para algunas aplicaciones, las capas tan delgadas depositadas por *inkjet* se convierte en un inconveniente en aquellas aplicaciones electrónicas donde la reducción de la resistencia cuadro es una característica crucial. El escaso espesor es un problema a resolver, por ejemplo, en los dispositivos de radiofrecuencia. La impresión de muchas capas para obtener varias micras de grosor no puede competir con serigrafía y son necesarias técnicas complementarias para superar este problema. En esta tesis se ha demostrado que la combinación de *inkjet* y *electroless* puede ser una alternativa a la serigrafía para aplicaciones de RF.

Las conclusiones de forma más específica en cada campo de aplicación que se ha estudiado en esta tesis son:

(1) En cuanto a la electrónica flexible, la fabricación de dispositivos fiables es un desafío. Los sustratos flexibles comunes requieren baja temperatura en el post-tratamiento para el curado del material depositado y esto ha implicado que la plata sea el material más utilizado para las pistas conductoras. La plata es un material susceptible a la corrosión y durante esta tesis se ha demostrado la necesidad de la protección de las pistas para evitar el mal funcionamiento del dispositivo en funcionamiento prolongado. Más concretamente, se ha observado que la morfología del depósito de plata afecta fuertemente la velocidad de corrosión. En este sentido, la superficie lisa del depósito por inyección de tinta de plata que se obtiene tras la sinterización de las nanopartículas, dificulta el ataque de los agentes de corrosión, a diferencia de la estructura en forma de escamas de las pastas de plata de la serigrafía. Sin embargo, la película muy fina obtenida por impresión de *inkjet* promueve el fallo por fenómenos de puntos calientes. Ambos tipo de fallos se impide por el aislamiento de la atmósfera por una cinta de poliimida adhesivada o protección de oro por baño químico. También se ha demostrado que la combinación sinérgica de sustratos poliméricos con la electrónica impresa es una buena alternativa para sustituir el silicio monolítico y las tecnologías de cerámica en plataformas de sensores de gas, debido a su bajo coste, lo que se corrobora con el precio estimado mostrado en este tesis, y el bajo consumo de potencia de sus calefactores.

(2) La impresión de inyección de tinta se convierte en una técnica interesante para la fabricación de células solares de capa fina. La sustitución de las etapas de vacío por procesos atmosféricos reduce significativamente el coste de fabricación de células solares y módulos. En esta tesis se ha demostrado la idoneidad de la impresión de inyección de tinta para la síntesis de la capa absorbente de la celda solar usando precursores de cobre-zinc-estaño-azufre (CZTS). Se ha conseguido celdas de 6,55% de eficiencia tras la reducción del contenido de azufre en la formulación de la tinta y la optimización del espesor de capa. La reducción del contenido de azufre parece reducir la formación de fases secundarias durante la cristalización de la kesterita (CZTSSe) y el espesor optimizado subió hasta las 2 μm. Estos resultados se lograron sin rejilla metálica ni revestimiento anti-reflectante, lo que significa que el rendimiento de la celda se puede mejorar aún más con la inclusión de estas etapas en la fabricación final de la celda.

(3) En aplicaciones de RF, la inyección de tinta presenta la desventaja del escaso espesor de cada capa de impresión. En estos casos, la serigrafía es la mejor opción debido al grosor de depósito adecuado que permite buenas conductividades. Sin embargo, este inconveniente para *inkjet* se

puede superar mediante *electroless* y, además, aprovechar el potencial del *inkjet* debido a su alta resolución y al prototipado rápido. Esto se ha demostrado en la fabricación de inductores de espiral utilizando ambas técnicas de impresión logrando comportamientos electromagnéticos similares.

En el campo de las celdas fotovoltaicas de capa fina, la formulación de la tinta aún se debe optimizar en términos de contenido de zinc y azufre para mejorar la eficiencia de la celda. El dopaje alcalino de la capa de absorbente mediante la adición de sodio dentro de la formulación de la tinta, es de gran interés y se trabajará en un futuro. Además, se debe considerar las ventajas de la impresión digital de la tecnología de inyección de tinta para el diseño de células solares individuales adecuadamente dispuestas en serie o en paralelo se convierte en un enfoque interesante que debe ser considerado. Asimismo, tras partes de la celda solar, como el contacto frontal transparente o la rejilla metálica de plata, pueden ser impresas por *inkjet*.

En cuanto a los inductores de RF, la fabricación de inductores con mayor densidad de espiras para aumentar la inductancia por unidad de área sin detrimento de su factor de calidad será posible debido a la alta resolución de impresión alcanzable con *inkjet* y la posibilidad de alcanzar la conductividad adecuada por *electroless.* Por otra parte, la capacidad de ajuste y el rápido prototipaje de la tecnología de inyección de tinta pueden acelerar pruebas de diseño y simulaciones. Se está trabajando en el progreso para verificar estas capacidades potenciales de la combinación tecnológica propuesta.